



Agir, Muhammed Burak (2023) *Investigation of flow-flow, flow-surface, and multiphase interaction problems in rarefied gas dynamics*. PhD thesis.

<https://theses.gla.ac.uk/83405/>

Copyright and moral rights for this work are retained by the author

A copy can be downloaded for personal non-commercial research or study, without prior permission or charge

This work cannot be reproduced or quoted extensively from without first obtaining permission from the author

The content must not be changed in any way or sold commercially in any format or medium without the formal permission of the author

When referring to this work, full bibliographic details including the author, title, awarding institution and date of the thesis must be given

Enlighten: Theses

<https://theses.gla.ac.uk/>  
[research-enlighten@glasgow.ac.uk](mailto:research-enlighten@glasgow.ac.uk)

# Investigation of Flow-Flow, Flow-Surface, and Multiphase Interaction Problems in Rarefied Gas Dynamics

Muhammed Burak Agir

Submitted in fulfilment of the requirements for the  
Degree of Doctor of Philosophy

Aerospace Sciences Research Division  
James Watt School of Engineering  
College of Science and Engineering  
University of Glasgow



June 2022



# Abstract

Presently, with the development of technology, the need to study and understand high-speed rarefied gas flows has become an impending reality in terms of its potential assets to a wide spectrum of industries, ranging from interplanetary travel to coating technology. This study addresses the interactions of high-speed rarefied gas flows with one another, surfaces, and solid particles in order to ascertain high-speed rarefied gas behaviours in various applications. Three different interaction scenarios -two of which rely on numerical analysis and one which is based on the development of a novel solver- are investigated, where computations are conducted with a direct simulation Monte Carlo (DSMC) solver, *dsmcFoam+*, and a particle-laden rarefied gas multiphase flow solver, *rarefiedMultiphaseFoam*, within the framework of an open-source tool, OpenFOAM.

Rarefied shock-shock interactions have a crucial impact on aerodynamic performance and aero-heating characteristics in supersonic and hypersonic flight platforms. A shock-shock interaction problem can arise in high-speed vehicles, where an oblique shock on one part of the body impinges on a bow shock from a different part of the body and the nature of the interaction can change as the vehicle increases in altitude to a more rarefied environment. Part of this research examines the outcomes of a numerical study investigating the formation of Edney shock patterns from type-I to type-VI as a result of shock-shock interactions at different rarefaction levels. The free-stream flow is at a Mach number of 10. Both geometrical and rarefaction parameters in shock-shock interaction problems determine what type of Edney pattern is formed. As the flow becomes more rarefied, the regions of enhanced thermo-mechanical loading spread further over the surface but their peak values decrease. It is known that these shock interactions can have unsteady behaviour in the continuum regime; current works show that although increasing rarefaction tends to move the flow towards steady behaviour, it is still possible to have unsteady flow behaviour under more rarefied conditions.

In another case, the interactions of high-speed rarefied flows with one another and a surface are analysed. The canting axis of thrusters on space platforms, which likely operate in a vacuum environment with a high degree of flow rar-



efaction, is significant in order to create the desired torque for manoeuvring, maintaining orbit, eliminating perturbation forces, docking, etc. Therefore, the interactions of expanding plumes with one another and with solid surfaces in multi-nozzle arrays are inevitable. In order to gain a better understanding of the effect of nozzle configurations and conditions on the plume-plume and plume-surface interactions, a simulation matrix is carried out for a sonic nozzle. As nozzle arrays are packed more tightly together, the plume-plume interactions become stronger, which has an influence on the stagnation line density and temperature profiles. For a given stagnation temperature, the spacing between nozzles in the array does not have a strong influence on the normalised surface pressure, but there is an increase in the maximum normalised shear stress as the distance between the nozzles increases. There is a significant difference in the results for double and quadruple nozzle arrays, with greater normalised stagnation pressures and shear stresses found as the number of nozzles in the array is increased. For a single nozzle, increasing the stagnation temperature does not have a significant effect on the normalised surface pressures, but does increase the maximum normalised shear stress and the measured heat flux on the surface. For arrays of double and quadruple nozzles, the number of nozzles has a much greater influence on the measured surface pressure, surface shear stress, and surface heat transfer than the stagnation temperature. In the last case, the effect of the impingement height on the plume and surface parameters is discussed while maintaining all the parameters of the 1000 K single plume case but with varying impingement heights. It is found that the smaller impingement height results in a denser plume, and a greater impact on the surface. However, higher impingement heights result in a wider distribution on the surface as the plume can expand more.

With the awareness of a lack of a solver for rarefied gas flows-solid particle interactions, the final case in this thesis focuses on the development, benchmarking and testing of a multiphase open-source code, *rarefiedMultiphaseFoam*. Such a solver provides applicable benefits such as modelling of the transport of unburnt solid propellant in rocket a plume, and simulating of the impingement of two-phase plume on a surface in a vacuum environment, as well as providing numerical solutions in terms of surface coating technology, where multiphase gas and solid flows are employed, etc. This *dsmcFoam+* based solver is capable of simulating one-way coupling interactions. This type of particle-laden rarefied gas flow has two components: the rarefied gas flow itself and the solid particles transported by the gas flow. The main restriction is that the solid phase surrounded by the gas phase is assumed to be in the free-molecular regime with respect to the solid particle diameters and that it is a one-way coupling, so that only the

effect of gas particles on the solid particles is considered. *rarefiedMultiphaseFoam* can produce results for steady and transient one-way coupling problems in zero-dimensional (0D), one-dimension (1D), two-dimensions (2D) (both planar and axisymmetric), and three-dimensions (3D). Two benchmarking cases on momentum and energy transfer from gas molecules to solid particles, and free expansion of a two-phase jet flow are presented. The reliability of the solver is further demonstrated through a test case on surface coating using the Aerosol Deposition Method. The benchmarking cases yield results that are in good agreement with theoretical, experimental, and numerical data in the literature.



**University of Glasgow**  
**College of Science and Engineering**  
**Statement of Originality**

**Name:** Muhammed Burak Agir

**Registration Number:**

I certify that the thesis presented here for examination for a PhD degree of the University of Glasgow is solely my own work other than where I have clearly indicated that it is the work of others (in which case the extent of any work carried out jointly by me and any other person is clearly identified in it) and that the thesis has not been edited by a third party beyond what is permitted by the University's PGR Code of Practice.

The copyright of this thesis rests with the author. No quotation from it is permitted without full acknowledgement.

I declare that the thesis does not include work forming part of a thesis presented successfully for another degree.

I declare that this thesis has been produced in accordance with the University of Glasgow's Code of Good Practice in Research.

I acknowledge that if any issues are raised regarding good research practice based on review of the thesis, the examination may be postponed pending the outcome of any investigation of the issues.

**Signature:** Muhammed Burak Agir

**Date:** 30.06.2022



# Publications

- **M.B. Agir**, C. White, K. Kontis, “The Effect of Increasing Rarefaction on the Formation of Edney Shock Interaction Patterns: Type-I to Type-VI”, *Shock Waves*, vol. 32, pp. 733–751, 2022.
- C. White, Z. Cao, **M.B. Agir**, and N. Vasiliadis, “Drag on a Sphere Over a Range of Knudsen Numbers and Speed Ratios”, In *32nd International Symposium on Rarefied Gas Dynamics, Seoul, South Korea*, July 2022.
- **M.B. Agir**, C. White, and K. Kontis, “Impact of Stagnation Temperature and Nozzle Configuration on Rarefied Jet Plume Interactions,” *Journal of Spacecraft and Rockets*, vol. 59, no. 5, pp. 1536-1551, 2022.
- Z. Cao, **M.B. Agir**, C. White, K. Kontis, “An OpenFOAM Based DSMC Solver For Rarefied Two-phase Flow”, *Computer Physics Communications*, vol. 276, p. 108339, 2022.
- G. Li, **M.B. Agir**, K. Kontis, T. Ukai, and S. Rengarajan, “Image Processing Techniques for Shock Wave Detection and Tracking in High Speed Schlieren and Shadowgraph Systems”, In *Journal of Physics: Conference Series*, vol. 1215, no. 1, p. 012021, 2019.



# Contents

<b>Abstract</b>	<b>i</b>
<b>Publications</b>	<b>vii</b>
<b>List of Tables</b>	<b>xiii</b>
<b>List of Figures</b>	<b>xv</b>
<b>Nomenclature</b>	<b>xxi</b>
<b>Acknowledgements</b>	<b>xxvi</b>
<b>1 Introduction</b>	<b>1</b>
1.1 A Background on Rarefied Gas Dynamics . . . . .	1
1.1.1 Classification of Flow Regimes . . . . .	2
1.1.2 Kinetic Theory . . . . .	8
1.2 Thesis Outline . . . . .	12
1.3 Research Objective and Contribution . . . . .	13
<b>2 Direct Simulation Monte Carlo</b>	<b>15</b>
2.1 The Algorithm of DSMC . . . . .	18
2.1.1 Particle Movement . . . . .	20
2.1.2 Collision Procedure . . . . .	21
2.1.3 Sampling and Averaging . . . . .	24
2.2 DSMC Codes . . . . .	25
2.2.1 DS1V, DS2V, and DS3V . . . . .	25
2.2.2 MONACO . . . . .	26
2.2.3 SPARTA . . . . .	26
2.2.4 SMILE . . . . .	27
2.2.5 <i>dsmcFoam</i> , <i>dsmcFoam+</i> . . . . .	27
2.3 A Benchmarking Case: Supersonic Corner . . . . .	30
2.3.1 Problem Description . . . . .	30



2.3.2	Results and Discussion . . . . .	31
2.3.3	Summary . . . . .	37
<b>3</b>	<b>The Effect of Increasing Rarefaction on Edney Shock Interactions</b>	<b>38</b>
3.1	Introduction . . . . .	38
3.2	Computational Considerations . . . . .	44
3.2.1	Problem Description . . . . .	44
3.2.2	High Performance Computing . . . . .	46
3.3	Results and Discussion . . . . .	47
3.3.1	Steady Flow Field . . . . .	49
3.3.2	Unsteady Flow Field . . . . .	62
3.4	Summary . . . . .	65
<b>4</b>	<b>Impact of Stagnation Temperature and Nozzle Configuration on Rarefied Jet Plume-Plume and Plume-Surface Interactions</b>	<b>68</b>
4.1	Introduction . . . . .	68
4.2	Problem Description . . . . .	73
4.2.1	Axisymmetric mesh simulations . . . . .	76
4.2.2	Quarter-symmetry mesh simulations . . . . .	76
4.3	Results and Discussion . . . . .	78
4.3.1	<i>dsmcFoam+</i> benchmarking simulations of single plume application . . . . .	79
4.3.2	Multi-nozzle normal impingement to the surface at a plume stagnation temperature of 300 K . . . . .	82
4.3.3	Increasing stagnation temperature in a single nozzle . . . . .	88
4.3.4	Multi-nozzle normal surface impingement with increasing stagnation temperature . . . . .	91
4.3.5	Changing impingement height in a single nozzle at a plume stagnation temperature of 1000 K . . . . .	96
4.4	Summary . . . . .	99
<b>5</b>	<b>An Open-source One-way Coupling Solver for Two-phase Rarefied Flows: <i>rarefiedMultiphaseFoam</i></b>	<b>102</b>
5.1	Introduction . . . . .	102
5.2	Modelling of Multiphase Flows . . . . .	104
5.2.1	Two-Fluid Model . . . . .	104
5.2.2	Discrete Particle Method . . . . .	105

5.2.3	A Brief Summary of Eulerian-Eulerian and Eulerian-Lagrangian Models . . . . .	105
5.2.4	Modelling of Transport of Solid Spherical Particles in a Rarefied Gas Flow . . . . .	106
5.3	Computational Code Development . . . . .	111
5.4	Benchmark Testing of <i>rarefiedMultiphaseFoam</i> . . . . .	121
5.4.1	Benchmark Case A: Momentum and Energy Transfer from Gas Molecules to Solid Particles . . . . .	121
5.4.2	Benchmark Case B: Free expansion of two-phase jet flow . . . . .	126
5.5	A Test Case: Surface Coating by the Aerosol Deposition Method . . . . .	131
5.6	Summary . . . . .	137
<b>6</b>	<b>Conclusions</b>	<b>138</b>
6.1	Summary . . . . .	138
6.2	Future Work . . . . .	140
<b>7</b>	<b>Appendix</b>	<b>142</b>
7.1	The Contours of Mach Number for Altering Knudsen Number and Cylinder Position . . . . .	142
7.1.1	The free-stream flow at $\text{Kn} = 0.0067$ . . . . .	142
7.1.2	The free-stream flow at $\text{Kn} = 0.0134$ . . . . .	144
7.1.3	The free-stream flow at $\text{Kn} = 0.0268$ . . . . .	145
7.2	Additional Data for Altering Stagnation Temperatures and Orientations of Multi-nozzle Configurations . . . . .	147
7.2.1	Plume Results for $T_0 = 500$ K . . . . .	147
7.2.2	Surface Results for $T_0 = 500$ K . . . . .	148
7.2.3	Plume Results for $T_0 = 700$ K . . . . .	149
7.2.4	Surface Results for $T_0 = 700$ K . . . . .	151
7.2.5	Plume Results for $T_0 = 1000$ K . . . . .	152
7.2.6	Surface Results for $T_0 = 1000$ K . . . . .	153
7.3	Benchmarking of Adhesive Wall Patch . . . . .	154



# List of Tables

2.1	The mesh properties of plates . . . . .	31
3.1	Knudsen numbers, Reynolds numbers, and free-stream densities. .	45
3.2	VHS parameters of the gas species. . . . .	46
3.3	The Edney shock interaction types and flow characteristics with changing Knudsen number, $Kn$ , and the height at which the centre of the cylinder is positioned, $H$ . . . . .	49
3.4	Comparison of type-IV cases for all three Knudsen numbers. $H$ is the cylinder height, $\theta$ is the angular position on the cylinder surface where the peak pressure $C_p$ , is found. . . . .	53
4.1	Initial properties at the sonic nozzle exit for the different stagnation temperatures for axisymmetric single plume applications, where $n$ is number density and $V_{sonic}$ is the sonic velocity. . . . .	74
4.2	Microscopic values for free-jet flow at $T_0 = 300$ K for axisymmetric single plume applications. . . . .	76
5.1	Parameters for the validation simulations of thermophoretic forces.	126
5.2	Simulations parameters of two-phase jet flow free expansion. . . .	128
5.3	Properties of aluminium particles. . . . .	134
5.4	Properties of thermoplastic surface. . . . .	134
5.5	Properties of stuck solid particles at changing source pressures, at $t = 0.001$ s. . . . .	136



# List of Figures

1.1	Classification of the flow regimes by Knudsen number. . . . .	2
1.2	The speed distribution of a dilute gas molecule at an arbitrary temperature. The area of the shaded rectangular shows the probability of finding a molecule in the range of $dv$ . The probability $P$ tends to zero as $v$ tends to infinity. . . . .	9
2.1	Flowchart of DSMC solvers' algorithm. . . . .	19
2.2	An illustration of DSMC cells and particles. . . . .	19
2.3	The used geometry in test case. . . . .	30
2.4	Contours of heat transfer coefficient from (a) <i>dsmcFoam+</i> , and (b) Bird. . . . .	32
2.5	Contours of streamwise skin friction on the x-axis from (a) <i>dsmcFoam+</i> , and (b) Bird. . . . .	33
2.6	Contours of normalised temperature at certain locations from <i>dsmcFoam+</i> , and Bird. . . . .	34
2.7	Contours of normalised density at certain locations from (a) <i>dsmcFoam+</i> , and (b) Bird. . . . .	35
2.8	Contours of Mach number at certain locations from <i>dsmcFoam+</i> , and Bird. . . . .	36
3.1	Edney's shock interaction pattern classifications. BS: bow shock, IP: impingement point, IS: impinging shock, SL: shear layer, TS: transmitted shock. . . . .	39
3.2	A schematic to indicate how the Edney flow patterns may change during a hypersonic flight with an increasing altitude. . . . .	41
3.3	Schematic of the problem set up. . . . .	45
3.4	Benchmarking of <i>dsmcFoam+</i> , through aerothermodynamic load distribution on the cylinder surface. . . . .	47
3.5	Pressure coefficient distributions at $Kn = 0.0067$ . . . . .	51
3.6	Pressure coefficient distributions at $Kn = 0.0134$ . . . . .	51

3.7	Pressure coefficient distributions at $Kn = 0.0268$ . . . . .	52
3.8	Heat transfer coefficient distributions at $Kn = 0.0067$ . . . . .	54
3.9	Heat transfer coefficient distributions at $Kn = 0.0134$ . . . . .	54
3.10	Heat transfer coefficient distributions at $Kn = 0.0268$ . . . . .	55
3.11	Surface friction coefficient distributions at $Kn = 0.0067$ . . . . .	56
3.12	Surface friction coefficient distributions at $Kn = 0.0134$ . . . . .	56
3.13	Surface friction coefficient distributions at $Kn = 0.0268$ . . . . .	57
3.14	The location of $C_f \approx 0$ on the cylinder surface at three different rarefaction levels. . . . .	57
3.15	The comparison of surface heat transfer at the most severe case for the three different Knudsen numbers. . . . .	58
3.16	The comparison of change in density and temperature through free-stream to the surface for the most severe case at each of the three different Knudsen numbers. . . . .	59
3.17	Mach number contours in the steady interaction region for the most severe cases in different rarefaction levels. The Mach contours are shown for the values of Mach numbers 1, 1.5, 2, 2.5, 3, 4, 5, 6, 7, 8, and 9. . . . .	61
3.18	Contours of Mach number, showing the unsteady mechanisms in a shock-shock interaction at $H = 49$ mm, $Kn = 0.0067$ , and $t =$ $1.195 \times 10^{-3}$ s. The numbers on the contour lines denote the Mach numbers. . . . .	63
3.19	Plot showing the number of DSMC particles and average linear kinetic energy in an unsteady simulation; $Kn = 0.0134$ , $H = 49$ mm. . . . .	63
3.20	Mach number contours showing flow field unsteadiness at $Kn =$ $0.0067$ , $H = 49$ mm. . . . .	64
4.1	Simplified schematic representation of exhaust plume behaviours: (a) over expansion ( $P_a \gg P_e$ ), (b) perfect expansion ( $P_a = P_e$ ), and (c) under expansion ( $P_a \ll P_e$ ), where $P_a$ is the ambient pressure, and $P_e$ is the pressure at the nozzle exit plane. . . . .	69
4.2	Schematic of flate plate impingement. . . . .	75
4.3	The matrix of rocket plume-surface simulations according to mesh topology, and nozzle configurations. The parameter $x$ of $Dx$ repre- sents the distance between nozzle centres in mm. The triangle ex- emplifies the axisymmetric mesh, the half circle the half-symmetric mesh, the two circles the double nozzle configuration, and the four circles the quadruple nozzle configuration. . . . .	77

4.4	The mesh topology of quadruple plume simulation. . . . .	78
4.5	Benchmarking of <i>dsmcFoam</i> + results against data in the literature. Results are plotted along a radial line starting at the stagnation point. . . . .	80
4.6	<i>dsmcFoam</i> + results of multi-nozzle plume-plume interactions for changing distance between the nozzles at $T_0 = 300$ K. . . . .	85
4.7	<i>dsmcFoam</i> + results for surface properties from multi-nozzle arrays at $T_0 = 300$ K. . . . .	88
4.8	<i>dsmcFoam</i> + results of single-nozzle plume-surface impingement with increasing stagnation temperature. . . . .	89
4.9	<i>dsmcFoam</i> + results of single-nozzle plume-surface impingement with increasing stagnation temperature. . . . .	91
4.10	<i>dsmcFoam</i> + results of multi-nozzle array plume-plume impingement with changing nozzle-to-nozzle distance and increasing stagnation temperature. The results are presented along an axial line extending from the centre of a nozzle outlet to the surface. . . . .	93
4.11	<i>dsmcFoam</i> + results of multi-nozzle plume-surface impingement with increasing stagnation temperature at a constant nozzle-to-nozzle distance, $D = 3$ mm. The results are plotted along a radial line starting directly below the centre of the nozzle outlet on the surface. . . . .	95
4.12	<i>dsmcFoam</i> + results of single-nozzle plume-surface impingement with altering the distance between the nozzle outlet and impingement surface. . . . .	97
4.13	<i>dsmcFoam</i> + results of single-nozzle plume-surface impingement with altering the distance between the nozzle outlet and impingement surface. . . . .	98
5.1	The alteration in phase of gas flows according to inter-phase coupling modes. . . . .	103
5.2	Directory structure of <i>rarefiedMultiphaseFoam</i> . . . . .	112
5.3	The algorithm of <i>rarefiedMultiphaseFoam</i> . . . . .	120
5.4	Computational domain and boundary conditions. . . . .	122
5.5	Drag force ratio for a spherical solid particle in a Maxwellian distribution. . . . .	123
5.6	Heat flux ratio for a spherical solid particle in a Maxwellian distribution. . . . .	124
5.7	Thermophoretic force per unit area on a motionless spherical solid particle. The results of continuum and free-molecular, as the two limiting regimes, are included for reference. . . . .	125



5.8	Computational domain of two-phase free expansion. . . . .	127
5.9	Free expansion of two-phase jet flow with varying source pressure, showing the formation of a solid particle beam. . . . .	129
5.10	Solid angle variation with source pressure. Comparison of results from <i>rarefiedMultiphaseFoam</i> and experiment. . . . .	130
5.11	Schematic of an ADM application. . . . .	131
5.12	Computational domain of two-phase free expansion and sticking solid particle on a surface. . . . .	133
5.13	Deposition of aluminium particles on the substrate at $t = 0.001$ s, showing the distribution percentage of solid particles throughout computational surface cells for the three different source pressures. . . . .	135
7.1	The free-stream flow at $Kn = 0.0067$ - <i>continued</i> . . . . .	142
7.1	The free-stream flow at $Kn = 0.0067$ . . . . .	143
7.2	The free-stream flow at $Kn = 0.0134$ . . . . .	144
7.3	The free-stream flow at $Kn = 0.0268$ - <i>continued</i> . . . . .	145
7.3	The free-stream flow at $Kn = 0.0268$ . . . . .	146
7.4	<i>dsmcFoam+</i> results of multi-nozzle array plume-plume impinge- ment with changing nozzle-to-nozzle distance - <i>continued</i> . . . . .	147
7.4	<i>dsmcFoam+</i> results of multi-nozzle array plume-plume impinge- ment with changing nozzle-to-nozzle distance. . . . .	148
7.5	<i>dsmcFoam+</i> results of multi-nozzle array plume-plume impinge- ment with changing nozzle-to-nozzle distance - <i>continued</i> . . . . .	148
7.5	<i>dsmcFoam+</i> results of multi-nozzle array plume-plume impinge- ment with changing nozzle-to-nozzle distance. . . . .	149
7.6	<i>dsmcFoam+</i> results of multi-nozzle array plume-plume impinge- ment with changing nozzle-to-nozzle distance - <i>continued</i> . . . . .	149
7.6	<i>dsmcFoam+</i> results of multi-nozzle array plume-plume impinge- ment with changing nozzle-to-nozzle distance. . . . .	150
7.7	<i>dsmcFoam+</i> results of multi-nozzle array plume-plume impinge- ment with changing nozzle-to-nozzle distance. . . . .	151
7.8	<i>dsmcFoam+</i> results of multi-nozzle array plume-plume impinge- ment with changing nozzle-to-nozzle distance. . . . .	152
7.9	<i>dsmcFoam+</i> results of multi-nozzle array plume-plume impinge- ment with changing nozzle-to-nozzle distance. . . . .	153
7.10	The prediction of coefficient of restitution as a function of the residual interference models. . . . .	154
7.11	Adhesion force versus separation distance with varying surface roughness value of <i>rms</i> . . . . .	155

7.12 Heat transfer between a colliding particle with a wall as a function of the impact $Fo$ . . . . .	156
---	-----



# Nomenclature

## UNITS

The units of measurement used throughout this thesis are compliant with the *Système Internationale*. Where relevant exceptions to this rule have been noted in the text.

## SYMBOLS

The symbols used in this thesis have been defined at relevant points in the text. The following Greek letters, miscellaneous symbols, and abbreviations have been employed.

## Greek Letters

Letter	Description
$\alpha_p$	Isothermally Diffuse Reflected Gas Molecules
$\alpha_{wall}$	Isothermally Diffuse Reflecting Wall Surface
$\beta$	Most Probable Molecular Speed
$\Gamma$	Solid Beam Expansion Angle
$\gamma$	Specific Heat Ratio
$\delta$	Discrete Increment
$\delta_{ij}$	Kronecker Delta
$\delta l$	Discrete Distance Between Nearist-neighbour Sites
$\delta t$	Discrete Time
$\varepsilon_p$	Specularly Reflected Gas Molecules
$\varepsilon_s$	Solid Volume Fraction
$\varepsilon_{tr}$	Translational Energy of a Collision Partner
$\varepsilon_{wall}$	Specularly Reflecting Wall Surface
$\varepsilon_y$	Ratio of Yield Strength
$\zeta$	Number of Internal Degree of Freedom
$\zeta_{rot}$	Number of Rotational Degree of Freedom

$\eta$	Poisson's Ratio
$\Theta$	Polar Angle
$\theta$	Angular Position
$\theta_{vib}$	Characteristic Vibrational Temperature
$\kappa$	Hypersonic parameter
$\Lambda$	Recovery Factor
$\lambda$	Mean Free Path
$\lambda$ -point	Triple Point in the Shock-Shock Interactions
$\mu$	Viscosity
$\nu$	Collision Frequency
$\nu_{solid}$	Normal Component of Solid Velocity
$\Xi$	Correction Factor
$\xi$	Collision Term
$\rho$	Density
$\varrho_T$	Tangential Momentum Accommodation Coefficient
$\sigma_T$	Collision Cross-section
$\tau$	Shear Stress / Viscous Stress Tensor
$\tau_c$	Total Contact Time
$\Upsilon$	Elevation Angle
$\Phi$	Scattering Asimuthal Angle
$\phi$	Angle of Attack
$\varphi$	Characteristic Flow Dimension
$\chi$	Convergent/Divergent Angle of a Nozzle
$\psi$	Porosity
$\Omega$	Solid Angle
$\omega$	Viscosity Exponent

## Miscellaneous Symbols

Symbol	Description
$\mathcal{R}$	Radius of Hemispherical Asperity
$\mathfrak{R}_f$	Uniform Deviate
$\wp$	Solid Particle Thermal Accommodation Coefficient

## Abbreviations

Abbreviation	Acronym
ADM	Aerosol Deposition Method
BGK	Bhatnagar-Gross-Krook Model
CFD	Computational Fluid Dynamics
DEM	Discrete Element Model
DUGKS	Discrete Unified Gas Kinetic Scheme
DFR	Drag Force Ratio
DLR	Deutsches Zentrum für Luft- und Raumfahrt
DOE	The United States Department of Energy
DOF	Degree of Freedom
DPM	Discrete Particle Model
DSMC	Direct Simulation Monte Carlo
DVM	Discrete Velocity Method
ESA	European Space Agency
FFA	Sweden's Flygtekniska Försöksanstalten
FFT	Fast Fourier Transform
Fo	Fourier Number
GDM	Gas Deposition Method
GPL	General Public License
GUI	Graphical User Interface
HFR	Heat Flux Ratio
HPC	High Performance Computer
HyDS	Hybrid Direct Simulation
JMS	Jet Molding System
Kn	Knudsen Number
LB	Larsen-Borgnakke
LGPL	Lesser General Public License
Ma	Mach Number
MD	Molecular Dynamics
MEMS	Microelectromechanical Systems
MOC	Method of Characteristic
MPI	Message Passing Interface
MSS	Mir Space Station
NASA	National Aeronautics and Space Administration
NSF	Navier-Stokes-Fourier
NTC	No-time-counter

OAA	Own Ambient Atmosphere
ODE	Ordinary Differential Equation
ONERA	French Office National d'Etudes et de Recherches Aéronautiques
OpenFOAM	Open Field Operation and Manipulation
Pr	Prandtl Number
Q-K	Quantum Kinetic
R13	The regularised 13 Moment Equations
R26	The Regularised 26 Moment Equations
RCS	Reaction Control System
Re	Reynolds Number
RWF	Radial Weighting Factor
SMILE	Statistical Modelling in Low-Density Environment
SPARTA	Stochastic Parallel Rarefied-gas Time-accurate Analyzer
TCE	Total Collision Energy
TMAC	Tangential Momentum Accommodation Coefficient
TPMC	Test Particle Monte Carlo
VHS	Variable Cross-section Hard Sphere
VSS	Variable Cross-section Soft Sphere
YNP	Yttria Nanoparticle
0D	Zero-dimensional
1D	One-dimensional
2D	Two-dimensional
3D	Three-dimensional





# Acknowledgements

There are many people to whom I owe gratitude for their endless support, guidance, and encouragement. Without them, this thesis would be little more than thoughts, numbers, and doodles on a page.

Firstly, I would like to thank my supervisors Dr. Craig White and Prof. Konstantinos Kontis for their unwavering support, patience, and guidance throughout my time at the University of Glasgow.

Thank you to Dr. Hossein Zare-Behtash for all the advice and support, be it academic or professional, and for being as close as a third supervisor to me.

It has been a privilege to be part of the ESA-ESTEC Vacuum Chamber Facility Team at the University of Glasgow, under the supervision of Dr. White, Dr. Zare-Behtash, and Prof. Kontis. I also thank the University of Glasgow's IT staff, especially Mr. Christopher Nicol, and computational cluster facilities and staff, including Mr. Grant Quinn, responsible for Buckethead, and Mr. Mark Meenan, in charge of Headnode, for their technical support, as well as Dr. Vincent Casseau for his assistance in initiating me to OpenFOAM programming, Dr. Süha Tuna for his support in the compiling of OpenFOAM on computing clusters and learning MPI libraries, and the Edinburgh Parallel Computing Centre (EPCC) for their HPC and MPI trainings.

I am grateful to Prof. Erkan Öterkuş and Dr. Selda Öterkuş for their kindness and support throughout the years and for their willingness to share their knowledge and expertise, Prof. Ahmet Samancı for his supervision and pivotal guidance in my postgraduate education, Prof. Mehmet Kanoğlu for his time spent on discussing heat transfer, particularly essential for Chapter 5 of this thesis, my former supervisors Dr. Thomas Scanlon for introducing OpenFOAM to me, and Prof. Oğuzhan Yılmaz for his contributions to me as a freshman engineering student, Prof. Melike Nikbay for the enlightening discussions we have had during my research, and Mr. Brendan Harris, the best academic English tutor ever.

My sincere thanks to the members of the Aero-Physics Laboratory, particularly Mr. Ziqu Cao, Dr. Guoshuai Li, Mr. Thomas Andreou, Mr. Senthilkumar Subramanian, Mr. Hassam Guevara Jelid, Mr. Ting Tsung Chang, Mr. Christo-

pher Scholes, Dr. Michael Wojewodka, Dr. Andrew Cusick, and Mr. Fan Jiang for their support and friendship at all times. I also thank Dr. Kiril Boychev, Dr. Oleksandr Zhdanov, Dr. David Pickles, Mr. Alfonso Martínez Carmena, Mr. Julio Pizano Flores, Dr. Paulo Valente Klaine, and Dr. Joao Battistella Nadas, Dr. Yusuf Sambo, and Mr. Rafael Castelo Branco Goulart, aka Captain, may he Rest in Peace.

Dr. Metin and Mrs. Belgin Öztürk, Mr. İbrahim Mızrak, Mr. Mehmet Burak Önal, Mr. Nozir Shokirov, Dr. Önder and Mrs. Seda Canbulat, Dr. Oğuzhan Murat, Mr. Ömer Faruk Çakmak, Dr. Ahmet Uğur Atılan, Mr. Çağrıbey Şahin, Mr. Ömer Yatçı, Mr. Yusuf Bülbül, Mr. Abdulhadi Odeh, Mr. Michael Green-corn, Ms. Catherine MacNeil, Mr. Kinan Bezem, Ms. Katherine Ross, Mr. Süleyman Karabal, Dr. İbrahim Akıncı, Mr. Sheik Abdul Malik, Ms. Maisie Keogh, Dr. Şafak Bayram, Dr. Olgun Güven and Mrs. Monica Hızır, Dr. Barış Biçer, Mr. Ümran Kaya, Mr. Ömer Faruk Kuruöz, Ms. Melis Pişiren, Ms. Imane ElMouhib, Ms. Narmeen Ahmed, and Ms. Yujin Wang have been some of my greatest support during the ups and downs of my Ph.D.

I owe thanks to the community in the UK that has never made me feel too far from home - Mr. Erkut and Mrs. Sonia Öztürk, Mr. Enes and Mrs. Zeynep Tzampaz Mola Mehmet, the Topsögüt family, Mr. Haluk Savaş, Dr. Yusuf Ziya and Mrs. Sümeyye Öğretici, Ms. Ayşenur Türkmen, Mr. Fuat Balaban, Dr. Murat and Mrs. Hilda Bozkurt, Mr. Fatih Kerem Boz, Mr. Fatih and Mrs. Zeynep Şeyda Tıraş, Dr. Emre Dokuzparmak, Mr. Ali Utku and Mrs. Ayşe Demir, Mr. Burak Kızılkaya, Mr. Burak Serhat Sakarya, Mr. Çağlar Hamarat, Mr. Arda Gyunesh, Mr. Oğuzhan Aydıre, and the Glasgow University Turkish Society and Association of Turkish Alumni and Students in Scotland families.

This research would not have been possible without the financial support of the Republic of Turkey's Ministry of National Education Scholarship (MoNE-1416). Mr. Hasan Ünsal, Former Education Counsellor in London, and Mr. Atakan Doğan, Education Attaché in Edinburgh, have been very supportive and understanding.

I will always be grateful for Ms. Sadia Rania Mohiuddin, my partner in crime, for her patience, understanding, unending faith in me at all times, and for believing in me - sometimes more than I did in myself.

Finally, though words would never suffice to express the extent of my gratitude, I would like to thank my parents Mustafa and Nazife, my siblings Medine, Merve, Kevser, and İhsan Emre, as well as Koray, and my wee men Gökem Ey-men and Melih Kağan. It is with your blessings that I have become who I am today.



96:[1-5]

*To Mom and Dad*

Sizin sayenizde ve sizin için

Because of, and for you



# Chapter 1

## Introduction

### 1.1 A Background on Rarefied Gas Dynamics

The modelling of fluid systems can be categorised as either continuous or particulate. The continuum model ignores the molecular nature of fluids and describes them as a continuous matter for which macroscopic quantities can be specified as spatial and temporal, whereas the molecular approach uses probabilistic and deterministic methods to define the flow parameters in space and time. The continuum model applies the conservation of mass, momentum, and energy in order to define the fluid properties at every point using nonlinear partial differential equations. This differential calculus allows for the specification of the properties of a small enough element in the whole control volume. In addition to the continuum approach, the fluid is generally considered to be in pseudo-thermodynamic equilibrium and the macroscopic properties of the flow consist of the averages of microscopic properties. The shear stress and heat flux are expressed by lower-order macroscopic variables. Particularly in gas flows, when the density decreases, the average distance between the molecules increases and the degree of rarefaction of gas flow increases. For this reason, the Navier-Stokes-Fourier (NSF) equations cannot be used for mathematical modelling of the rarefied gas flows; the transport terms of the NSF equations consist of macroscopic variations of the flow and the decrease of density causes the continuum assumptions and the linear form of the constitutive relations for the heat flux and shear stress in the NSF equations to breakdown; therefore, the NSF equations can no longer be applied for mathematical modelling of the gas flow [1, 2].

### 1.1.1 Classification of Flow Regimes

The degree of rarefaction and the regime of a gas flow are determined using the Knudsen number, i.e.  $Kn = \lambda/L$ , which is a basic criterion and dimensionless parameter, where  $\lambda$  is the mean free path and  $L$  is a characteristic size of a problem. The mean free path is the average distance a molecule travels between collisions [3]. The characteristic flow dimension can be represented by the system size and the gradients of macroscopic parameters,  $\varphi$ , i.e.  $L = \varphi/\nabla\varphi$  [4, 5]. When the Knudsen number approaches zero, the inter-molecular interactions increase and thermal equilibrium can be obtained in a short time scale [6]. As the Knudsen number tends to infinity, the inter-molecular interaction rate between the gas molecules decreases and the degree of rarefaction increases. The classification of flow regime is summarised in Figure 1.1.

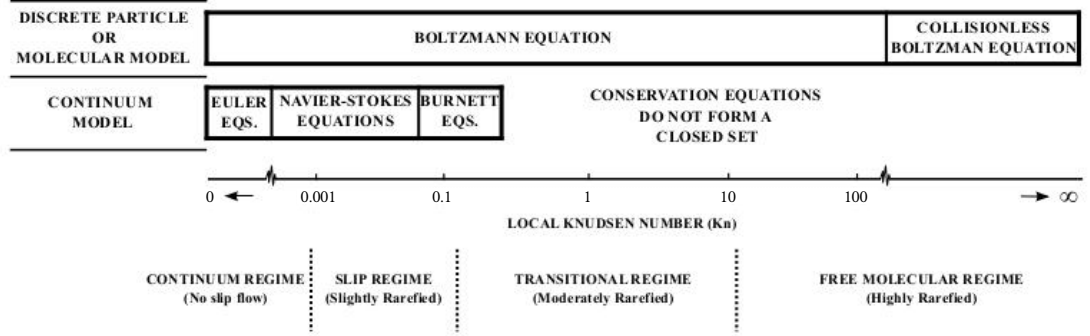


Figure 1.1: Classification of the flow regimes by Knudsen number, adapted from Ref. [7].

When  $Kn > 0.001$ , it is well-known that non-equilibrium effects become important, as the rate of gas-surface interactions decreases (i.e. the velocity slip and temperature jump phenomena become important). As the Knudsen number increases further, the transition regime is approached, where  $0.1 < Kn < 10$ . In this range, inter-molecular collisions are still important, but they are not occurring at a high enough rate to maintain local thermodynamic equilibrium even in the bulk flow. Finally, in the free-molecular regime,  $Kn > 10$ , inter-molecular collisions are very unlikely to take place and are not an important mechanism for the transfer of mass, momentum, and energy.

#### Continuum Regime

In continuum flow regimes, the movement of viscous, compressible and heat conducting flows can be defined by the NSF equations [8]. The parameters are spec-

ified as averages of the macroscopic structure of the fluid, meanwhile small fluid elements can be described using differential calculus [2]. Thus, the continuum system can be defined as shown in Equations 1.1–1.5, which are the continuity equation, the components of the momentum equation, and the energy equation for compressible, three-dimensional, viscous flow in partial differential, nonconservation form respectively [9], i.e.

$$\rho \frac{D\rho}{Dt} + \rho \nabla \cdot \mathbf{V} = 0, \quad (1.1)$$

$$\rho \frac{Du}{Dt} = -\frac{\partial p}{\partial x} + \frac{\partial \tau_{xx}}{\partial x} + \frac{\partial \tau_{yx}}{\partial y} + \frac{\partial \tau_{zx}}{\partial z} + \rho f_x, \quad (1.2)$$

$$\rho \frac{Dv}{Dt} = -\frac{\partial p}{\partial y} + \frac{\partial \tau_{xy}}{\partial x} + \frac{\partial \tau_{yy}}{\partial y} + \frac{\partial \tau_{zy}}{\partial z} + \rho f_y, \quad (1.3)$$

$$\rho \frac{Dw}{Dt} = -\frac{\partial p}{\partial z} + \frac{\partial \tau_{xz}}{\partial x} + \frac{\partial \tau_{yz}}{\partial y} + \frac{\partial \tau_{zz}}{\partial z} + \rho f_z, \quad (1.4)$$

$$\begin{aligned} \rho \frac{D}{Dt} \left( e + \frac{V^2}{2} \right) = & \rho \dot{q} + \frac{\partial}{\partial x} \left( k \frac{\partial T}{\partial x} \right) + \frac{\partial}{\partial y} \left( k \frac{\partial T}{\partial y} \right) + \frac{\partial}{\partial z} \left( k \frac{\partial T}{\partial z} \right) \\ & - \frac{\partial(u p)}{\partial x} - \frac{\partial(v p)}{\partial y} - \frac{\partial(w p)}{\partial z} + \frac{\partial(u \tau_{xx})}{\partial x} + \frac{\partial(u \tau_{yx})}{\partial y} + \frac{\partial(u \tau_{zx})}{\partial z} \\ & + \frac{\partial(v \tau_{xy})}{\partial x} + \frac{\partial(v \tau_{yy})}{\partial y} + \frac{\partial(v \tau_{zy})}{\partial z} + \frac{\partial(w \tau_{xz})}{\partial x} + \frac{\partial(w \tau_{yz})}{\partial y} \\ & + \frac{\partial(w \tau_{zz})}{\partial z} + \rho \mathbf{f} \cdot \mathbf{V}, \end{aligned} \quad (1.5)$$

where  $\rho$  is the density,  $t$  is the time,  $\mathbf{V} = u\mathbf{i} + v\mathbf{j} + w\mathbf{k}$  is the velocity vector,  $p$  is the pressure,  $\tau$  is the viscous stress tensor,  $\dot{q}$  is the rate of volumetric heat addition per unit mass (capturing effects such as radiation absorption or emission),  $\mathbf{f}$  is the body force per unit mass,  $e$  is the internal energy per unit mass,  $V^2/2$  is the kinetic energy per unit mass,  $k$  is the thermal conductivity, and  $T$  is the temperature. The subscripts  $x$ ,  $y$ , and  $z$  represent the directions in a Cartesian co-ordinate system and  $\frac{D}{Dt}$  is the substantial derivative. The conduction heat flux is expressed through Fourier's law in Equation 1.5.

The movement of a viscous fluid can be expressed by the NSF equations. At these low Knudsen number ranges, the inter-molecular collisions are dominant and equilibrium is maintained. As the Knudsen number approaches zero, the transport terms become negligible in the continuum momentum and energy equations because of negligible molecular diffusion. Therefore, the NSF equations



reduce to the inviscid Euler equations [2].

### Slip Regime

The slip regime flow is accepted as an early transition regime. In this regime, the NSF equations can still be used to model the flow [10] if regions of non-equilibrium near solid surfaces are carefully accounted for. The molecules of the fluid interact less with the surface, therefore, the value of the flow variables differ from that at the surface [11]. The sudden changes in velocity and temperature are known as *velocity slip* and *temperature jump*, respectively. Applying the NSF equations, the velocity slip can be expressed using Maxwell's velocity slip boundary condition [12] for planar surfaces where the wall normal is in the  $y$ -direction, as

$$U_g - U_s = \frac{2 - \varrho_m}{\varrho_m} \lambda \left( \frac{\partial u}{\partial y} \right)_s + \frac{3}{4} \frac{\mu}{\rho T_g} \left( \frac{\partial T}{\partial x} \right)_s. \quad (1.6)$$

The temperature jump can be expressed using Von Smoluchowski's jump boundary condition [13] for planar surfaces, as

$$T_g - T_s = \frac{2 - \varrho_t}{\varrho_t} \left[ \frac{2\gamma}{(\gamma + 1)} \right] \frac{\lambda}{Pr} \left( \frac{\partial T}{\partial y} \right)_s, \quad (1.7)$$

where  $U_g$  and  $U_s$  are the gas and surface velocities,  $T_g$  and  $T_s$  are the gas and surface temperatures,  $\varrho_m$  is known as the tangential momentum accommodation coefficient (TMAC),  $\varrho_t$  is the thermal-accommodation coefficient,  $\rho$  is the fluid density,  $\mu$  is the viscosity,  $Pr$  is the Prandtl number,  $\lambda$  is the mean free path,  $\gamma$  is the specific heat ratio, and the subscript  $s$  represents properties at the surface.

### Transition and Free-Molecular Regimes

In the transition and free-molecular regimes, the constitutive equations that connect the heat transfer and shear stress to other parameters and linear transport terms in partial differential equations are no longer valid. The Boltzmann equation is an integro-differential expression offered by Boltzmann in 1872 to define all regimes as seen in Figure 1.1. For a single species monatomic gas, the Boltzmann equation is [1]

$$\frac{\partial}{\partial t}(nf) + \mathbf{c} \frac{\partial}{\partial r}(nf) + \mathbf{F} \frac{\partial}{\partial c}(nf) = \int_{-\infty}^{\infty} \int_0^{4\pi} n^2 (f^* f_1^* - f f_1) c_r \sigma_T d\Omega dc_1, \quad (1.8)$$

where  $(nf)$  is product number of density and the normalised velocity distribution function,  $\mathbf{c}$  and  $\mathbf{c}_r$  are molecular and relative molecular velocities, respectively,  $\mathbf{F}$  is an external force per unit mass,  $f$  and  $f_1$  are velocity distribution functions of molecules at  $\mathbf{c}$  and  $\mathbf{c}_r$ , respectively,  $\sigma_T$  is collision cross-section of molecule,  $\Omega$  is solid angle,  $(*)$  represents post-collision variables,  $t$  and  $r$  are time and physical space, respectively [11, 14].

There are some analytical difficulties in solving the Boltzmann equation. One of them is mathematical complexity. A notable instance for mathematical difficulty of the Boltzmann equation from Ref. [1] is that the velocity distribution of a 1D steady rarefied gas flow becomes 3D in phase space, further causing computational complexity.

Another limit of this equation can be found in its application for continuum cases, where the mean free path is extremely small, and are modeled using the Euler or NSF equations. The collision term can safely be ignored for the collisionless or free-molecular flow regime. However, the collisions at the inter-molecular level are still significant in the transition regime. In order to solve the Boltzmann equation for transition regimes, analytical techniques, which make assumptions and simplifications, have been developed. These are known as *moment methods*. The moment equations are created by multiplication of the Boltzmann equation and a molecular quantity,  $Q$ , which can be molecular mass,  $m$ , molecular momentum,  $mc$ , or molecular energy,  $1/mc^2$  and the integration of velocity space. The moment equation is

$$\frac{\partial}{\partial t}(n\bar{Q}) + \nabla(nc\bar{Q}) - nF\frac{\partial\bar{Q}}{\partial c} = \Delta[Q], \quad (1.9)$$

where  $\Delta[Q]$  is the collision integral and defined as

$$\Delta[Q] = \int_{-\infty}^{\infty} \int_0^{4\pi} n^2(f^*f_1^* - ff_1)c_r\sigma_T d\Omega dc_1. \quad (1.10)$$

This equation is known as the *equation of change* or *transfer equation*. Higher-order fluid dynamic problems are modeled using extended or generalised hydrodynamic equations [14]. However, there are still some restrictions for the applications of these equations to high-order problems. For instance, the regularised 13 moment (R13) equations are limited to the early slip flow regime [15]. Therefore, the regularised 26 moment (R26) equations are necessary to model up to Knudsen number 1 while obtaining accurate results for velocity and temperature profiles [15, 16]. The R26 equations have been linearised to analyse Kramers' problem and the Knudsen minimum [17].

In the literature, several numerical attempts were implemented for the sake of solving the Boltzmann equation deterministically. In order to maintain the physical data of the collision procedure, a continuous velocity space is approximated by a fixed set of discrete velocities [18]. This technique is called the *discrete velocity method* (DVM) [19]. However, Wu *et al.* states [18] that the formation of a discrete collision system on the velocity nodes is inevitable in this application. This situation causes a very high computational cost as the post-collision velocity data is also stored on the velocity nodes. Ref. [18] summarises some approaches which were applied to decrease computational expenses, such as assuming a direct approximation of the collision operator [20], the application of a hybrid method -a mixture of stochastic and deterministic approaches- [21–24], the mapping of the post-collision velocities in the velocity nodes using an interpolation scheme [25, 26], etc.

While DVM was constructed for hard sphere molecules [27] in [18], an accurate numerical kernel technique was also proposed for hard sphere molecules in order to compute the linearised [28] in [18] and the full non-linear collision operators [29, 30] in [18]. This is called the *finite-difference method*. The method was implemented for a 1D temperature jump problem in order to accurately calculate distributions of temperature and density using a finite difference scheme [28].

A 2D problem was attempted using a technique [31], which was inspired by the application of Fourier transform techniques for the solution of the Boltzmann equation for Maxwell molecules [18]. The *Fourier spectral method* was proposed by Ref. [31] for the solution of the spatially homogeneous Boltzmann equation. In this method, the distribution function is expanded in the Fourier series, and the finite difference is discretised in time and velocity space. Thus, the method aims to evaluate the collision operator accurately and to reduce the computational expense [31]. Since the method has been enhanced for various types of problems, such as the *spectral-Lagrangian method* for elastic and inelastic collisions, as well as space-homogeneous problems, for instance, 1D Fourier heat and shock flows, the application of fast Fourier transform (FFT), a modified fast spectral method for solving space-inhomogeneous problems, etc. Although the modified fast spectral method presents reliable results for the solution of the Boltzmann equation for the rarefied gas regime, the main problem of developing a hybrid solver for the continuum regime kinetic models or Navier-Stokes equations lies in specifying the location of the two different regimes and determinations of interface between the continuum and rarefied regimes. Furthermore, in order to meet the conditions, a velocity domain twice the size of the region where the distribution function can support the solution is needed. This causes a waste of computing memory and

time, especially in a 3D velocity-space [18]. It is deduced that the simulation of a large span of spatial and temporal scales is quite challenging [32].

The *discrete unified gas kinetic scheme* (DUGKS) is developed to solve multiscale flows on the basis of kinetic models. However, the finite-volume DUGKS shows differences in the modelling of interface flux and gas evolution as opposed to the classical kinetic methods. Meanwhile, the reconstruction of the distribution function in DUGKS on interfaces of cells for the collision effects and gas particle transports in time-steps is implemented by solving the kinetic equation in time and space. This method should be advanced/improved in terms of the usage of memory, the efficiency of DUGKS in unsteady problems, implicit as well as high-order spatial and temporal discretizations, and converge accelerations, etc. [32].

Another approach, which is known as *model equations*, was introduced for simplifying the collision term of Boltzmann equation. A well-known approximation is the Bhatnagar-Gross-Krook (BGK) model, which is applicable for solving small problems involving small perturbations from equilibrium, i.e. the model can be linearised and solved relatively easily [33],

$$\frac{\partial}{\partial t}(nf) + \mathbf{c} \frac{\partial}{\partial \mathbf{r}}(nf) + \mathbf{F} \frac{\partial}{\partial \mathbf{c}}(nf) = n\nu(f_0 - f), \quad (1.11)$$

where  $\nu$  is collision frequency,  $c$  and  $r$  are the velocity and position vectors of a particle, respectively, and  $f_0$  is the Maxwell distribution function.

After all these applications of the moment and models, a solution to the Boltzmann equation has been much sought after to accurately capture the correct gas particle physics and flow phenomena. Herein, the direct simulation methods can provide solutions for one of the complexities of the Boltzmann equation: the collision integral. The direct simulation methods store and update the positions, velocities, and energies of registered simulator particles, which are representative of the real molecules, at each time-step. According to Bird [1], direct simulation Monte Carlo (DSMC) is the most successful method so far in order to simulate the rarefied gas flows in the transition regime. DSMC is a transient stochastic particle-based method which is based on the kinetic theory of rarefied gases [11]. This technique is applied throughout this thesis in order to solve different interaction problems involving high-speed rarefied gas flows such as shock-shock, shock-surface, and shock-solid particle interactions at various rarefaction levels. The DSMC method is comprehensively explained in Chapter 2.

### 1.1.2 Kinetic Theory

Kinetic molecular theory is a statistical method to describe the dynamics - movement and interactions - of a large amount of the submicroscopic gas particles using macroscopic dimensions [34]. The properties of multi-interacted molecules are calculated by high-order differential equations or multi-dimensional integrals. These equations are reduced to investigate the binary interactions of dilute gases [35]. Classical Newtonian mechanics can be used to assume the force and separation distance of the molecules and ordinary differential equations (ODEs) can be set for the motion of all molecules as

$$\frac{d^2}{dt^2}r_i = \frac{1}{m} \sum_{\substack{j=1 \\ j \neq i}}^N F_{ij}, \quad (1.12)$$

where  $m$  is the mass of a single molecule, and  $r_i$  is the position of a single molecule. Because of the large amount of representative particles (a cubic centimeter of a rarefied gas at standard conditions comprises  $2.687 \times 10^{19}$  number of molecules), the system size and computational load increase proportionally [35, 36].

#### The Maxwell-Boltzmann Distribution

The Maxwell-Boltzmann distribution is a kinetic molecular theory to determine the motion of molecules instantaneously using a distribution calculations, which is consistent for maximal states. The speed probability distribution,  $P_v(v)$ , where the velocity of a molecule is between  $v$  and  $v + dv$  [36], is

$$P_v(v)dv = 4\pi \left( \frac{m}{2\pi k_B T} \right)^{3/2} v^2 e^{-\frac{1}{2}mv^2/k_B T} dv, \quad (1.13)$$

where in Equation 1.13,  $k_B$  is Boltzmann constant,  $m$  is molecular mass, and  $T$  is local macroscopic translational temperature. The other variables of the distribution can be derived from this probability. For instance, the average molecular speed is

$$\bar{v} = \int_0^\infty v P_v dv = \sqrt{\frac{8k_B T}{\pi m}}. \quad (1.14)$$

The most probable thermal velocity,  $v_{mp}$  is found at the maximum of  $P_v(v)$ , i.e.

$$\left. \frac{d}{dv} P_v(v) \right|_{v=v_{mp}} = 0, \quad (1.15)$$

which gives

$$v_{mp} = \sqrt{\frac{2k_B T}{m}}. \quad (1.16)$$

The kinetic energy of each molecule is calculated by average squared speed or root mean square speed,  $v_{rms}$ , i.e.

$$v_{rms}^2 = \int_0^\infty v^2 P(v) dv = \frac{3k_B T}{m}. \quad (1.17)$$

The Maxwell-Boltzmann distribution was reviewed from Ref. [37]. Figure 1.2 shows 3D Maxwell-Boltzmann speed distribution.

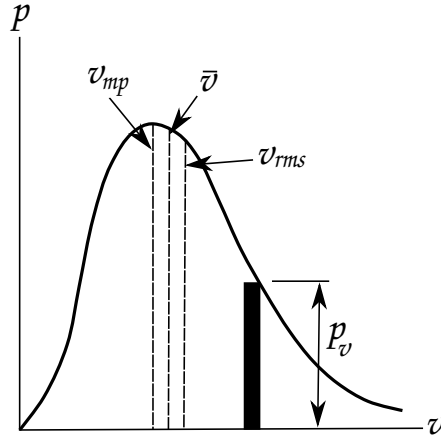


Figure 1.2: The speed distribution of a dilute gas molecule at an arbitrary temperature. The area of the shaded rectangular shows the probability of finding a molecule in the range of  $dv$ . The probability  $P$  tends to zero as  $v$  tends to infinity.

Bird [38] offers an alternate expression of the Maxwellian distribution. The average of the properties at microscopic (molecular) level constitute the macroscopic (continuum) properties. Therefore, the distribution of molecular properties provides information about the degree of the departure from equilibrium. The distribution function,  $f$ , can be specified for any molecular variable,  $Q$ . The fraction of any molecular quantity is in  $Q$  to  $Q + dQ$  range, where the distribution function is

$$dN/N = f dQ. \quad (1.18)$$

The Maxwellian (equilibrium) distribution,  $f_0$ , is a well-known function to calculate thermal speeds of the gas molecules in equilibrium at a temperature value,  $T$ . The distribution function  $f_0$  - also mentioned in Equation 1.11 - is

$$f_0 = (\beta^3/\pi^{3/2}) \exp(-\beta^2 c'^2), \quad (1.19)$$

and

$$\beta = (2k_B T/m)^{-1/2}, \quad (1.20)$$

where  $\beta$  is a temperature related variable and known as the reciprocal of most probable speed, and  $c'$  is the peculiar or thermal velocity of a molecule.

### Macroscopic Properties

The relationship between microscopic and macroscopic quantities was mentioned previously. Here, some definitions of macroscopic properties for a simple gas in equilibrium or non-equilibrium are described as per Bird's books [1, 38]. The number density,  $n$ , can be defined as the average number of molecules,  $\bar{N}$ , in a volume,  $V$ , i.e.

$$n = \frac{\bar{N}}{V}, \quad (1.21)$$

and the mass density,  $\rho$ , is the sum of the different species densities and specified by the number of density and the mass of a molecule,  $m$ , i.e.

$$\rho = \sum_{p=1}^s (m_p n_p) = n \bar{m}, \quad (1.22)$$

where  $s$  is the number of species in the gas mixture. As stated in Bird [1], "A bar over a quantity or expression donates the average value over all molecules in the sample." The following macroscopic quantities are related to the molecular motion. The macroscopic velocity,  $\mathbf{c}_0$ , is the product of the momentum flux and mean instantaneous molecular velocity,  $\mathbf{c}$ , i.e.

$$\mathbf{c}_0 = \frac{1}{\rho} \sum_{p=1}^s (m_p n_p \overline{\mathbf{c}_p}) = \overline{m \mathbf{c}} / \bar{m}, \quad (1.23)$$

and the thermal (or peculiar) velocity,  $\mathbf{c}'$ , the difference between molecular and flow velocities is

$$\mathbf{c}' = \mathbf{c} - \mathbf{c}_0. \quad (1.24)$$

Pressure is a two-direction function at the molecular level, therefore, it is a tensor, which has nine components. The pressure tensor is

$$\mathbf{p} = n \overline{m \mathbf{c}' \mathbf{c}'}, \quad (1.25)$$

if the components of  $\mathbf{c}'$ , which are  $u'$ ,  $v'$ , and  $w'$ , are in the  $x$ ,  $y$ , and  $z$  directions, respectively. The momentum flux in the  $x$  direction with normal in the  $y$  direction

is

$$p_{xy} = \overline{nm u' v'}, \quad (1.26)$$

and scalar pressure can be defined as

$$p = \frac{1}{3} \overline{nm(u'^2 + v'^2 + w'^2)} = \frac{1}{3} \overline{nm c'^2}. \quad (1.27)$$

Equation 1.27 is the product of the average of three normal components of pressure tensor. The viscous shear stress,  $\boldsymbol{\tau}$ , is specified as the negative of pressure tensor with the scalar pressure subtracted from the normal components, i.e.

$$\boldsymbol{\tau} \equiv \tau_{ij} = -(\rho \overline{c'_i c'_j} - \delta_{ij} p), \quad (1.28)$$

where  $\delta_{ij}$  is the Kronecker delta such that

$$\begin{aligned} \delta_{ij} &= 1 \text{ if } i = j \\ \delta_{ij} &= 0 \text{ if } i \neq j. \end{aligned}$$

The average kinetic energy related with the thermal movement of a molecule is

$$\frac{3}{2} R T_{tr} = e_{tr} = \frac{1}{2} \overline{c'^2}, \quad (1.29)$$

where  $R$  is the specific gas constant. Equation 1.29 may be combined with Equation 1.27 to give

$$p = \frac{2}{3} \rho e_{tr}. \quad (1.30)$$

The temperature,  $T$ , is a necessary gas property, but the ideal gas equation can be applied to a rarefied gas flow - even in a non-equilibrium condition - to define the translational kinetic temperature,  $T_{tr}$  [38], i.e.

$$T_{tr} = \frac{1}{3k_B} \overline{m c'^2}. \quad (1.31)$$

Monatomic molecules only have translational energy, therefore, their translational temperature is simply their temperature. The specific energy affiliated with the internal modes,  $e_{int}$ , consists of rotational,  $e_{rot}$ , vibrational,  $e_{vib}$ , and electronic,  $e_{el}$ , energy modes, i.e.

$$e_{int} = e_{rot} + e_{vib} + e_{el}, \quad (1.32)$$

and the internal energy can be described by associating the temperature of each internal mode,  $T_{int}$  with their degrees of freedom (DOF), i.e.

$$\frac{1}{2} \zeta R T_{int} = e_{int}, \quad (1.33)$$



where  $\zeta$  is the number of internal DOF.

The rotational temperature is described as

$$T_{rot} = \frac{2me_{rot}}{k_B\zeta_{rot}}, \quad (1.34)$$

where  $\zeta_{rot}$  is the number of rotational DOF. In equilibrium, the translational temperature is equal to the rotational temperature (for a case that the vibrational and electronic energies are ignored). The overall kinetic temperature,  $T_{ov}$ , can be specified for a non-equilibrium gas that is the weighted average of the translational and internal modes, i.e.

$$T_{ov} = \frac{3T_{tr} + \zeta T_{int}}{3 + \zeta}. \quad (1.35)$$

Finally, the heat flux,  $\mathbf{q}$ , can be defined as [1]

$$\mathbf{q} = \frac{1}{2}n\overline{mc'^2\mathbf{c}'} + n\overline{e_{int}\mathbf{c}'}, \quad (1.36)$$

where  $e_{int}$  is the internal energy of a single molecule.

## 1.2 Thesis Outline

In Chapter 2, DSMC is presented as the method employed for the numerical analysis of cases throughout this thesis. From a wide perspective, the history, modern state-of-art, computational codes, and a benchmarking case for the *dsmcFoam+* code is presented.

In Chapter 3, the effects of rarefaction and geometrical parameters on Edney shock-shock and shock-surface interactions are investigated. A simulation matrix, where the variables are three different Knudsen numbers and the position of the bow shock generator, is carried out in order to understand the change in the shock interaction behaviours and surface parameters.

In Chapter 4, the interactions of under-expanded sonic jets with one another and an impingement surface are examined by conducting a matrix of numerical analysis. A common issue in the application, which is plume-plume and plume-surface interactions in a vacuum environment, is chosen to observe how the flow structure and parameters of the plumes change when interacting with each other, and the alteration in the surface parameters. These alterations are investigated as a function of increments in the plume stagnation temperature, various nozzle configurations in a rocket motor, and hovering height of a single nozzle configuration.

In Chapter 5, the interaction of rarefied gas flows with solid particles is dis-

cussed. The one-way coupling of particle-laden rarefied gas flows are numerically implemented to provide a solution for two-phase flows, where the rarefied gas regime is a carrier, and the solid phase is transported. With the implementation of Green's functions for monatomic and polyatomic gas phases of rarefied flows, the effect of carrier gas phase on the solid phase is examined by a newly developed *dsmcFoam+* based multiphase solver, *rarefiedMultiphaseFoam*. The *rarefiedMultiphaseFoam* solver is tested through benchmarking cases, and an application case is then simulated to show the capability of the computational code.

In Chapter 6, the outcomes of the research presented in this thesis are highlighted, and future work based on the research framework of this thesis is covered.

### 1.3 Research Objective and Contribution

With the advancement in technology, the prediction of rarefied gas interaction behaviours in various conditions has become a necessity for a wide range of application fields from manufacturing to the space industry. That is why this thesis focuses on the examination of the interactions of high-speed rarefied gas flows with each other, a surface, and solid particles as rarefied gas flows present diverse interaction behaviours depending on domain geometry, flow parameters and rarefaction level, the properties of vacuum environments, etc. Hence, a well-known method for the simulation of rarefied gas flows, DSMC, constitutes the base of this research while examining the different interaction physics. A free and open-source parallelised DSMC solver, *dsmcFoam+*, is used for the rarefied gas regime such as Edney shock-shock & shock-surface, and plume-plume & plume-surface interactions. However, the *dsmcFoam+* solver is also extended to account for rarefied gas and solid particle interactions in a new solver, *rarefiedMultiphaseFoam*, as a part of the C++ based open source fluid dynamics toolbox of OpenFOAM. This novel multiphase solver is capable of solving one-way interactions of rarefied gas flows and solid particles including default features of *dsmcFoam+* for the rarefied gas regime, as well as developing and customising abilities for the solid regime. The main contributions of this study are outlined as follows:

- Considering a hypersonic platform with an increasing altitude, the effect of Knudsen number as well as the shock interaction location on Edney shock interaction types, the behaviour of diffused flow through the surface and unsteady effects, the impingement character and severity on the surface parameters, etc. are discussed in detail to present a wider approach about shock-shock interactions and their impacts on surface parameters.

- For under-expanded sonic jets, rarefied gas plume-plume and plume-surface interactions are examined as a function of the flow parameter, the stagnation temperature, geometrical effects, packing configuration of rocket motors (the distances between the nozzles that eject the rarefied gas flow in the environment), and nozzle stand off height. A detailed examination is presented to deduce the interactions of under-expanded rarefied gas flows in a vacuum environment.
- A robust solver, *rarefiedMultiphaseFoam*, based on the open-source DSMC solver, *dsmcFoam+*, has been implemented within the framework of OpenFOAM-2.4.0-MNF. This thesis has contributed to the development of the one-way coupling segment of the solver, which simulates the effect of rarefied gas flows on solid particles in multiphase interaction problems. Additional features for pre-processing and post-processing are also applied for the newly developed multiphase computational code.
- The default *dsmcFoam+* boundary conditions are extended for the *rarefiedMultiphaseFoam* solver, and customised boundary models are also implemented for the investigation of the interactions of surfaces and solid particles transported by rarefied gas flows.
- The benchmarking of *rarefiedMultiphaseFoam* is completed against theoretical, numerical, and experimental data in the literature. A test case, a surface coating process by application of the Aerosol Deposition Method, is run to show the capability of the solver and solid particle-wall interactions.

## Chapter 2

# Direct Simulation Monte Carlo

The direct simulation Monte Carlo (DSMC) method was introduced by G.A. Bird in 1963 [39] for probabilistic simulation of dilute gas problems in the transition regime using representative particles in phase space [38]. This method simulates the trajectories and interactions of gas atoms/molecules using representative particles, known as *simulators*, and can be used for the simulations of large scale systems such as a full scale of satellite to micrometer or nanometer sized devices. These simulators represent a large number of real atoms/molecules in a simulation. In this method, the physical concepts of dilute gases are applied and Boltzmann equation is used to derive physical assumptions. Garcia [36] states that there are many computational methods that use stochastic methods and DSMC is one such dominant method. DSMC and the Boltzmann equation have some limitations, i.e. molecular chaos assumptions and restrictions for dilute gas problems due to being based on kinetic theory [7].

Before the introduction of the DSMC method, dense gases and molecules in a container had been simulated using Alder & Wainwright [40]’s molecular dynamics (MD) method, through the relaxation of molecules to the Maxwellian distribution, where they initially all were assigned the same velocity. However, this method was limited to 100 molecules because of the high computational time and storage capacity. In addition, 100 molecules were not sufficient to gain information from high speed distributions. This is because MD applies a direct solution and numerical approach solving coupled ODEs at a time-step,  $\Delta t$ , for particle motion and collision. Therefore, MD is quite convenient for liquids and dense gases to calculate interactions between certain numbers of neighbour molecules, but it is inefficient for the simulation of rarefied gas molecules. In rarefied gas flow modelling, it is assumed that the particles encounter binary collisions with one of the probable collision partners [41]. Consequently, the usage of MD is limited to a small number of particles and timescale [35, 36]. For

these reasons, a novel stochastic technique - DSMC - that uses the Monte Carlo theorem, and is valid for normal and low densities was offered by Bird [39]. In the DSMC method, the particle motions are deterministically handled using the individual velocity vectors of DSMC particles at a small time-step. Collisions are stochastically investigated as particle positions are updated and the stochastic selection is carried out using the Monte Carlo theorem.

The first application of probability and random number generation on a gas simulation was pioneered by William Anderson, Lord Kelvin's assistant in the 1900s [4]. The method was enlarged to be used for the solution of various problems described by differential equations. The theorem was named *Monte Carlo* by Edward Teller, Stanislaw Ulam, and John von Neumann in 1946 [42]. In the Monte Carlo theorem, random numbers are created and this process is repeated many times. The answer is obtained from an approximation of the required quantity of random numbers. In the application of this method, the first random number does not provide the correct answer for the studied condition. Therefore, a source of random numbers, called *pseudorandom*, is created deterministically and the statistical test is stopped when the test reaches the randomness status [43]. Thus, DSMC selects the probable collisions in a flow using a random number generation method. Using the probability decreases the computational expenses and makes it possible to simulate higher number of particles and their collisions. Bird could determine more than 30,000 collisions per computational hour for a system which had 500 DSMC particles using the Silliac computer at University of Sydney in the early stages of DSMC.

As the DSMC technique matured, Bird [44] extended the method to be able to simulate the shock wave structures of a simple gas. Afterwards, Bird [45] simulated the binary mixture of argon-helium using the theoretical contribution of Sherman [46] as a reference. Sherman specified the velocity trend for a medium strength shock wave in a steady flow of a binary perfect gas mixture using the numerical integration of the Navier-Stokes equations. However, the numerical integration is useful for stronger shocks of simpler pure-gas problems. It is important to highlight the need for the accuracy of the results for normal to strong shocks and gas mixtures that consist of different molecular weights. Sherman pointed out the acceleration problems of different species. A small initial mole fraction of heavy component in a mixture accelerates before slowing down in the wave. A numerical solution was offered by Bird [45] as an extension of the previous study [47]. In the paper [45], all molecules are specified by smooth rigid elastic spheres of diameter  $d$  and mass,  $m$ . The species in the mixture are in equilibrium at the same temperature and non-dimensional distances are related with mean

free path. This numerical study allows for the sampling of all flow properties and obtaining temperature information of gas components in a mixture within the wave. The difficulties of Bird's approach are complexity and scattering. The increase in the of number of species makes the calculation more complex as seen in Equations 2.1 and 2.2 [48].

$$\lambda_0 = \frac{1}{\pi(N_{01} + N_{02})} \left[ \frac{N_{01}}{2^{\frac{1}{2}} N_{01} d_1^2 + N_{02} \{(d_1 + d_2)^2/4\} \{1 + (m_1/m_2)\}^{\frac{1}{2}}} + \frac{N_{02}}{2^{\frac{1}{2}} N_{02} d_2^2 + N_{01} \{(d_1 + d_2)^2/4\} \{1 + (m_2/m_1)\}^{\frac{1}{2}}} \right], \quad (2.1)$$

where the subscripts 1 and 2 show species and  $N_0$  is the upstream number density. The mean free path calculation for a simple gas is

$$\lambda_0 = (2^{\frac{1}{2}} \pi d^2 N_0)^{-1}. \quad (2.2)$$

In order to obtain accurate results whilst using Bird's approach, the initial number of populated molecules of each species should be equal and altered in order for the collision procedures to be able to represent the actual number of real molecules. For a typical case, the simulation was run on an English Electric KDF-9 computer in 30 minutes. Afterwards, Bird [49] investigated the deterioration of the equilibrium in translational and rotational modes for diatomic gas molecules.

The 1D flow problems were managed by Bird using rough-sphere models. However, the usage of DSMC and its application on various problems has increased. When an individual collision is simulated by a numerical method using Monte Carlo, any simplification cannot be done on the collision integral in principle. In practice, the computational solution of the binary collision of polyatomic gas mixtures becomes more prohibitive. Therefore, a statistical method was introduced by Larsen & Borgnakke (LB) [50] to examine the redistribution of energy and to specify the number of degrees of freedom, collision and post-collision probabilities, as well as angular distribution of relative velocities. The LB model applies the concept of relaxation to individual collisions and statistically interprets the results in a manner suitable to the simulation algorithm of the Monte Carlo theorem. Soon after, Bird [51] introduced a novel particle model known as variable cross-section hard sphere (VHS). The model specifies the mean free path, viscosity of the gas, relative velocities of the collision pairs using their collision

cross-sections with an agreement of empirical results.

In early implementations of DSMC, approximate physical models, mathematical models, and mechanical analogs, such as the hard-sphere approach have been used, however, these models could not represent a real gas well and applying the DSMC technique was difficult. The hard sphere model has many implementation advantages such as its easy application for constant cross-section models and computational efficiency because of treating the scattering as isotropic in the centre of mass frame of reference. However, when the approach is implemented in DSMC, the arbitrary cut-off in deflection angle or diameter has to be imposed and the extension of inverse power law becomes indefinite. Additionally, the definition of deflection angle for each collision is very complex. That is why phenomenological molecular models have been preferred to simulate the movement of real gases. VHS is a technique that takes advantage of the hard sphere model's simplicity and combines it with the enhanced accuracy of the inverse power law. This power model uses a coefficient of viscosity that depends on temperature. Moreover, VHS does not need arbitrary cut-off in deflection angle and diameter. Although the VHS model is employed in many applications, the variable soft sphere (VSS) model is also used to reproduce the Schmidt number for diffusing gas mixtures. This model was introduced by Koura & Matsumoto [52] in order to provide the same computational and analytical simplicity as VHS, where VHS has some of the basic collision principles of the hard sphere model and covers the isotropic scattering law with an empirical modification [38].

## 2.1 The Algorithm of DSMC

The basis of the DSMC algorithm is the creation of a control volume and meshing, populating DSMC particles (initialisation), movement and tracking of DSMC particles, collision computing, and sampling as summarised in Figure 2.1.

In a DSMC simulation, the control volume of interest is divided into computational cells and the particles travelling in the domain are allowed to collide during a time-step [53]. These computational cells are necessary to provide volumes for calculating macroscopic quantities and for implementing near-neighbour collisions and representing other motion of particles as seen in Figure 2.2.

In order to capture the collisions in a realistic manner, for all DSMC simulations, the cell size and the time-step should be smaller than the local mean free path, the cell residence time, and the mean collision time. The cell residence time,  $t_{res}$ , and mean collision time,  $t_{mc}$ , are calculated as

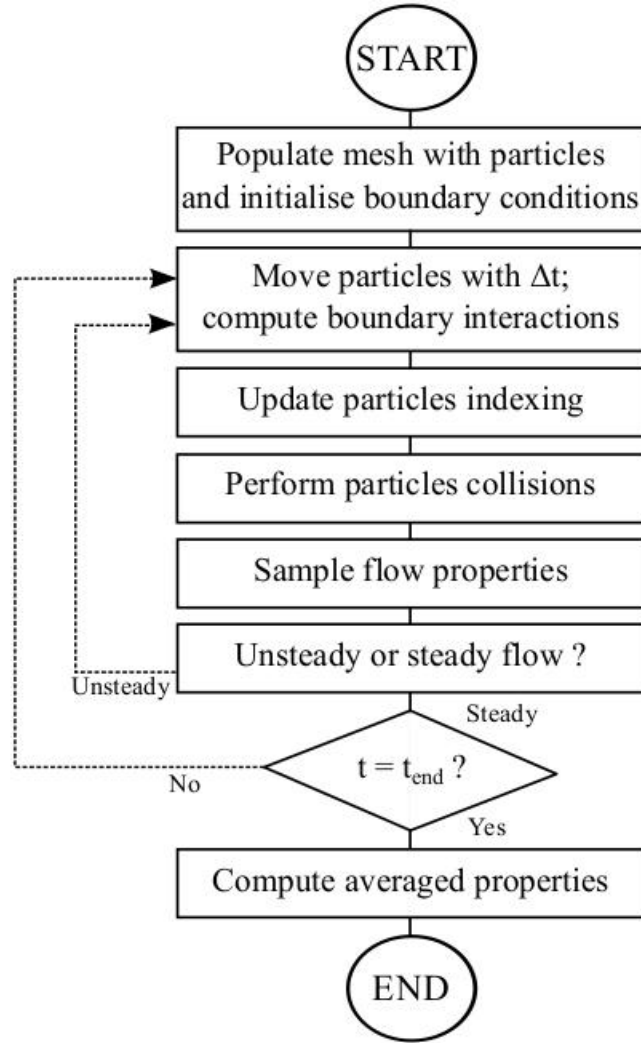


Figure 2.1: Flowchart of DSMC solvers' algorithm [7].

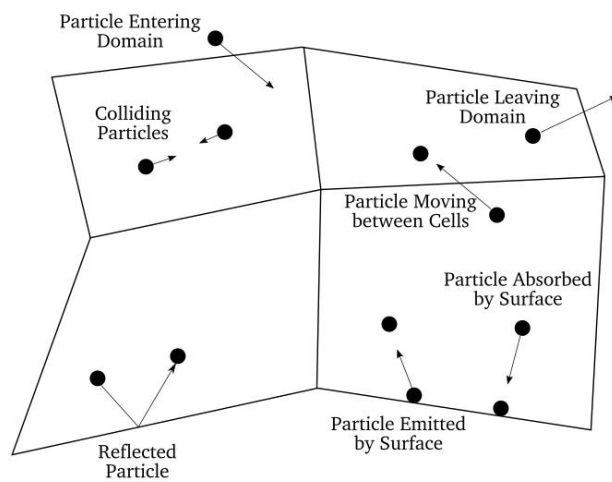


Figure 2.2: An illustration of DSMC cells and particles, adapted from [53].



$$t_{res} = \frac{\Delta x}{(v_{mp} + U_{\infty})}, \quad (2.3)$$

and

$$t_{mc} = \frac{\lambda}{v_{mp}}, \quad (2.4)$$

where  $\Delta x$  is the cell size,  $v_{mp}$  is the most probable thermal velocity,  $U_{\infty}$  is free-stream flow velocity, and  $\lambda$  is mean free path. The most probable thermal velocity is

$$v_{mp} = \sqrt{\frac{2k_B T_{\infty}}{m}}, \quad (2.5)$$

where  $k_B$  is the Boltzmann constant,  $1.380658 \times 10^{-23}$  J K<sup>-1</sup>,  $T_{\infty}$  is the temperature of the dilute gas flow, and  $m$  is molecular mass. In DSMC simulations, at least 20 particles per cell are suggested for accurate statistics [54]. The number of equivalent particles, i.e. the number of real atoms/molecules represented by each DSMC particle, is calculated as

$$n_{Particles} = \frac{n_{\infty} V_{cell}}{n_{EquivalentParticles}}. \quad (2.6)$$

The potential collisions of a large number of DSMC particles are determined using the Monte Carlo theorem. As in the algorithm of statistical methods, a DSMC analysis is performed for a large amount of time-steps to reduce scatter and statistical errors. Additionally, all of these particles are tracked in a large number of DSMC computational cells. For all of these reasons, DSMC is a computationally expensive technique, however, parallel computing, high performance computers (HPCs), and the no-time-counter method (NTC) make DSMC more applicable.

NTC is a form of determination to generate the correct number of collisions in a collision cell with  $N$  simulated particles using an acceptance-rejection probabilistic procedure. The control volume of a gas is split into cells and sub-cells. This restricts possible collisions to near-neighbour events and ensures that the correct collision rate is obtained [1, 38].

### 2.1.1 Particle Movement

This is the first stage of the main loop of the DSMC algorithm. All DSMC particles are moved through a distance corresponding to the product of the time-step and their individual velocity vectors. During this phase, the interactions with

surfaces and boundaries such as surface reflections, moving between processors, leaving the system from the deletion boundary, etc. are also handled [11]. At an inlet, the DSMC particles can be generated from the Maxwellian number flux across a boundary interface with an equilibrium gas,  $\dot{N}_{in}$ :

$$\dot{N}_{in} = n \left[ \exp(-s_n^2) + \pi^{1/2} s_n \{1 + \operatorname{erf}(s_n)\} \right] / (2\pi^{1/2}\beta), \quad (2.7)$$

and

$$\beta^{-1} = \left\{ m / (2k_B T) \right\}^{1/2}, \quad (2.8)$$

with

$$s_n = u_0 \beta, \quad (2.9)$$

where  $n$  is number density,  $s_n$  is speed ratio,  $\beta^{-1}$  is the inverse of the most probable molecular speed,  $m$  is the number flux of molecules of mass,  $k_B$  the is Boltzmann constant,  $T$  is the stationary gas temperature, and  $u_0$  is the stream velocity [38].

In this pre-processing step, the positions, velocity vectors, and types of DSMC particles are defined and the macroscopic values of density, temperature, etc. are specified by the user [6].

### 2.1.2 Collision Procedure

After moving all DSMC particles in the control volume, pre-collision positions and velocities of the particles are registered, as is the index of cell occupancy for each particle, which is required for the determination of collision and sampling procedures. The collision pairs of DSMC particles are selected randomly and their probability of collision is calculated using an acceptance-rejection procedure based on the probability ratio

$$\frac{P}{P_{max}} = \frac{\sigma c_r}{(\sigma c_r)_{max}}, \quad (2.10)$$

where  $\sigma c_r$  is the product of the collision cross-section and the relative speed of the collision pair and the sub-script *max* is the maximum value of this product that has been found in the current cell.

In order to capture the correct number of collisions and calculate the number of possible collision partners in a DSMC cell over a time-step, numerous methods are employed and Bird [38] states that the collision pair selection is the most

critical part in the collision procedure. Various collision schemes have also been used to ensure that the correct number of collisions take place, such as the simplified Bernoulli trial collision scheme [55, 56], the majorant collision frequency (MCF) [57], the Simplified Bernoulli Trials (SBT) collision algorithm and the transient adaptive subcell (TAS) (the SBT-TAS technique) [58], the symmetrized and simplified Bernoulli trial collision scheme [59], etc. However, as mentioned in section 2.1, Bird introduced [60] the NTC scheme to select the possible collision pairs in a cell, as in Equation 2.11.

$$^{1/2}N(N-1)F_N(\sigma c_r)_{max}\Delta t_{cell}/V_{cell}, \quad (2.11)$$

where  $N$  is the instantaneous number of DSMC particles in the cell [1],  $F_N$  is the number of real particles represented by a DSMC simulator,  $(\sigma c_r)_{max}$  is the maximum product of total collision cross-section and relative speed,  $\Delta t_{cell}$  is the time-step, and  $V_{cell}$  is the volume of a collision cell.

In order to decrease the computational expense of Eq. 2.10, an acceptance-rejection scheme is applied step by step as listed below [36]:

1. Calculation of number of collisions:

The number of collisions is calculated in order to test for acceptance using the NTC scheme.

2. The random selection of collision candidate particles,  $i$  and  $j$ :

Early DSMC simulations were run with a small number of DSMC cells and particles - corresponding to twenty or thirty particles in each cell as Bird reports [38] -, which brought to attention the fact that the distance between collision pairs. The cell size should be smaller than the mean free path to capture the collision event [61]. Therefore, the sub-cell technique, which is a computational technique that allows computational cells to be split into multiple sub-cells during the collision partner selection procedure, was introduced. In this way, only the particles within the same sub-cells are allowed to collide, and therefore collision pair selection from *near-neighbours* is promoted, which gives a realistic transfer of mass, momentum, and energy. Thus, the physical realism of DSMC simulations is increased [11] by promoting a realistic transfer of mass, momentum, and energy.

## 3. Collision acceptance:

Herein, each collision pair is tested using the acceptance-rejection method, where the collision is accepted if

$$\frac{c_r}{(c_r)_{max}} > \mathfrak{R}_f, \quad (2.12)$$

where  $\mathfrak{R}_f$  is a randomly generated number in the interval of  $[0,1)$  and  $(c_r)_{max}$  denotes the maximum relative velocity in the DSMC cell [36].

The inelastic collisions of diatomic or polyatomic molecules with the energy exchange between the translational and rotational modes are conducted by Larsen-Borgnakke (LB)'s *Statistical Collision Model with Unrestricted Energy Exchange* method [50]. In this version of the model, the rotational energy adjustment is applied to one collision event in every  $Z_{rot}$ , which is the rotational relaxation collision number. In order to increase the physical realism, the “restricted energy exchange” model was introduced by Larsen and Borgnakke to apply the change in the rotational energy to all collisions of diatomic or polyatomic gas by the adjustment of  $1/Z_{rot}$ . However, this fraction model was insufficient in terms of detailed balancing [38]. Finally, in order to achieve a realistic rate of rotational relaxation, the LB model solely considers a particular number of collisions as inelastic [11]. After the acceptance of the collision, the LB method checks the rotational relaxation and accepts if

$$\frac{1}{Z_{rot}} > \mathfrak{R}_f, \quad (2.13)$$

where  $Z_{rot}$  is the rotational relaxation number, and  $\mathfrak{R}_f$  is a randomly generated number in the interval of  $[0,1)$  and the rotational energy of the particle is then renewed. For energy conservation, the available total translational energy of the collision partner,  $\varepsilon_{tr}$ , decreases to adjust for rotational relaxation, and the new post-collision relative velocity,  $c_r^*$ , becomes

$$c_r^* = \sqrt{\frac{2\varepsilon_{tr}}{m_r}}, \quad (2.14)$$

where  $\varepsilon_{tr}$  is the available total translational energy after the energy adjustment for rotational relaxation, and  $m_r$  is the reduced mass of the collision partner [11].

## 4. Calculation of relative speeds:

Once a collision pair has been selected, their post-collision velocities should be computed by resetting the velocities of both particles [36]. With the

application of the conservation of linear momentum, the centre of mass velocity,  $\mathbf{c}_{cm}$ , is not affected by the collision, therefore,

$$\mathbf{c}_{cm} = \frac{1}{2}(\mathbf{c}_i + \mathbf{c}_j) = \frac{1}{2}(\mathbf{c}_i^* + \mathbf{c}_j^*) = \mathbf{c}_{cm}^*, \quad (2.15)$$

and

$$c_r = |\mathbf{c}_i - \mathbf{c}_j| = |\mathbf{c}_i^* - \mathbf{c}_j^*| = c_r^*, \quad (2.16)$$

where the superscript (\*) indicates the post-collision variables. In order to complete the calculation of relative velocity,

$$\mathbf{c}_r^* = c_r^*[(\sin\Upsilon \cos\Phi)\hat{\mathbf{x}} + (\sin\Upsilon \sin\Phi)\hat{\mathbf{y}} + \cos\Upsilon\hat{\mathbf{z}}], \quad (2.17)$$

where the scattering azimuthal angle,  $\Phi$ , is selected as

$$\Phi = 2\pi\Re_f, \quad (2.18)$$

which is uniformly distributed in a range of 0 to  $2\pi$  because  $\Re_f$  is a randomly generated number in the range of  $[0,1]$ . The elevation angle,  $\Upsilon$ , can be found by the probability density  $P_\Upsilon(\Upsilon)d\Upsilon = 1/2 \sin \Upsilon d\Upsilon$ , using the change of variable  $q = \sin \Upsilon$ , so  $P_q(q)dq = 1/2 dq$ , where  $q$  is uniformly distributed in the interval of  $[-1, 1]$  [36]. Ultimately, the post-collision velocities can be expressed as

$$\mathbf{c}_i^* = \mathbf{c}_{cm}^* + \left( \frac{m_j}{m_i + m_j} \right) \mathbf{c}_r^*, \quad (2.19a)$$

$$\mathbf{c}_j^* = \mathbf{c}_{cm}^* - \left( \frac{m_j}{m_i + m_j} \right) \mathbf{c}_r^*. \quad (2.19b)$$

5. The final step:

Steps 2 and 4 are repeated for the correct number of candidates calculated in Step 1.

### 2.1.3 Sampling and Averaging

After calculating the collisions, the sampling procedure begins to calculate macroscopic properties of the flow by sampling the quantities at each time-step and in each computational cell. Section 1.1.2 presents a summary of the sampling procedure. However, before starting the sampling procedure, DSMC simulations must be allowed to run until a pseudo-steady state condition is reached. Once this

is reached, the particle properties can be sampled for a long enough period to reduce the scatter in the resolved macroscopic flow fields [54]. It is important to note that the scatter in DSMC results is not a result of the stochastic nature of the method - it is a natural physical phenomenon that is also present in fully deterministic methods such as MD.

## 2.2 DSMC Codes

The DSMC method has been widely used for the solution of rarefied gas flow problems. Therefore, a variety of DSMC codes with different features have been developed. In this section, a brief overview is presented for some popular DSMC codes with their descriptions, applications, and capabilities in order to summarise the developments in DSMC codes, as various DSMC codes have been utilised in the reference studies in this thesis.

### 2.2.1 DS1V, DS2V, and DS3V

Three different versions of Bird's DSMC codes, DS1V, DS2V, DS3V, are presented on his website [62]. DS1V is the first version of his Fortran open-source code to simulate 1D steady and unsteady planar, cylindrical, and spherical rarefied gas flows in a wide range from non-reacting monatomic molecules to reacting gas mixtures.

Despite DS1V being a solver to test the DSMC algorithm, Bird advanced the DSMC solver and described DS2V as “a well established visual interactive DSMC program” [62]. DS2V is a 2D DSMC solver for both steady and unsteady flows, taking into account the flow gradients in two axes. This version also brings new features such as the optional disabling of the nearest-neighbour collisions, automatic cell adaption with respect to local mean free path, a graphical user interface (GUI), etc. Previously, the software was a 32-bit program, which restricts the accuracy and is subject to computational issues with round-off errors [60] but with one of the latest updates, the program was updated to 64-bit [62].

DS2V and DS3V are quite similar DSMC computation codes by having the same features and capabilities. The differences of DS3V to DS2V are that this solver is capable of simulating 3D rarefied gas flows, however, it does not have a GUI as DS2V does. The executables of both DS2V/3V are still on the website.

### 2.2.2 MONACO

Another parallelised mature DSMC code was developed by Dietrich and Boyd [63] in 1995 with an optimised scalar and parallel application. In order to achieve high computing performance, the solver localises the data structure using the computational cells as well as the simulations which are run in parallel. Thus, any cell can be assigned to any processor, and the load balancing procedure can be conducted with distributing equal load on each processor while keeping the communications among the nodes at a minimum. The solver is capable of creating structured and unstructured meshes in order to describe the boundary conditions as well as the geometry in 2D and 3D. Furthermore, Ref. [63] states that MONACO can also simulate the flow with multi-species and various models, such as the LB model [50], Bergemann & Boyd's model [64] for energy exchange in internal mode, and Dietrich's model [65] for energy exchange in chemical reactions. The use of the MONACO solver is restricted to users in the USA [11].

### 2.2.3 SPARTA

SPARTA (**S**tochastic **P**Arallel **R**arefied-gas **T**ime-accurate **A**nalyzer) is a parallel, open-source, and C++ based solver. The key features of the solver include [66–68]:

- 2D, 2D-axisymmetric, and 3D simulations,
- Cartesian cell with local refinements,
- global boundary conditions and surface reflection with specular and diffuse models,
- chemistry models of total collision energy (TCE) and quantum kinetic (Q-K), and reactions,
- cell weighting of particles, and static and dynamic load balancing,
- cell, global, and surface statistics with a time-averaging option.

The solver was developed by Sandia National Laboratories and the United States Department of Energy (DOE). Although the solver is covered by GPL, the GNU Lesser General Public License (LGPL) may be applied occasionally.

### 2.2.4 SMILE

SMILE (Statistical Modelling In Low-Density Environment) is a parallel, FORTRAN90 based, DSMC solver with a C++ based user-interface and a free cross-platform wxWidgets GUI library. The solver was developed by the Laboratory of Computational Aerodynamics in the Khristianovich Institute of Theoretical and Applied Mechanics, which is the Siberian Branch of the Russian Academy of Sciences. The key features of the solver include [69]:

- arbitrary 2D, axisymmetric, and 3D simulations,
- collision modelling in a two-layer rectilinear adaptive mesh, and dynamic grid adaptation according to local mean free path,
- variable gas species capacities with an extendable chemical database,
- implementation of the majorant collision frequency method for the collision partner selection,
- implemetation of the TCE model for chemical reactions,
- elastic collisions, i.e. VHS and VSS, and inelastic collisions, i.e. the LB model with translation-rotation and translation-vibration energy transfers.

Although the solver has a website, it does appear that the code is not ready for distribution.

### 2.2.5 *dsmcFoam*, *dsmcFoam+*

OpenFOAM (**O**pen-source **F**ield **O**peration **A**nd **M**anipulation)<sup>1</sup> is an object-oriented, C++ software suite, released under the GNU<sup>2</sup> GPL (General Public License), collection of executables and libraries that are used mainly to solve computational fluid dynamics (CFD) problems. The executables within the OpenFOAM framework comprise of solvers and utilities, which are employed to solve the physical problem and pre- and post-processings operations, respectively. In terms of pre-processing, OpenFOAM provides powerful meshing tools to create structured and unstructured meshes, whilst the OpenFOAM mesh conversion tools give more flexibility to users to prepare a mesh using various meshing software and to convert their output to formats compatible with OpenFOAM. In the processing stage, a wide range of simulations such as incompressible and compressible flows

---

<sup>1</sup>[www.openfoam.org](http://www.openfoam.org)

<sup>2</sup>[www.gnu.org/licenses](http://www.gnu.org/licenses)



with different turbulence models, non-Newtonian fluids, multi-phase flows, heat transfer, combustion, solid mechanics, and financial modelling, etc. can be simulated by OpenFOAM's solvers. Furthermore, the code is open-source, can be easily extended, and is well-documented, giving the opportunity to users to make changes to default solvers and customise them according to their needs or create their own solvers instead of running the simulations on a black box, top-level syntax, and abstracted utilities, where the users cannot control or interfere with the background computations. For post-processing, although OpenFOAM has some tools for raw data extraction from the simulations, raw data extraction and flow visualisation can also be post-processed using ParaView, which is provided with OpenFOAM, or other software, such as Tecplot.

The development of a DSMC solver within OpenFOAM was pioneered by the implementation of an MD solver [70,71], called *mdFoam*, to simulate the flow problems at a discrete level. Afterwards, the fundamental features of the MD code such as particle initialisation, particle tracking, etc. were modified according to the algorithm of the DSMC method in order to create a new solver for rarefied gas flows, named *dsmcFoam* [61]. The features of *dsmcFoam* are listed in Ref. [61] as

- steady-state or transient simulations,
- parallel processing capability,
- arbitrary 2D/3D geometries,
- structured/unstructured meshes,
- automatic 8 sub-cell generation to promote near-neighbour collisions<sup>3</sup>,
- arbitrary number of gas species,
- free-stream flow boundaries,
- Maxwellian diffuse or specular surface interactions,
- no-time-counter collision partner selection,
- rotational energy mode,
- LB rotational energy redistribution,
- variable hard sphere collision model,

---

<sup>3</sup>see § 2.1.2

- cyclic (periodic) boundaries.

DSMC solvers generally have these essential features, but the weaknesses of this solver were improved upon in the new updated version, named *dsmcFoam+*, for solving practical rarefied gas problems with high functionality. The weaknesses in the old version were updated as listed by Ref. [6],

- arbitrary axisymmetric geometries,
- vibrational energy,
- electronic energy,
- chemical reactions,
- gravitational force controller,
- mass flow rate measurement,
- simulation quality reports,
- improved boundary condition handling,
- dynamic load balancing.

Many other DSMC solvers also include these features [62, 66, 69]. The new version of the solver can be employed by *dsmcFoamPlus* executable, though there are other supporting pre- and post-processing executables/applications. For instance, the *dsmcInitialise* utility populates DSMC simulator particles in the mesh. The basic algorithm of a steady-state *dsmcFoam+* simulation can be expressed by the following steps:

1. Create computational cells,
2. Specify boundary conditions, the properties of species and initial macroscopic flow properties, and time-step,
3. Populate DSMC simulators employing *dsmcInitialise*,
4. Run the simulation using *dsmcFoamPlus*,
5. Start sampling once the solution has reached a steady-state condition,
6. Post-processing of the simulation's outcomes.

*dsmcFoam+* has been consistently updated with the addition of new functions and applications. Thus, it is significant to present the accuracy of the solver before running larger simulations and extending the solver's capabilities. The following section presents a benchmarking of *dsmcFoam+* against Bird [1]'s results.

## 2.3 A Benchmarking Case: Supersonic Corner

The *dsmcFoam+* solver is an updated DSMC code with extended capabilities and different features, is widely employed in this thesis. Therefore, it is significant to compare the accuracy of *dsmcFoam+* results by a reference case. The supersonic corner flow of argon gas is an example test case from Bird’s “Molecular Gas Dynamics and the Direct Simulation of Gas Flows” monograph [1]. The problem is modelled using *dsmcFoam+* for the benchmarking of the solver to simulate the flow that passes between the corner of two plates that perpendicular to each other. The plates are  $0.25\text{ m} \times 0.18\text{ m}$  in size as shown in Figure 2.3.

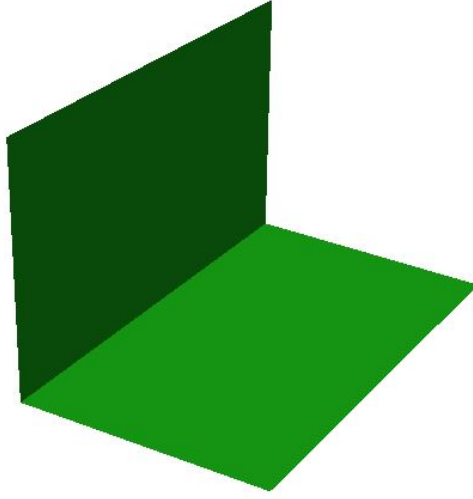


Figure 2.3: The used geometry in test case.

### 2.3.1 Problem Description

In the simulation, the temperature of the dilute argon gas free-stream gas,  $T_\infty$ , is 300 K and the velocity,  $U_\infty$ , is  $1936\text{ ms}^{-1}$ . The rarefied gas flow passes over the corner of the perpendicularly-mounted flat plates, which are held at 1000 K temperature, and the freestream number density,  $n_\infty$ , is  $1 \times 10^{20}\text{ m}^{-3}$ . The VHS mean free path is 0.0129 m and the characteristic length is 0.3 m, therefore, the overall Knudsen number is 0.043, meaning the flow is in the slip regime.

With given data, the most probable thermal velocity, the cell residence time, and the mean collision time are calculated as  $353.393\text{ ms}^{-1}$ ,  $5.634 \times 10^{-6}\text{ s}$ , and  $3.65 \times 10^{-6}\text{ s}$ , respectively. The time-step of the simulation is selected as  $5 \times 10^{-7}\text{ s}$ , smaller than both the cell residence time and mean collision time. In order to meet the other condition of catching the inter-molecular collisions, the cell size is

chosen to be smaller than the mean free path. The domain size and number of cells are shown in Table 2.1.

Table 2.1: The mesh properties of plates

Plate Number	Domain Size (m)	Number of Cells
1	$0.5 \times 0.18 \times 0.18$	$10 \times 36 \times 36$
2	$0.25 \times 0.18 \times 0.18$	$50 \times 36 \times 36$

The number of cells and the constant cell volume,  $V_{cell}$ , are 77760 and  $1.25 \times 10^{-7} \text{ m}^3$ , respectively. The number of equivalent particles is also selected as  $6 \times 10^{11}$ , populating at least 20 particles in each cell.

### 2.3.2 Results and Discussion

Figures 2.4, 2.5, 2.6, 2.7, and 2.8 compare contours of heat transfer, skin friction, normalised temperature, normalised density, and Mach number from *dsmcFoam+* and Bird [1].

Figure 2.4 shows the contours of heat transfer coefficient on the plates. Heat transfer coefficient,  $C_h$ , is calculated from the change in overall heat transfer rate,  $\dot{Q}$ , i.e.

$$C_h = \frac{\dot{Q}}{1/2 \rho_\infty U_\infty^3}, \quad (2.20)$$

where  $\rho_\infty$  and  $U_\infty$  are free-stream mass density and free-stream velocity, respectively.

As seen in Figure 2.4, the heat transfer coefficient is low at the outer edges of plates. The highest value of the heat transfer coefficient was displayed at two lobes, which is very close to the leading edges and the junction. In general, heat transfer contours in both solutions are very similar which means that *dsmcFoam+* has obtained an accurate solution for heat transfer effects.

Figure 2.5 represents the contours of stream-wise skin friction, which is along the x-axis. The skin friction coefficient,  $C_{fx}$ , on the x-axis was calculated as

$$C_{fx} = \frac{\tau}{1/2 \rho_\infty U_\infty^2}, \quad (2.21)$$

where  $\tau$  is surface shear stress.

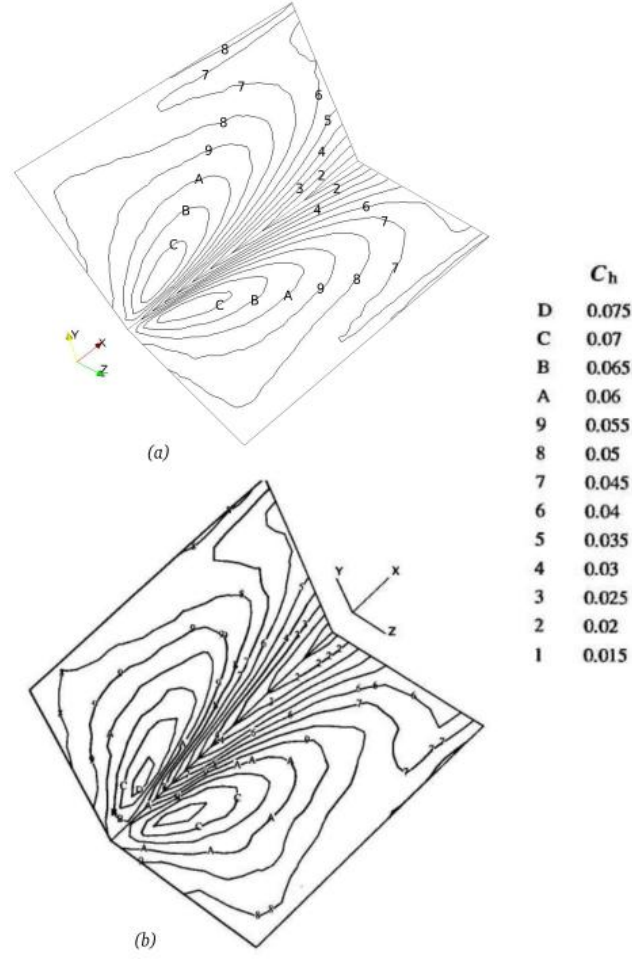


Figure 2.4: Contours of heat transfer coefficient from (a) *dsmcFoam+*, and (b) Bird [1].

The skin friction coefficients on the streamwise axis were calculated based on the x-component of the shear stress and the coefficient represented in Figure 2.5. The contours of the skin friction coefficient on the x-axis have quite similar patterns with the heat transfer coefficient. In addition, the values of the skin friction coefficient is twice the heat transfer coefficient values in some regions. According to the kinetic theory of perfect gases, viscosity and conductivity change with the square root of the temperature. *dsmcFoam+* provided this relation between the mechanical and thermal behaviours of the fluid flow, as expressed in Ref. [72], in the results of skin friction and heat transfer coefficients. Furthermore, the results from *dsmcFoam+* show the same trend as Bird's [1] solution.

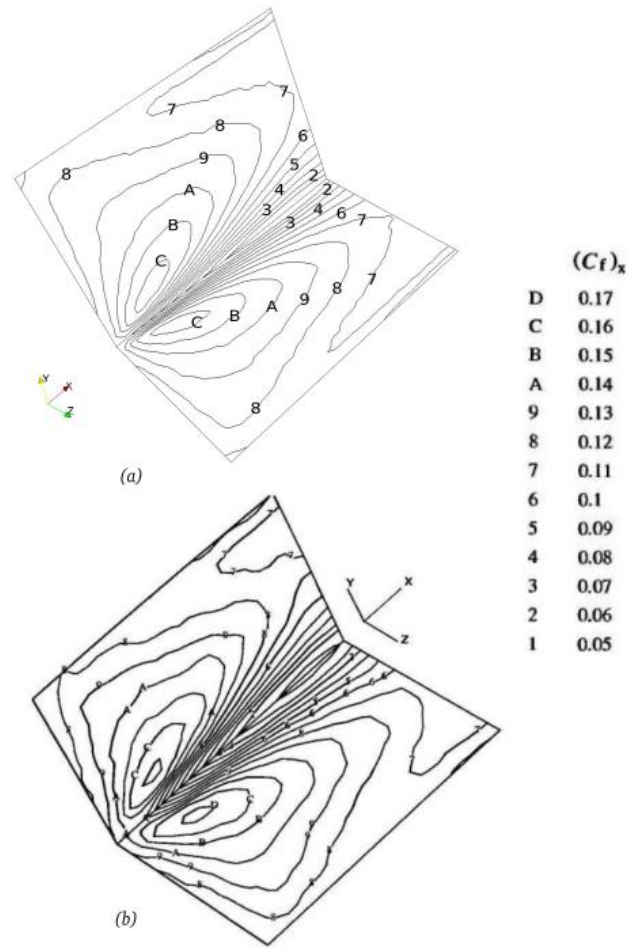


Figure 2.5: Contours of streamwise skin friction on the x-axis from (a) *dsmcFoam+*, and (b) Bird [1].

Figure 2.6 displays contours of normalised temperature predictions from *dsmcFoam+* and Bird [1]. The contours of normalised temperature for 4 cross-sections throughout the control volume are compared in Figure 2.6. In the vicinity of the leading edge and junction, the value of normalised temperature is higher than the outer corner. Going towards the trailing edge, the normalised temperature increases at the outer corners and decreases at the junction. The results from *dsmcFoam+* and Bird [1] are compared in Figure 2.6 and it is seen that the results from *dsmcFoam+* show an excellent agreement with Bird's [1] predictions.

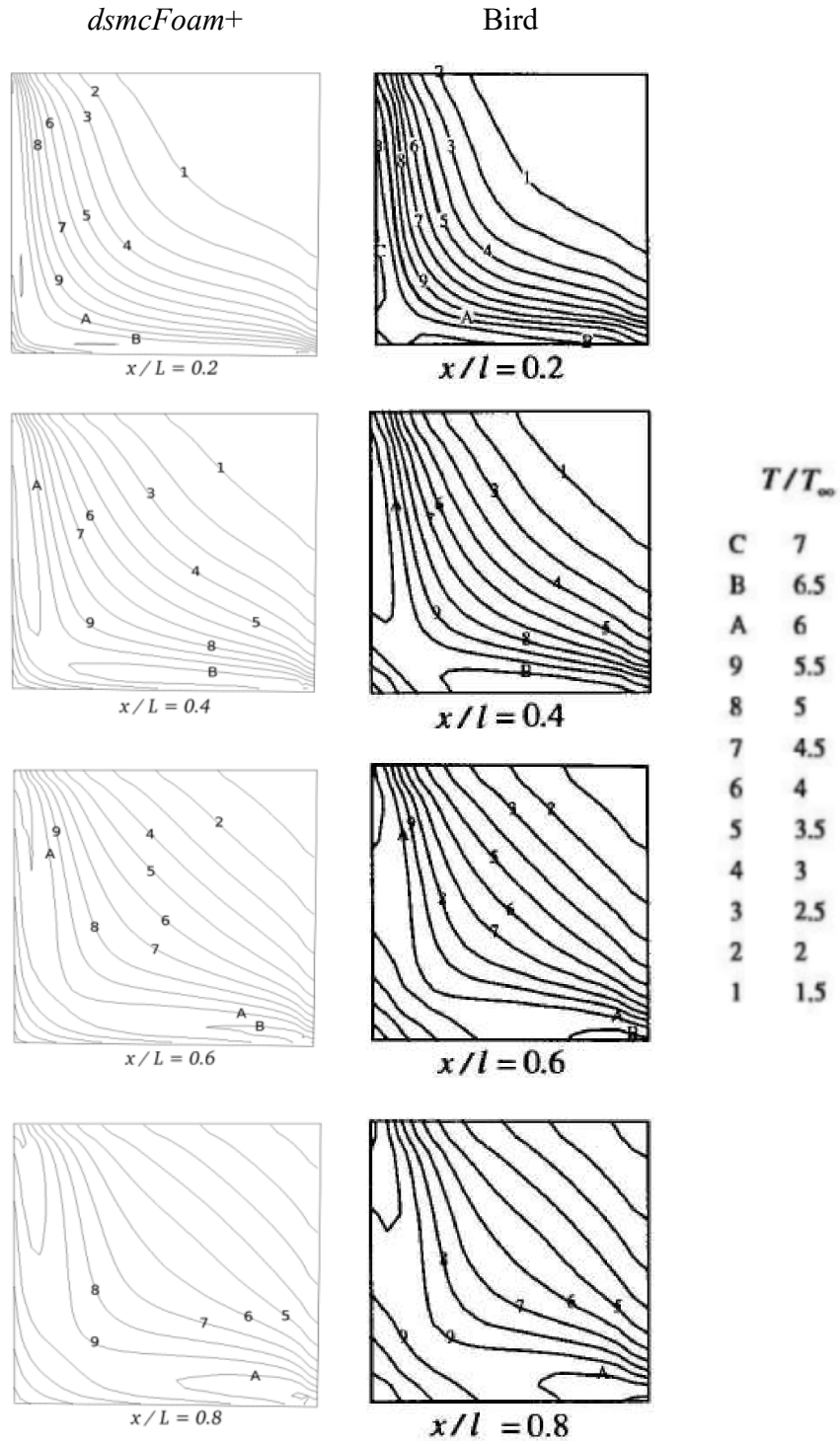


Figure 2.6: Contours of normalised temperature at certain locations from *dsmcFoam+*, and Bird [1].

Figure 2.7 shows the contours of normalised density in several cross-sectional planes, which are perpendicular to the stream-wise direction. The patterns of the normalised density contours are different from normalised temperature contours. At regions near the leading edge and junction, high values are seen for normalised

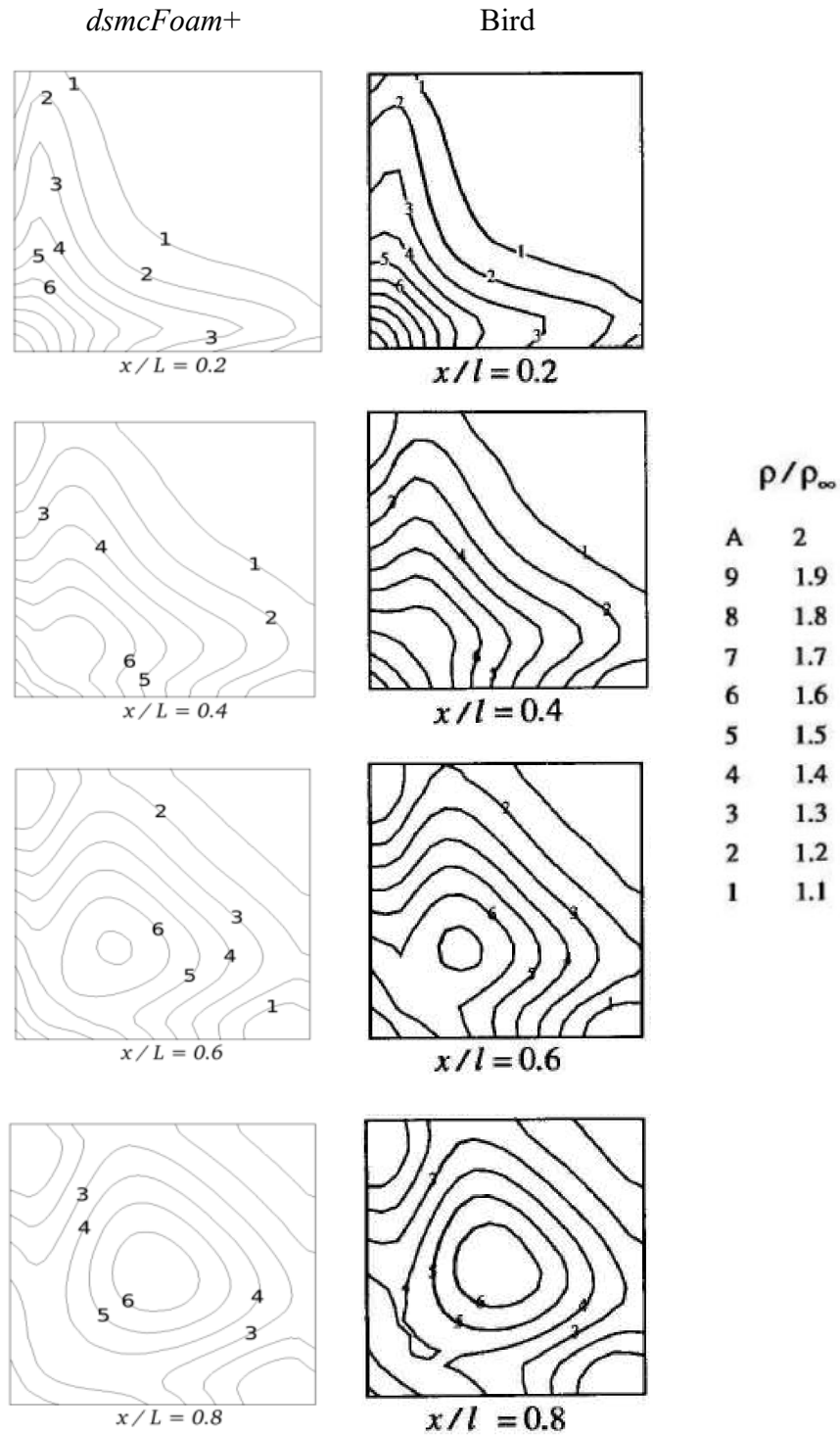


Figure 2.7: Contours of normalised density at certain locations from (a) *dsmcFoam+*, and (b) Bird [1].

density and the lower values at the outer corners. However, a dense and isolated region occurs in the middle of the control volume further downstream. *dsmcFoam+* successfully provided the previously mentioned changes in normalised



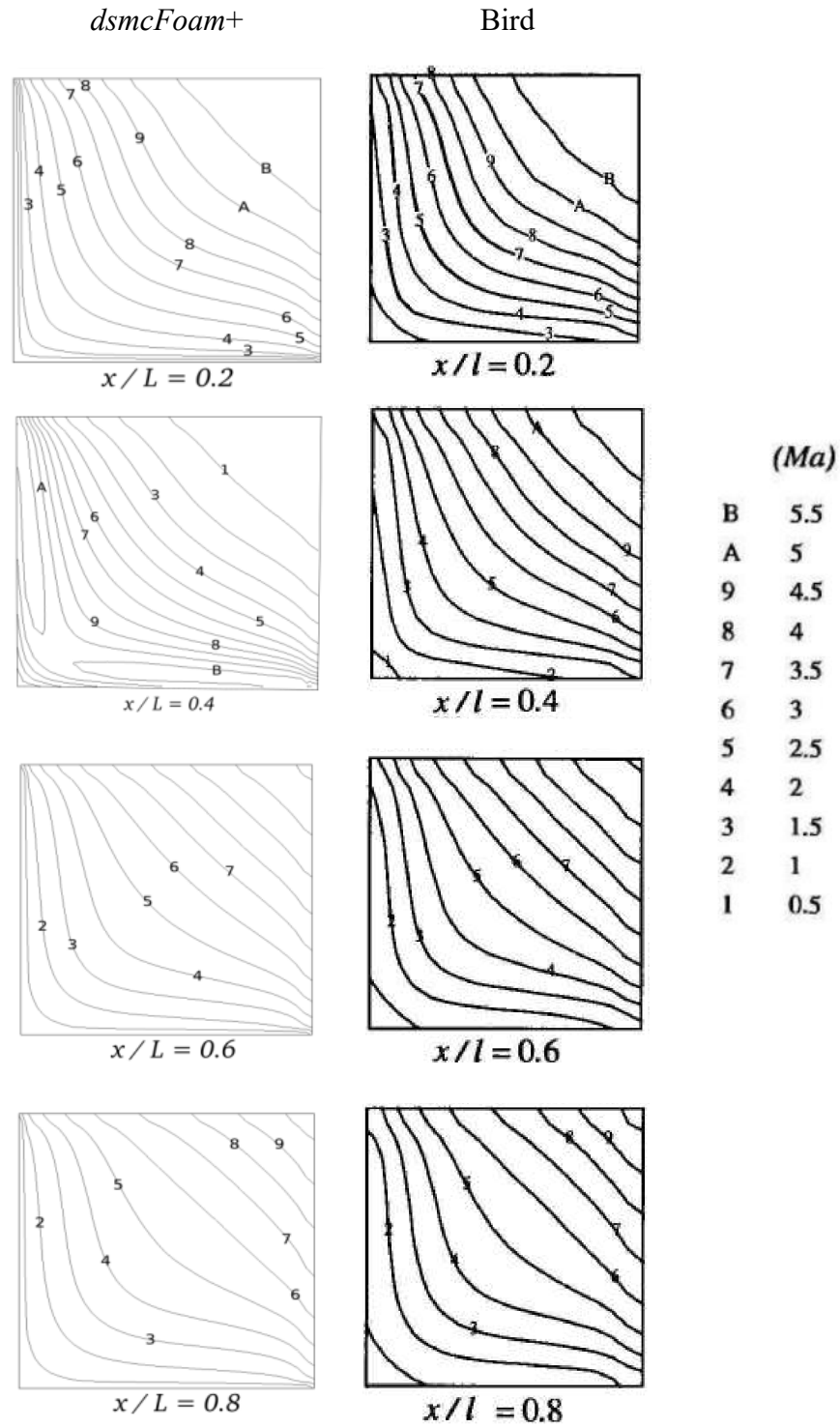


Figure 2.8: Contours of Mach number at certain locations from *dsmcFoam+*, and Bird [1].

density value and the results from *dsmcFoam+* match those of Bird [1].

Figure 2.8 demonstrates predictions of *dsmcFoam+* and Bird [1] for variations in Mach number by taking cross-sections perpendicular to the free-stream flow

throughout the control volume. As expected, whilst the temperature and density values increase near the leading edge and junction in the inlet, the gas slows down and a subsonic flow occurs. For this reason, the slip velocity increases in the vicinity of the outer corner and going throughout the outlet. As a result, the speed of gas flow reaches supersonic values around the outer corner.

### 2.3.3 Summary

An excellent agreement between the outcomes of *dsmcFoam+* and Bird [1] is obtained. This presents that the capabilities and accuracy of *dsmcFoam+* is reliable for further simulations of dilute gas problems and the solver can be used with confidence to simulate the more complex flow physics and to build up novelties as based on the *dsmcFoam+* computational code.

# Chapter 3

## The Effect of Increasing Rarefaction on Edney Shock Interactions

### 3.1 Introduction

Shock-shock interaction problems in the aerospace industry have been extensively studied due to their crucial impact on aerodynamic performance and aero-heating characteristics in supersonic and hypersonic flight platforms. A shock-shock interaction problem can arise in high-speed vehicles where an oblique shock from one part on the body impinges on a bow shock from a different part on the body. The result can be greatly increased local pressure and heat loads on a surface [73]. A well-documented example of the problem was detected during an X-15 research flight. An investigation indicated that a shock interaction pattern formed in the vicinity of a ramjet-pylon [74] and severe structural damage was caused by an increase in local heat flux due to an oblique shock generated by the ram jet spike tip, spike flare, or cowl lip interacting with a bow shock ahead of the pylon leading edge.

The shock-shock impingement phenomenon was widely investigated by Edney for different geometries in the blowdown tunnel of Sweden's Flygtekniska Försöksanstalten (FFA) [75, 76]. Edney categorised this shock interaction phenomenon with six different types, I-VI, as illustrated in Figure 3.1, for various regions with respect to where the interaction occurs around a bluff body that is used to create a bow shock.

Starting below the body, a type-I interaction is formed, and this transitions through types II-VI as the shock interaction point increases in height relative to the body, e.g. a type-VI interaction is formed when the two shocks meet above

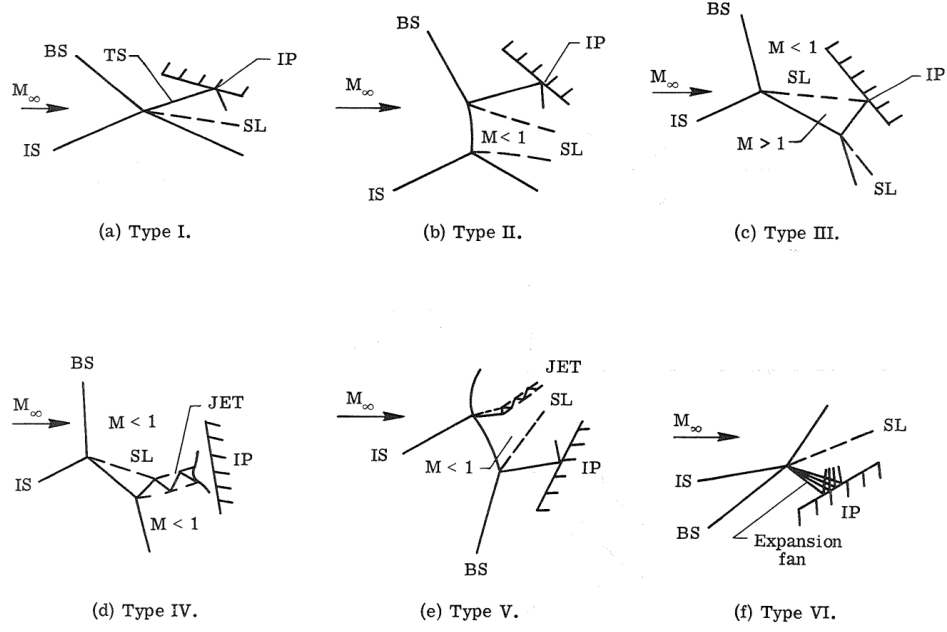


Figure 3.1: Edney's shock interaction pattern classifications. BS: bow shock, IP: impingement point, IS: impinging shock, SL: shear layer, TS: transmitted shock [77].

the solid body.

Type-I and II interactions exist as a result of the intersection of two shocks from opposite families and these weak interactions create aerothermal loadings because of the crossing of a terminating shock and a boundary layer below the sonic region. The type-III pattern is another weak impingement that creates a shear layer, which is emitted from the shock intersection point and attaches to the bluff body surface. Shock-shock interactions in the vicinity of the stagnation point of a bluff body dramatically increase the heat and pressure loads; the flow exhibits the highest perturbation in type-IV interactions. In this case, the interaction is such that a supersonic jet forms at the first triple point and reaches behind the bow shock, where the flow would otherwise be subsonic. In addition, a shear layer and a transmitted impingement occur at the second triple point. This supersonic jet impingement in type-IV interactions leads to augmented pressure and heat loads where the supersonic jet penetrates behind the bow shock and terminates at the solid surface. As the intersection point moves towards the upper side of the sonic line, it transitions to a type-V interaction, and the effect of the supersonic jet impingement on the surface gradually decreases. However, boundary layer interactions still lead to perturbations in heat and pressure loads. In a type-VI pattern, two weak shocks interact and create a supersonic expansion fan, which interacts with the boundary layer. This pattern does impact local heating

and pressure to the same extent as type-IV or V interactions, however, type-VI problems are significant in terms of predicting the onset of type-V [77, 78].

Sanderson [79] states that the existence of shock impingement patterns depends on the gas properties, the angle and strength of the shocks, the geometry of the shock generators, and the relative location of impingement on the bow shock. Numerous computational modelling studies have been conducted on shock-shock interactions at hypersonic speeds using the continuum NSF equations [78, 80–84]. The operation of hypersonic vehicles is likely to take place at high altitudes where the atmosphere becomes rarefied resulting in the continuum and local thermodynamic equilibrium assumptions to breakdown, making the use of the NSF equations questionable. Additionally, the constitutive relations that connect heat transfer and shear stress to other parameters, and linear transport terms in the NSF equations become invalid as flow rarefaction increases. With increasing cruising altitude of hypersonic platforms, the Knudsen number increases and the Reynolds number decreases as the aircraft operates in a relatively low density atmosphere [85]. Therefore, even the member of the same Edney shock-shock interaction types present different properties with increasing Knudsen number. Figure 3.2 summarises how the structure of a type-IV interaction alters while the platform is increasing the flight altitude.

The modelling of a shock-shock interaction heating on the surface of a cowl lip caused by the impingement of a weak incident shock on a stronger bow shock has been studied in the past. The pioneering study of Pot *et al.* [86] was conducted via experiment in the French Office National d’Etudes et de Recherches Aérospatiales (ONERA) R5Ch low-density wind tunnel in order to analyse the local heat flux and pressure increase in type-III and IV patterns at low Reynolds number. In the experimental setup, a compression ramp forms an oblique shock wave ahead of a strong bow shock generated by the bluff body. The experimental results indicate that a supersonic jet in type-IV and shear layer effects in type-III, promote increased aerothermodynamic loads on the bluff body surface. Although this study provides a dataset for type-III and IV Edney shock interactions at a constant rarefaction level, in order to enhance the understanding of the effect of changing flow and geometrical conditions, various geometrical setups with altering flow properties are required for a realistic understanding of a hypersonic vehicle with a cruise altitude that takes it through different rarefaction regimes during climb and descent.

Carlson and Wilmoth [87] applied the DSMC method to solve the type-IV interaction for a hypersonic platform at a Mach-15 and 35-km altitude cruise condition using Bird’s two dimensional/axisymmetric (G2) code. The authors

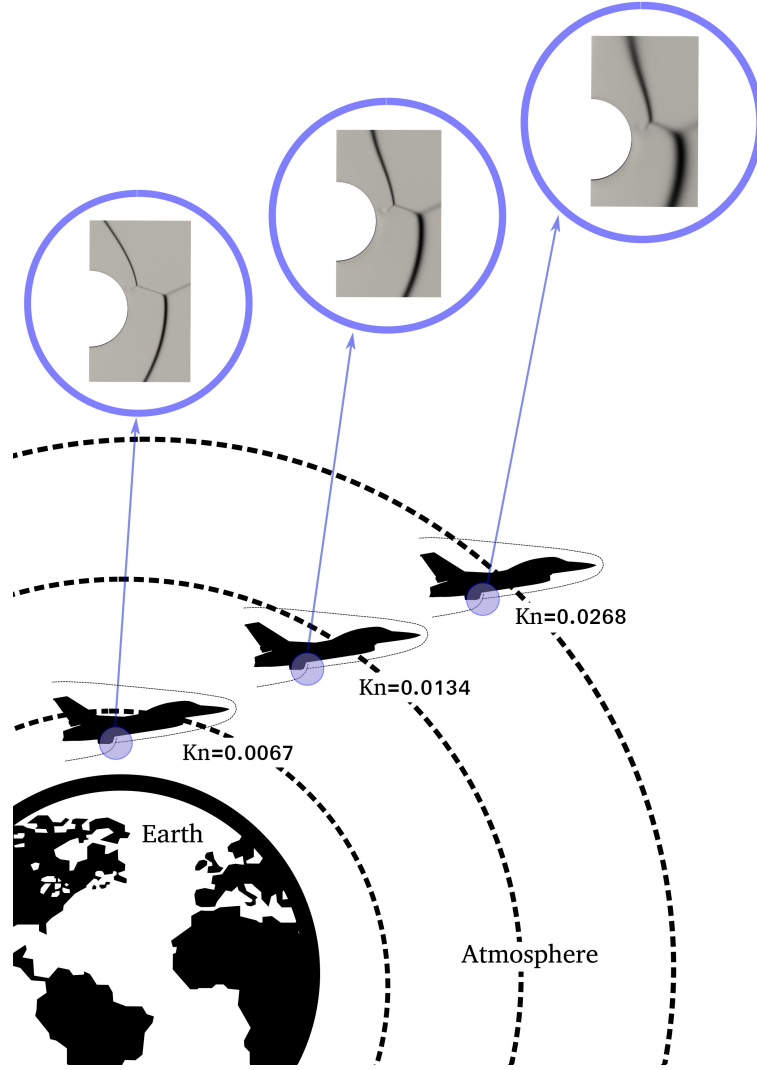


Figure 3.2: A schematic to indicate how the Edney flow patterns may change during a hypersonic flight with an increasing altitude.

state that the flow is in the transition regime as a result of the altitude and that non-continuum and non-equilibrium effects should be taken into account since a purely continuum solution will not be able to correctly predict the flow physics. In this study, several cases altering the position of the incident shock impingement are performed using a coarse computational grid in order to distinguish type-IV interactions roughly. The worst-case scenario of type-IV is then selected with respect to surface heat transfer information rather than different geometrical configurations. Then, the grid around the surface and the shock interaction region is refined to predict the surface heating accurately and to observe the dispersion and viscous interaction of supersonic jet flow. Mach number and temperature contours around the cylinder and the distribution of heat transfer and surface

pressure plots of the cylinder surface are measured for a generic flight condition at a constant cruise altitude.

Moss *et al.* [88] simulated the shock-shock and shock and boundary-layer interactions in type-III and IV interactions for a generic Mach-10 flight condition, building on the experience of Carlson and Wilmoth [87]. In this study, the ONERA experiment [86] was numerically replicated using Bird's [89] 2D/axisymmetric DSMC code. This study compares the effect of varying distance between the shock generator wedge and the cylinder, which changes the interaction type by altering the impingement location of the incident shock wave. The free-stream properties were kept constant and the surface pressure and heating-rate distributions for eight different shock generator positions were measured. Information on the density and temperature changes in the flow-field, Mach and density contours around the cylinder, and the location of zero shear stress are presented for the severe type-IV interaction. Moss *et al.* also showed that DSMC results with local grid refinement and local time-steps are in very good agreement with the experimental results and are able to predict the distributions and peak locations of pressure and heating-rate. Moss *et al.* examined only type-III and IV interactions at a constant Knudsen number.

Xiao *et al.* [90] conducted a simulation of a double-cone geometry in order to investigate Edney type-IV interactions using various molecular models such as hard sphere, VHS, and VSS. The numerical set up is designed to create a type-IV interaction, with different flow-field properties used. The authors presented a comparison of molecular models and experimental results using the pressure coefficient and Stanton number. It is found that hard sphere and VHS models are more accurate than VSS for the simulations of Edney type-IV shock impingements.

Zuppardi and Boffa [91] investigated the effects of increasing rarefaction and variation in Mach number on the shock wave-boundary layer interactions. The extension of the interaction region, intensity of the shock wave, aerodynamic loads, heating rates, slip velocity, and temperature are evaluated and measured on a flat plate upon which a shock wave impinges, for various cases between 55 and 57 km altitude test conditions using Bird's 2D/axisymmetric DS2V code. Zuppardi [92] then extended the former study and the study by Moss *et al.* [88], using the same test conditions as a reference, evaluated the effect of increasing rarefaction in a type-IV interaction using the 2D axisymmetric DSMC code DS2V. In this study, the geometrical setup is the same as the ONERA experiment [86] and the effect of altering the Knudsen number is examined. The study reports that with increasing rarefaction, the shock thickness increases and the impingement point

of the incident shock becomes indistinguishable at higher altitudes. Moreover, the peak location of heating-rate and aerodynamic loads and temperature profile throughout the shock wave varies depending on the rarefaction level. The study investigates the effect of rarefaction in a type-IV pattern. However, other Edney types and the results of gradual changes in the location of the bluff body and Knudsen number are not discussed.

White and Kontis [93] also carried out DSMC simulations to examine the effect of rarefaction on shock interaction physics and surface parameters for a type-IV interaction pattern and found similar results as Moss *et al.* [88]. The study demonstrates that when the rarefaction level is increased by decreasing gas density, but maintaining all other dimensional parameters the same, the location of the peak in heat transfer, pressure, and skin surface friction coefficients move through the upper sonic-line, with the magnitudes of the coefficients decreasing. Mach number contours for three different Knudsen numbers are also compared in the study, which show the change in impingement location of the incident shock wave and the lack of a supersonic jet and terminating shock as rarefaction increases. Therefore, this study presents a dataset solely for increasing rarefaction; the effect of geometrical configuration was not considered at the same time. The authors employed *dsmcFoam+* and the solver provides promising results when compared with numerical [88, 90] and experimental [86] results in the literature.

Cruise at hypersonic flight produces a complicated flow-field around the aircraft, such as shock-shock interactions. The steadiness of the interaction pattern depends on the geometrical parameters of the shock generators and the flow properties. According to Grasso *et al.* [94], the impingement location also affects the steadiness of the interaction. Lind & Lewis [95] applied the thin-layer approximation to the 2D NSF equations to simulate a type-IV case at Mach 8 in continuum flow. They observed the formation of unsteadiness, which distorts the flow between the bow shock and shock generator. Shear layers shed between shock layers produce a frequency of unsteadiness, which is associated with the movement of the supersonic jet with the same frequency. Furthermore, the study reveals that the location of peak pressure, the strength of the shock, and the position of shock impingement and supersonic jet flow has a significant impact on the behaviour of the flow unsteadiness. Yamamoto *et al.* [96] focused on the unsteadiness in Edney interactions considering thermochemical nonequilibrium. The authors state that the unsteadiness characteristic is strongly tied with the location of impingement and the stand-off distance of the shock. The paper presents detailed information about the period of oscillation and the movement of the supersonic jet, with the unstable behaviour being classified as a new type-VII interaction. However,



Windisch *et al.* [97] pointed out that the flow still touches the surface, allowing for it to be classified as a type-IVa interaction. Windisch *et al.* [97] studied the jet flow structure of type-IV cases and presented an insight into the thermochemical nonequilibrium. The wall quantities and jet flow dynamics of a unsteady flow are identified through numerical solutions for a nitrogen gas atmosphere.

Even when the geometry remains the same, the literature indicates that a change in the degree of rarefaction of the upstream flow leads to different impingement locations and alteration in the strength of the shock waves. Therefore, another significant parameter that can influence the type of Edney shock pattern that is produced is flow rarefaction. In addition, Refs. [79, 88] state the impact of the relative location of the bow shock generator to the oblique shock generator on the flow physics. It is known in the continuum regime that Edney shock interactions can display unsteady behaviour, but this has not been observed in rarefied flows previously. Therefore, the work in this chapter generates a new simulation matrix with varying Knudsen number and shock interaction locations. In the present study, 2D DSMC simulations of eleven different geometries at three different Knudsen numbers are carried out using the *dsmcFoam+* code.

## 3.2 Computational Considerations

### 3.2.1 Problem Description

In the present work, six types of Edney patterns are investigated by replicating the geometrical dimensions of Refs. [86] and [88]. The geometry consists of an isosceles triangle shock generator with a  $10^\circ$  leading angle and a wedge positioned into the flow at an angle of  $10^\circ$  with the horizontal axis. The wedge is represented by a  $20^\circ$  ramp and an extended planar surface with  $L1 = L2 = 0.50771$  m spanwise length in 2D *dsmcFoam+* simulations. The bow shock generator is a cylinder of diameter  $D$ , with its centre located at distance of  $L3$  and a height of  $H$ . Initially, the longitudinal position of the cylinder centre to the leading edge of the wedge and the distance from the horizontal axis are set at  $L3 = 0.102$  m, and  $H = 0.053$  m, respectively, as in the reference studies for benchmarking of the *dsmcFoam+* results. Afterwards, in order to investigate the variation of shock-shock interaction patterns and augmentation of aerothermodynamic loads on the cylinder surface while the free-stream parameters remain constant, the impingement point of the oblique shock on the bow shock is controlled by altering the  $H$  value from 43 to 63 mm in 2 mm increments. The experiment [86] was conducted with a model width-to-cylinder diameter ratio of 6.25. This is assumed

to be wide enough that a 2D flow assumption can be made at the centre of the cylinder's length, allowing for 2D *dsmcFoam+* simulations to be performed. The schematic of the numerical and experimental set up are illustrated in Figure 3.3.

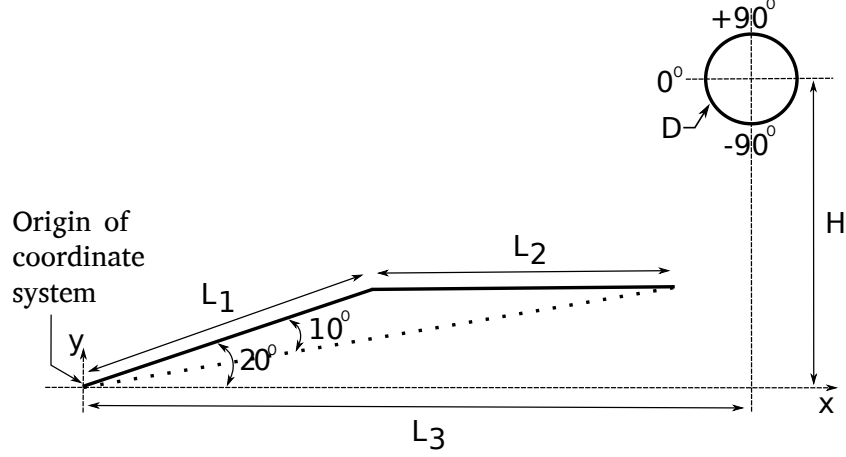


Figure 3.3: Schematic of the problem set up.

In the experiment [86], a contoured nozzle with a diameter of 0.2 m and nominal stagnation conditions of 2.5 bar and 1050 K provides a uniform free-stream environment. The test was held with static test conditions of Mach number,  $Ma_\infty = 10$ ; velocity,  $U_\infty = 1450 \text{ ms}^{-1}$  and temperature,  $T_\infty = 52.5 \text{ K}$ .

In order to investigate the effect of rarefaction with increasing altitude, the geometrical matrix above is tested at a constant Mach number and increasing Knudsen number by reducing the gas density. The relation of the Knudsen, Reynolds, and Mach numbers can be expressed as  $Kn \propto Ma/Re$ . The Knudsen number is based on the diameter of the bluff body,  $D$ , and the mean free path in the free-stream gas, calculated from the VHS model [51]. The viscosity is calculated from the VHS power law for the determination of the Reynolds number, which is  $\mu_\infty = 4.99 \times 10^{-6} \text{ Pa s}$ . The Reynolds number,  $Re = \rho_\infty U_\infty D / \mu_\infty$ , is also calculated for each case and the free-stream parameters are presented in Table 3.1 for the different simulations.

Table 3.1: Knudsen numbers, Reynolds numbers, and free-stream densities.

$Kn$	$Re$	$\rho_\infty \text{ (kg m}^{-3}\text{)}$
0.0067	1820	$3.916 \times 10^{-4}$
0.0134	910	$1.958 \times 10^{-4}$
0.0268	455	$9.790 \times 10^{-5}$

For the present study, the non-reacting gas model is considered as a mixture of

21% oxygen and 79% nitrogen and the energy exchange between the translational, rotational, and vibrational modes are taken into account. The properties of the VHS model gas species are given in Table 3.2.

Table 3.2: VHS parameters of the gas species.

	N <sub>2</sub>	O <sub>2</sub>
Viscosity exponent, $\omega$	0.74	0.77
Reference diameter, $d_{ref}$ (m)	$4.07 \times 10^{-10}$	$3.96 \times 10^{-10}$
Molecular mass, $m$ (kg)	$46.5 \times 10^{-27}$	$53.12 \times 10^{-27}$
Rotational degree of freedom, $\zeta_{rot}$	2	2
LB VHS rotational relaxation collision number, $Z_{rot}$ [1]	5	5
Characteristic vibrational temperature, $\theta_{vib}$ (K)	3371	2256

The fully diffuse Maxwellian reflection kernel is used to model the gas-surface interactions. The surface temperature is held constant at 300 K. *dsmcFoam+* has a varying value of  $Z_{vib}$  that is calculated based on the collision temperature of each individual collision event.

### 3.2.2 High Performance Computing

The simulations were carried out on two different high performance computing clusters at the University of Glasgow. The numerical expense of the DSMC simulations varies according to the rarefaction levels and the level of unsteadiness of shock-shock interactions, which depends on the geometrical setup of the simulated case. In addition, in order to capture the inter-molecular collisions more precisely, the meshes are locally refined using an adaptive mesh technique, where refinement regions are detected by the sampling of local mean free path data. Although a typical simulation in this work was performed on 24 cores and required 134 hours of wall time, the total run time of one simulation varies depending on the number of mesh refinements in order to reach the final result. Therefore, each case has to run multiple times with different locally refined meshes in order to capture the correct inter-molecular and surface collisions.

For efficient parallel running, the cases are decomposed such that each core is assigned a similar number of DSMC particles. Approximately 1 million simulator DSMC particles are assigned to each core, but to compensate for the unsteadiness effect, the number of computing cores are increased by 1.3 times in the unsteady simulations. With the movement of the DSMC particles throughout the control

volume, the weighting on each computational core gradually becomes imbalanced and the performance between the cores changes. The load balancing feature of *dsmcFoam+* is used to keep the distribution of weighting on each core stable by allowing a maximum imbalance of 10% by number density.

### 3.3 Results and Discussion

In the literature, the Edney shock interaction problem has been studied experimentally and computationally with various DSMC codes from different aspects. This study aims to enlarge that of White and Kontis [93], by extending the geometrical matrix while varying the level of rarefaction. Herein, in order to obtain the effect of increasing rarefaction level on shock-shock interactions, the free-stream flow is considered at three different Knudsen numbers. At the same time, the geometrical setup with altering the vertical position of the bow shock generator cylinder,  $H$ , is shown in Figure 3.3.

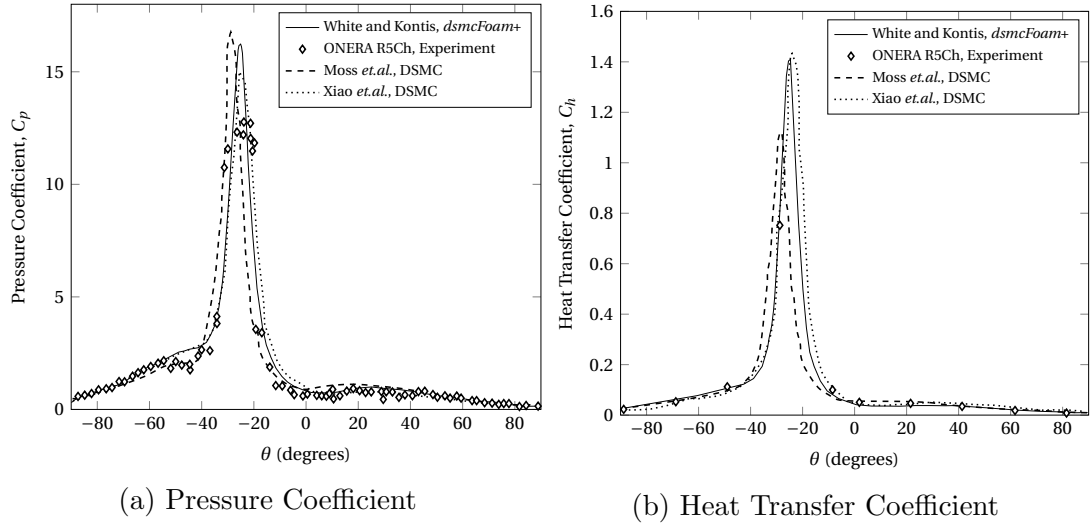


Figure 3.4: Benchmarking of *dsmcFoam+*, through aerothermodynamic load distribution on the cylinder surface [93].

As illustrated in Figure 3.4, the pressure and heat transfer coefficients from White and Kontis, calculated using *dsmcFoam+*, are compared with other studies [86, 88, 90], which have the same case set up. As the results of *dsmcFoam+* simulations of this thesis, which are the replication of White & Kontis [93], match with White & Kontis [93]’s ones, they are not shown in Figure 3.4 so as to avoid repetition. *dsmcFoam+* provides reasonable results when compared with those from the experiment. *dsmcFoam+* predicted a peak pressure value of approximately three normalised units higher than the experiment, but this difference might be caused by the finite width-to-diameter ratio of the experiment being

idealised as 2D in the simulations, or a deficiency in the resolution of the pressure tapping holes in the experiment. The *dsmcFoam+* outcomes are in a good agreement with other results of numerical references. Furthermore, the heat flux was measured at only ten locations in the experiment, making it impossible to obtain the exact location of the peak value from the experimental data. *dsmcFoam+* predicts a maximum heat transfer coefficient of 1.4 on the surface of the bow shock generator cylinder at around  $-25^\circ$  (see Figure 3.3 and note that negative angles are clockwise in the convention being used), which is in close agreement to the results of experiment and other DSMC codes.

It is highlighted in both numerical references that the size of the numerical mesh is a substantial parameter affecting the accuracy of the results. This is because the mean free path changes locally as the density and temperature gradients form, therefore, local mesh refinement is a necessity to capture the collision statistics correctly. Moss *et al.* states that three different meshes were created with 9200 (coarse), 63510 (intermediate), and 97060 (fine) cells when the free-stream Knudsen number is constant and indicated the mesh sensitivity using the pressure distributions and surface heating results. In *dsmcFoam+*, the simulations are run with about 1 million cells, where local refinement regions are created to ensure the cell sizes are smaller than the local mean free path throughout. In *dsmcFoam+*, the mesh refinement is not automatic, but can be performed at write intervals (i.e. at the user-defined intervals of physical time at which results are written to disk) manually, or using appropriate scripts, e.g. Python or bash.

In many practical conditions, these flows are unsteady [98]. Therefore, as the DSMC simulations were being run, the number of DSMC simulators and the average linear kinetic energy were monitored. It is observed that these properties fluctuate at a ‘steady’ state for each case, however, negligibly small changes can be accepted as steady since the unsteady effects, such as the shedding of the shear layer and movement of the supersonic jet, do not influence the results. Depending on the rarefaction level and the position of the cylinder, the amplitude of the monitored parameters and their trends can become large, indicating unsteady, cyclical, behaviour with time. The flow characteristics of each case, including a statement of whether it was found to have a steady-state solution or not, are summarised in Table 3.3. It can be seen that the flow conditions are steady for many of the simulations performed (e.g. all values of  $H$  greater than 51 mm), but at the two lower Knudsen numbers studied, the flows become unsteady for  $H$  of 49 mm and below. However, the flow rarefaction tends to move the flow back towards a steady solution, as is evident for the results at  $Kn = 0.0268$  at  $H$  of 49 mm and below. The unsteadiness is a strong function of the shock interaction

Table 3.3: The Edney shock interaction types and flow characteristics with changing Knudsen number,  $Kn$ , and the height at which the centre of the cylinder is positioned,  $H$ .

$Kn$	$H$ (mm)					
	63	61	59	57	55	53
0.0067	Steady	Steady	Steady	Steady	Steady	Steady
	Type-I	Type-I	Type-I	Type-II	Type-III	Type-IV
0.0134	Steady	Steady	Steady	Steady	Steady	Steady
	Type-I	Type-I	Type-II	Type-III	Type-IV	Type-IV
0.0268	Steady	Steady	Steady	Steady	Steady	Steady
	Type-I	Type-II	Type-III	Type-IV	Type-IV	Type-IV
$Kn$	$H$ (mm)					
	51	49	47	45	43	
0.0067	Steady Type-IV	Unsteady	Unsteady	Unsteady	Unsteady	
0.0134	Steady Type-IV	Unsteady	Unsteady	Unsteady	Unsteady	
0.0268	Steady	Steady	Steady	Steady	Steady	
	Type-IV	Type-V	Type-V	Type-VI	Type-VI	

locations and strengths, both of which are affected by flow rarefaction. It can also be observed that an increase in flow rarefaction brings about a change in the Edney interaction type at higher values of  $H$ , e.g. the interaction remains type-I for  $H = 59$  mm and  $Kn = 0.0067$ , but for the same height it becomes a type-II and type-III interaction at  $Kn = 0.0134$  and  $Kn = 0.0268$ , respectively.

### 3.3.1 Steady Flow Field

Data presented in this section provides insight to the effects of rarefaction level and varying shock impingement location on the augmentation of aerothermodynamic loading on the cylinder surface and the development of various Edney shock-shock interaction types, as seen in Table 3.3, when the flow achieves a steady state solution. Figures 3.5-3.13 compare the aerothermodynamic properties on the cylinder surface at different Knudsen numbers and values of  $H$ . Pressure,  $C_p$ , heat transfer,  $C_h$ , and surface friction,  $C_f$ , coefficients are calcu-

lated as

$$C_p = \frac{P - P_\infty}{\frac{1}{2}\rho_\infty U_\infty^2} \quad (i), \quad C_h = \frac{q}{\frac{1}{2}\rho_\infty U_\infty^3} \quad (ii), \quad C_f = \frac{\tau}{\frac{1}{2}\rho_\infty U_\infty^2} \quad (iii), \quad (3.1)$$

respectively, where  $P$  and  $P_\infty$  are local and free-stream pressure,  $q$  is local heat flux,  $\tau$  is local surface friction,  $\rho_\infty$  and  $U_\infty$  are the density and velocity of the free-stream.

### Pressure coefficients

The initial Knudsen number selected is 0.0067, which is the same as previous studies [86, 88, 90, 93]. Figure 3.5(a) shows the distribution of the pressure coefficient on the cylinder surface as  $H$  is altered between 63 mm and 57 mm. At these heights, type-I and type-II patterns are found, with peak pressure coefficients forming between  $-10^\circ$  and  $-20^\circ$  on the cylinder surface (see Figure 3.3). However, the peak point moves towards lower side of the cylinder at  $H = 57$  mm, where the flow pattern remains type-II, but is close to becoming a type-III pattern. A strong type-III can then be seen in Figure 3.5(b) at  $H = 55$  mm, with a peak at  $51.5^\circ$ . The most severe interactions are at  $H = 53$  mm and  $H = 51$  mm, which have an approximately three times greater pressure coefficient than the type-III interaction. The peak location of pressure shifts from  $-30.8^\circ$  at  $H = 53$  mm to  $-11^\circ$  at  $H = 51$  mm. The highest pressure coefficient is found at  $Kn = 0.0067$  when the cylinder centre is positioned at  $H = 53$  mm. When the distance between the reference surface and the centre of the cylinder is decreased below 51 mm, the flow-field structure transforms to unsteady, which will be discussed later.

Figure 3.6 shows the surface pressure coefficients at  $Kn = 0.0134$ . The pressure distribution of type-I and type-II interactions show a similar pattern to those with  $Kn = 0.0067$ . In addition, at both  $Kn = 0.0067$  and 0.0134, the location of maximum pressure coefficients of type-I interaction patterns are measured as 1.86 at  $H = 61$  mm and 63 mm. In terms of type-I interactions, the maximum  $C_p$  is found at  $-11^\circ$  when  $Kn = 0.0067$  and  $H = 61$  mm, and  $Kn = 0.0134$  and  $H = 63$  mm. The stagnation point is located at  $-12^\circ$  when  $Kn = 0.0067$  and  $H = 63$  mm, and at  $-15^\circ$  when  $Kn = 0.0134$  and  $H = 61$  mm. As shown in Table 3.3, a type-II pattern takes place at  $H = 59$  mm when  $Kn = 0.0134$ , however, a type-II interaction is not found until  $H = 57$  mm when  $Kn = 0.0067$ . In addition, when the stagnation point locations are compared for these cases, it is seen that the peak pressure value can be measured at  $-55^\circ$  in both cases but

a 1.15 times greater  $C_p$  value is found at  $Kn = 0.0134$ . Similarly, type-III cases are observed at  $H = 57\text{mm}$  and  $-50^\circ$  when  $Kn = 0.0134$  and at  $H = 55\text{mm}$  and  $\sim -51.5^\circ$  at  $Kn = 0.0067$ .

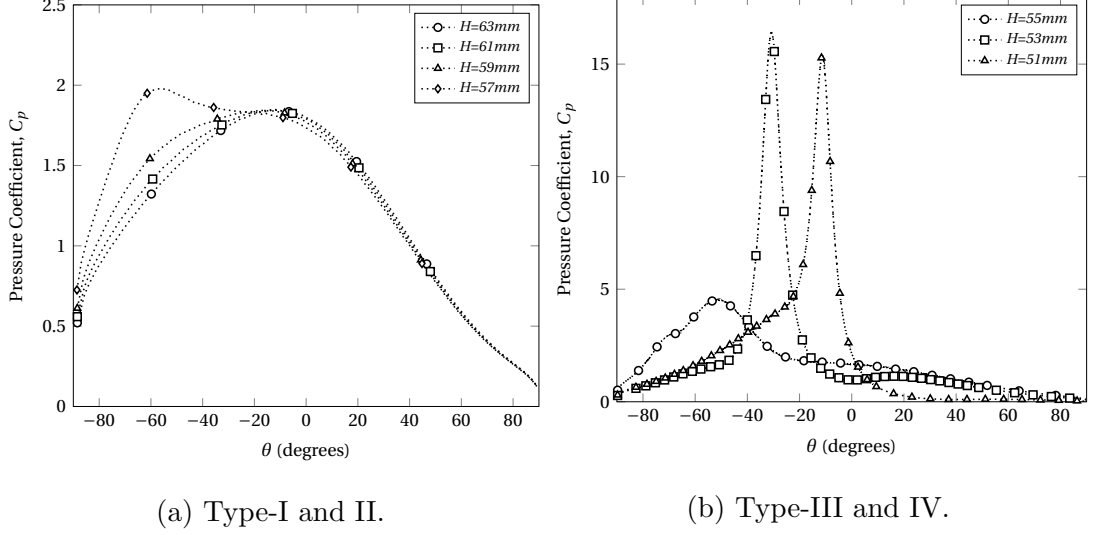


Figure 3.5: Pressure coefficient distributions at  $Kn = 0.0067$ .

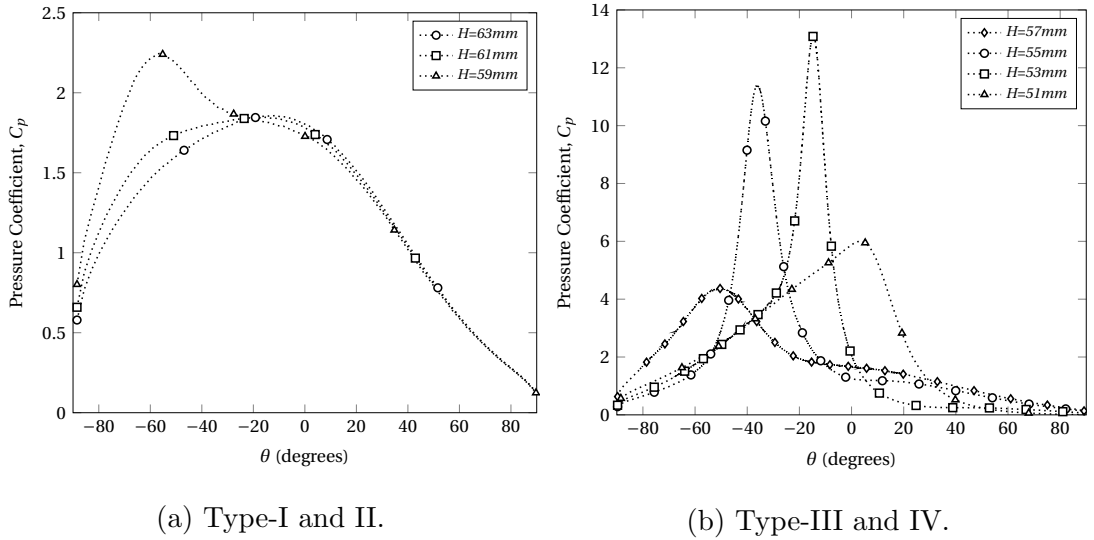
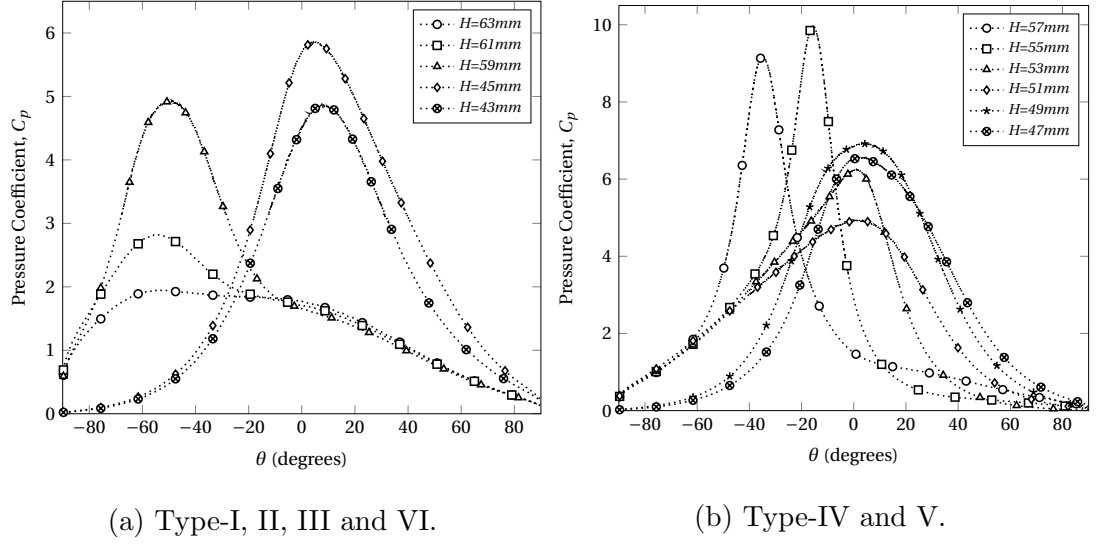


Figure 3.6: Pressure coefficient distributions at  $Kn = 0.0134$ .

Figure 3.7 shows the surface pressure coefficients obtained for a flow-field with  $Kn = 0.0268$ . The peak value of  $C_p$  for a type-I interaction is found at  $-50^\circ$ , which is further towards the lower side of the cylinder compared to the two lower rarefaction levels. It is observed in all three Knudsen numbers that the peak locations of the type-II interactions are found at around  $-54^\circ$ . However, the type-I and II patterns have a greater impact on the surface compared to the lower Knudsen numbers and the peak is 1.05 and 1.35 times greater for type-I and type-II interactions, respectively. The maximum impact of type-III interactions for all



Figure 3.7: Pressure coefficient distributions at  $Kn = 0.0268$ .

three Knudsen numbers is found at almost the same location on the surface,  $-49^\circ$ , with 1.33 times higher magnitude than the average value of the lowest and moderate rarefaction levels. At  $Kn = 0.0067$  and  $0.0134$ , type-IV patterns influence the surface pressure coefficients between  $-36^\circ$  and  $5^\circ$ , but the affected zone is slightly restricted at  $Kn = 0.0268$  to  $-35^\circ$  to  $2^\circ$  at different  $H$  values. The transformation of Edney shock types at greater  $H$  values is also found at this rarefaction level. For instance, type-IV is observed for the first time at  $Kn = 0.0067$  and  $H = 53\text{mm}$ , at  $Kn = 0.0134$  and  $H = 55\text{mm}$ , and at  $Kn = 0.0268$  and  $H = 57\text{mm}$ . In addition, the type-IV pattern occupies a wider range of  $H$  when the flow becomes more rarefied, i.e.  $51 - 53\text{mm}$  at  $Kn = 0.0067$ ,  $51 - 55\text{mm}$  at  $Kn = 0.0134$ , and  $51 - 57\text{mm}$  at  $Kn = 0.0268$ . At  $H = 51\text{mm}$  and  $53\text{mm}$  for  $Kn = 0.0268$ , type-IV patterns become weaker than those for  $H = 55$  and  $57\text{mm}$ . Although these two type-IV interactions show the typical pattern of a type-IV impingement with terminating shock near the cylinder surface etc., the type-V cases at  $H = 47\text{mm}$  and  $49\text{mm}$  have more impact quantitatively on the surface pressure coefficient around  $3.25^\circ$ . When  $H$  is shortened to  $43\text{mm}$  and  $45\text{mm}$ , type-VI interactions are seen in the vicinity of  $4.6^\circ - 7.3^\circ$ , with a peak pressure coefficient which is slightly less than in the type-V interactions.

When the type-IV interactions are compared for all three Knudsen numbers, it is observed that the interactions produce greater peak pressure coefficients at the less rarefied flow-field condition as shown in Table 3.4, which is in contrast to the results of the type-I, II, and III interactions. This is because the diffused shock wave into the bow shock passes between the strong shear layers, which prevent the distribution of the diffused shock wave, and strikes through the surface almost

perpendicularly and more pointedly compared to the type-I, II, and III cases. The highest impact of the type-IV interaction at  $Kn = 0.0067$  and  $0.0134$  is found at  $H = 53$  mm. For  $Kn = 0.0134$  at  $H = 51$  mm that the interaction is tending towards a type-V interaction and the peak pressure coefficient is reduced to around 6. At  $Kn = 0.0268$ , this evolution of shock patterns starts earlier when  $H = 53$  mm as the severity of the type-IV interaction begins decreasing. The maximum pressure coefficient at the highest Knudsen number is measured at  $H = 55$  mm, which is quantitatively the lowest when compared with the other most severe cases both at the lowest and moderate Knudsen numbers.

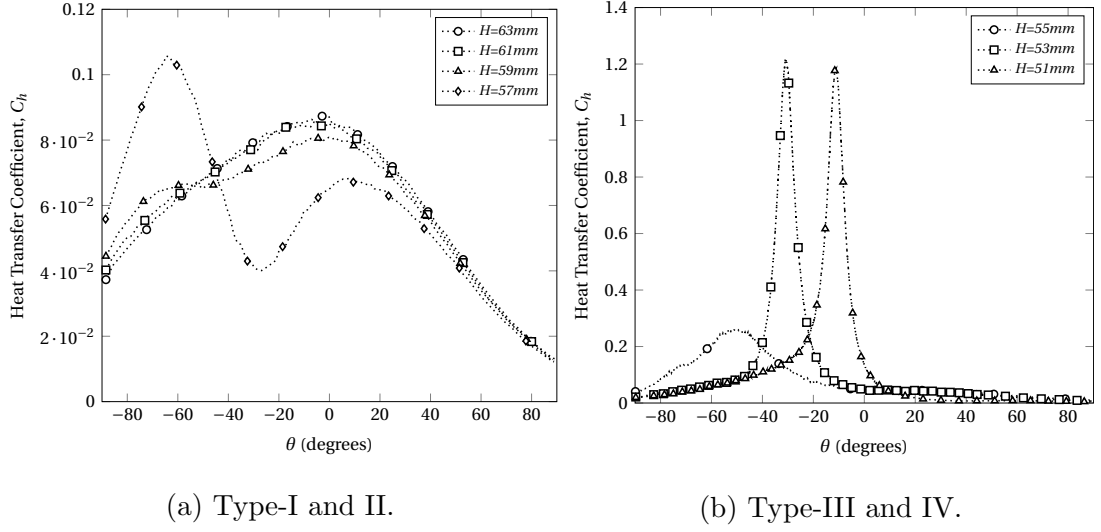
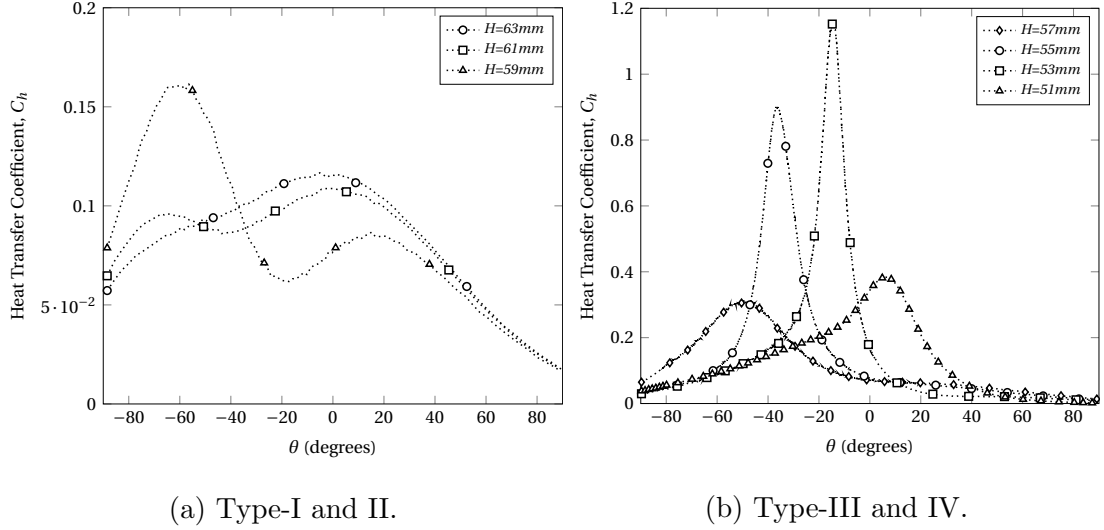
Table 3.4: Comparison of type-IV cases for all three Knudsen numbers.  $H$  is the cylinder height,  $\theta$  is the angular position on the cylinder surface where the peak pressure  $C_p$ , is found.

$H$	$Kn = 0.0067$		$Kn = 0.0134$		$Kn = 0.0268$	
	$\theta$	$C_p$	$\theta$	$C_p$	$\theta$	$C_p$
57 mm	-		-		-35.01	9.18
55 mm	-		-36.14	11.39	-15.61	9.96
53 mm	-30.79	16.44	-14.41	13.12	0.98	6.25
51 mm	-11.32	15.32	3.86	6.02	2.11	4.94

### Heat transfer coefficients

Figure 3.8 shows the augmentation of surface heating coefficient,  $C_h$ , as a function of vertical separation distance from the cylinder. The results are very similar to the pressure coefficient described above, with the type-I and type-II interactions generating modest increases in the heating load and the type-IV interactions showing severe local heating loads. As expected, the peaks of pressure and heat transfer coefficients are located at the same positions on the cylinder surface.

Figures 3.9 and 3.10 show the distribution of  $C_h$  at  $Kn = 0.0134$  and  $0.0268$  along the cylinder surface. At first sight, it can be seen that the patterns of surface heating at both the moderate and the highest Knudsen number show similarities to those at  $Kn = 0.0067$ , however it should be emphasised that the impact of the type-I, II, and III interactions rises with increasing rarefaction. In contrast, the surface heating of the type-IV cases are more severe at  $Kn = 0.0067$  although the number of type-IV patterns increases with increasing rarefaction, which is the same trend as explained in the pressure coefficient section. It can

Figure 3.8: Heat transfer coefficient distributions at  $Kn = 0.0067$ .Figure 3.9: Heat transfer coefficient distributions at  $Kn = 0.0134$ .

be noted that the aerothermodynamic loads are more evenly distributed along the cylinder surface when the interaction is a type-I or type-II, but is far more localised in type-IV.

Type-II patterns have a fluctuating trend in Figures 3.8(a), 3.9(a), and 3.10(a). When the oblique shock impinges at  $Kn = 0.0067$  and  $H = 57\text{ mm}$ ,  $Kn = 0.0134$  and  $H = 59\text{ mm}$ , and  $Kn = 0.0268$  and  $H = 61\text{ mm}$ , the maximum surface heating value of the type-II interaction is observed at  $-63^\circ$ ,  $-61^\circ$ , and  $-55^\circ$  on the cylinder surface, respectively. The value of wall heat flux then decreases until  $-20^\circ$  at the lowest and the moderate Knudsen number and  $0^\circ$  at the highest one, then, at all three Knudsen numbers, a second peak exists, which is quantitatively smaller in magnitude than the first one. Windisch *et al.* [97] state that the sur-

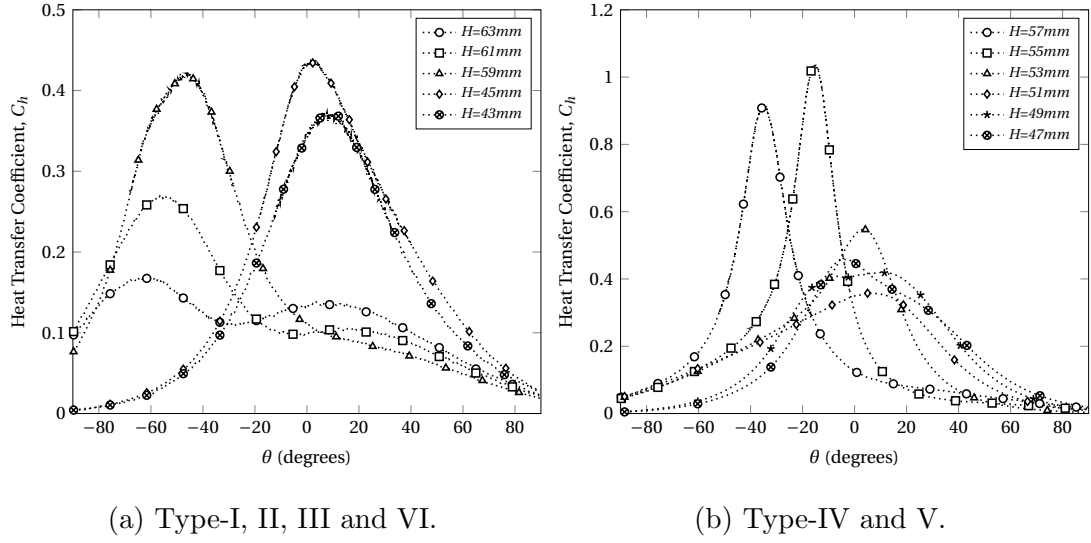


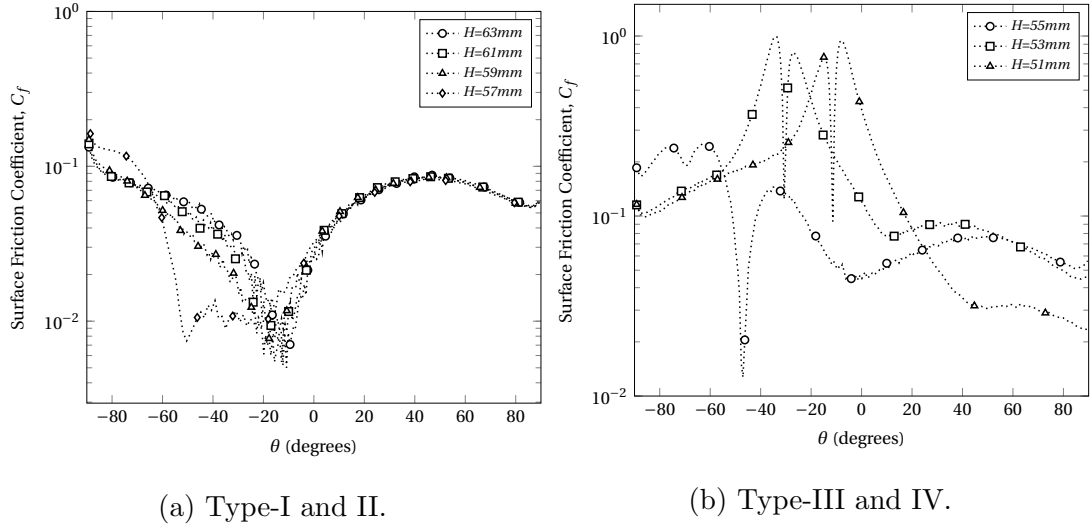
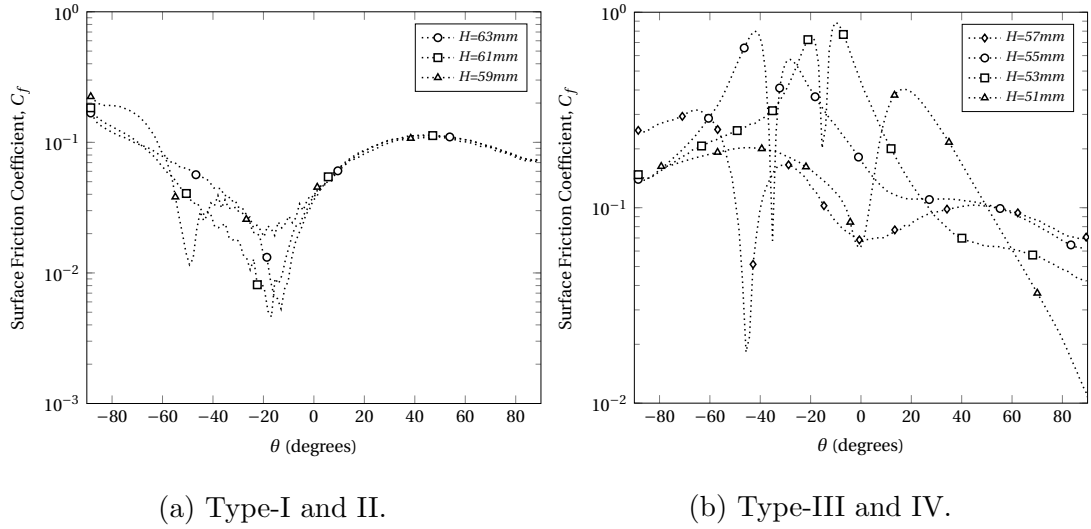
Figure 3.10: Heat transfer coefficient distributions at  $Kn = 0.0268$ .

face quantities reflect the flow characteristics. They add, “[t]he closer the jet is located to the wall, the higher the observed wall heat flux”. In these cases, the stagnation point exists on the lower side of the cylinder and the section with an upward flow is pushed back from the vicinity of the surface, resulting in a dramatic decrease in heating magnitude, and afterwards the flow begins to reattach to the surface at the location of the second peak.

### Surface friction coefficients

Figures 3.11, 3.12 and 3.13 show the distributions of the surface friction coefficient. At the stagnation points, there are local minima in the shear stress, with peaks on either side. Again, the type-III and type-IV interactions show higher peak values of surface friction coefficient than type-I and type-II interactions.

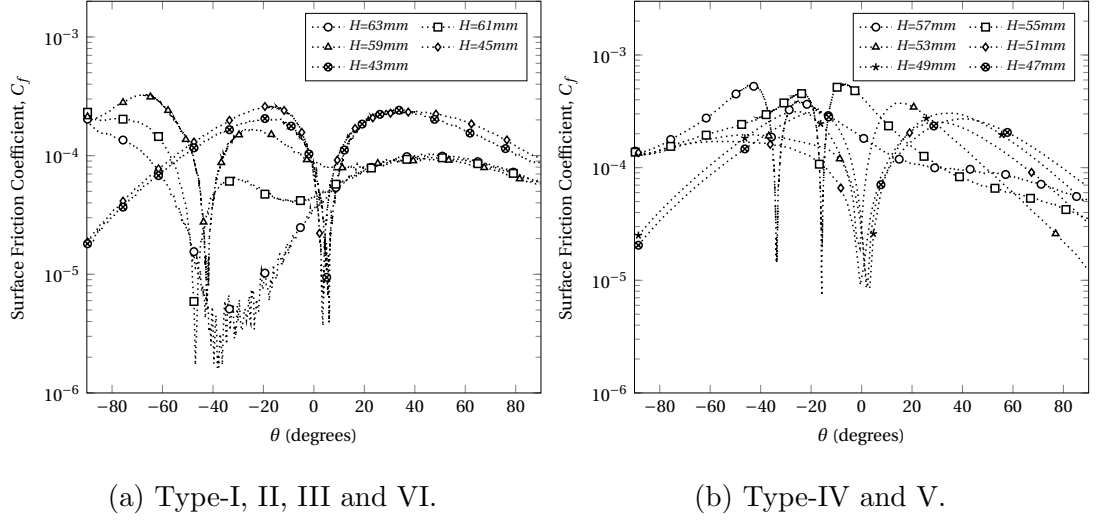
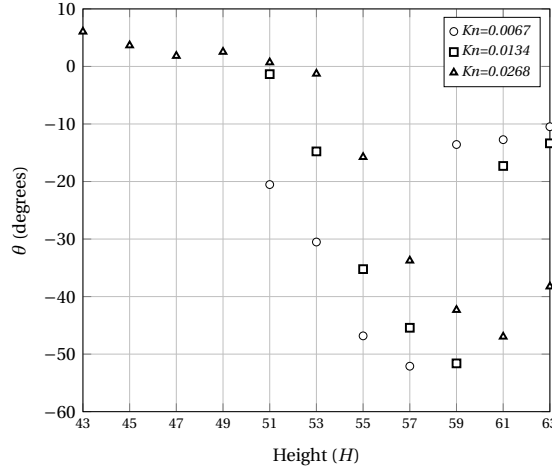
When the surface friction plots are examined, it is clear that the magnitude of the lowest shear stress is detected around the points of maximum  $C_p$  and  $C_h$ ; i.e. at the stagnation point. Compared to the lowest Knudsen number cases, the minimum value of type-I, II, and III interactions at a moderate Knudsen number ( $Kn = 0.0134$ ), is slightly greater. However, this situation reverses for type IV cases where the lowest Knudsen number cases provide higher minimum values. An inspection of Figures 3.11(b), 3.12(b), and 3.13(b) allows for the observation that for type-III and IV patterns at the lowest and moderate Knudsen number cases, and type-IV and V at the highest Knudsen number cases, the minimum surface friction coefficient occurs between two peaks. This shows that the flow impinges the surface, where the  $C_f \approx 0$  and the subsequent flow then begins accelerating across both the upper side and the lower side of the cylinder. The effect of  $C_f$  in

Figure 3.11: Surface friction coefficient distributions at  $Kn = 0.0067$ .Figure 3.12: Surface friction coefficient distributions at  $Kn = 0.0134$ .

type-IV and V is quite similar, apart from changes in the distribution of friction trends on the surface, and  $C_f$  is not as severe at the highest Knudsen number as at the moderate and the lowest ones.  $C_f$  of type-VI interactions are neither as strong as type-IV and V nor as weak as type-I and II interactions. The change in location of the peak points of aerothermodynamic loadings on the surface due to alterations in rarefaction levels can also be tracked using  $C_f \approx 0$  locations as shown in Figure 3.14.

### An overview of the surface parameters

Surface parameters: The locations of maximum value of  $C_h$  and  $C_f \approx 0$  on the cylinder surface follow a similar trend to that of  $C_p$  as shown in Figures 3.7, 3.10,

Figure 3.13: Surface friction coefficient distributions at  $Kn = 0.0268$ .Figure 3.14: The location of  $C_f \approx 0$  on the cylinder surface at three different rarefaction levels.

and 3.13. In type-I, II, III at  $Kn = 0.0268$ , the magnitude of  $C_h$  is approximately 1.4, 1.625, and 1.35 times, respectively, greater than the measured  $C_h$  at  $Kn = 0.0134$ . However,  $C_f$  at  $Kn = 0.0268$  is lower than the values at the moderate Knudsen numbers. As explained for  $C_p$ , increasing Knudsen number reduces the aerothermodynamic loading effect of the type-IV interaction on the surface. For instance, the averaged value of the type-IV patterns at the moderate Knudsen number is 1.38 times greater than those at the highest Knudsen number. In addition to the type-IV cases, stronger interactions occur on the lower side of the surface. Comparing the severity of the type-IV and V patterns at  $Kn = 0.0268$  shows that the type-IV interactions, which form around  $0^\circ$  or the upper side of the surface, are slightly weaker than some of type-V interactions. As expected, the effect of the type-VI interactions are slightly weaker than the type-V and

stronger than the type-I and II patterns. However, shortening  $H$  decreases the severity of type-VI gradually and the maximum heating point moves clockwise around the cylinder surface.

In order to compare the effect of changing rarefaction levels, the most severe cases at three different Knudsen numbers are compared in Figure 3.15. As seen in the data of maximum pressure and heat distributions on the surface, at the lowest and the moderate rarefaction levels, the maximum heat transfer coefficients are at  $H = 53$  mm. Figure 3.15 shows the peak points of surface loading shifting clockwise towards  $0^\circ$  with a more significant shift occurring between the lowest and the moderate Knudsen numbers, while there is negligible difference between the moderate and the highest Knudsen numbers. At the highest Knudsen number, the slope of the plot and the magnitude of the heat transfer coefficient are lower than the other two Knudsen numbers, however, unlike the lowest and the moderate Knudsen numbers, the peak value is found at  $H = 55$  mm.

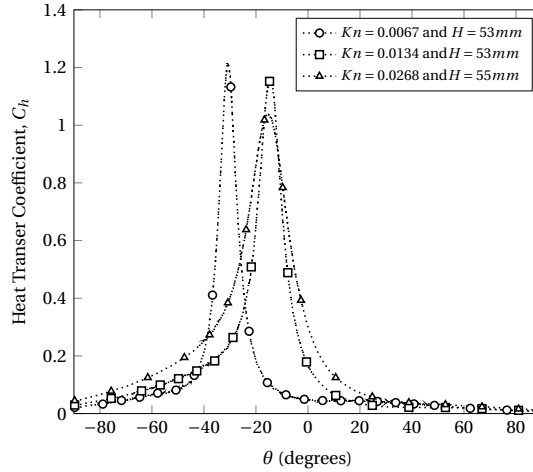


Figure 3.15: The comparison of surface heat transfer at the most severe case for the three different Knudsen numbers.

### Horizontal parameters of flow from the free-stream to the surface

Experimentally, the density and the rotational temperature have been measured by a DL-CARS technique at ONERA. The parameters were measured at heights of 0 mm to  $-5$  mm along a horizontal line. In Figure 3.16, the *dsmcFoam+* results at the  $y = -2$  mm location, which is around the height of the first- $\lambda$  point, are compared with the outcomes in the literature. At  $y = -2$  mm, the data collection line crosses different shock interactions depending on rarefaction, i.e. the data collection line passes above the second- $\lambda$  point for all three Knudsen numbers, the line is slightly above the first- $\lambda$  point at  $Kn = 0.0067$ ; however,

the line is positioned just below the second- $\lambda$  point at  $Kn = 0.0134$  and  $Kn = 0.0268$ . When the experimental and numerical results of normalised density are compared, *dsmcFoam+* predicts the formation of the bow shock to be sooner but follows the same trend as the experiment and other numerical work. The density increases suddenly as the data extraction line passes through the bow shock, however fluctuations in normalised density depend on rarefaction levels and shock-shock interactions. The maximum density value is measured on the surface and a jump in normalised density to 20 is obtained at  $Kn = 0.0134$  as the data collection line corresponds to the impingement point of the supersonic jet on the cylinder surface as shown in Figure 3.16(a).

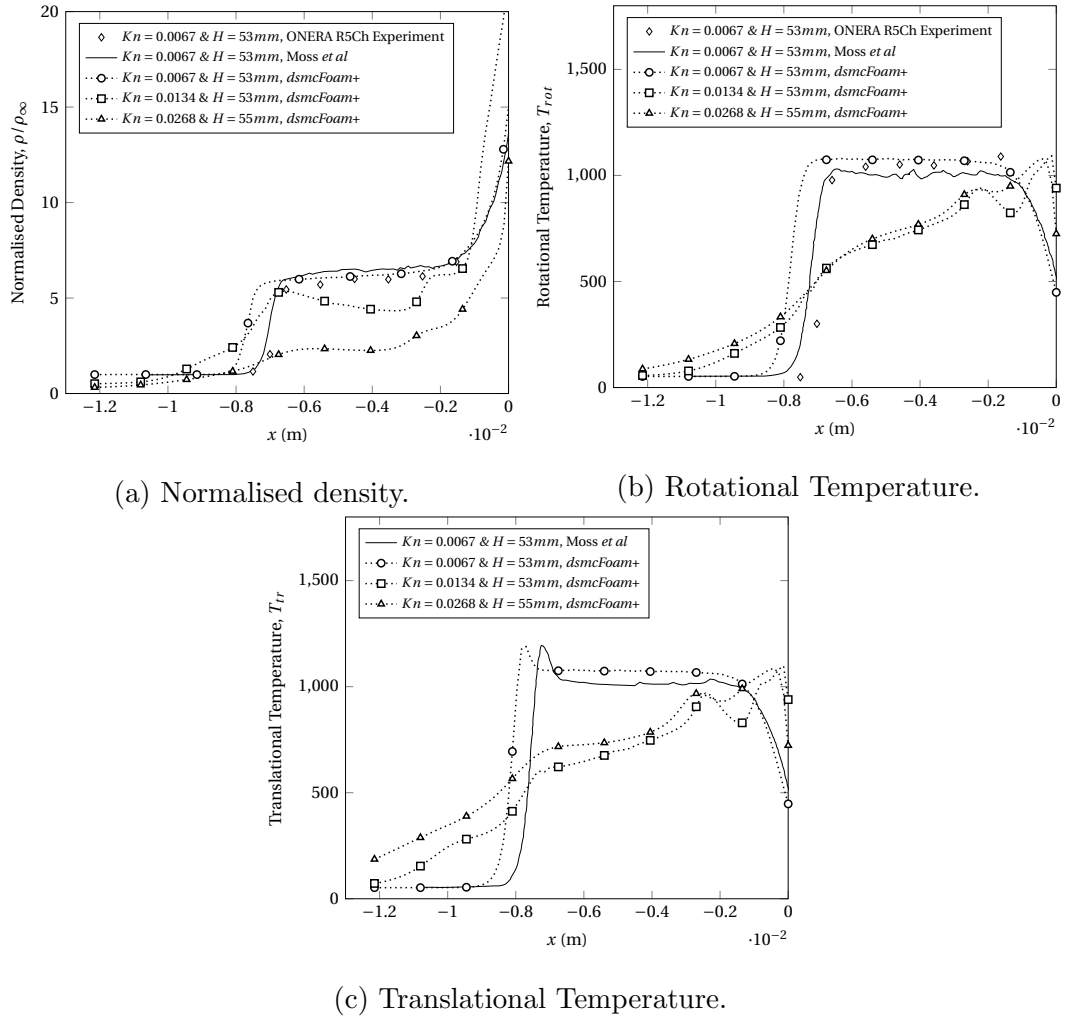


Figure 3.16: The comparison of change in density and temperature through free-stream to the surface for the most severe case at each of the three different Knudsen numbers.

The computational and experimental results of density and temperature show good agreement. Figures 3.16(b) and (c) show the trends of rotational,  $T_r$ , and translational,  $T_{tr}$  temperatures along the same lines as the density analysis above.



For all cases, the data collection line is the same geometrically, but it does not represent the same location of the flow physics, due the rarefaction effects changing the structure of the flow field. As seen in Figure 3.16, the incident shock intersects the bow shock at  $Kn = 0.0067$  later than other rarefaction levels due to the shorter stand-off distance of the bow shock. Therefore, the impingement point is obtained at around  $x = -8$  mm in both experimental and numerical results for  $Kn = 0.0067$ . The post-shock conditions can be examined in the temperature distribution after the peak point. The stand-off distance of the bow shock at  $Kn = 0.0134$  and  $0.0268$  is greater than  $Kn = 0.0067$ , which allows for the observation that the increasing trend starting at  $x = -12$  mm data extraction line in the  $Kn = 0.0134$  and  $0.0268$  cases can be explained through a coincidence between the start of the data collection line and the pre-shock region of the oblique shock. The *dsmcFoam+* results predict a slightly larger shock standoff distance than Moss *et al.* [88], which may be due to different meshes; both simulations use the same rotational relaxation number,  $Z_{rot} = 5$ , which is also accepted as a temperature independent value of 5 by Bird [38].

### Mach contours

This section summarises the structure of steady flow-fields by the contours of Mach number for the most severe cases of the type-IV patterns at three different rarefaction levels. The Mach contours of other steady cases, which are given in Table 3.3, are presented in § 7.1. As aforementioned, the computational domain has the oblique shock generator wedge, which generates the shock that targets to impinge to the bow shock created by the cylinder. As expected, the simulation presents a high fidelity solution for this impingement, where the formation and structure of shock waves can be obtained clearly.

Figure 3.17 shows the Mach number contours in the steady interaction region for the most severe cases in different rarefaction level. As the Knudsen number increases, the shock wave thicknesses increase, which changes the location of the shock impingement. It can also be seen that the supersonic jet that reaches behind the bow shock becomes weaker with increasing Knudsen number and the impingement point on the cylinder surface tends the move clockwise around the cylinder surface as the Knudsen number increases.

Once the oblique shock impinges on the bow shock, a  $\lambda$ -point is formed, which is the intersection point of the bow shock, oblique shock, and upper shear layer. The disrupted bow shock and lower shear layer also create a second- point, as illustrated in Figure 3.18 in detail. Between these shear layers, many compression and expansion waves take place and the flow diffuses into the bow shock at

supersonic speed, called a supersonic jet, and then the flow carries on to terminate against the cylinder surface, which is named the terminating shock wave. The location and structure of these components of Edney interactions might differ due to the flow properties such as rarefaction level and geometrical setup including the value of  $H$ .

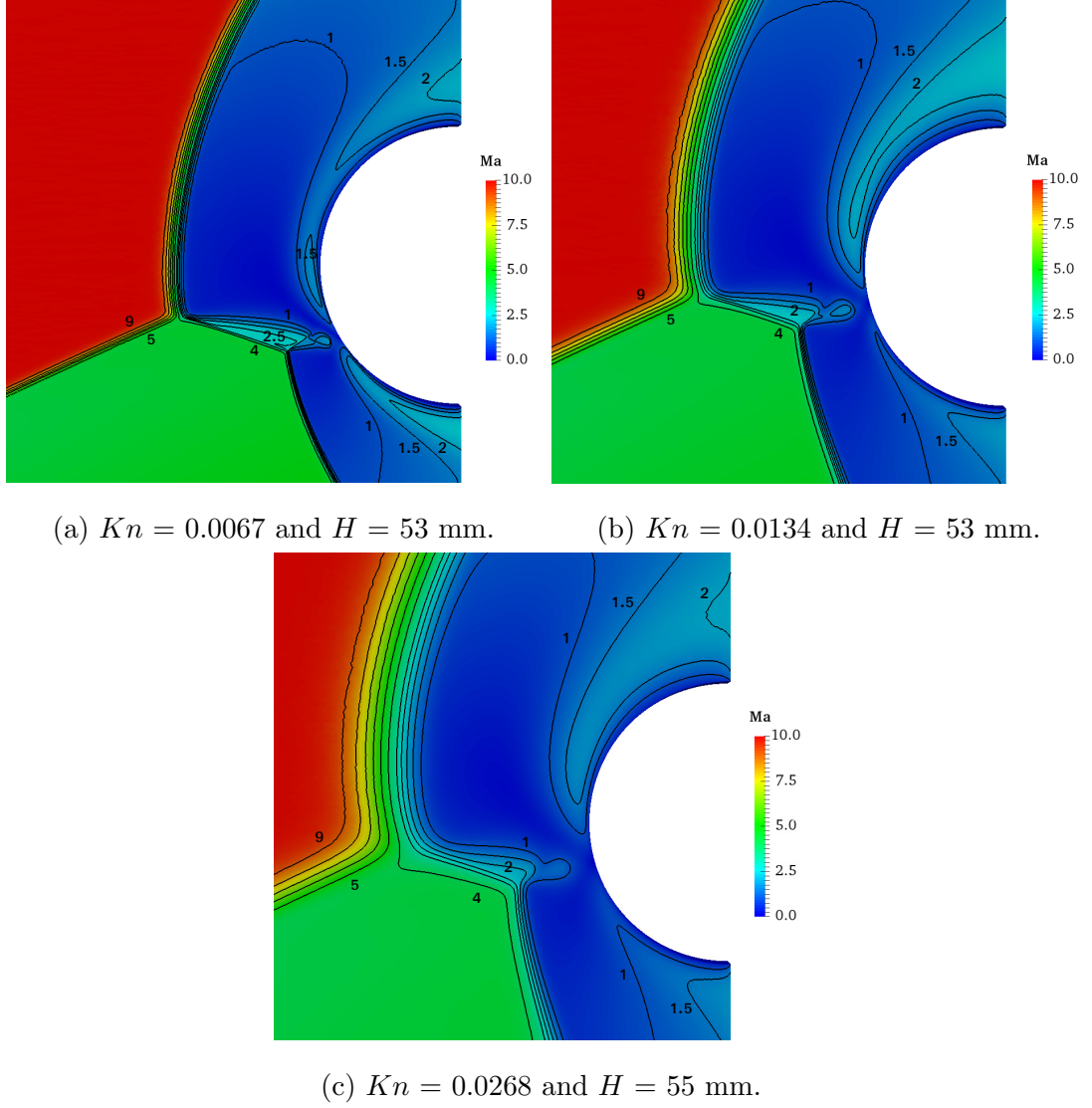


Figure 3.17: Mach number contours in the steady interaction region for the most severe cases in different rarefaction levels. The Mach contours are shown for the values of Mach numbers 1, 1.5, 2, 2.5, 3, 4, 5, 6, 7, 8, and 9.

The comparison of the Knudsen number and  $H$  show that the more severe type-IV cases occur at  $H = 53$  mm when  $Kn = 0.0067$  and  $0.0134$ , and  $H = 55$  mm when  $Kn = 0.0268$ . At the lowest Knudsen number, i.e.  $Kn = 0.0067$ , the impact of impingement is the greatest as the supersonic jet region diffuses behind the bow shock more than other two cases, i.e.  $Kn = 0.0134$  and  $Kn = 0.0268$ , and the terminating shock strikes through a point on the cylinder surface with a

higher velocity. In addition, the occupancy of the supersonic region decreases with increasing rarefaction. It is also observed that the diffusion velocity of the flow in the bow shock alters more suddenly at the lowest rarefied flow, whereas this takes place relatively more gradually at the highest rarefied flow. The thicknesses of bow and oblique shocks, and the stand-off distances of the bow shocks increase proportionally with increasing rarefaction of the flow-field.

### 3.3.2 Unsteady Flow Field

To address the unsteady mechanisms, the flow field features are visualised with Mach contours at  $1.195 \times 10^{-3}$  s for the  $Kn = 0.0067$ ,  $H = 49$  mm case in Figure 3.18. The simulations are too large to perform ensemble averaging and so, to reduce the scatter, the results have been averaged for 500 time-steps on either side of  $1.195 \times 10^{-3}$  s, for a total of 1000 samples.

The different unsteadiness phenomena strongly depend on each other and due to this coupling, the changes in each create an impact on others, such as the strength of the shocks, and relocation of shocks including the bow shock stand-off distance. The impingement of the oblique shock on the bow shock alters the bow shock curvature, which is the first- $\lambda$  point, and the relocation of the bow shock then causes the formation of the second- $\lambda$  point below. A supersonic jet forms between the shear layers, which initiates at the  $\lambda$ -points, and following a terminating shock which diffuses into the flow behind the bow shock. As the terminating shock diffuses across the upper side of the cylinder, variations can be observed in the bow shock location and curvature, leading to an oscillation in the stand-off distance, as indicated by the horizontal green arrow drawn on the bow shock in Figure 3.18. The rotation mechanism of the terminating shock is indicated by the white arrows in Figure 3.18. In addition, the terminating shock relocates, as indicated in Figure 3.20, and contributes to the unsteady mechanism by attaching to (or detaching from) the cylinder surface as shown by the vertical green arrow. The movement through both green arrows are coupled as the shedding effect of the flow has an impact on the stand-off distance of the bow shock. The strength of expansion and compression features in the supersonic jet region and the terminating shock sub-zone vary as they are crucially coupled to the longitudinal compression and expansion of subzones in the direction of yellow arrows. The direct interconnection of a supersonic jet and the terminating shock without interruptions is the usual pattern of a type-IVa shock interaction.

Figure 3.20 shows the evolution of the flow field at  $Kn = 0.0067$  and  $H = 49$  mm, illustrating the unsteadiness. In this case, the most severe unsteadiness effects are due to the impingement location of the oblique shock. Figure 3.19

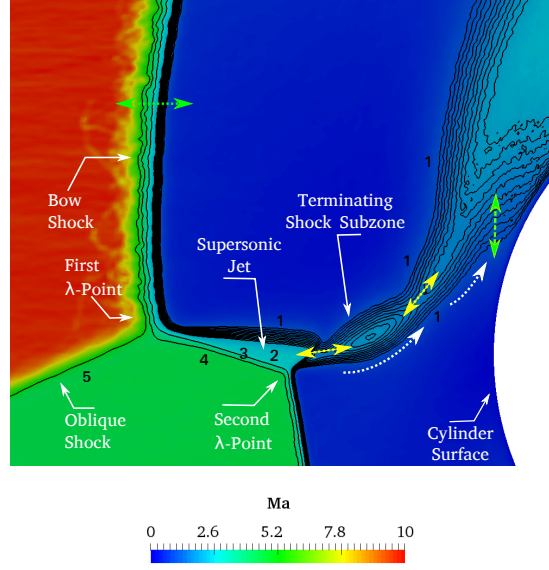


Figure 3.18: Contours of Mach number, showing the unsteady mechanisms in a shock-shock interaction at  $H = 49$  mm,  $Kn = 0.0067$ , and  $t = 1.195 \times 10^{-3}$  s. The numbers on the contour lines denote the Mach numbers.

shows the number of DSMC simulators and average linear kinetic energy by time-step. The observed oscillations show the unsteadiness of the case -as geometries with a steady state solution achieve constant values that level off.

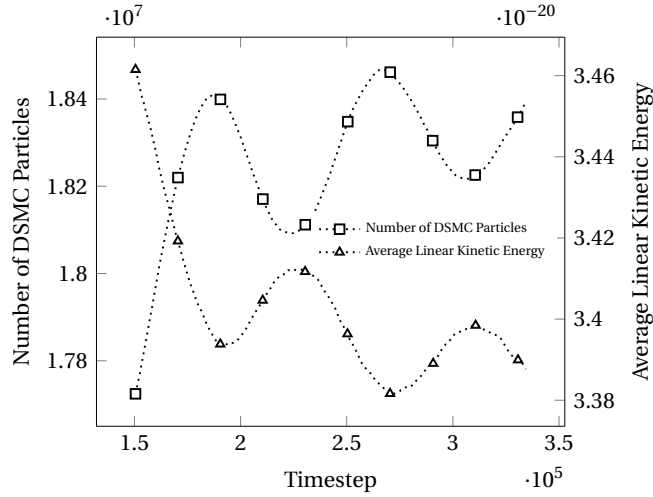


Figure 3.19: Plot showing the number of DSMC particles and average linear kinetic energy in an unsteady simulation;  $Kn = 0.0134$ ,  $H = 49$  mm.

As shown in Figure 3.20(a), the shock-shock interaction initially takes place at a location horizontally aligned to the centre of the cylinder. The experimental result of Grasso *et al.* [94] shows that the most critical condition happens when the supersonic jet travels nearly perpendicular to the surface as seen in Figure 3.20(a), which shows the early stage of the impingement and diffusion of the terminating shock in the bow shock. Lind and Lewis [95] state that the unsteadiness of a

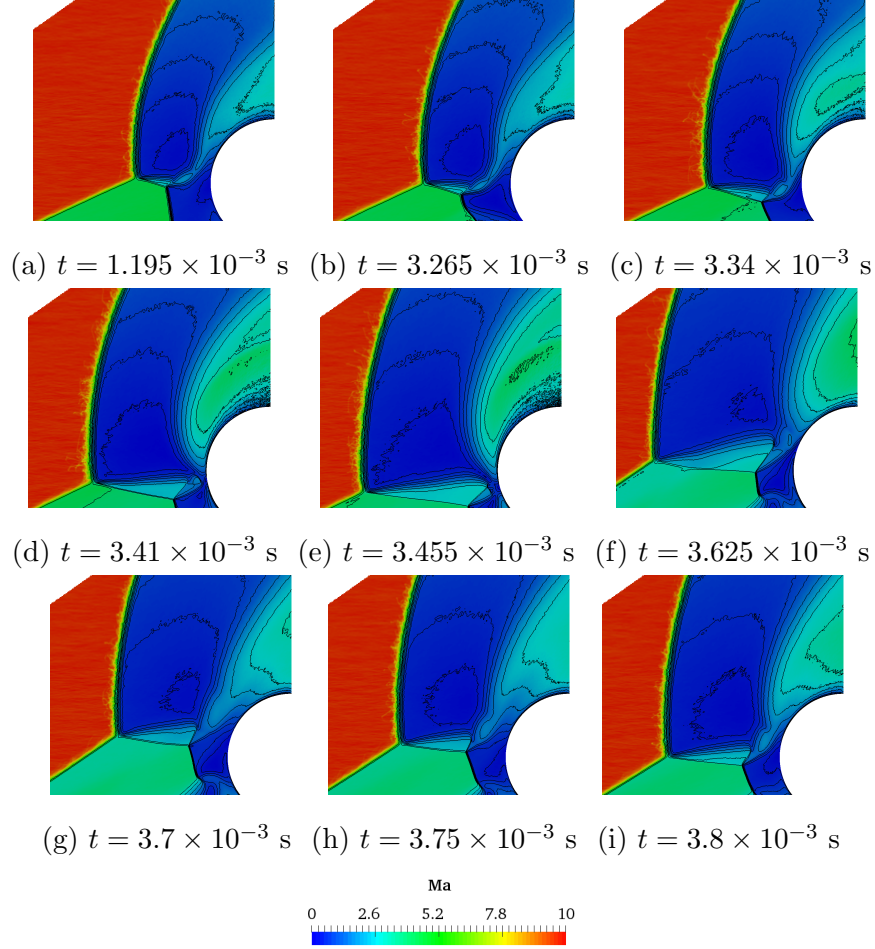


Figure 3.20: Mach number contours showing flow field unsteadiness at  $Kn = 0.0067$ ,  $H = 49$  mm.

type-IV pattern depends on the strength and angle of the oblique shock and the shock impingement location. However, apart from moderate hypersonic flows, the unsteadiness is not related to the changes in hypersonic upstream flow. Ref. [95] expressed the progression of unsteady jet flow as “the high-frequency jet unsteadiness is seen to be related to the formation of a vortex near the junction of upper shear layer and the termination point of the supersonic jet, its breakdown, and then its propagation along the upper portion of the cylinder, causing shear layers to be generated and then shed.” Yamamoto *et al.* [96] state that the supersonic jet travels towards the upper side of the surface without stagnating. This flow pattern of the supersonic jet detachment lies in the type-IVa classification [97].

The most dominant unsteadiness mechanism in this case is the interconnection of the supersonic jet and the terminating shock as previously mentioned. It should be emphasised that the flow in the bow shock is neither inherently stable nor periodically unsteady and that the type-IVa pattern is relatively stable until

$3.3 \times 10^{-3}$  s, but a highly unsteady flow then emerges due to changes in the expansion/compression wave features in the jet flow and deformations in the type-IVa structure are observed between the  $3.4 \times 10^{-3}$  s and  $3.6 \times 10^{-3}$  s time intervals. An interruption takes place in the terminating shock and the jet flow separates into two parts, where the supersonic flow accelerates through the upper and lower side of the stagnation point and creates a small subsonic region just below the zero degree point of the cylinder surface.

A complete cycle starts and ends at  $3.6 \times 10^{-3}$  s with the turning of the jet flow along the upper side of the cylinder at  $3.8 \times 10^{-3}$  s, respectively, giving a cycle frequency of  $\sim 5$  kHz. At  $3.45 \times 10^{-3}$  s, the tip of the terminating shock approaches the cylinder surface, but then starts moving upward together with flow rotation in the terminating shock at  $3.6 \times 10^{-3}$  s, which is the approximate start-time of a whole cycle of the jet flow, as shown by the white arrows in Figure 3.18. The jet finally reconnects with the upper part of the previously separated jet flow. This transition feature supports the evolution of a type-IV interaction pattern into type-IVa. When reaching the upper turning location at an approximate time of  $3.7 \times 10^{-3}$  s and  $3.75 \times 10^{-3}$  s, both stand-off distance between the near wall and diffused jet flow, and the bow shock to the cylinder significantly decreases. The oscillation of the flow field completes the half-cycle and begins a downward motion in order to complete the cycle at  $3.8 \times 10^{-3}$  s. The driving mechanism of the unsteady movement can be noted as the longitudinal expansion/compression of the supersonic jet and rotations in the terminating shock. This discussion is only for a single Knudsen number, but the results previously shown in Table 3.3 show that increasing Knudsen number results in the flow field tending towards being steady rather than transient.

### 3.4 Summary

Numerical solutions of Edney shock-shock interactions for three different Knudsen numbers and eleven geometrical setups are presented using the DSMC method. Steady flow fields are found for all conducted simulations when  $H$  is greater than 51 mm. However, the flows tend to show unsteady behaviour at the lowest,  $Kn = 0.0067$ , and the moderate,  $Kn = 0.0134$ , Knudsen numbers for  $H$  values of 49 mm or lower. At these heights, the flow reverts back to a steady state when the Knudsen number is increased to 0.0268. Computed results of aerothermodynamic loading, such as pressure, surface heating, and friction coefficients on the surface indicate that type-I to IV Edney interactions at the lowest and moderate Knudsen numbers can be observed, but that six types of Edney interactions are captured

when the flow reaches the highest Knudsen number. The results show that when the rarefaction level of a non-reacting hypersonic free-stream flow is increased,

1. type-I, II, and III cases become more severe,
2. the number of type-IV patterns found increases,
3. when the most severe type-IV cases are sorted in order of strength of shock interactions, higher surface loading occurs
  - at  $H = 53$  mm, while the second most severe does so at  $H = 51$  mm at the lowest Knudsen number;
  - at  $H = 53$  mm, and less severe at  $H = 55$  mm at the moderate Knudsen number;
  - and at  $H = 55$  mm, with the second most severe at  $H = 57$  mm.

This shows that the formation of severe type-IV interactions relies on higher  $H$  values as the rarefaction level increases.

4. the comparison of maximum heating values at all Knudsen numbers shows that when the flow is more dense, the interaction has the highest impact on the surface and is more focused on a point on the surface. However, going through the more dilute flow, the surface aerothermodynamic loading plots have a more distributed trend and less effect on the surface when compared to lower rarefaction levels,
5. the aerothermodynamic surface loading of the type-IV interactions increases when the pattern tends to change to type-V,
6. type-VI patterns show a stronger effect than type-I, II, III at the highest rarefaction level.

Concerning the density and temperature change of flow field from free-stream to the surface, *dsmcFoam+* predicts the existence of the bow shock slightly sooner at the lowest rarefaction level when compared with experimental and numerical results. However, the trends of density and temperature variations in the post-shock region are in good agreement.

Further simulations of shock-shock interactions show that unsteady cases are observed at the lowest and moderate Knudsen numbers at  $H = 49$  mm and lower values, where the flow pattern fluctuates between type-IV and type-IVa. In the literature, this effect of supersonic jets, which forms in a region between the upper and the lower shear layers, are discussed to a great extent. However,

a tight connection/contribution of the terminating shock effect on the unsteady mechanism and the attachment/detachment of the fringe flow with the movement of pressure waves and the shedding effect are also visibly observed at the lowest Knudsen number when  $H = 49$  mm. In addition, the stand-off distance of the bow shock oscillates. The rarefaction level has a quantitative impact on the stand-off distance, and the frequency of the oscillation, which decreases in proportion to the rarefaction. The movement of sub-zones in the post-shock region, e.g. supersonic jet, terminating shock, are strongly coupled and drive the unsteady mechanism. With the increase of rarefaction levels, the energy of the bow shock decreases although the thickness of the bow shock increases.



# Chapter 4

## Impact of Stagnation Temperature and Nozzle Configuration on Rarefied Jet Plume-Plume and Plume-Surface Interactions

### 4.1 Introduction

Assorted types of thrusters with different propellants and sizes are employed for space missions of launching, attitude control, maintaining orbit, manoeuvring, etc. These platforms have a wide thrust ranging from 1 mN to millions of Newtons. Depending on the possible perturbation forces and targeted accuracy of a platform's position, the location of rockets on the platform and their thrust may vary to reach the desired torque requirements. Although there are many parameters for the selection of propulsion systems regarding mission demands, the specific impulse,  $I_{sp}$ , is an essential quantity, which defines the accessible thrust,  $F_t$ , per unit mass flux of expelled propellant,  $\dot{m}_{prop}$ ,

$$I_{sp} = \frac{F_t}{\dot{m}_{prop}}. \quad (4.1)$$

The pressurised exhaust gas is expanded through a nozzle geometry and exits to the surrounding atmosphere and forms a plume. Rocket exhaust plumes have different properties depending on mass flow rate, stagnation pressure and temperature, environmental conditions in which exhaust gases are released, and the type of propellant used. Additionally, before the exhaust products enter into

the nozzle, the flow is heated in some cases to gain maximum efficiency and to increase the specific impulse. For these reasons, the exhaust gas temperature is altered due to the propellant types or thrust demands. In addition, a plume forms depending on the altitude because of the change in ambient pressure. An over expanded flow, where the exit pressure from the nozzle is lower than the ambient pressure leads to the formation of a relatively slender plume, with possible flow separation before the nozzle exit is reached. Higher in the atmosphere, the ambient pressure is reduced and so the exit pressure is greater than ambient and the flow is under expanded, continuing to expand once it leaves the nozzle. Both of these situations result in a less than optimum operation and reduced thrust. At one specific point, the flow is perfectly expanded, i.e. the nozzle pressure is equal to the ambient pressure, and the maximum amount of thrust is generated. These three situations are illustrated in Figure 4.1. Furthermore, the mission type or operation of space platforms have an impact on the plume impingement on a solid surface. Mass flux of exhaust gas products impinging on a surface may be greater during docking operations than in orbit control manoeuvres since it is assumed that the relatively dense portion of the plume interacts with the surface during docking [99].

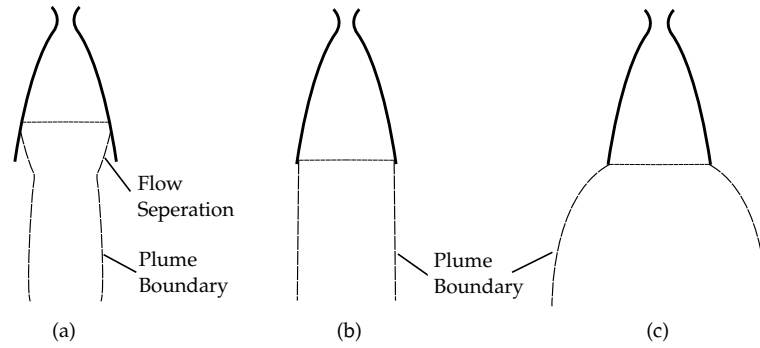


Figure 4.1: Simplified schematic representation of exhaust plume behaviours: (a) over expansion ( $P_a \gg P_e$ ), (b) perfect expansion ( $P_a = P_e$ ), and (c) under expansion ( $P_a \ll P_e$ ), where  $P_a$  is the ambient pressure, and  $P_e$  is the pressure at the nozzle exit plane.

Depending on the nozzle location, plume-surface interactions can form compressed shocks and boundary layers, which can be obtained in continuum flow. However, in a vacuum environment, the shape of plumes change such that a barrel shock no longer exists, plumes tend to expand further, etc. Dettleff [99] explains the expansion of low-density exhaust plumes in a vacuum environment with higher velocities as “[t]he nozzle area ratio [...] is typically in the order of 50 so that the exit Mach number is typically about 5”. Therefore, highly expanded

and accelerated plumes tend to interact more with other plumes in multi-nozzle systems and the surfaces of platforms through diffusion and scattering in space applications. Plume flow problems have been investigated by Vick *et al.* [100], Boettcher and Legge [101], Lengrand [102], etc. as stated in Ref. [99] and for various impingement scenarios, such as perpendicular impingement to the surface [103], laterally located thrusters on the sides of platform bodies [104, 105], and for nozzles positioned at an angle to the surface [106–108]. These studies contribute to a better understanding for some problems in application. For instance, a different canting of the thruster axis is employed to control attitude and manoeuvring as the torque requirements play a crucial role on the position of the thruster, yet this brings some impingement effects including contamination, disturbance of torques and forces, thermal loading, gas deposition, etc. on the surface of space platforms. If the orientation of the nozzle axis is altered to reduce rocket plume-surface interaction, the produced torque may not meet the requirements. Moreover, the canting of the axis angle affects the distribution of heat load and opposite torque. The configurations of nozzle systems should be designed to obtain maximum torque with a low plume-surface interaction. This is of significant research interest since impingement affects operational lifetime and essential functions of platforms.

The impingement effect of the different types of plumes, such as cold gas, products of chemical reactions and ion thrusters on a spacecraft surface - in terms of the ejecta dynamics and plume physics as mentioned in Ref. [109] - has been a significant topic of both numerical and experimental studies for some time. Thus, the modelling of single plume and multi-plume interactions at different ambient conditions is the first step of the impingement investigations. A single exhaust plume may start in the continuum regime and tend towards the free-molecular regime as it expands. Thus, the employed numerical approach for plume modelling may differ depending on the flow regime of a plume and hybrid approaches may be required for a complete solution of a plume simulation.

Ivanov and Markelov [110] simulated spacecrafts which operate at low Earth orbit. These platforms create their own ambient atmosphere (OAA) due to the use of Reaction Control Systems (RCS) that are formed of multiple thrusters. Therefore, the peripheral effect of OAA was a research interest for the Astra-2 experiment, where the plume of a cold argon thruster interacted with the Mir Space Station (MSS). This computational study presents a wide-range of solutions for the various flow regimes of the plume, from continuum to rarefied, in a large spatial scale from the nozzle to the far-field. The simulation of the plume was conducted using the Navier-Stokes equations for the continuum part, DSMC

for the rarefied part, and the test particle Monte Carlo (TPMC) for the free-molecular regime section of the plume. Another study by Ivanov *et al.* [111] presents the same complete solution approach for a different plume simulation. The interaction between two parallel nitrogen free jet plumes were modelled with a 3D DSMC code to investigate the plume-plume interactions. For the plume-surface interactions, the simulation of a plume exhausted by a 20 N thruster impinging on the surface of the European Space Agency (ESA)'s XMM satellite was conducted by employing the TPMC method. The results of the impingement simulations of two plumes indicate that a total axial force of 6.2 N, which corresponds to the loss of 15% of the total nominal thrust of the two thrusters, is created on the surface. Another CFD-DSMC modelling [112] approach was conducted for the plume-surface interactions by the National Aeronautics and Space Administration (NASA) to simulate the docking case, named F3U, of an orbiter to the MSS during the STS-74 mission. In this study, the separation distance between the spacecraft and space station is selected as 5 m to investigate the impingement of a highly expanded plume on the surface of the space station. However, these studies do not present detailed solutions for the effect of multi-nozzle configurations and changing stagnation temperatures on the plume-plume and plume-surface impingement parameters in a vacuum environment.

A further study on a CFD-DSMC combined approach [113] is employed to model the plume of a monopropellant thruster while discharging a jet flow plume into a vacuum environment. A density based Navier-Stokes solver is applied to predict the flow physics around the nozzle exit, and DSMC provides a solution to the far-field for the three types of propellant species of  $H_2$ ,  $N_2$ , and  $NH_3$ . A complete analysis of nozzle plume systems is also proposed by Ref. [114] through dividing the control volume of interest into two parts as CFD and DSMC regions, with coupling occurring at the continuum breakdown location. The author states that the DSMC predictions are in a good agreement with the experimental results, even in the regions where the CFD returns inaccurate data or fails such as in the translational non-equilibrium regions, which is an expected result.

Different coupled methods has been also applied to simulate the plume in further studies. Boyd and Starkt [115] simulated the combustion processes and produced data for an expanded plume from various radial distances by employing the Simons model [116], the Method of Characteristic (MOC) [117], and DSMC. Although the motivation of plume-spacecraft surface interaction initiated this study, the work solely focuses on the change in the flow parameters from the inside of the thruster to the far-field of the plume. The plume of a monopropellant hydrazine thruster is simulated using DSMC and MOC in Ref. [118] and the

authors state that DSMC offers more accurate data than MOC for the estimation of surface impingement effects at the free-molecular regime of the plume.

For plume-plume interactions, an investigation of four JP4/LOX 56.4927 J (500 lbf) water-cooled rocket engines at two different ambient pressures was experimentally and numerically conducted to measure the plume-induced base pressure and heating parameters. The simulation of the plume physics was completed using the Loci-CHEM NS CFD solver for the highest-fidelity predictions [119]. The study shows the importance of plume-plume interaction research, but falls short in covering a solution for the plumes at rarefied regimes. Another study [120] describes a methodology to solve the plume-plume (by operating two nozzles of the Shuttle Primary RCS) and plume-surface interaction for single and double nozzle(s) applications during the docking maneuver of a shuttle orbiter to the MSS. Three regimes of plume flow-field are simulated using the Navier-Stokes equations and DSMC, through a solver called LaRC 3S DSMC code; the impingement of the plume with the surface is also simulated by the DSMC code. The pressure forces on the surface of the MSS and the changes in plume density are calculated for different nozzle types, such as single and double with various thruster types. Further outcomes of the plume, including velocity, temperature, surface shear stress, surface heating, etc. and the changes in configuration of the nozzles at the dual systems are not provided.

Boyd *et al.* [121] performed DSMC simulations for expanding nitrogen flow into a near-vacuum condition through a small sonic nozzle, and also compared the results to experimental data. Afterwards, another DSMC simulation was conducted by Boyd *et al.* [103] to provide a solution for another plume impingement problem during a space-based experiment. The Gravity Probe B experiment required precise measurement, therefore, a drag free environment was needed to reduce the Newtonian torques. The payloads on the space platform were cryogenically cooled and in order to increase the efficiency, boil-off helium was employed as a propellant and emitted throughout the host space platform. This impingement slightly distorts the maintained environment with disturbance torques, contamination, surface thermal loading, etc. Therefore, the authors conducted a series of numerical simulations to further understand the effect of the impingement angle of the plume, and the plume quantities with changing mass flow rate such as dynamic pressure and mass flux. In this study, there was no mention of the computational DSMC code, plume-plume impingement, the effect of altering stagnation temperature, and the impingement surface parameters.

Kannenberg [106] investigated several types of problems, such as impinging a nitrogen plume on an axisymmetric body, the plume effect of a hydrazine thruster

on a solar array panel, the impact of a free nitrogen jet onto an inclined flat surface, etc. using the DSMC method. The flat plate impingement case in this work is based on some experiments conducted in Deutsches Zentrum für Luft- und Raumfahrt (DLR)'s the high vacuum facility in Göttingen to measure the pressure and shear stress [107] and heat transfer [108] on a flat plate beneath the nozzle. In order to numerically assess the effect of the orientation of the impingement surface, a geometrical setup of the single plume simulations was performed, with the angle of attack ranging from 90 to 0 degrees. The DSMC method indicated promising results in the validation cases when compared with the experiments. The flat plate impingement cases in this study provides the changes in plume and surface parameters as a function of the plume impingement angle from a single thruster.

This chapter aims to enlarge the understanding of the plume-plume and plume-surface interactions in a vacuum environment. Firstly, the distance between the nozzles in a double and quadruple thruster setup is altered to examine the effect on plume-plume and plume-surface properties. In addition to the investigation of the geometrical effects, the changes in plume structure and impingement on the surface with heated flow is evaluated by increasing the stagnation temperature of the plume jet flow. Thus, this study presents a wide simulation matrix with varying nozzle-to-nozzle distance for multi-nozzle applications, and a range of stagnation temperatures for single and multi-thruster systems. In this present study, 2D axisymmetric and 3D DSMC simulations are carried out by using *dsmcFoam+* code. OpenFOAM is an unconditionally 3D code, but planar 2D cases can be simulated using a mesh that is one cell deep and has the 'empty' patch type applied on two parallel patches, which constrains particle positions to the centre of the mesh in that direction, but maintains 3D velocities for collisions. For 2D axisymmetric cases, a 5 degree slice of the geometry, which again is a single cell wide in the symmetry direction, is employed and specular walls are applied in the symmetry direction to ensure that the correct velocities are obtained. 1D flows are just a special case of planar 2D flows, with periodic boundaries applied in one of the other directions, such that flow variables will only change in a single direction.

## 4.2 Problem Description

The combustion temperature of rocket propellants can change depending on the propellant type and burn time. In a vacuum environment, a highly under-expanded exhaust flow will create a wide plume with a high Mach number due to

free expansion downstream [99]. As such, highly rarefied expanding plumes can interact with both the surfaces of space platforms that thrusters are mounted on, and each other in a system that consists of multi-nozzles.

In this study, rarefied free jets of nitrogen and impingement on a flat plate are investigated using the DSMC method. These are performed for single and multi-nozzle configurations. The numerical works are performed using *dsmc-Foam+*. Initially, a single plume, generated by a sonic orifice, with a stagnation temperature  $T_0$  of 300 K is simulated, due to the availability of numerical and experimental studies [106–108] for benchmarking. Afterwards,  $T_0$  is gradually increased up to 1000 K while maintaining the 1000 Pa stagnation pressure. At a sonic speed, the ratio of total pressure to stagnation pressure,  $P_t/P_0$ , and the ratio of total temperature to stagnation temperature,  $T_t/T_0$  are calculated as 0.528 and 0.833, respectively. The Knudsen number also changes with the stagnation temperature through the relation

$$Kn = \frac{Ma}{Re} \sqrt{\frac{\gamma\pi}{2}}. \quad (4.2)$$

As an example, the initial flow properties of rarefied exhaust gas in the axisymmetric domain with varying stagnation temperatures are summarised in Table 4.1.

Table 4.1: Initial properties at the sonic nozzle exit for the different stagnation temperatures for axisymmetric single plume applications, where  $n$  is number density and  $V_{sonic}$  is the sonic velocity.

$T_0$ (K)	$Kn$	$Re$	$n$ (m <sup>-3</sup> )	$V_{sonic}$ (m s <sup>-1</sup> )
300	0.008	147.9	$1.53 \times 10^{23}$	322.3
400	0.011	103.5	$1.14 \times 10^{23}$	372.1
500	0.015	78.5	$9.19 \times 10^{23}$	416.1
600	0.019	62.6	$7.66 \times 10^{23}$	455.8
700	0.023	51.7	$6.56 \times 10^{23}$	492.3
800	0.028	43.8	$5.74 \times 10^{23}$	526.3
900	0.032	37.8	$5.10 \times 10^{23}$	558.2
1000	0.037	33.2	$4.59 \times 10^{23}$	588.4

The background pressure in the high vacuum facility in Göttingen, Germany was set at 0.045 Pa for the surface pressure and surface shear stress experiment [107], and at twice of that previous experiment [108], which is 0.090 Pa, for the surface heat transfer experiments. In this chapter, the background number density, and the translational and rotational temperatures are imposed to be

$1.086 \times 10^{19} \text{ m}^{-3}$ , and 300 K, respectively, for all numerical simulations in order to model the pressure of the experimental tank.

The VHS model is employed to simulate the collisions. The energy exchange between modes is handled with a serial application of the LB technique. The VHS model properties of nitrogen are presented in Table 3.2.

The interactions of multiple plumes with each other and the impingement of single and multiple plumes on a flat surface are investigated using an illustrated numerical setup, referenced from a numerical study [106]. A circular sonic nozzle, with an exit radius of 1 mm is located at  $H = 40 \text{ mm}$  above a flat plate, which is modelled as a fully diffuse Maxwellian wall held at a fixed temperature of 300 K. The surface is large enough,  $2l_x = 240 \text{ mm} \times 2l_y = 240 \text{ mm}$  in size, in order to be able to observe the impingement effects such as the surface friction coefficient, temperature and pressure distribution, etc. and to analyse the backflow reflected from the plate. The problem geometry is shown in Figure 4.2.

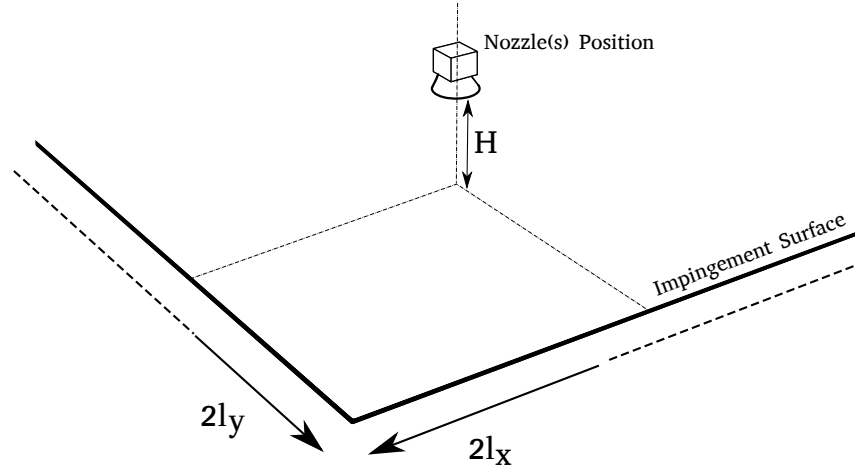


Figure 4.2: Schematic of flate plate impingement.

The DSMC cell size and time-step should be smaller than mean free path and mean collision time, respectively, in order to obtain an accurate solution. The mean free path can be calculated using the VHS model as,

$$\lambda = (2\mu_c/15)(7 - 2\omega)(5 - 2\omega)(2\pi RT)^{-1/2}/\rho. \quad (4.3)$$

Using Eq. 4.3 [51], the mean free path is calculated as  $8.269 \times 10^{-6} \text{ m}$  at the stagnation temperature of 300 K. Other DSMC variables are needed to determine the selection of the time-step, such as the most probable thermal velocity  $V_{mp}$ ,



the mean collision time  $t_{mc}$ , and the cell residence time  $t_{res}$ . These have been calculated and are presented in Table 4.2.

Table 4.2: Microscopic values for free-jet flow at  $T_0 = 300$  K for axisymmetric single plume applications.

$V_{mp}$ (ms <sup>-1</sup> )	85.227
$t_{res}$ (s)	$1.13 \times 10^{-8}$
$t_{mc}$ (s)	$2.15 \times 10^{-8}$

The time-step and cell size are chosen as  $5 \times 10^{-9}$  s and  $3 \times 10^{-6}$  m according to the calculations.

### 4.2.1 Axisymmetric mesh simulations

In order to reduce the computational demand, the benchmarking simulation, with the 300 K stagnation temperature, is completed in a 2D axisymmetric domain; a half-symmetry simulation is also performed to validate the results for the 3D applications. The radial weighting factor (RWF) method is employed in the axisymmetric simulations to balance the number of DSMC simulator particles between the cells around the axis of rotation and distant cells [122]. The expansion ratio of the cells is increased radially and axially since the local mean free path increases and larger mesh sizes are sufficient to capture the collisions. A mesh with a total of 440,380 cells is used. The DSMC particles are introduced at the inlet patch corresponding to the sonic nozzle exit plane and move through the control volume as the simulation proceeds.

### 4.2.2 Quarter-symmetry mesh simulations

Promising results are achieved using an axisymmetric mesh when compared with Refs. [106–108]. There is no question of whether the multi-nozzle simulations can use an axisymmetric mesh topology, because the geometry of the two- and four-nozzle arrays result in a fully 3D flow field, but quarter symmetry can be taken advantage of. In order to increase the number of nozzles and verify the use of quarter and half symmetrical simulations, the problem at  $T_0 = 300$  K is repeated using a half symmetry mesh topology and the outcomes of both simulations overlap. After verification and benchmarking simulations, a matrix of simulations is designed as given in Table 4.3 to investigate both the plume-plume interactions and the changes in the surface properties depending on number of plumes and stagnation temperature.


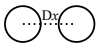
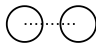
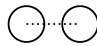
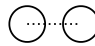

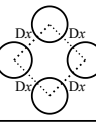
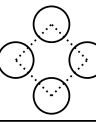
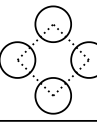
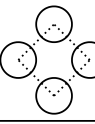


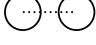
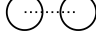
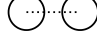
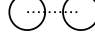
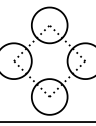
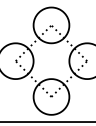
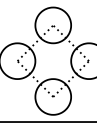
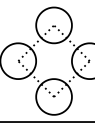


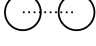
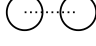
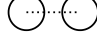
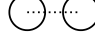
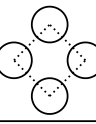
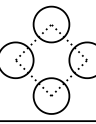
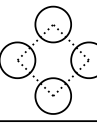
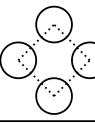



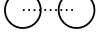
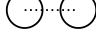
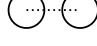
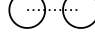
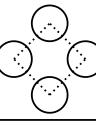
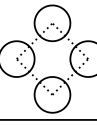
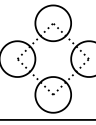
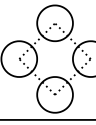
$T_0$	Single Plume	D3	D6	D9	D12
300 K					
					
400 K					
500 K					
					
600 K					
700 K					
					
800 K					
900 K					
1000 K					
					

Figure 4.3: The matrix of rocket plume-surface simulations according to mesh topology, and nozzle configurations. The parameter  $x$  of  $Dx$  represents the distance between nozzle centres in mm. The triangle exemplifies the axisymmetric mesh, the half circle the half-symmetric mesh, the two circles the double nozzle configuration, and the four circles the quadruple nozzle configuration.

Multi-nozzle simulations are run with the same nozzle radius and domain extents as used for the axisymmetric mesh. A control volume is created by 3D hexahedral blocks and the patches are specified as outlet, symmetry plane, and wall, as shown in Figure 4.4. Creating a half-circular inlet and mirroring the geometry/entire control volume at the symmetry planes significantly reduces the computational cost of the quarter-symmetry simulation run. The corner point ‘C’ – the mid-point of the distance  $x$  given in Table 4.3 – marks the half distance ( $x/2$ ) between the two inlet patches, the first of which is placed in the control volume and the second, virtually mirrored by the symmetry plane. The wall patch with a surface temperature of 300 K represents the flat plate.

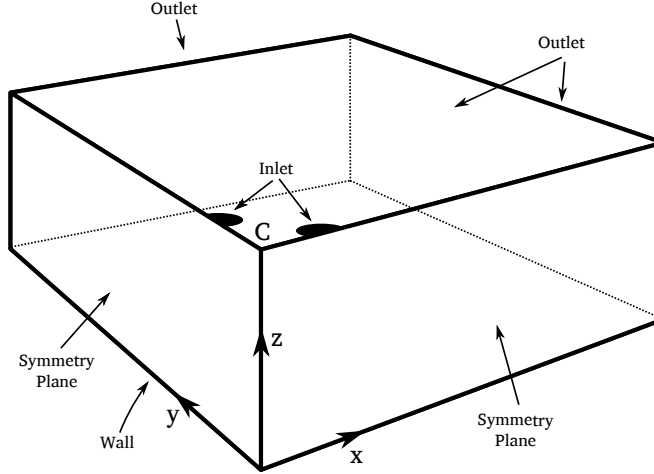


Figure 4.4: The mesh topology of quadruple plume simulation.

### 4.3 Results and Discussion

The accuracy of the *dsmcFoam+* simulations at  $T_0 = 300$  K is verified against numerical [106] and experimental data [107, 108]. Although the properties and measurements of the plume flow field are not provided by the experiments, the prediction of surface parameters by the numerical methods indicate accurate results. Therefore, it can be deduced that the flow is captured correctly. In order to compare the prediction of DSMC solvers with the experiments [107, 108], surface parameters are plotted. The surface shear stress and pressure are normalised as,

$$\hat{\tau} = \frac{\tau}{p_0} \left( \frac{H}{r} \right)^2, \quad (4.4)$$

and

$$\hat{p} = \frac{p}{p_0} \left( \frac{H}{r} \right)^2, \quad (4.5)$$

respectively, where  $p_0$  is maintained at 1000 Pa for all cases.

As Kannenberg [106] states, the flow is free-molecular at the surface. The change in density and mean free path are assumed to vary with the square of the distance from the nozzle exit. Therefore, the Knudsen number at the surface reaches the order of 10. The surface parameters in the free-molecular regime depend on the properties of the incoming flow to the surface, as the scattering gas particles do not interact with the incoming gas and the surface. In Ref. [106], the pressure on a point is expressed as the integration of normal momentum flux over the scattering and incoming gas particles [123] and the density is modelled depending on the throat density and the location in a polar coordinate system [124]. The other surface parameters, such as surface shear stress, transferred energy, etc.

can be derived from tangential momentum and the energy difference of the integral of scattering and incoming gas particles as previously applied for the surface pressure and density. In order to eliminate the effects of/dependence on the variables in the calculations, the normalisation is applied, however, the effect of stagnation pressure cannot be neglected as shown in Eqs (4.4) and (4.5).

### 4.3.1 *dsmcFoam*+ benchmarking simulations of single plume application

In this case, the consistency of *dsmcFoam*+ results with the axisymmetric and half-symmetric mesh topologies are compared with Refs. [106], [107], and [108] for the normal impingement of an exhaust plume on the surface at  $T_0$  of 300 K. The results are shown as a function of distance,

- *line 1*: through an axial line extending from the centre of the nozzle exit to the surface, and
- *line 2*: through a radial line, which is from a point directly below the exit of the nozzle to the end point of the surface for the surface measurement.

The normalised results show good agreement with the referenced data sets and the patterns show the same trend. The benchmarking dataset of plume and surface parameters are compared in Figure 4.5.

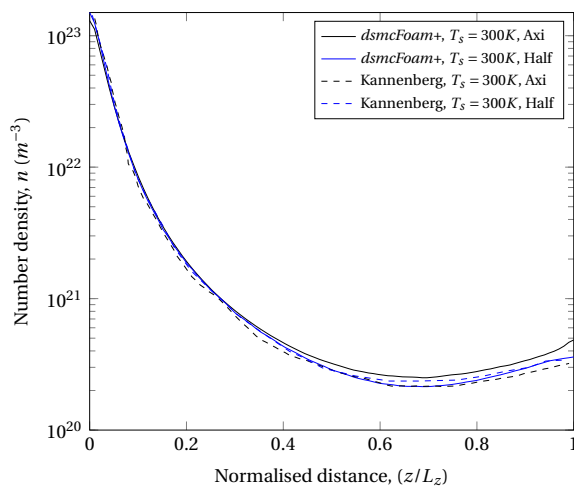
#### Plume parameters

Complementing the experimental data, the simulation results show how the plume parameters change along an axial line directly below the nozzle exit, see Figures 4.5(a-c). It is clear that the flow density initially decreases proportionally as a function of the axial distance, i.e. [99]

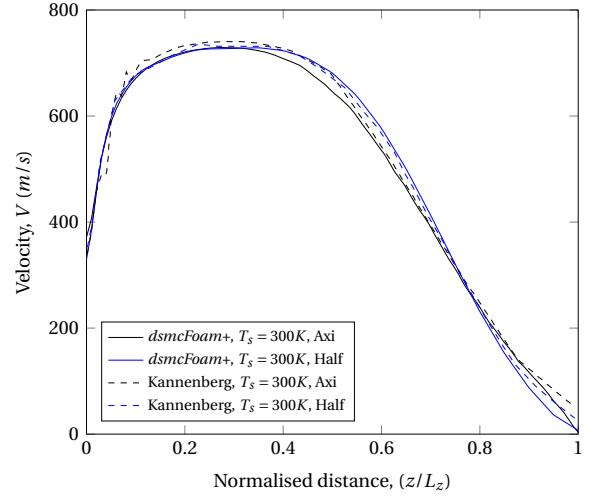
$$\rho \sim \frac{1}{z^2}, \quad (4.6)$$

when a plume is released in a vacuum environment without any obstruction. However, in this case, the plume impinges on a solid surface, therefore, the density gradually begins to increase again after a normalised distance of 0.7 as the plume is brought to rest by the presence of the solid surface. The plume velocity data shows that the gas initially accelerates as it leaves the sonic nozzle, quickly reaching its limiting velocity,  $u_{lim}$ , which is a function of stagnation temperature, i.e.,

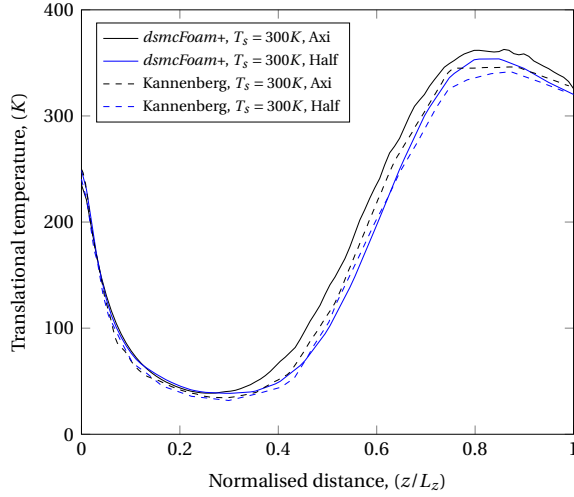
$$u_{lim} = \sqrt{\frac{2\gamma}{\gamma - 1} RT_0}. \quad (4.7)$$



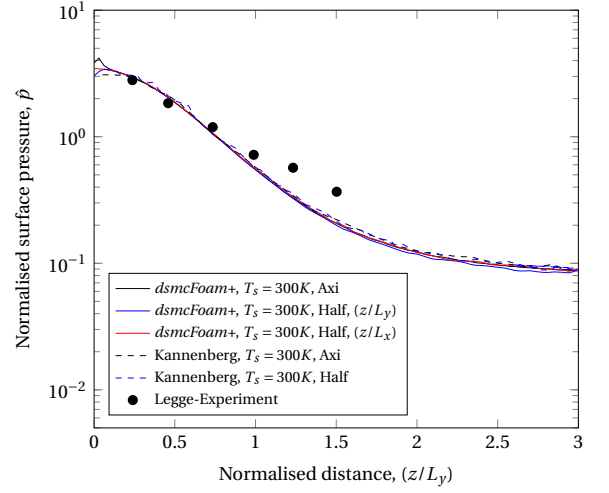
(a) Number density from the nozzle outlet to the surface.



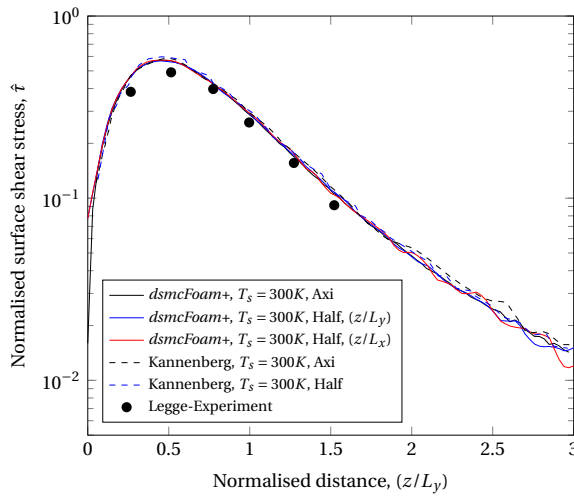
(b) Velocity from the nozzle outlet to the surface.



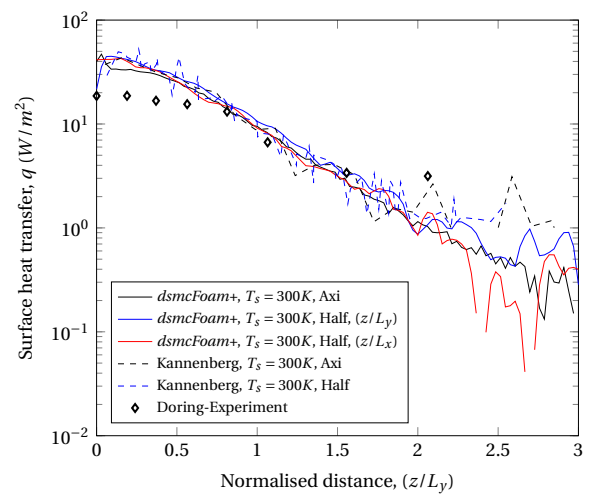
(c) Translational temperature from the nozzle outlet to the surface.



(d) Normalised surface pressure profile.



(e) Normalised surface shear stress profile.



(f) Surface heat transfer profile.

Figure 4.5: Benchmarking of *dsmcFoam+* results against data in the literature [106–108]. Results are plotted along a radial line starting at the stagnation point.

This approach predicts the limit velocity of the gas in the far-field under the assumption that the flow is purely isentropic. As shown in Figure 4.5(b), the gas velocity reaches the maximum, remains constant for a while, and starts decreasing as it approaches the solid surface. The link between the velocity and temperature distributions can clearly be observed in Figure 4.5(b). As the gas initially expands, it cools and it then begins to increase in temperature again as it recompresses near the surface. Finally, the temperature near the surface tends towards the fixed surface temperature of 300 K due to the diffuse boundary condition used in the simulations.

### Surface parameters

Figure 4.5(d) shows the distribution of the surface pressure. As expected, the pressure reaches the maximum value at the stagnation point. As the radial location increases, the dynamic pressure,  $P_{dyn}$ , increases, therefore so does the stress on the surface. The maximum value of the dynamic pressure can be estimated as per Roberts method [125, 126]

$$\frac{P_{dyn_{max}}}{H} = \sqrt{\frac{2}{(\kappa + 4)}}, \quad (4.8)$$

where

$$\kappa \equiv \gamma(\gamma - 1)Ma^2, \quad (4.9)$$

$\kappa$  is given in Ref. [127]. As observed in Figure 4.5(e), the surface shear stress is low at the stagnation point where the velocity is low and then increases gradually as the component of velocity parallel to the surface (which is proportional to the dynamic pressure) increases and then decreases again as the parallel velocity component begins to decrease.

Dettleff's simplified heat flux equation [99] for a high angle of attack of the plume impingement is given as

$$\dot{q} \approx \phi \frac{\rho}{2} u^3 \left( 1 - \frac{\gamma + 1}{2\gamma} \frac{T_w}{T_0} \right) \sin \alpha. \quad (4.10)$$

Herein, the recovery factor, i.e.  $\Lambda \approx 2\gamma/(\gamma + 1)$ , is a non-dimensional parameter of heat transfer at the free-molecular regime impingement indicating when thermal equilibrium, i.e.  $\dot{q} \approx 0$ , is reached during the impingement. If the recovery factor is greater than 1, i.e.  $\Lambda > 1$ , the equilibrium temperature of the plate is greater than the stagnation temperature of the flow [99]. In this case, at the stagnation point, the heat flux in Figure 4.5(f) shows that there is a relatively

small amount of heat transfer observed, as the stagnation temperature of the flow is 300 K. However, the translational temperature rises slightly above 300 K when it approaches the surface. Going from the stagnation point on the surface to the far-field, the surface heat transfer quantitatively decreases as seen in Figure 4.5(f). Dettleff [99] expresses the relation between the heat transfer and distance as

$$\dot{q} \sim \frac{1}{\sqrt{x}}. \quad (4.11)$$

### Results of *dsmcFoam+* versus others in the literature

Figure 4.5(a-c) show the distribution of plume parameters from the nozzle outlet to the surface, from two different solvers, *dsmcFoam+* and MONACO [106], for two different mesh topologies; axisymmetric and half-symmetry. Data along the plume impingement axis shows that axisymmetric and half-symmetry simulations of *dsmcFoam+* are complementary and these results also approximately match MONACO's outcomes despite small deviations between axisymmetric and half-symmetry results.

Considering that there are fewer DSMC simulators per-cell in the half-symmetry simulations compared to the axisymmetric topology for the same flow field, the statistical fluctuations are larger for *dsmcFoam+* and MONACO solutions as seen in Figure 4.5(d-f). In addition to the matching data sets of numerical solutions, available experimental measurements are also employed to verify the accuracy of the numerical solutions. Even though the experiments provide a scarce range of data throughout a radial line that starts from the stagnation point to far-field on the surface, both *dsmcFoam+* and MONACO match well, but neither solver recovers the pressure after a normalised distance greater than unity, which suggests that the background pressure in the experiments may have been greater than reported. The heat flux is also over-predicted by both DSMC solvers in comparison to the experiments.

### 4.3.2 Multi-nozzle normal impingement to the surface at a plume stagnation temperature of 300 K

A motor that has multiple rockets may be employed on spacecraft platforms during maneuvers in a vacuum environment while docking, for rendezvous or maintaining position. Herein, the notable feature is that the resulting plumes impinge on the surface, so the task should be the evaluation of plume-plume interactions, along with plume-surface interactions. Koppenwallner [128] studied the interaction of twin nozzles with different rarefaction levels. For free-molecular

impingement, it is observed that the plumes simply pass through each other, which is consistent with Ref. [99] at  $Kn_p \gg 1$  in Equation 4.12, where it is stated that undisturbed mutual plume penetration is possible, as the plume suddenly expands in the vacuum environment. For example, in the quadruple plume case at  $T_0 = 300$  K and  $D = 3$  mm that is discussed in detail later in the current section, the mean collision rate is measured as  $5.2 \times 10^7 \text{ s}^{-1}$  in the vicinity of the outlet of the nozzles. Then, the suddenly expanded plumes start to interact with each other, but the mean collision rate reaches its minimum value of  $6 \times 10^3 \text{ s}^{-1}$  going towards the impingement surface. When the plume reaches the vicinity of the impingement surface, the recompression process begins, where the mean free path decreases and the mean collision rate increases to  $5 \times 10^5 \text{ s}^{-1}$ . To sum up, in order to understand the changes in the centre of the plume core, interaction plane, and the properties at the impingement surface due to the plume-plume impingement as a function of nozzle-to-nozzle distance and increasing stagnation temperature, a simulation matrix is run and the results for plume properties and surface parameters are compared for single, double, and quadruple configurations.

### Plume parameters

As previously emphasised, the local Knudsen number in a plume varies and the flow may become free-molecular before it reaches the impingement surface in the simulated vacuum environment. However, in this case, an assessment is also valuable in deducing the change in the Knudsen number in the region of plume-plume interaction, which allows for the interpretation of how the interaction regime locally alters. The penetration Knudsen number is then defined by Ref. [99] as

$$Kn_p(\Theta) = \frac{1}{2} \frac{Kn_o}{A_{pl}^o} \frac{D}{2r_n} \frac{1}{\sin^2 \Theta} \frac{1}{f(\Theta)}, \quad (4.12)$$

with

$$A_{pl}^o = A_{pl} \frac{\rho_n}{\rho_o}, \quad (4.13)$$

where the distance of  $D/2$ , indicated in Table 4.3, is the sole parameter that is altered, while other variables are kept constant in the impingement simulations of identical nozzles. The local changes in the Knudsen number can also be expressed by the relation of  $\lambda_p \sim 1/\rho_s$ . In addition, the resulting plume impingement on the surface should be evaluated in order to compare how the aerothermodynamic loading changes through the surface as a function of the number of nozzles and the nozzle-to-nozzle distance in multi-nozzle applications.

In this section, two types of rocket motors, consisting of identical double



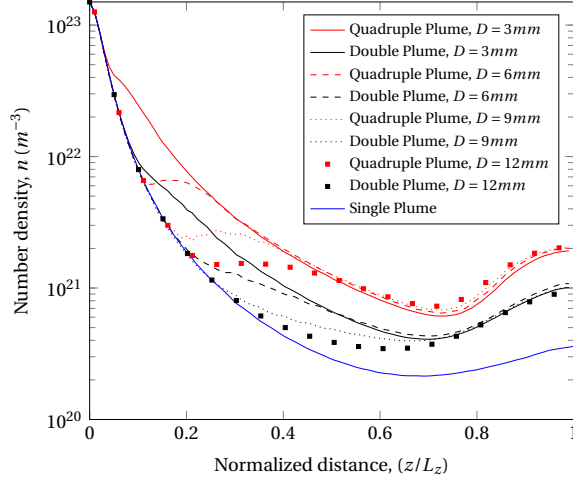
and quadruple nozzles, hover at a height of  $H = 40$  mm above a solid surface. Furthermore, in order to deduce the effect of the centre-to-centre distance between the nozzles,  $D$  is varied as shown in the simulation matrix of Table 4.3. The initial conditions of the flow are maintained as given in Table 4.1 for  $T_0 = 300$  K.

Figure 4.6 shows the plume-plume penetration results of *dsmcFoam+* from the nozzle outlet to the surface. The data extraction line is chosen to observe the penetration effect through an axial line, where the lines are:

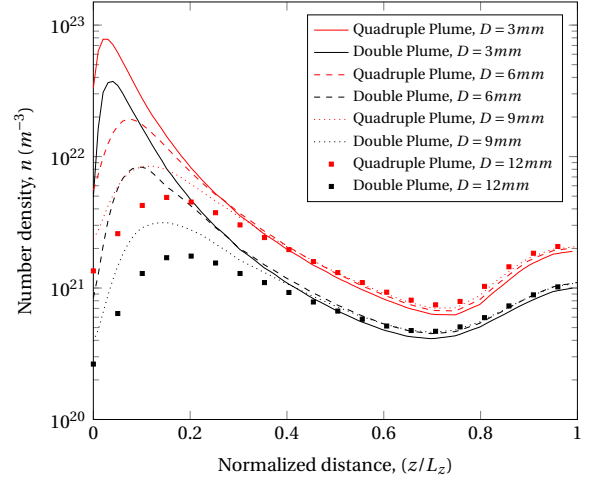
- *line 3*: from the centre point of one of the nozzle exits to the surface, and
- *line 4*: at the mid-point of the nozzle array, i.e. point-C in Figure 4.4, to the surface.

The distribution of normalised density along line 3 is shown in Figure 4.6(a) for various separation distances,  $D$ . From the measurements along line 3, the density distribution is independent of the number of nozzles for a short distance and matches the profile of a single nozzle. As the number of nozzles in the system increases and the distance between the nozzles is held constant, the normalised distance where the profiles diverge moves closer to the origin. The increase in density in the vicinity of the surface is more distinct in the multi-nozzle applications. The mass flow from each nozzle is constant, hence, there is a higher mass flow in the multi-nozzle simulations and a higher density near the surface where the plumes have expanded into one another -an expected result. The effect of the distance between the nozzles on the density distribution while the plume is approaching the surface can be compared for the same number of nozzles. In general, as the distance between the nozzles is increased, the normalised location at which the profiles deviate from the single nozzle result increases, with an array of 4 nozzles separated by 3 mm showing the faster deviation as the plumes begin to interact more strongly with one another earlier in the expansion process when they are closer together. In the compression region near the surface, i.e. from a normalised distance of  $\sim 0.7$ , the density profiles become independent of the distance between the nozzles.

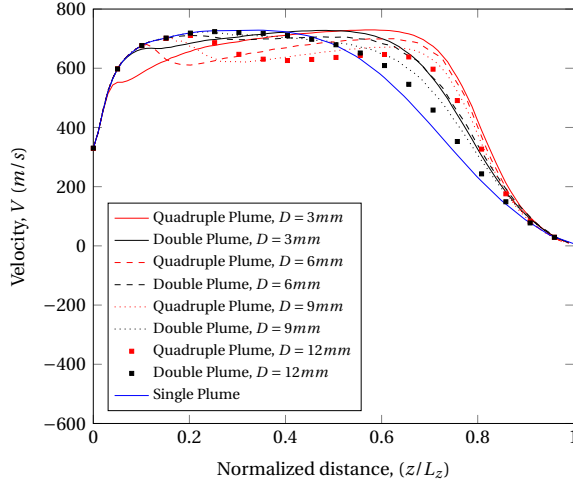
Figure 4.6(b) shows the data extracted along line 4. The density initially increases as the gas expanding from the nozzle exit reaches the centre of the array and then decreases as the gas continues to expand. The effect is more pronounced as the number of nozzles is increased and the spacing between them is decreased. For the same number of nozzles, the profiles become independent of the spacing relatively quickly compared to along line 3; the overall effect of  $D$  becomes negligible after a normalised distance of  $\sim 0.4$ .



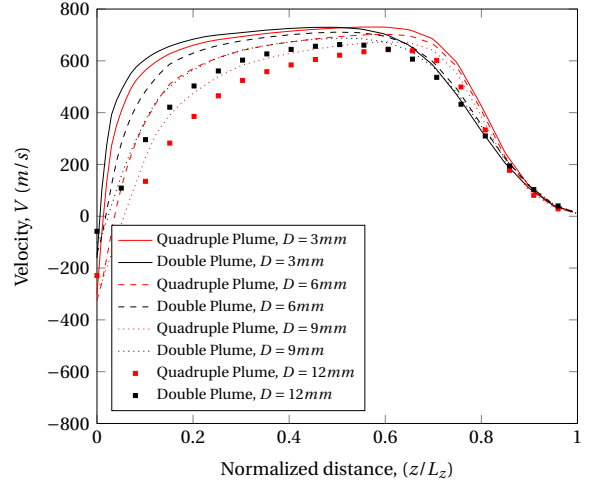
(a) Number density along line 3.



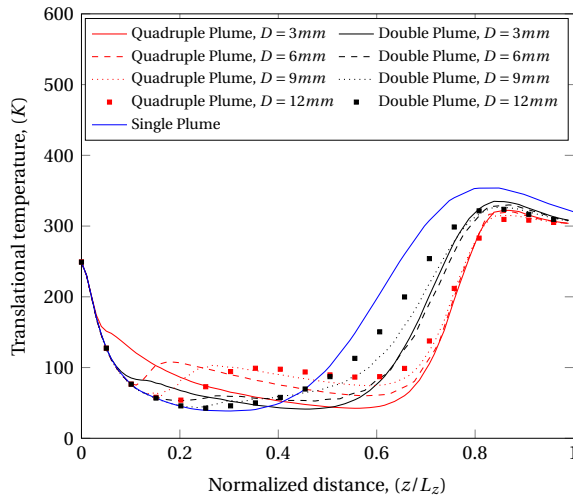
(b) Number density along line 4.



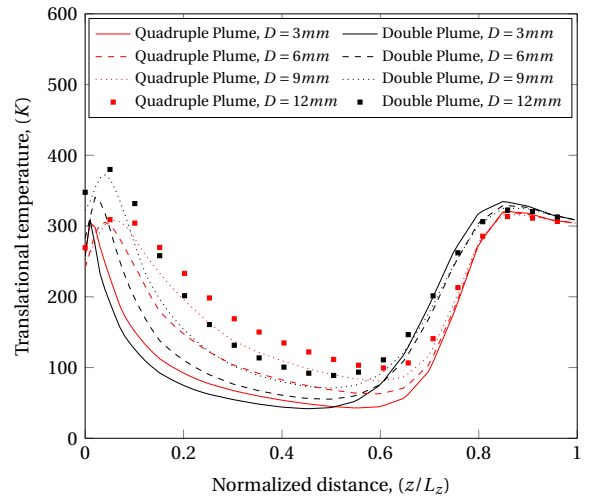
(c) Velocity along line 3.



(d) Velocity along line 4.



(e) Translational temperature along line 3.



(f) Translational temperature along line 4.

Figure 4.6: *dsmcFoam+* results of multi-nozzle plume-plume interactions for changing distance between the nozzles at  $T_0 = 300$  K.

Figure 4.6(c) shows the plume velocity along line 3. As previously discussed in detail, the single plume impingement data from line 3 shows that the plume accelerates after discharging in the vacuum surrounding it and then reaches the limiting velocity, which is reached after a normalised distance of  $\sim 0.2$ . The plume then starts decelerating and stagnates as it arrives at the surface. Examining double plume impingement cases shows the effect of separation distance  $D$  on the plume velocity. For an array of two nozzles with a separation distance of  $D = 12$  mm, the velocity distribution along the impingement axis shows a fairly similar trend with the single-plume, with the deceleration being slightly quicker. Moving the nozzles closer to each other causes a delay in reaching the limiting velocity and allows the gas to move closer to the surface before it begins to decelerate. When an array of four nozzles is considered, the same effects are more pronounced and can be observed more clearly.

Figure 4.6(c) shows the plume velocity along line 4. The velocity is initially negative due the vacuum boundary condition and flow expanding into the region behind the nozzle exit. It should be noted that although the trend of reaching the limiting velocity is generally maintained, it takes a greater normalised distance for this to be reached as the distance between the nozzles increases. The plume from an array of four nozzles decelerates faster than that for an array of two nozzles and the velocity for all cases obtain the same values after a normalised distance of  $\sim 0.9$ , when the flow is being brought to rest by the presence of the solid surface.

Figure 4.6(e) shows the measurement of translational temperature along line 3. The inverse proportion between the flow velocity and the temperature is clearly explained in Eq. 4.7. As can be observed from Figures 4.6(c) and (e), the overall trend of velocity and temperature are in a good agreement, although the translational temperature of the single nozzle does not overlap with the resulting plume of multi-nozzle arrays. As seen in Figures 4.6(d) and (f), the backflow of the four nozzle array is faster than the double plume configuration, the change in the translational temperature of four nozzle array is thus slightly lower than in the double nozzle configuration.

### Surface parameters

The aerothermodynamic loading data of the plumes on the surface is extracted along a radial line, named *line 5* here, that extends from where the stagnation point would be in a single nozzle array radially outwards.

Figure 4.7 shows the extracted data of plume-surface interactions along line 5. The distribution trends of the surface parameters in a single nozzle impinge-

ment are discussed in detail in § 4.3.1, the impacts of plume-plume penetration and resulting plumes on the surface show slightly different patterns of surface parameters and quantitatively higher impingement effects than the single plume application. When comparing the surface pressure created by different nozzle arrays at the stagnation point on the surface, it is clear that the surface pressure increases with the number of nozzles, as shown in Figure 4.7(a). In addition, when comparing the multi-nozzle arrays among themselves, the change in the distance between the nozzles in both double and quadruple arrays does not significantly affect the surface pressure distribution. The differences between the effect of double and quadruple systems disappear in the range of normalised distances between 0.9 and 1.7, where in all cases of four nozzle arrays, the surface pressure decreases gradually, but tighter nozzle arrays introduce a delay in coinciding with the profile for a double nozzle array. Moreover, the surface pressure value becomes equal in single and multi-nozzle systems around the normalised distance of 2.5 on the surface. In all cases, the maximum pressure is always directly below the centre of the array, there are not multiple stagnation points below each nozzle, which shows that the four plumes have effectively merged in to a single plume before interacting with the surface. This is due to the plumes being under-expanded.

Figure 4.7(b) shows surface shear profiles. It is observed that the multi-nozzle arrays result in a higher shear stress than the single application at the stagnation point on the surface. There is only one peak of surface shear stress in each case because the under-expanded plumes have effectively merged in to a single plume before reaching the surface. When a multi-nozzle array within itself is examined, the quadruple simulations at  $D = 3$  mm create a slightly greater shear stress at the stagnation point than the double one. Following this, as the  $D$  value increases, the results become independent of the number of nozzles in the array; the double and quadruple configurations create the same impact at the stagnation point in terms of shear stress.

The heat transfer rate for multi-nozzle applications is observed to be slightly higher than the single plume impingement around the stagnation point on the surface as shown in Figure 4.7(c). For each nozzle array configuration, it can be said that the results are almost independent of the nozzle separation distance  $D$  at large radial distance along the surface. Going through the far-field of the surface, the heat transfer rate gradually decreases in inverse proportion to the distance, which is expressed in Eq. 4.11.

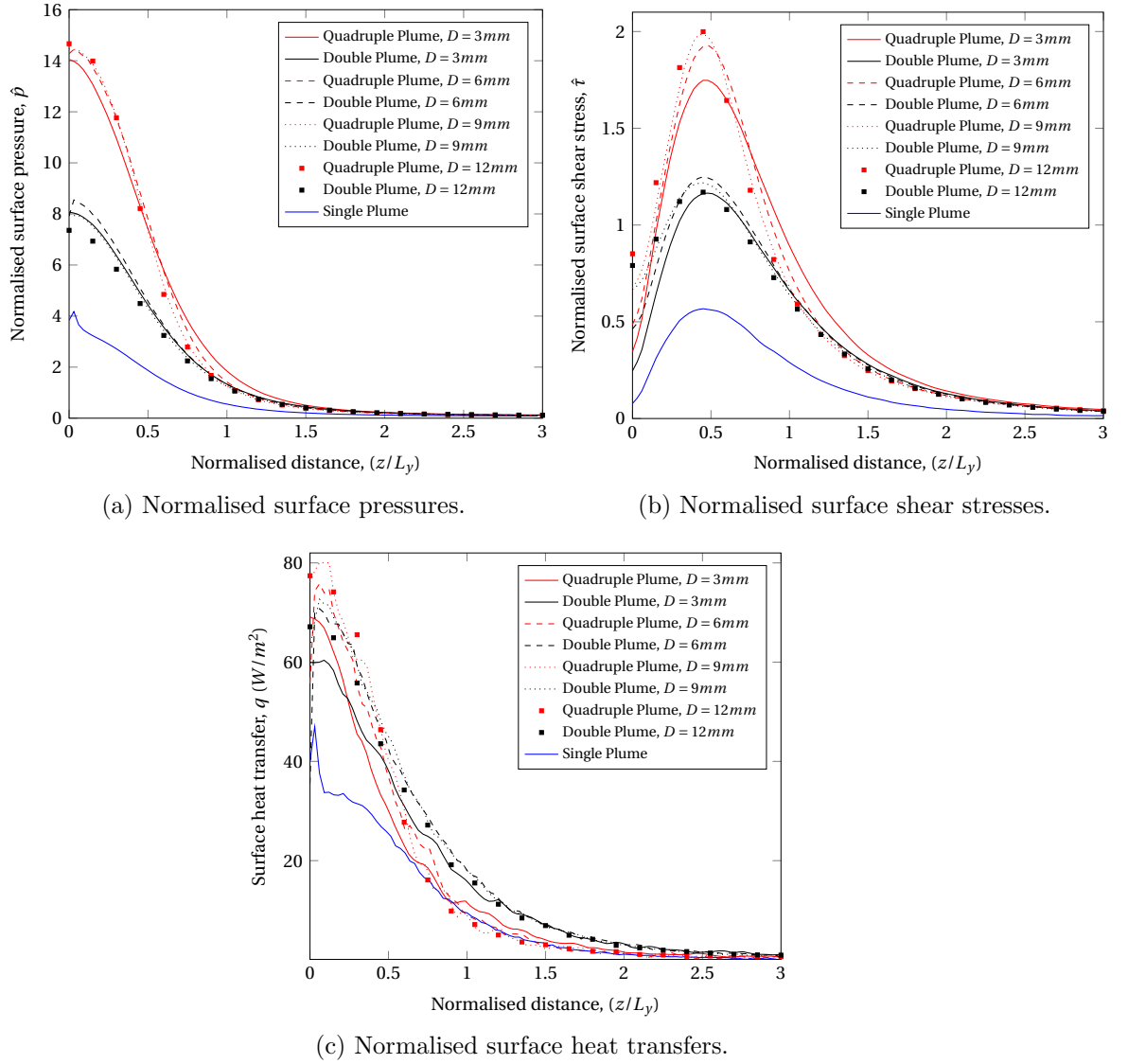


Figure 4.7: *dsmcFoam+* results for surface properties from multi-nozzle arrays at  $T_0 = 300$  K.

### 4.3.3 Increasing stagnation temperature in a single nozzle

In order to gain various specific impulses from the motors, the propellants may be fired with different stagnation temperatures. In this study, the stagnation temperature is increased, but the flow remains sonic at the nozzle exit and the stagnation pressure is held constant at 1000 Pa.

#### Plume parameters

In this section, a single nozzle hovers at  $H = 40$  mm above a solid surface and the stagnation temperature of the plume varies from 300 K to 1000 K. Figure 4.8 shows the properties along an axial data extraction line, which starts from the

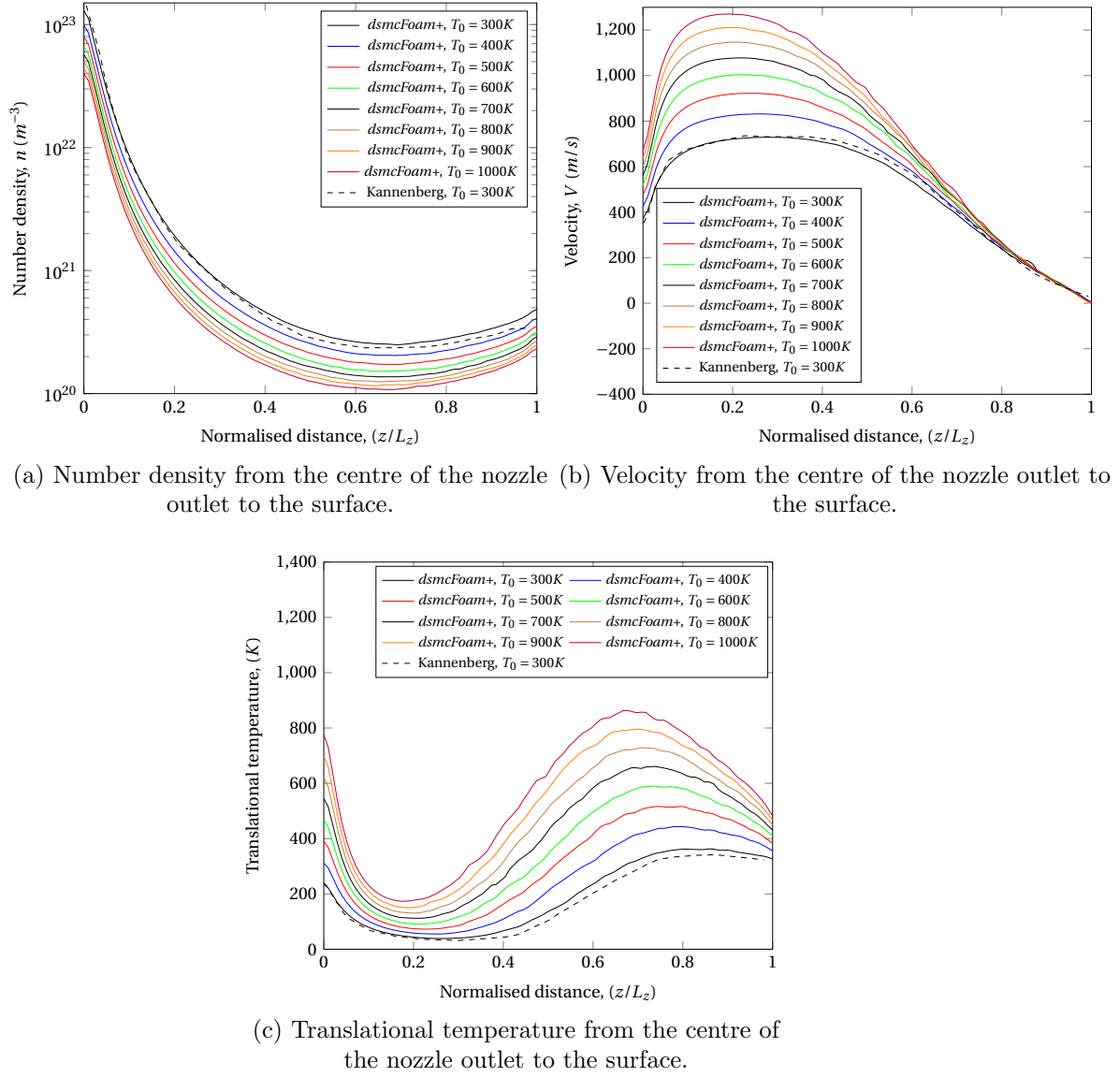


Figure 4.8: *dsmcFoam+* results of single-nozzle plume-surface impingement with increasing stagnation temperature.

centre of the nozzle exit and extends to the surface. Figure 4.8(a) shows the number density along this line. As the stagnation temperature is increased, the inlet number density reduces while the stagnation pressure is held constant at 1000 Pa for all cases. The mass flow rate will reduce when the stagnation temperature increases, as choked mass flow rate is directly proportional to the stagnation pressure (held constant here) and inversely proportional to the square root of stagnation temperature. The results for all of the stagnation temperature cases performed here are qualitatively similar, with an initial expansion and recompression near the surface. The density decreases as the stagnation temperature increases.

The velocity profiles throughout the plume centre for different stagnation tem-

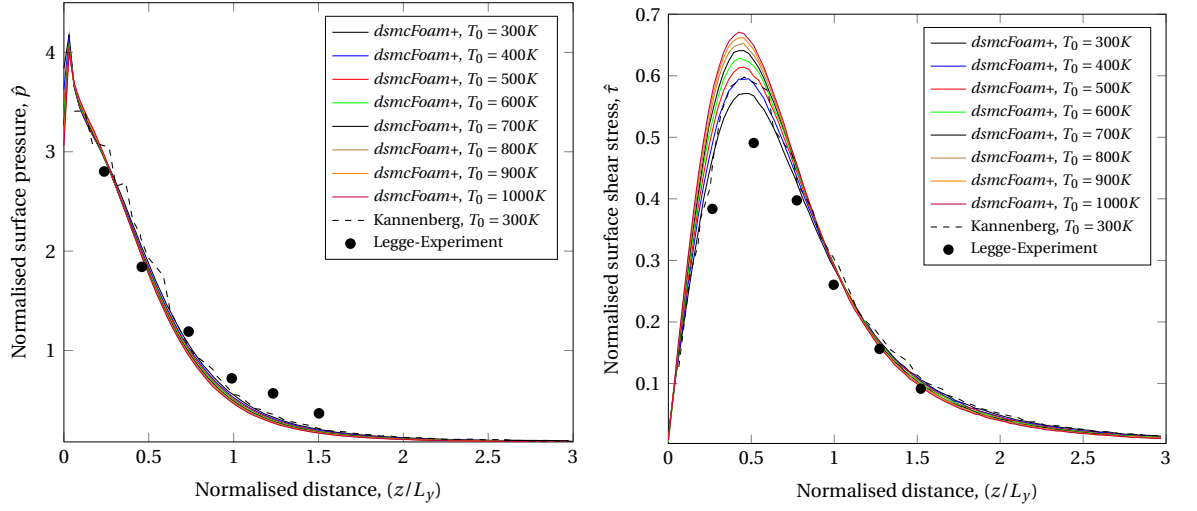
peratures are plotted in Figure 4.8(b). The plume is discharged into the vacuum environment at sonic velocity,  $V_{sonic} = \sqrt{\gamma RT}$ . Since the stagnation-to-static temperature ratio remains the same, the inlet velocity increases with the stagnation temperature. It should be also noted that the maximum plume velocity is a function of the stagnation temperature, as given in Eq. 4.7. In addition, with increasing stagnation temperature, the distance travelled with the maximum velocity decreases. Figure 4.8(c) shows the distribution of translational temperature from the nozzle outlet to the impingement surface. The temperatures initially decrease as the gas expands, and then begin to increase as the gas is compressed by the presence of the surface. There is then a further decrease in the gas temperature, which is due to the influence of particles that strike the diffuse wall at a temperature of 300 K and then are able to penetrate back up through the plume for a certain distance. As the stagnation temperature increases, the gas density decreases, therefore, the degree of rarefaction increases; the result of this is a greater temperature jump as the stagnation temperature increases.

### Surface parameters

At a constant hovering altitude, the peak surface pressure at the impingement point is inversely proportional to the hypersonic parameter as previously explained in Eqs. (4.8) and (4.9).

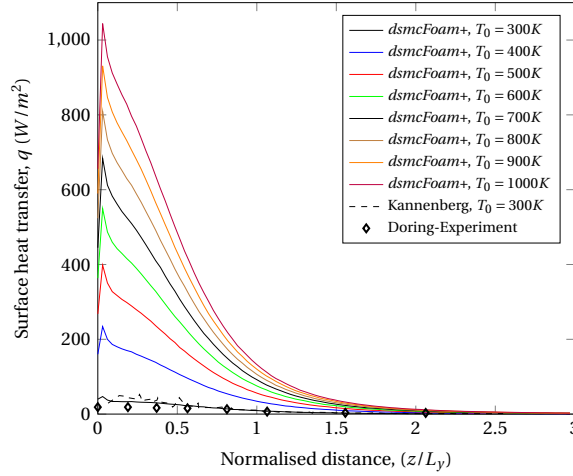
The distribution of surface pressure is plotted in Figure 4.9(a) for a range of stagnation temperatures. At first glance, it is seen that increasing the stagnation temperature causes a slight reduction in the surface pressure despite starting at the normalised distance of 0.4. As mentioned previously, a continuous RWF is applied in this study for the axisymmetric domains in order to maintain a reasonably constant number of DSMC simulator particles as the cell volumes quickly increase from the symmetry axis. However, this application in axisymmetric solutions causes a measurement error - a reduction in the scalar pressure measurement near the surface due to the effect of the number of tentative collisions on the mean collision time near the axis [122] as can be observed in Figure 4.9(a) around the stagnation point on the surface.

Figure 4.9(b) presents the shear stress distribution on the impingement surface for increasing stagnation temperature. It is clearly seen that the shear stress in the vicinity of the stagnation point on the surface is not affected by the changing temperature because in all cases the flow velocity is very low around the stagnation point, as discussed in § 4.3.1. Subsequently, the shear stress proportionally increases with the increase in the stagnation temperature up to the normalised distance of 0.5 and shows a decreasing trend until the normalised distance of



(a) Normalised surface pressures.

(b) Normalised surface shear stresses.



(c) Normalised surface heat transfer rates.

Figure 4.9: *dsmcFoam+* results of single-nozzle plume-surface impingement with increasing stagnation temperature.

1. After this point the far-field of the surface, the surface shear stress and the stagnation temperature have an inverse proportion as a result of increasing local rarefaction with increasing the stagnation temperature.

For the surface heat transfer, as shown in Figure 4.9(c), as the stagnation temperature increases, so too does the heat flux at the stagnation point and in all cases the heat transfer decreases with radial distance.

#### 4.3.4 Multi-nozzle normal surface impingement with increasing stagnation temperature

As the increasing stagnation temperature of the plume is discussed for a single nozzle application in the previous section, the multi-nozzle configurations with



increasing stagnation temperatures are now considered. In this section, the same flow properties of the single nozzle configuration are applied as inlet parameters for each of the nozzles. While the distance between the motor and the surface is maintained, the stagnation temperature and the nozzle-to-nozzle distances are increased to observe the changes in the resulting plume and the effects of the plume and impingement surface interactions.

### Plume parameters

In order to discuss the effect of temperature on the plume-plume interactions, the stagnation temperatures are gradually increased for arrays with two and four nozzles. Furthermore, the impact of nozzle-to-nozzle distance on the plume-plume interaction is also investigated by varying the distance  $D$ .

Figure 4.10 shows flow profiles for multi-nozzle arrays with increasing stagnation temperatures for the nozzle-to-nozzle distances of  $D = 3$  mm and 9 mm. The data is extracted throughout an axial line, which starts at the centre of a nozzle outlet and extends to the solid surface. Figures 4.10(a) and (b) show the change in number density along the core of a plume for  $D = 3$  mm and 9 mm, respectively. In general, the profiles for the two different arrays remain similar as the stagnation temperature changes, with the profile being shifted to lower values of density with an increase in the stagnation temperature. This is because the inlet number density decreases as the stagnation temperature increases and also higher flow temperatures lead to higher limiting velocities. In all cases, the plume initially expands freely, then begins to diverge in shape as two or more plumes begin to interact with one another. However, there is still an overall expansion until near the surface where the flow is recompressed.

Figures 4.10(c) & (d) show the velocity profile of a disrupted plume by the impingement of plume(s) for  $D = 3$  mm and 9 mm, respectively. The plume-plume interactions disturb the velocity trends of the plume core in some cases, which will be detailed in § 4.3.4. Herein, the nozzle-to-nozzle distance  $D$ , the number of nozzles in the array, and the stagnation temperature are the key parameters to deduce the location and impact of the plume-plume interaction on the velocity profile. Figure 4.10(c) shows the velocity distributions for multi-nozzle configurations when  $D = 3$  mm. As expected, the penetration effect is more severe in the quadruple array than in the double array, which can be observed with the reduced acceleration of the plume from a normalised distance of 0.05. As the temperature and velocity have a linear relationship, it should also be noted that the velocity profile generated by the quadruple array reaches the same limiting velocity as the double array, but the deceleration near the surface is delayed for the quadru-

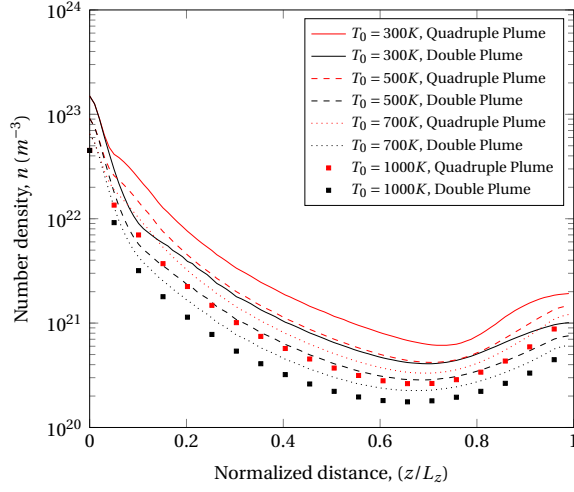
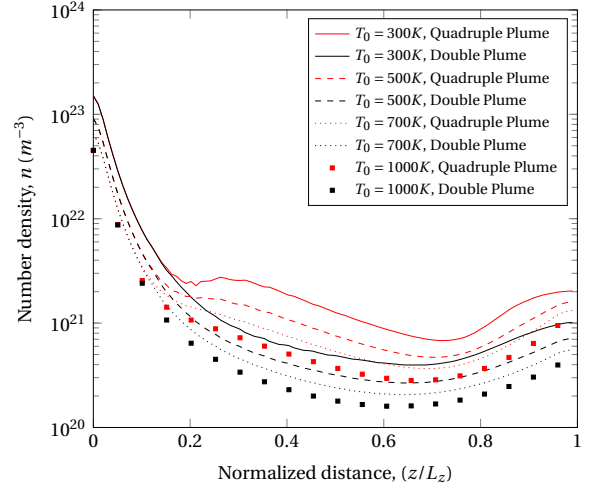
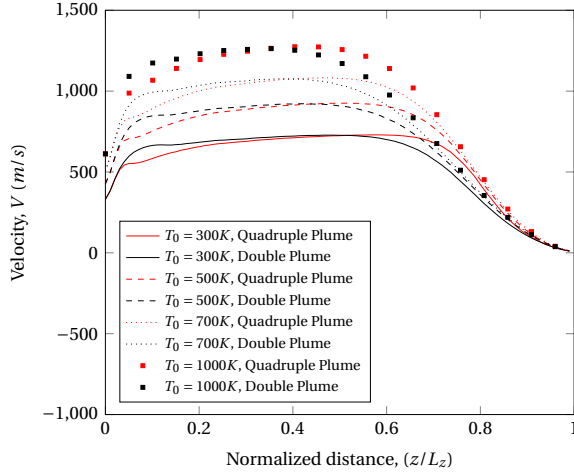
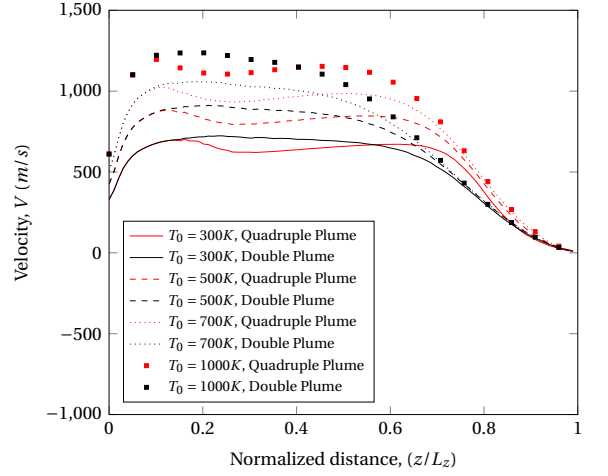
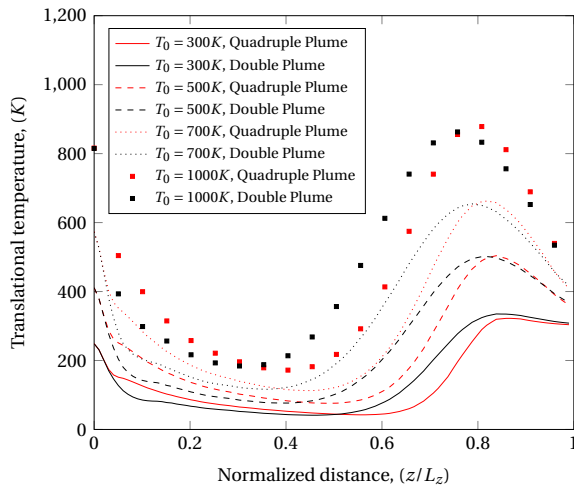
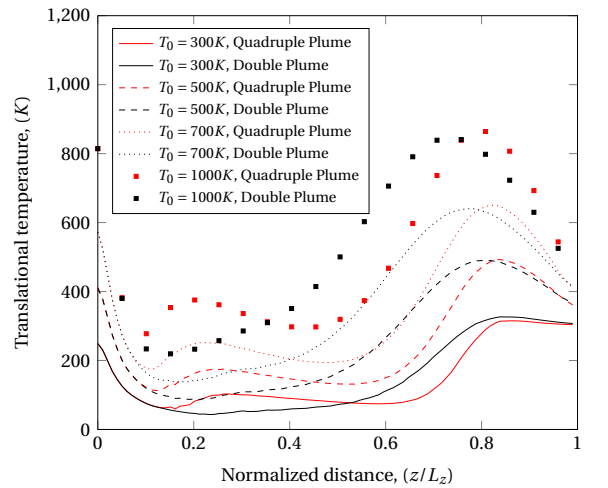
(a) Number density profiles,  $D = 3$  mm.(b) Number density profiles,  $D = 9$  mm.(c) Velocity profiles,  $D = 3$  mm.(d) Velocity profiles,  $D = 9$  mm.(e) Translational temperature profiles,  $D = 3$  mm.(f) Translational temperature profiles,  $D = 9$  mm.

Figure 4.10: *dsmcFoam+* results of multi-nozzle array plume-plume impingement with changing nozzle-to-nozzle distance and increasing stagnation temperature. The results are presented along an axial line extending from the centre of a nozzle outlet to the surface.

ple arrays. Figure 4.10(d) presents the data from a plume core at  $D = 9$  mm. The comparison of quadruple and double arrays at all temperatures shows that the disturbance of plume-plume interaction on the velocity profile in the plume core is negligibly small in the double nozzle array compared to the quadruple ones. When compared Figures 4.10(d) & (e), the location of the plume-plume interaction is delayed to around a normalised distance of 0.2 in the quadruple configuration, compared to 0.05 when  $D = 3$  mm. Due to the plume-plume interactions, the gas flow is decelerated and then recovers to its limiting velocity before being decelerated by the presence of the solid surface.

Figures 4.10(e) & (f) show the temperature profiles in a plume core, including the effect of interaction with other plumes, while the stagnation temperature increases gradually and  $D$  is varied from 3 mm to 9 mm. In all cases, the gas initially cools as it expands, then the temperature begins to increase again as it recompressed near the surface, before finally approaching the constant surface temperature of 300 K. For equal stagnation temperatures, it is clear that the plume temperature decreases less rapidly for a quadruple nozzle array than a double array and that the recompression near the surface is delayed further in a quadruple array. The quadruple and double array profiles remain the same for longer in the  $D = 9$  mm results as it takes longer for the plumes to expand enough to begin interfering with one another. As the stagnation temperature is increased, the temperature profiles are increased all along the normalised distance and there is a larger temperature jump at the surface and, the gas temperature decreases due to diffuse reflections from the impingement surface with a temperature of 300 K.

### Surface parameters

The surface parameters are measured along line 5, as defined in § 4.3.2. Here, only the surface data for  $D = 3$  mm is shown in Figure 4.11, as there is negligible difference between the surface impingement data observed at  $D = 3$  mm and various nozzle orientations.

As shown in Figure 4.7, when the plume temperature is kept constant at 300 K, the distance between the nozzles does not have an impact on the distribution of the surface impingement parameters. However, the number of nozzles in the array quantitatively affects the aerodynamical loading on the surface. It should be highlighted that the surface pressure and surface shear stress are greater in the multi-nozzle arrays rather than the single plume impingement, and that the quadruple array creates a higher impact at the stagnation point on the surface than the double one. Using the data of the quadruple and double arrays when

$T_0 = 300$  K and  $D = 3$  mm, the results of Figure 4.7 can be linked to that of Figure 4.11 in order to enhance the understanding of the effect of the increasing plume stagnation temperature in the multi-nozzle applications on the impingement surface.

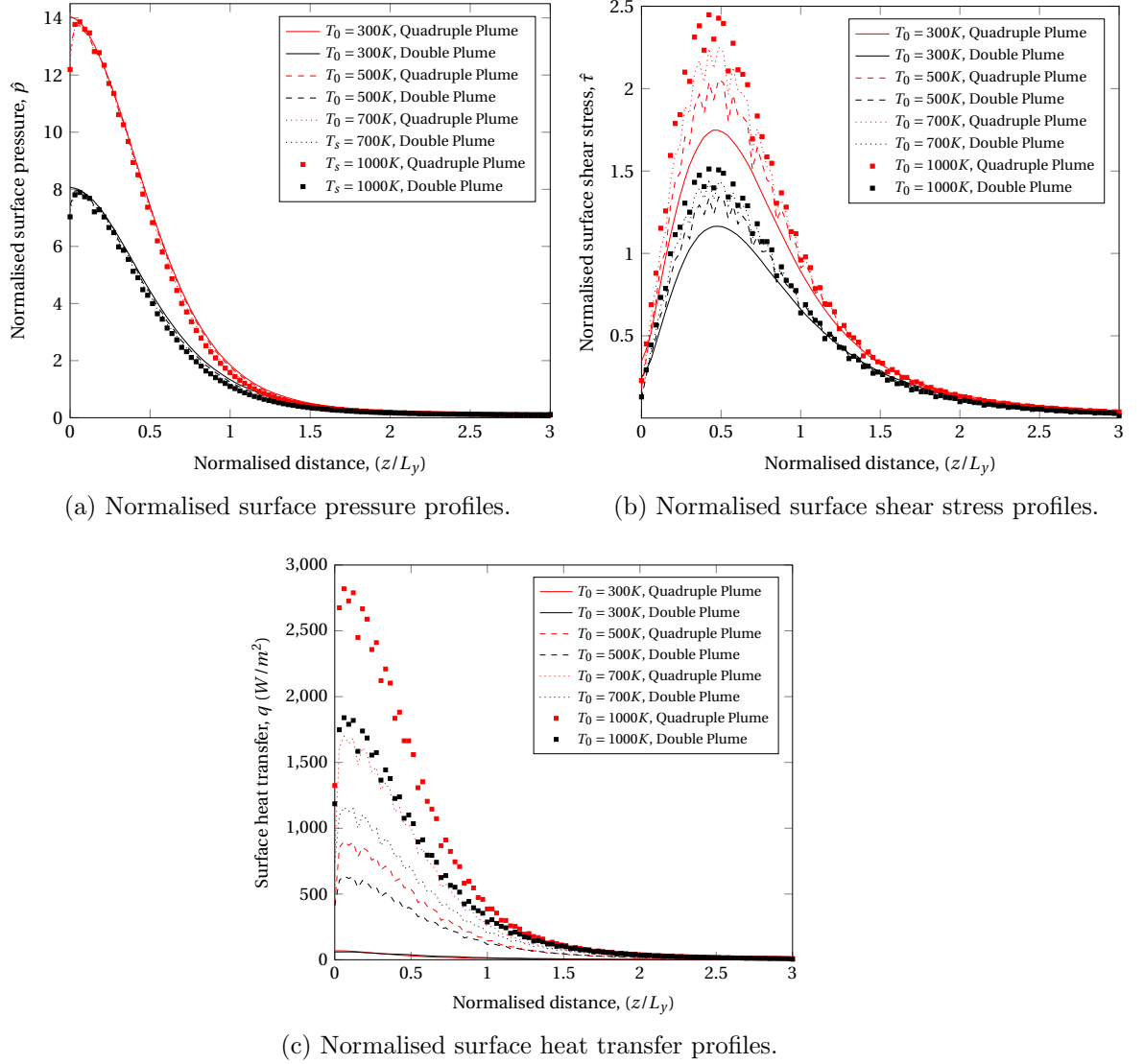


Figure 4.11: *dsmcFoam+* results of multi-nozzle plume-surface impingement with increasing stagnation temperature at a constant nozzle-to-nozzle distance,  $D = 3$  mm. The results are plotted along a radial line starting directly below the centre of the nozzle outlet on the surface.

Figure 4.11(a) shows the change in surface pressure as a function of increasing stagnation temperature. The distribution of the surface pressure depends on neither the distance between the nozzles nor the plume temperature. The impingement effect on the surface stagnation point of the quadruple array is 1.73 times greater than the double array as discussed previously, regarding the surface impact parameters of resulting plumes in Section 4.3.2.

Figure 4.11(b), which presents the surface shear stress for increasing stagnation temperature at a constant nozzle-to-nozzle distance of 3 mm, and that increasing the stagnation temperature slightly increases the value of the normalised surface shear stress for both double and quadruple arrays.

When the distance between the nozzles is kept constant and the stagnation temperature is gradually increased, the surface heat flux acts as a function of the plume stagnation temperature, as seen in Figure 4.11(c). The quadruple array causes a higher peak heat transfer to the surface than the double array, however, the difference of the heat transfer value between quadruple and double arrays for the same stagnation temperature disappears around the normalised distance of 1.25.

### 4.3.5 Changing impingement height in a single nozzle at a plume stagnation temperature of 1000 K

Previously, single and multi nozzle configurations at a constant hovering height,  $H = 40$  mm, had been investigated to deduce plume-plume and plume-surface interactions. However, in order to understand the effect of hovering height on the plume parameters and surface impingement, the value of  $H$  is gradually altered between 30 mm and 60 mm. While altering the nozzle height, the inlet flow properties and the initial conditions of the stagnation temperature of 1000 K are maintained and the simulations are run using an identical nozzle geometry.

#### Plume parameters

Figure 4.12 shows plume properties through an axial data extraction line from the centre of the nozzle exit to the impingement surface.

Figure 4.12(a) shows the number density along the extraction line. As the impingement distance is increased, the number density decreases inversely proportionally because there is not as much time for the flow to expand before reaching the solid surface. The density versus distance relation was also explained in Eq. 4.6.

Figure 4.12(b) shows the change in velocity along the data extraction line. The data of plume velocity shows that the discharged gas from higher heights accelerates faster and reaches the limiting velocity earlier than that from lower heights. Although the gas discharged into the vacuum environment from different heights stagnates upon arrival at the impingement surface, after reaching the limiting velocity, there is an inverse proportion between the gas velocity and the impingement height, meaning that the gas travels slower when it is discharged

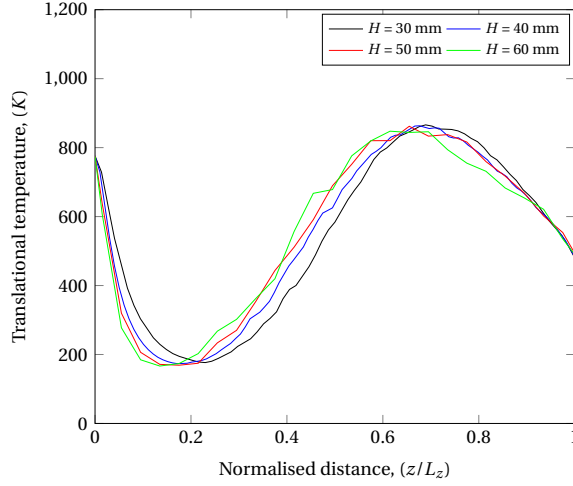
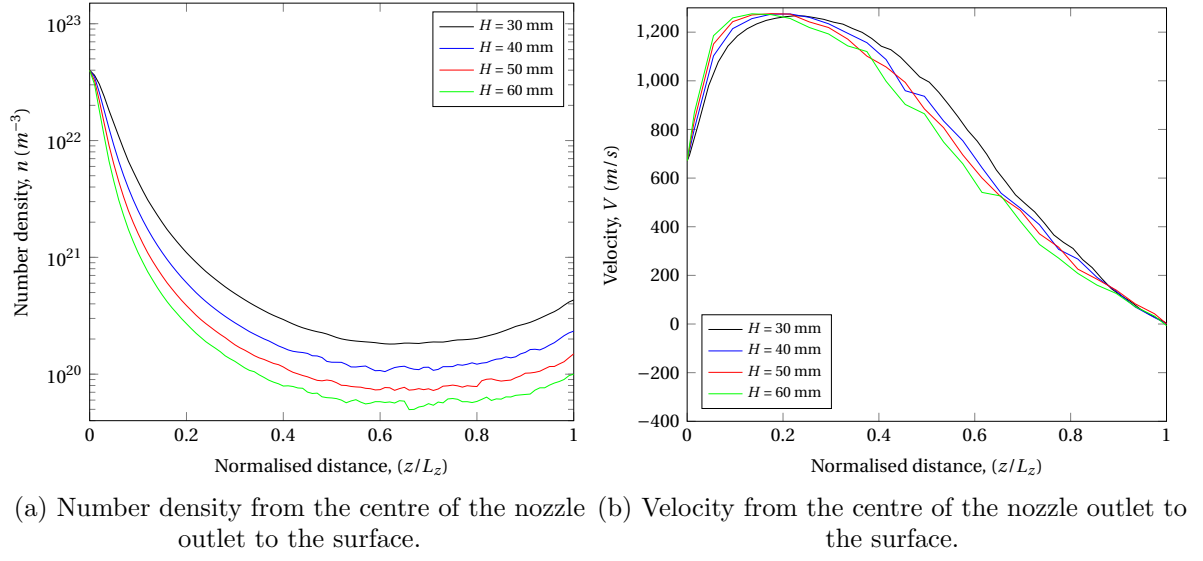


Figure 4.12: *dsmcFoam*+ results of single-nozzle plume-surface impingement with altering the distance between the nozzle outlet and impingement surface.

from higher heights.

Figure 4.12(c) shows translational temperature distributions. When the gas expands, the temperature decreases and then begins to increase again as the plume is compressed by the presence of the surface, but begins to decrease towards the surface temperature of 300 K after a normalised radial distance of 0.7. This is because particles that strike the surface are reflected diffusely at 300 K and can penetrate some distance back up the plume, as previously discussed in § 4.3.3.

### Surface parameters

At a constant plume stagnation temperature of 1000 K, the surface impingement effects of a single nozzle plume are evaluated for various hovering altitudes. The surface impingement data is extracted through the centre of the plume stagnation point to the far-field. The radial distance of the data extraction line is normalised using the reference hovering altitudes, which are  $H = 30$  mm, 40 mm, 50 mm, and 60 mm. Figure 4.13 shows the normalised surface parameters.

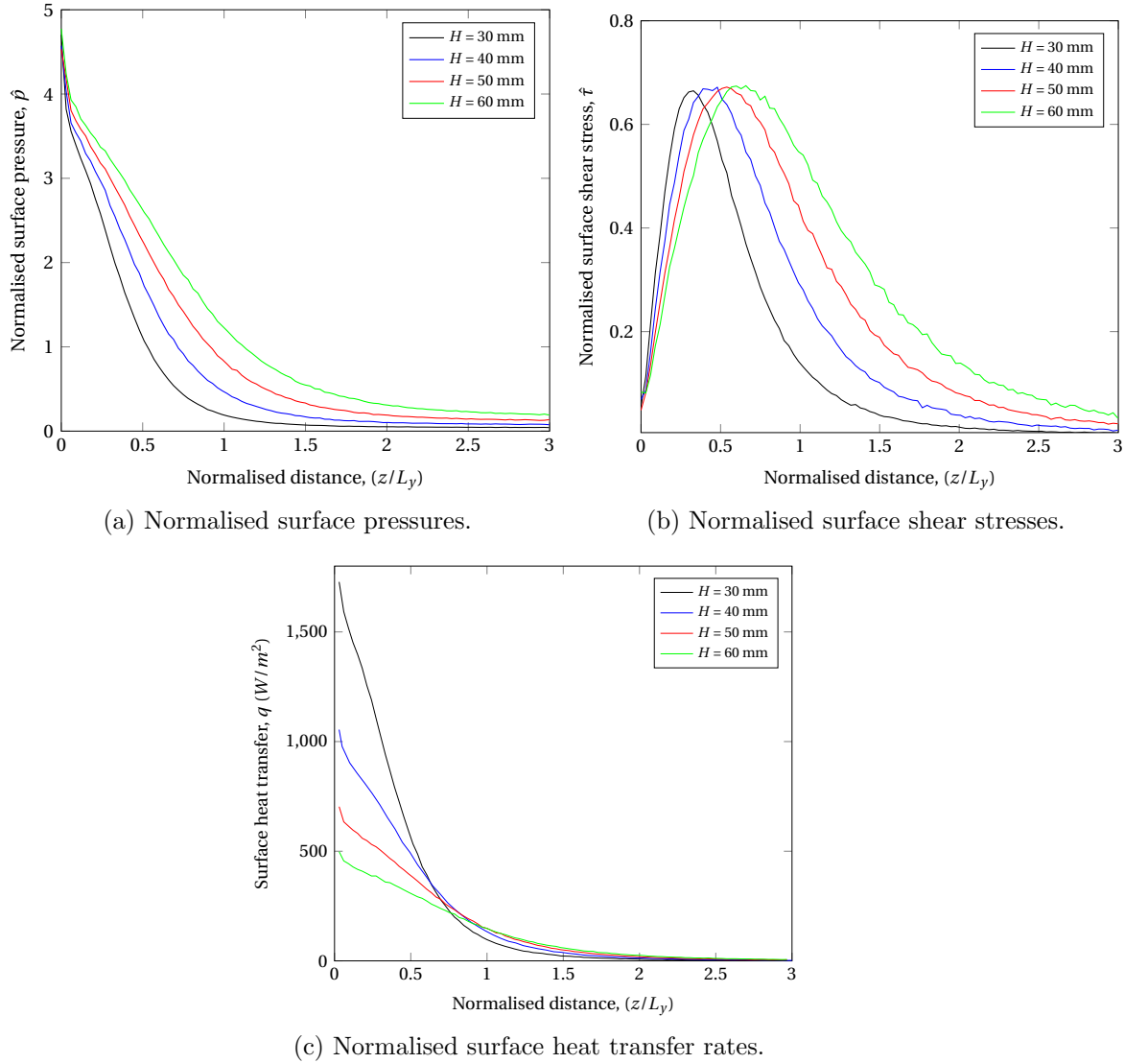


Figure 4.13: *dsmcFoam+* results of single-nozzle plume-surface impingement with altering the distance between the nozzle outlet and impingement surface.

Figure 4.13(a) presents a dataset to deduce the impact of altering impingement height,  $H$ , on the surface pressure. As expected, the closer hovering altitude causes a higher surface pressure at the stagnation point on the surface. However, the severity of the impingement effect reduces faster as can be seen in

Figure 4.13(c). Figure 4.13(a) aims to show the surface pressure data independent from geometrical effects for a fair comparison. According to these normalised results, all four nozzles create equal pressure on the surface as expected, although taking the nozzles to higher hovering altitudes, from  $H = 30$  mm to 60 mm, postpones and distributes the surface effects to wider surface fields. In the far-field, around the normalised distance of 2, the dependence of the surface pressure on the impingement height gradually reduces.

Figure 4.13(b) shows the change in the surface shear stress through the radial data extraction line. The closer impingement height causes the highest shear stress on the surface and the location of the formation of the peak shear stress is delayed by increasing the hovering height. Between the normalised distance  $\sim 0.5$  and  $\sim 0.8$ , the surface shear stress shows a reducing trend for all hovering distances. However, higher impingement heights cause more shear stress in the far-field of the impingement surface.

Figure 4.13(c) shows the distribution of surface heat transfer for the range of hovering altitude. When a plume with a stagnation temperature of 1000 K impinges on the surface, the surface heating increases around the stagnation point. Going through the normalised distance of  $\sim 0.7$ , the surface heat transfer caused by a plume, for which the hovering altitude is shortened, reduces so an inverse proportion between the hovering distance and the surface heat transfer can be obtained. In the far-field of the surface, after the normalised distance of  $\sim 2$ , the effect of hovering altitude cannot be detected for the surface heat transfer.

## 4.4 Summary

This work is a study on the effect of changing rocket motor configurations with increasing stagnation temperature on the plume-plume interactions as well as plume-surface interactions.

The results of constant stagnation temperature with variations in the number and configuration of nozzles show that the increment in number of nozzles and a tighter array results in earlier plume-plume impingement in the axial direction, which results in a quicker deviation from the results of a single plume. Packing the nozzles closer together results in a greater density at the surface stagnation point and delays the recompression near the surface.

When the stagnation temperature is gradually increased in the single plume simulations, the density at the nozzle exit decreases accordingly. The plume with a higher temperature accelerates more quickly. After the recompression, there is a greater temperature jump at the surface as the stagnation temperature



increases. For the surface parameters, a denser plume, i.e. one with a lower stagnation temperature, results in a slightly greater impact on the surface in terms of normalised pressure, but the opposite trend is observed for the normalised shear stress and surface heat transfer, with the higher stagnation temperatures resulting in greater impact on the surface properties.

In another application, the number of nozzles and the stagnation temperature are increased, while the distance between the nozzles is altered. The examination of the resulting plume-plume impingement indicates that the colder and more tightly packed arrays with more nozzles result in an earlier and a greater impact on the density trend along an axial line from a nozzle exit. Increasing the stagnation temperature accelerates the gas to a higher velocity, but the resulting plumes, independent of the number of nozzles, decelerate further downstream of the nozzle exit and stagnate on the surface. The trend of the translational temperature changes in the plume core region along the impingement axis as a result of plume-plume penetration. However, quadruple and double nozzle arrays at the same stagnation temperatures reach the surface with the same temperatures and the effect of the distance between the nozzles become negligible. This is also applicable for surface parameters as the impingement effect is not a function of the nozzle-to-nozzle distance. Quadruple arrays result in a higher surface pressure at the stagnation point than double arrays, but the surface pressure becomes equal for all cases at a large radial distance. For the normalised surface pressure data, the number of nozzles is more significant than the stagnation temperature. However, a slight effect of the stagnation temperature can be found on the normalised surface shear stress. A flow with a higher stagnation temperature and more nozzles produces a slightly higher normalised surface shear stress. As expected, greater stagnation temperatures result in a higher heat flux on the surface, but also in the vicinity of the impingement region where the effect of the number of nozzles is clearly observed. The effect of the number of nozzles at higher plume temperatures disappears at a large radial distance.

The effect of the impingement height is also discussed in this chapter. The single nozzle impingement is performed for changing hovering altitude simulations while maintaining other plume and nozzle parameters. Keeping the nozzle closer to the impingement surface creates a denser plume as the plume gas molecules can barely escape from the suction of the outlet patches. However, the plumes travel at approximately the same velocity and temperature but going through the higher altitudes causes the limit velocity and maximum temperature value to be reached earlier than the plumes of other lower altitude nozzles. The impact of the plumes on the surface increases when the nozzle is located closer to the

surface. However, higher altitude impingements create numerically lower but more distributed impact values on the surface. Therefore, it is possible to see that the nozzle with a higher hovering altitude creates slightly higher surface impact parameters when compared to other lower positioned ones.

# Chapter 5

## An Open-source One-way Coupling Solver for Two-phase Rarefied Flows: *rarefiedMultiphaseFoam*

### 5.1 Introduction

Particle-laden gas flows in fluidised beds are a significant class of multiphase flows and are quite common in a range of diverse fields from medicine to volcanology, such as sedimentation, lubricated transport, spray implementations, etc. Therefore, many techniques have been developed for continuum and discrete flow types to predict the interactions of gas and solid particles (drag forces), solid particle-particle (collision forces) phases, and solid particle-wall [129]. Either both phases in a multiphase flow have been extensively expressed by Eulerian governing equations [130] or mixtures of discrete particle and continuum gas phases have been modelled by the combination of Lagrangian (for particle phase) and Eulerian (for fluid phase) approaches [131]. Particle-laden rarefied gas flows can be commonly found in different applications such as the manufacturing of semiconductors and microelectromechanical systems (MEMS). Another notable example is that a fired solid-propellant thruster's plume in a low pressure environment consists of a mixture of unburnt solid particles such as  $\text{Al}_2\text{O}_3$  and a rarefied gas flow. The prediction of the physics of these carried solid particles becomes crucial due to their radiative properties and their significant contribution to the mass in the plume. Herein, the question “*How can a mixture of rarefied gas and solid particle flow be simulated?*”, becomes increasingly relevant.

Another challenge with gas-solid flows is the classification of inter-phase coupling by the interaction of the phases with each other. Elgobashi [132] classified the inter-phase coupling modes using the solid volume fraction,  $\varepsilon_s$ . In one-way coupling, the gas phase affects the solid particle movements for very small inertia. In addition, the fluid phase is considered pure flow, therefore, hydrodynamical forces affect the motion of solid particles. In this case, the solid particle-particle interactions are assumed to be negligible. In two-way coupling, the effects of the solid particle phase become significant on the fluid phase, which is now considered to be affected by the existence of the solid particles. In four-way coupling, in addition to fluid-solid particle interactions, solid particle-particle interactions are crucial. That is why a multilevel approach should be applied to predict the fluids behaviour at different levels [133]. In addition to aforementioned inter-phase modes, the change in the rarefaction level of carrier gas flows according to inter-phase modes is also summarised in Figure 5.1.

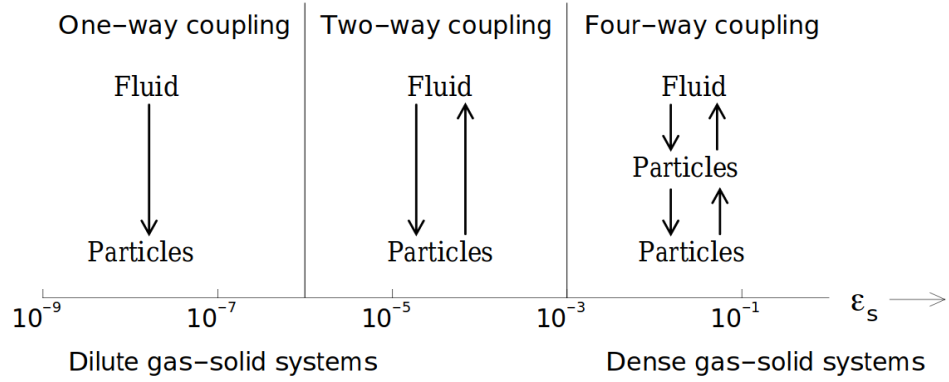


Figure 5.1: The alteration in phase of gas flows according to inter-phase coupling modes [132].

The gas flow phase in one-way coupling systems may be rarefied. Increasing the density of gas flow phase alters the inter-phase coupling modes. For this reason, the modelling of multiphase flows, which is the mixture of gas flows and solid particles, can be considered in different scales from micro to macro levels. For instance, micro-scale approaches are used to simulate the particle-laden flows at the particle level, and at the meso-scale, the modelling is based on Eulerian formulations. The macro-scale (or engineering model) is described by using empirical or semi-empirical correlations.

## 5.2 Modelling of Multiphase Flows

This section addresses some prominent numerical models for the simulation of multi-phase flows.

### 5.2.1 Two-Fluid Model

The gas and solid phases at the large scale can be modelled using a CFD-type Eulerian model. In this approach, both phases are treated as continuum flows and are considered as interpenetrating continua, therefore, constitutive equations are applied to evaluate the local averages. This model translates the mathematical expression of local mean variables to point level Navier-Stokes equations for the fluid phase and uses Newtonian equations of motion for the solid particles. Thus, the momentum balances for the gas and solid particle phases can be represented [134]. In the two fluid model, the balance of mass, momentum, and thermal energy equations formulate the conservation equations for both phases. The local averages of a phase are connected to the other phase and the interaction terms, momentum and energy transfer, and are represented in the balance equations. For instance, the continuity, momentum, thermal energy equations of fluid and solid phase are separately described for each phases as seen in the example Eqs. 5.1 and 5.2.

Continuity equation of the fluid phase:

$$\frac{\partial(\psi\rho_f)}{\partial t} + (\nabla\psi\rho_f\mathbf{u}) = 0. \quad (5.1)$$

Continuity equation of the solid phase:

$$\frac{\partial[(1-\psi)\rho_s]}{\partial t} + [\nabla(1-\psi)\rho_s\mathbf{v}] = 0. \quad (5.2)$$

In the previous governing equations, porosity is  $\psi$ , density is  $\rho$ , the fluid phase velocity vector is  $\mathbf{u}$ , and the fluid phase velocity vector is  $\mathbf{v}$ .

Eulerian/Eulerian approaches are also commonly used for dense solid particle flows to predict the particle-viscous and interparticle stresses using gradients of volume fractions. In volume fraction calculations, the local concentration of the fluid phase is determined at any time for a control volume [130]. To sum up,

although modelling using Eulerian approaches have low memory requirements and provide a simple two-way coupling [135], the method cannot be applied all types of fluid flows due to the breakdown of continuum relations as well as Ref. [135]’s statement that the application of Eulerian tracking for the solid particles is not suitable for a wide range of solid particle sizes.

### 5.2.2 Discrete Particle Method

An MD originated method was initiated in the 1950s by Alder and Wainwright [136]. Afterwards, Cundall and Strack [137] proposed the discrete particle model (DPM) or the discrete element model (DEM). This model monitors particles’ motions particle by particle and the particles’ interactions are investigated per contact. Therefore, the movement of each particle is tracked and the contact forces are calculated. The results from the particles are globalised and provide a propagation of the medium disturbances, which is a dynamic process. Therefore, the propagation speed is a function of the discrete particles’ movement. In most of the DPM technique applications, the interaction between fluid and solid phases are expressed by gas-phase dynamics that are based on Navier-Stokes equations, where a standard scheme is used to integrate the forces, which come from gas phase and solid particle collisions, on solid particles with a large order of magnitude gas flow. For this reason, a specification for drag force and collision calculation is needed for this level [133].

In these kind of classical methods, such as CFD-DEM, each solid particle in a large system and their collisions are tracked, and a discrete time-step, which should be 20-60 times smaller than the collision time, is set to resolve collisions in the domain. Due to the increase in computational expense because of collision tracking with a small time-step in Lagrangian solutions, either the use of supercomputers or development of simplified models becomes inevitable to speed up multiphase simulations at various concentration levels.

### 5.2.3 A Brief Summary of Eulerian-Eulerian and Eulerian-Lagrangian Models

Fundamental methods for the simulation of particle-laden multiphase flows have been discussed previously. The Eulerian-Eulerian multiphase model solves the volume averaged Navier-Stokes for both phases, where the solid particles are considered continuum. Although this approach improves the simulation efficiency, it brings additional complexities, for instance the size distribution of solid particles, constitution law application for granular flows, etc. The Eulerian-Lagrangian

model simplifies the equation of motion and tracks the movement of individual particles in a Lagrangian frame. However, the accuracy and computational expense of gas-like and solid-like simulations vary depending on the energy and concentration of the system. Last but not least, while the aforementioned models provide either Eulerian or Lagrangian solutions for the simulations of solid phase, the fluid phase is solely modelled by the employment of Eulerian approaches. These methods may not be capable to solve the expansion of particle-laden rarefied gas flows in a high vacuum environment with sufficient accuracy. As Ref. [138] in [135] suggests, a DSMC based approach provides higher accuracy even at higher Knudsen numbers, as well as direct modelling at the molecular level, and unconditionally stable solutions.

#### 5.2.4 Modelling of Transport of Solid Spherical Particles in a Rarefied Gas Flow

This multiphase flow consists of two main components, where rarefied gas flows are assigned as a carrier phase, and transport solid particles. As mentioned in detail in Chapter 2, the DSMC method is a prominent and successful approach to simulate the motion of gas particles and provides a solution to the Boltzmann equation. Furthermore, the predisposition of DSMC to couple with other techniques gives an advantage to extend the method for the interpretation of physics of solid particles by specifying them as computational particles. In this way, the properties of solid particles, such as their mass, diameter, velocity, position etc, can be specified in a similar manner to how gas atoms/molecules are represented. Herein, the difference in the definition of gas molecules and solid particles should be emphasised; for the gas phase, the change in internal energy between the different modes and velocity take place as a result of inter-molecular collision between gas molecules, the energy, velocity and temperature change in the solid particle phase can be observed through collisions of gas molecules and solid particles, where solid particle-solid particle collisions do not exist in the current work as the solid particle phase is assumed to be a free-molecular flow with respect to the gas mean free path, i.e. the Knudsen number based on the gas mean free path and the solid particle diameter is free-molecular. Note that this does not mean that the gas phase itself is necessarily free-molecular and gas-phase collisions are still an important mechanism that must be accounted for in the typical DSMC manner. Finally, Gallis [139] states that a rarefied gas flow system with small distributed particles in a large scale rarefied gas flow creates a locally free-molecular regime around the solid particles, where the force and heat transfer on the solid

particles due to the gas molecules ought to be calculated. The progress in the numerical approaches on the transport of solid particles by the rarefied gas flow can be listed below as per Ref. [139].

- First, Epstein [140] calculated the drag force on the solid particle using the thermal speed while the gas regime employs the Maxwellian molecular velocity distribution function. In addition, the reflections of gas molecules from the solid particle are considered as either specular or diffuse isothermal or linear combinations of both these reflection modes.
- Baines [141] enhanced Epstein's approach for solid particles at arbitrary velocities.
- The thermophoretic force of a spherical solid particle while it is motionless in a gas, employing the Chapman-Enskog molecular velocity distribution function, was calculated by Waldmann [142]. This temperature gradient based approach presents the same force for those aforementioned reflection models, which are specular, diffuse isothermal, or a linear combination of these reflections.
- An advancement to Waldmann's approach was proposed by Tablot *et al.* [143] in order to apply to tangential momentum.
- Lees [144] extended the calculation of thermophoretic force on a motionless spherical solid particle case for a problem where the gas regime travels at the free-molecular regime between two parallel plates while their temperature changes. While this solution uses the two-sided Maxwellian molecular velocity distribution function for the free-molecular rarefied flow, Philips [145] employed the same velocity distribution function as a limiting case in the two-half-range Chapman-Enskog molecular velocity distribution function.

Gallis [139] states that although all of these studies present a solution using continuum Maxwellian or Chapman-Enskog molecular velocity distributions as a initial point for the solution, a DSMC-based approach is necessary to calculate the force and heat transfer on a spherical solid particle, where the molecular distribution velocity of rarefied gas flows is not initially necessary to start the solution. The one-way simulation of particle-laden rarefied gas flow using DSMC can be categorised into those for monatomic and polyatomic gas flows.



### Particle-laden monatomic rarefied gas flows

In this section, a method proposed by Gallis [139] for the determination of the force and heat transfer on a spherical solid particle by a monatomic rarefied gas flow with an arbitrary molecular velocity distribution function is expressed. In addition to the spherical shape of solid particles, the following is assumed regarding the solid particles:

- small with respect to the mean free path length of gas,
- small with respect to any length scale of a gas flow,
- at a uniform temperature,
- and adequately dilute in order to allow for it to be affected by gas molecules but the gas molecules are not affected by the motion and presence of the solid particles. Moreover, the Brownian fluctuations are neglected, which means that the suspended solid particles in a rarefied gas flow do not show random motions, because the solid particles are considered to be much heavier than the gas molecules.

Gallis [139] expresses that this approach for monatomic rarefied gas flows is developed with the combination of Maxwell [12] and Lord [146]’s gas-surface interaction models, where “integrals of the force and heat-transfer Green’s functions over the molecular velocity distribution function” [139]. The forces on,  $\mathbf{F}[f]$ , and heat transfer to,  $Q[f]$ , the solid particles can be calculated as

$$\mathbf{F}[f] = \int \mathbf{F}_\delta[\mathbf{c}]f[\mathbf{c}]d\mathbf{c}, \quad (5.3)$$

and

$$Q[f] = \int Q_\delta[\mathbf{c}]f[\mathbf{c}]d\mathbf{c}, \quad (5.4)$$

where  $\mathbf{c}$  is the relative velocity of gas molecules to solid particles,  $\mathbf{c} = \mathbf{u}_g - \mathbf{u}_p$ , and  $\int f[\mathbf{c}]d\mathbf{c} = 1$ . The integration is over all gas particles in the same computational cell as the solid particle under consideration. These expressions provide a linear superposition for the locally free-molecular solid particle system while gas molecules have various velocities. The Green’s functions calculate the force and heat transfer on the solid particles from the momentum change, e.g. addition and removal, and energy change by the reflection of gas molecules, e.g. specularly, isothermally, and adiabatically.

The force-Green’s function is the sum of these four processes [139]:

1. Delivery of momentum from gas molecules to solid particles.
2. Removal of momentum by specularly reflected gas molecules.
3. Removal of momentum by isothermally reflected gas molecules.
4. Removal of momentum by adiabatically reflected gas molecules.

Hence, the force-Green's function can be written as

$$\mathbf{F}_\delta[\mathbf{c}] = \frac{mN_g(\pi r_p^2)}{V_{cell}} \mathbf{c}_r \left[ \left( 1 + \frac{4}{9}(1 - \varepsilon_p)(1 - \alpha_p) \right) |\mathbf{c}_r| + \frac{\sqrt{\pi}}{3}(1 - \varepsilon_p)\alpha_p c_p \right], \quad (5.5)$$

where  $m$  is the mass of gas molecules,  $N_g$  is the number of real gas molecule represented by a DSMC simulator,  $r_p$  is the radius of solid particles,  $V_{cell}$  is the computational cell volume,  $\mathbf{c}$  is relative velocity,  $c_p$  is the solid particle thermal speed, which is  $c_p = (2k_B T_p)^{1/2}$ ,  $k_B$  is the Boltzmann constant,  $T_p$  is the solid particle temperature, while  $\varepsilon_p$  and  $\alpha_p$  are the fractions of specularly and isothermally diffuse reflected gas molecules, respectively.

The heat-transfer-Green's function is also the sum of the following four processes [139]:

1. Delivery of energy from gas molecules to solid particles. This corresponds to the momentum exchange rate, where the momentum of gas molecules,  $m\mathbf{c}$ , is replaced by their translational kinetic energy,  $m|\mathbf{c}|^2/2$ .
2. & 4. The summation of specularly and adiabatically reflected energy loss of gas molecules is  $\{\varepsilon_p + (1 - \varepsilon_p)(1 - \alpha_p)\}$ , where the translational kinetic energy of a gas molecule does not vary by these specularly and adiabatical reflections.
3. Removal of energy by isothermally reflected gas molecules equals to “the rate at which molecules are reflected isothermally multiplied by the ratio of the energy flux to the number flux of a half-Maxwellian molecular velocity distribution function at the [solid] particle's temperature,  $T_p$ ” [139].

The summation of these four expressions yields the heat-transfer-Green's function,

$$Q_\delta[\mathbf{c}] = (1 - \varepsilon_p)\alpha_p \frac{mN_g(\pi r_p^2)}{V_{cell}} |\mathbf{c}_r| \left( \frac{1}{2} |\mathbf{c}_r|^2 - c_p^2 \right), \quad (5.6)$$

which directly depends on isothermal reflections. Therefore, heat transfer becomes zero when  $\alpha_p = 0$ .

### Particle-laden polyatomic rarefied gas flows

In this section, Burt and Boyd [147]’s pioneering approach is explained for the calculation of force on and heat transfer to solid particles by polyatomic molecules with rotational energy. Herein and thereafter, the term polyatomic is used for diatomic and polyatomic gas molecules for simplicity. This method considers that the solid particles are [135]

- spherical,
- chemically inert,
- small enough - in this way, the solid particles can be solely influenced by gas molecules in the same computational cell.
- considered to be much heavier than gas molecules, therefore, the Brownian motion of solid particles is neglected, which means that the suspended solid particles in a rarefied gas flow do not show random motions, because the solid particles are considered to be much heavier than the gas molecules.

Burt [135] states that the solutions in the literature for particle-laden rarefied gas problems generally include solely specular and isothermal diffuse reflections, and proposes that the gas-solid interactions can be accurately modelled irrespective of adiabatic diffuse reflection as obtained in Epstein’s study [140]. Consequently, the modified expressions for polyatomic gas-solid particle one-way coupling interactions are derived, which involve the various energy modes of gas molecules such as translational, rotational, and vibrational as well as the isothermal diffuse reflection, while the gas molecules are fully accommodated to the solid particle temperatures [135]. However, Burt and Boyd [148] then report that the effect of the vibrational mode of polyatomic gas molecules on a solid particle can be neglected, therefore, the internal energy in the expressions for the inter-phase coupling is replaced by the rotational energy term. Thus, the corresponding force on the solid particle by polyatomic gas molecules can be calculated as [147]

$$\mathbf{F}_\delta [\mathbf{c}] = \frac{N_g (\pi r_p^2)}{V_{cell}} \left( m |\mathbf{c}_r| + \frac{\wp}{3} \sqrt{2\pi m k_B T_p} \right) \mathbf{c}_r, \quad (5.7)$$

and

$$Q_\delta [\mathbf{c}] = \frac{N_g (\pi r_p^2) \wp |\mathbf{c}_r|}{V_{cell}} \left( \frac{1}{2} m |\mathbf{c}_r|^2 + e_{rot} - \left( 2 + \frac{1}{2} \zeta_{rot} \right) k_B T_p \right), \quad (5.8)$$

where  $\wp$  is the solid particle thermal accommodation coefficient,  $e_{rot}$  is the rotational energy of an individual gas molecule,  $\zeta_{rot}$  is the number of rotational degree of freedom, and  $m$  represents the mass of a single gas molecule. Burt [135] emphasises that  $\wp$  is equal to a part of inter-phase collisions including diffuse reflection, however the remaining fraction of collisions can be expressed as  $1 - \wp$ , which comprises of specular reflection.

### 5.3 Computational Code Development

Particle-laden rarefied gas flow solvers are not as common as DSMC ones. Furthermore, most of the existing solvers are either in-house codes or not available for general public use. Therefore, in order to predict the physics of one-way coupling problems for rarefied multiphase flows, an open-source object-oriented C++ based solver, *rarefiedMultiphaseFoam*, is developed within the framework of OpenFOAM-2.4.0-MNF. The solver is freely available under the GNU GPL3 license. A pre-existing DSMC code, *dsmcFoam+*, released within OpenFOAM-2.4.0-MNF has been extended to add new capabilities in order to solve two-phase rarefied flows.

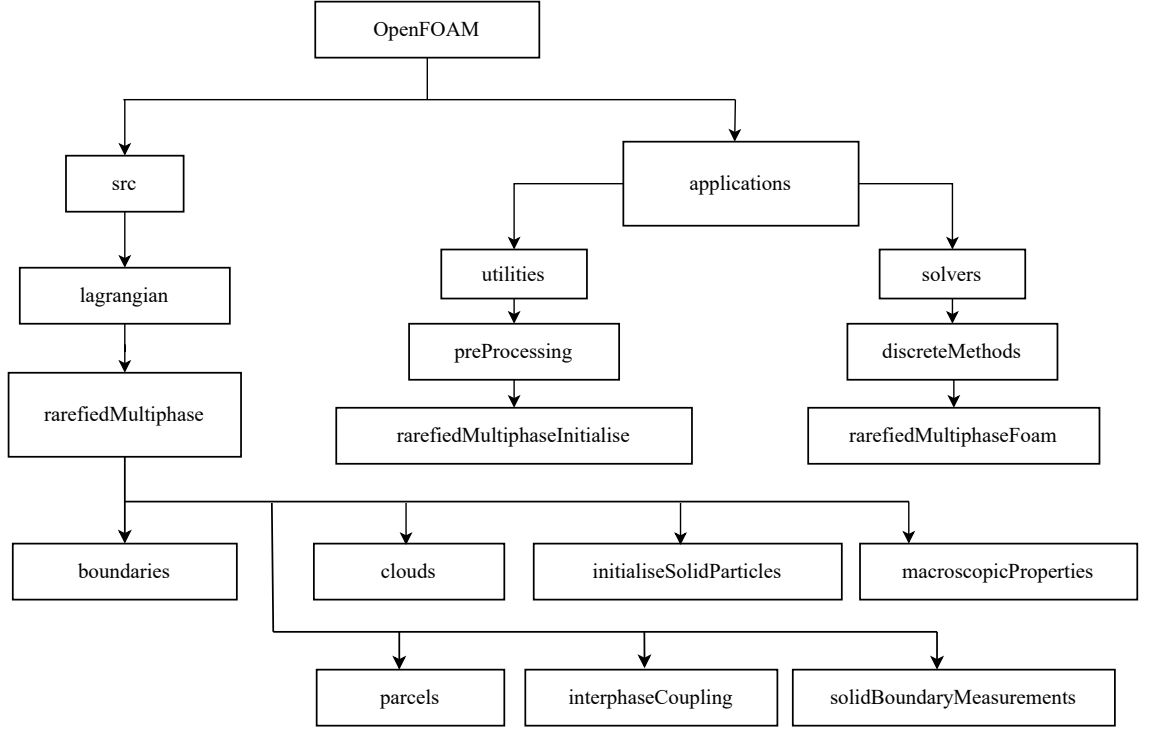
The fundamental features of *dsmcFoam+* are employed to capture the inter-molecular collisions and track the variables of the gas cloud. New *base* and *derived classes* are also developed to predict the inter-phase coupling and particle motion for the solid cloud. The *rarefiedMultiphaseFoam* directory structure is presented in Figure 5.2.

In each computational cell, which contains gas molecules and solid particles, the force and energy created by all DSMC molecules in a cell are summed. Firstly, the number of attempted DSMC particles to collide with a solid particle is selected within the same computational cell by the modified no-time-counter method [148] as shown in the following:

$$n_s = \frac{N_p n_g \pi r_p^2 (|\mathbf{c}_r|)_{\max} \Delta t}{V_{cell}}, \quad (5.9)$$

where  $N_p$  is the actual number of solid particles represented by one computational solid particle in the cell,  $n_g$  is the number of DSMC particles in the cell and  $|\mathbf{c}_r|_{\max}$  is the maximum pre-collision relative speed between solid particles and DSMC particles over a large number of time-steps. According to Ref. [148], the collision of DSMC and solid particles can be conducted if

$$\pi r_p^2 |\mathbf{c}_r| / (\pi r_p^2 |\mathbf{c}_r|)_{\max} > \mathfrak{R}_f, \quad (5.10)$$

Figure 5.2: Directory structure of *rarefiedMultiphaseFoam*.

where  $\mathfrak{R}_f$  is a randomly generated number in the interval of  $[0,1)$ . Afterwards, the gas data is passed to the solid particles in order to initiate and update the solid particle variables. The velocity and temperature of solid particles are updated as expressed below:

$$\mathbf{c}_p(t + \Delta t) = \mathbf{c}_p(t) + \frac{\sum \mathbf{F}_\delta[\mathbf{c}] \cdot \Delta t}{m_p}, \quad (5.11)$$

and

$$T_p(t + \Delta t) = T_p(t) + \frac{\sum Q_\delta[\mathbf{c}] \cdot \Delta t}{c_{sp}m_p}, \quad (5.12)$$

where  $c_{sp}$  is the solid particle specific heat,  $m_p$  is the solid particle mass,  $t$  is the current computational time and  $\Delta t$  is the time-step. Once solid particles are accelerated by applying Newton's second law, the velocity is updated using the Leapfrog method. During the inter-phase collision, there are some assumptions taken into considerations as listed below:

- The solid particles are spherical.
- The temperature of solid particles is spatially uniform, where no temperature gradient cannot be obtained between the solid particles.

- The volume of gas molecules are smaller than that of the solid particles. Furthermore, the local Knudsen number of solid particles, which is the ratio of mean free path of gas molecules to the diameter of solid particles, is greater than or equal to order one. This allows for the application of the locally free-molecular assumption and the negation of the effect of collisions between the incident and reflected molecules [148].
- There is no mass change between the gas and solid phases such as absorption, adsorption, etc.

### The general solution procedure of *rarefiedMultiphaseFoam*

Much like conventional CFD and DSMC simulations, a computational mesh is created by OpenFOAM's meshing tools such as *blockMesh* and *snappyHexMesh* to specify the physical extent of gas and solid phases in a domain. As aforementioned, in order to capture the inter-molecular collisions between gas molecules, the size of computational cells are decided as a fraction of the mean free path of the gas molecules. Furthermore, the time-step is also selected in the same manner, where the mean collision time of the gas molecules becomes the limiting parameter - as previously mentioned in § 5.2.4, the gas phase itself does not need to be free-molecular in this solver.

The boundary conditions of the domain created are specified as in two groups for gas and solid phases. While the gas phase employs the default *dsmcFoam+*'s boundary conditions, there are various types of boundary conditions derived for the solid phase as well such as inlet, outlet, inflow, cyclic, wall, etc. These general boundary conditions work with the same approach of the DSMC ones, for instance the outlet patch is a deletion patch upon arrival of solid particles, as in *dsmcFoam+*. However, some customised boundary conditions are also coded for the solid particle-wall interactions simulations, as listed in the following:

1. **Specular Wall Patch (*solidSpecularWallPatch*):** The solid particles hit the wall with a velocity and reflect back from the boundary with the sign of the normal component of the velocity inverted; the tangential components remain unchanged when the coefficient of restitution of the solid particles is equal to 1.
2. **Diffuse Wall Patch (*solidDiffuseWallPatch*):** The solid particles hit the diffuse wall with a velocity and reflect back with a new coefficient of restitution, which is calculated as a function of the incident velocity to the diffuse wall by using the mechanical properties of solid particles. A method

described in Ref. [149] is implemented to apply the relation between the solid particle incident velocity to the wall and the change in the coefficient of restitution. Jackson *et al.* [149] propose that if  $0.0005 < \varepsilon_y < 0.01$  and  $0.2 < \eta < 0.45$ , two empirical equations can be employed to calculate the new coefficient of restitution as shown below:

For  $0 < V_1^* < 1$

$$e = 1; \quad (5.13)$$

For  $1 < V_1^*$

$$e = 1 - 0.0361(\varepsilon_y)^{-0.114} \ln(V_1^*) (V_1^* - 1)^{9.5\varepsilon_y}; \quad (5.14)$$

where  $\varepsilon_y$  is the ratio of yield strength to elastic modulus ( $S_y/E$ ) and  $\eta$  is the Poisson's ratio of solid particles.  $V_1^* = V_1/V_c$ , where  $V_1$  is the magnitude of the solid particle velocity before hitting the wall and  $V_c$  is the critical velocity at the onset of plastic deformation.  $V_c$  can be calculated as

$$V_c = \sqrt{\frac{2U_c}{m}}, \quad (5.15)$$

with

$$U_c = \sqrt{\frac{(\pi C S_y)^5 R^3}{60 E'^4}}, \quad (5.16)$$

and

$$C = 1.295 \exp(0.736\eta), \quad (5.17)$$

where  $U_c$  is strain energy to cause the plastic deformation,  $m$  is the solid particle mass,  $C$  is the critical yield stress coefficient,  $R$  is the radius of hemispherical asperity and  $E'$  is the equivalent elastic modulus.

After calculating the coefficient of restitution,  $e$ , the reflected velocities of solid particles are updated by the normal,  $U_n$ , and tangential,  $U_t$ , velocities of solid particles.

$$\mathbf{U}_{solid_{reflect}} = e(U_n + U_t), \quad (5.18)$$

and the solid particle is reflected from the diffuse wall boundary surface with this new velocity.

3. **Adhesive Diffuse Heat Transfer Wall Patch (*solidRabinovicAdhesiveDiffuseHeatTransferWallPatch*):** The solid particles hit a diffuse wall with a velocity as in the diffuse wall patch. In this boundary condition, the effect of the temperature differences between the solid particles and wall, and the impact of viscoelasticity of solid particles are taken into account to calculate the heat transfer between solid particles and wall, and the viscoelastic losses during the collision of solid particles and wall boundary. Herein, some surface parameters play a crucial role on the heat transfer rate as proposed by Ref. [150], and adhesive force between the solid particles and surface due to the distance between the solid particles and surface, and the contact area as proposed by Refs. [151–153] in Ref. [154].

In order to calculate the adhesive force, Rabinovic *et al.*'s model [155], which is based on Rumpf's model [156], is applied as described in Ref. [154]. The adhesive force calculation formula of Rabinovic *et al.*'s model can be expressed as

$$F_{adh}^{Rabinovic} = \frac{A_H R}{6H_0^2} \left[ \frac{1}{1 + R/(1.48rms)} + \frac{1}{(1 + 1.48rms/H_0)^2} \right], \quad (5.19)$$

where  $A_H$  is the Hamaker constant,  $H_0$  is the separation distance,  $r$  is the radius of asperity,  $R$  is the solid particle radius, and  $rms$  is the root mean square of the surface roughness.

This boundary model then compares the adhesive force with the magnitude of solid particle force,  $mag(F_s)$ , to decide whether the solid particle sticks or reflects as per the procedure shown below:

- $F_{adh}^{Rabinovic} < mag(F_s)$ : If the solid particle is labeled as non-stuck, an instantaneous heat transfer during the contact time of the collision of a solid particle and wall. This boundary model applies an approach for the calculation of colliding heat transfer. The heat transfer model that is employed in this boundary condition is reached from Ref. [150]. The heat transfer between the wall and solid particles is a function of the thermal conductivity ratio,  $k'$ , and thermal diffusivity ratio,  $\alpha'$ , besides the effect of the Fourier number,  $nFo$ , i.e.  $f(Fo, \alpha', k')$  [150]. However, the materials of colliding particles and wall might be different in some cases. Therefore, the relative correction factor,  $\Xi$ , should be used, i.e.



$$\Xi(Fo, \alpha', k') = C(Fo, \alpha', k')/C(Fo, 1, 1), \quad (5.20)$$

with  $\alpha' = \alpha_{wall}/\alpha_{solid}$ , with  $\alpha_{wall} = k_{wall}/C_{pwall}\rho_{wall}$ , where  $\alpha_{wall}$  and  $\alpha_{solid}$  are the thermal diffusivities of the wall and a solid particle, respectively,  $k_{wall}$  and  $k_{solid}$  are the thermal conductivities of the wall and a solid particle, respectively,  $\rho_{wall}$  and  $\rho_{solid}$  are the densities of the wall and a solid particle, respectively,  $C_{pwall}$  and  $C_{psolid}$  are the specific heat of the wall and a solid particle, respectively; and  $k' = k_{wall}/k_{solid}$ . Equation 5.20 can be rewritten as

$$C(Fo, \alpha', k') = C(Fo, \alpha' = 1, k' = 1) \times \Xi(Fo, \alpha', k') \equiv \frac{e}{e_0}, \quad (5.21)$$

where  $e$  is the conductive energy transfer per impact, and  $e_0$  is the 2D asymptotic heat transfer calculation when  $Fo$  tends to zero. The result of the asymptotic analysis of the transient heat conduction equation for the two colliding objects of same materials, i.e.  $\alpha' = k' = 1$ , shows that the correction factor,  $C$ , has two limits depending on  $Fo$  [150]:

When  $Fo \ll 1$ :

$$C(Fo, \alpha' = 1, k' = 1) = 1 + 1.07646Fo, \quad (5.22)$$

When  $Fo \gg 1$ :

$$C(Fo, \alpha' = 1, k' = 1) = 0.605039 + 1.08748Fo^{1/2}, \quad (5.23)$$

Combining Equations 5.22 and 5.23:

$$C(Fo, 1, 1) \equiv g(Fo) \approx 0.605039 + \left[0.155994 + (1.182618 - 0.332298e^{-2Fo})Fo\right]^{1/2}. \quad (5.24)$$

The expressions of  $\Xi(Fo, \alpha', k')$ , and  $e_0$  can be calculated as

$$\begin{aligned} \Xi = 1 + & \frac{[0.95 Fo / (0.95 Fo + 0.5 Fo^{1/2} + 0.12)](\sqrt{\alpha'} - 1)}{1 + k'} + \\ & \left[1 - e^{-10(\log \alpha')^2}\right] \frac{0.0777}{0.7666 Fo^{-1/3} + Fo^{1/2}} (4k' / (1 + k')^2), \end{aligned} \quad (5.25)$$

where the characteristic impact Fourier number,  $Fo$ , can be calculated as

$$Fo = 2.9432752 \frac{\alpha_{solid}}{R\nu_{solid}}, \quad (5.26)$$

and Ref. [150] derived the heat transfer equation,  $e_0$ , by integrating the dimensionless heat flow rate,  $\dot{Q}^*(t)^*$ , over the entire collision period as

$$e_0 = \frac{C_0(T_{solid} - T_{wall})A_c t_c^{1/2}}{(\rho_{solid}C_{p_{solid}}k_{solid})^{-1/2} + (\rho_{wall}C_{p_{wall}}k_{wall})^{-1/2}}, \quad (5.27)$$

where the correction factor of  $C_0$  is 0.87093 for the same materials [150], and  $T_{wall}$  and  $T_{solid}$  are the temperatures of the wall and a solid particle, respectively. The maximum contact area,  $A_c$  can be calculated as

$$A_c = \pi R_c^2, \quad (5.28)$$

with

$$R_c = \left[ \frac{5m_{solid}R^2}{4E_{12}} \right]^{0.2} \nu_{solid}^{0.4}, \quad (5.29)$$

where  $R_c$  is the maximum contact radius,  $R$  is the radius of a solid particle,  $m_{solid}$  is the mass of a solid particle,  $\nu_{solid}$  is the normal vector of the velocity of a solid particle, and  $E_{12}$  can be calculated as

$$E_{12} = \frac{4/3}{(1 - \eta_{solid}^2)/E_{solid} + (1 - \eta_{wall}^2)/E_{wall}}, \quad (5.30)$$

where  $\eta_{wall}$  and  $\eta_{solid}$  are the Poisson's ratio of the materials of the wall and a solid particle, respectively, and  $E_{wall}$  and  $E_{solid}$  are the elastic modulus of the materials of the wall and a solid particle, respectively.

The total contact time,  $t_c$ , can be calculated as

$$t_c = 2\tau_c \left( \frac{5m_{solid}}{4E_{12}} \right)^{2/5} (R\nu_{solid})^{-1/5}, \quad (5.31)$$

where  $\tau_c = 2.9432752$ , which is a non-dimensional time when the contact area reaches the maximum value.

The different  $\Xi$  values for various types of materials can be calculated as a function of  $\alpha'$ :

◦  $\alpha' > 1$ :

$$\Xi(Fo, \alpha', k'), \quad (5.32)$$

◦  $\alpha' < 1$ :

$$\Xi(\alpha' Fo, 1/\alpha', 1/k'), \quad (5.33)$$

◦  $\alpha' = 1$ :

$$\Xi = 1. \quad (5.34)$$

Finally, the temperature of a hitting solid particle to the surface can be updated as:

◦  $T_{solid} > T_{wall}$ :

$$T_{solid_{reflect}} = T_{solid} - \frac{e\Delta t}{C_{p_{solid}} * m_{solid}}. \quad (5.35)$$

◦  $T_{solid} < T_{wall}$ :

$$T_{solid_{reflect}} = T_{solid} + \frac{e\Delta t}{C_{p_{solid}} * m_{solid}}. \quad (5.36)$$

where  $T_{solid_{reflect}}$  is the reflecting temperature of a solid particle, and  $\Delta t$  is the time-step. After updating the temperature of the solid particle due to it hitting the wall, the normal and tangential velocities of the solid particle are calculated by taking into account the coefficient of restitution as defined in the *solidDiffuseWallPatch* boundary condition as well as in order to update the reflecting velocity of a solid particles.

- $F_{adh}^{Rabinovic} > mag(F_s)$ : The solid particle is labeled as stuck. As the contact time of the solid particle approaches to infinity, the conductive heat transfer between the solid particle and the wall takes places until their temperatures become equal. When the conduction shape factor is considered, the calculation of heat transfer is modified from Table 4.1 in Ref. [157] as

$$q = 2\pi k_{solid} D_c (T_{wall} - T_{solid}), \quad (5.37)$$

where  $q$  is the steady-state heat transfer, and  $D_c$  is the contact diameter. Time for the stuck solid particle to reach the temperature of the wall can be calculated as

$$t = \frac{\rho_{solid} V_{solid} C_{p_{solid}}}{q} (T_{wall} - T_{solid}), \quad (5.38)$$

where the wall is considered as infinite, and  $V_{solid}$  is the volume of the spherical solid particle, which is  $D_{solid}^3/6$ . Afterwards, the normal and tangential velocities of solid particle are equalised to 0.

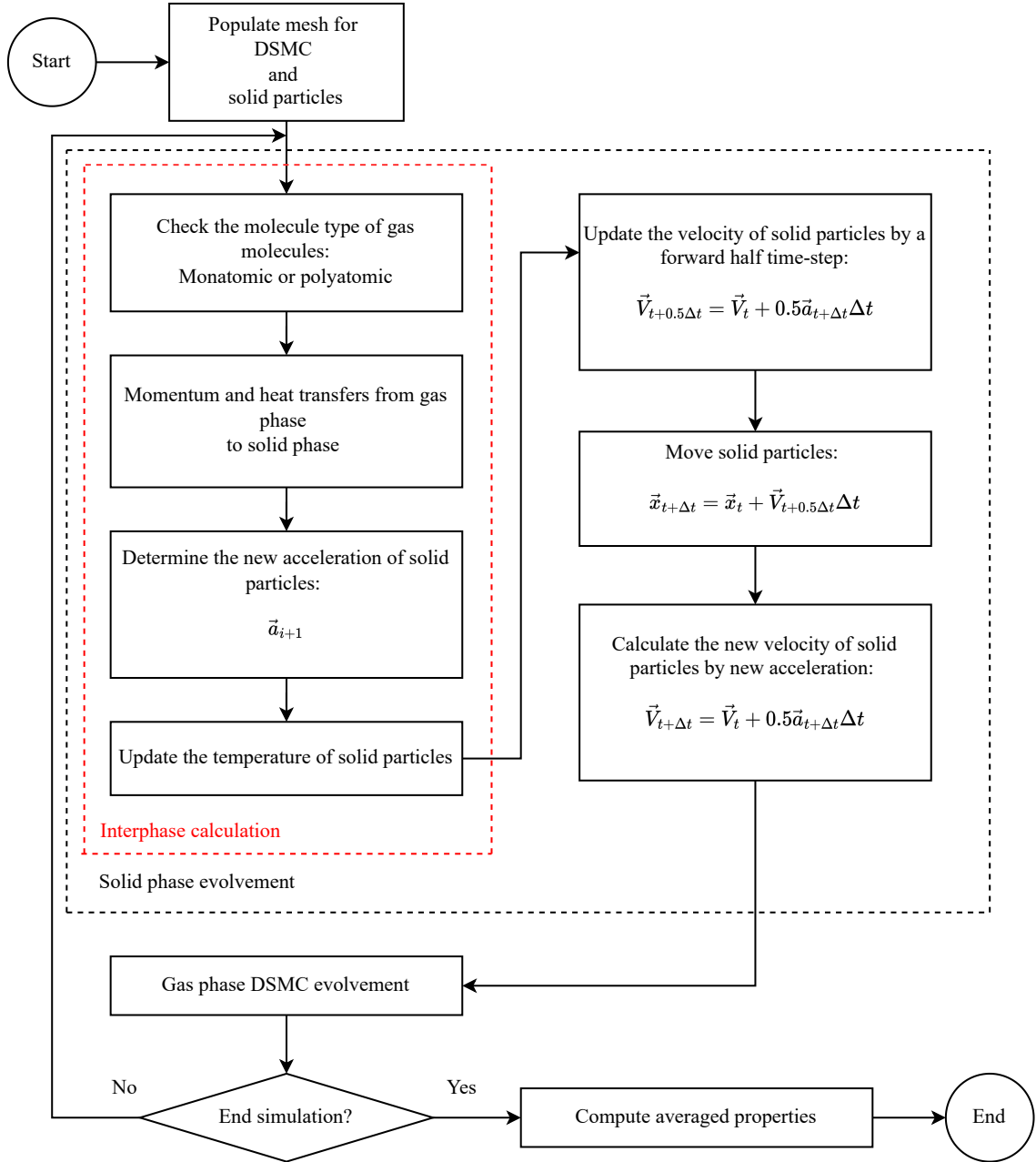
Following the mesh generation and prescription of boundary conditions, the following features of *rarefiedMultiphaseFoam* are run:

1. *rarefiedMultiphaseInitialise* - a pre-processing utility of the solver in order to create initial configurations and to populate DSMC particles with solid particles together in arbitrary geometries.
2. *rarefiedMultiphaseFoam* - Particle-laden rarefied gas one-way coupling solver.

As an overview, the algorithm of the *rarefiedMultiphaseFoam* solver can be shown in Figure 5.3.

The location of the utilities and solver are presented in Figure 5.2. The features of this *dsmcFoam+* based solver inherently consists of *dsmcFoam+*'s ones and the capabilities of the newly developed solver, *rarefiedMultiphaseFoam*, can be summarised as

- Steady and transient one-way coupling simulations,
- Parallelised computational code by the MPI (Message Passing Interface) libraries,
- Simulations in 0D, 1D, 2D (both planar and axisymmetric), and 3D,
- Newly developed boundary conditions for the solid phase,
- Newly developed inter-phase coupling model in order to calculate the momentum and energy transfer to solid particles from gas molecules.

Figure 5.3: The algorithm of *rarefiedMultiphaseFoam*.

Hereunder,

- Step 1. The solver firstly checks the type of gas molecule (monatomic vs polyatomic) and then chooses the solution approach among Gallis [139] and Burt & Boyd [147].
- Step 2. The inter-phase calculation of one-way coupling is executed to calculate how much momentum and heat is transferred to solid particles from gas molecules.

- Step 3. The velocities and positions of solid particles are updated using the Leapfrog method with a second order accuracy.
- Step 4. The evolution of gas phase is carried out using the DSMC algorithm of *dsmcFoam+* as shown in Figure 2.1.
- Step 5. The calculation of microscopic properties of gas and solid phases such as density, temperature, etc., i.e. sampling, is performed.
- Step 6. If the simulation is not concluded yet, the loop returns to Step 1 until it reaches the final time.

Thus, a newly developed solver, *rarefiedMultiphaseFoam*, for the simulation of particle-laden rarefied gas flows with one-way inter-phase coupling is introduced. In order to validate the solver, some benchmarking tests are carried out.

## 5.4 Benchmark Testing of *rarefiedMultiphaseFoam*

In this section, two main benchmark cases, which are an application of momentum and energy transfer to a solid particle from the surrounding gas phase, and the presence of a solid beam in a freely-expanded rarefied gas jet flow, are run to test the solver.

### 5.4.1 Benchmark Case A: Momentum and Energy Transfer from Gas Molecules to Solid Particles

The one-way coupling method, developed by Gallis *et al.* [139] for monatomic gas-solid interactions, then extended by Burt and Boyd [147] for polyatomic gas-solid particle interactions, is applied to determine the force,  $\mathbf{F}_\delta [\mathbf{c}]$ , and the heat flux,  $Q_\delta [\mathbf{c}]$ , on a stationary spherical solid particle using *rarefiedMultiphaseFoam*. Argon gas with the VSS collision model is selected for the rarefied gas phase. Bird [1] specifies the parameters of the VSS model for argon as;  $m = 66.3 \times 10^{-27}$  kg,  $\mu = 2.117 \times 10^{-5}$  kg m<sup>-1</sup>s<sup>-1</sup>,  $T_{ref} = 273$  K,  $\omega = 0.81$ , and  $\alpha = 1.4$ . The domain has a length  $L = 0.01$  m, split into  $100 \times 10$  square DSMC cells, as shown in Figure 5.4, with specularly reflecting surfaces at the top and bottom, i.e.  $\varepsilon_{wall3}$  &  $\varepsilon_{wall4} = 1$ . The inlet and outlet patches are defined as diffuse isothermally reflecting surfaces, i.e.  $\varepsilon_{wall1}$  &  $\varepsilon_{wall2} = 0$  and  $\alpha_{wall1}$  &  $\alpha_{wall2} = 1$  when  $T_{wall1}$  &  $T_{wall2}$  are 273 K.

### Benchmark Case A-1: Drag force ratio for a spherical solid particle in a Maxwellian distribution

A single solid particle is placed in the centre of the domain and assigned a velocity,  $u_p$ , of between 1 and 1000  $\text{ms}^{-1}$ . Since the aim in this set of simulations is to verify that the correct forces and energies are transferred to the solid particle, the solid particle is not allowed to move and the velocity and temperature are not updated. A computational cell is filled with 100 DSMC simulators for the statistical accuracy. The time-step is set as  $1 \times 10^{-7}$  s and the pressure is set as 13.33 Pa in order to ensure that the mean free path is smaller than the cell size of  $1 \times 10^{-4}$  m. The thermal speed of the argon gas is  $c_0 = (2k_B T m^{-1})^{1/2} = 337.2 \text{ ms}^{-1}$ .

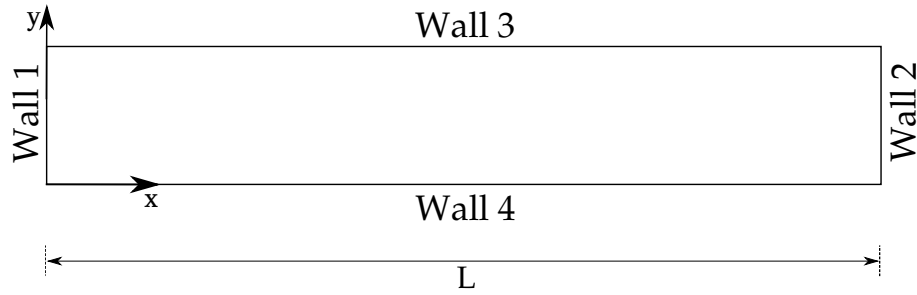


Figure 5.4: Computational domain and boundary conditions.

Figure 5.5 shows the drag force ratio (DFR) to solid particle speed ratio ( $u_p/c_0$ ). The DFR is a ratio between the drag force calculated from *rarefiedMultiphaseFoam*,  $\mathbf{F}[u_p, 0]$ , and from the Epstein drag force equation,  $\mathbf{F}_{Epstein}[u_p]$ , which is

$$\mathbf{F}_{Epstein} = -(mnc_0^2\pi r_p^2) \left\{ \left( \frac{8}{3\pi^{1/2}} \right) + (1 - \varepsilon_p) \left( \frac{T_p}{T_g} \right)^{1/2} \left( \frac{\pi^{1/2}}{3} \right) \right\} \left( \frac{\mathbf{u}_p}{c_0} \right), \quad (5.39)$$

where  $m$  is molecule mass,  $n$  is gas number density,  $r_p$  is the radius of a solid particle, and  $T_p$  and  $T_g$  are the temperatures of solid and gas phases, respectively. In Figure 5.5, the solid line represents the theoretical and numerical calculation of the DFR for the case when the solid particle and gas molecules are at the same temperature, i.e.  $T_p = T_g$ , and the dashed line presents another case where the solid particle temperature is set such that the heat transfer is zero between the solid particles and gas molecules, i.e.  $Q = 0$ . In order to achieve this,  $T_p$  and  $T_g$  are calculated from

$$Q = (mnc_0^3\pi r_p^2)(1 - \varepsilon_p) \left\{ k_1 \left[ \frac{u_p}{c_0} \right] - \left( \frac{T_p}{T_g} \right) k_2 \left[ \frac{u_p}{c_0} \right] \right\}, \quad (5.40)$$

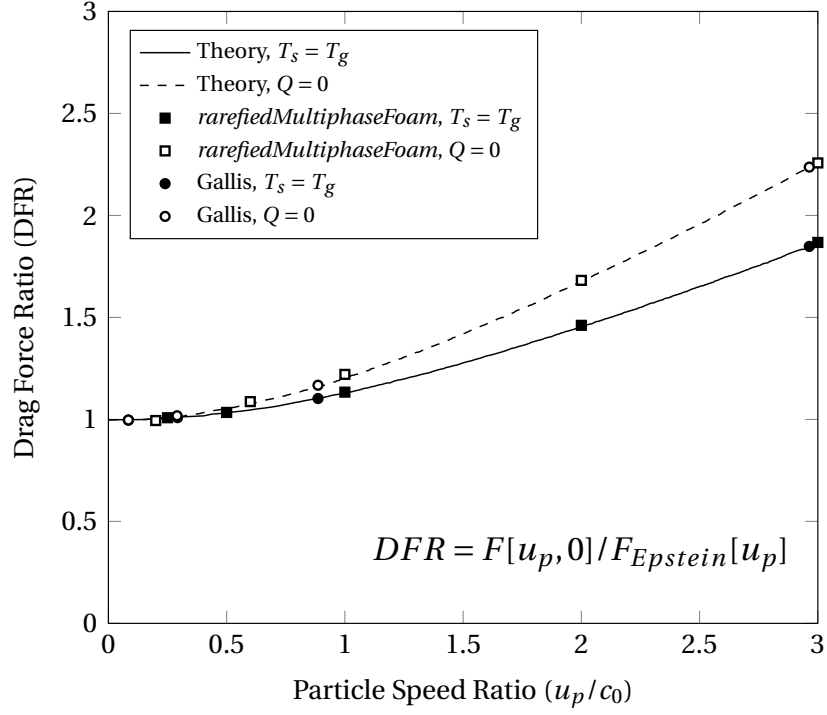


Figure 5.5: Drag force ratio for a spherical solid particle in a Maxwellian distribution.

with

$$k_1[s] = \frac{(3 + 12s^2 + 4s^4)erf[s] + (5 + 2s^2)serf[s]}{8s}, \quad (5.41)$$

and

$$k_2[s] = \frac{(4 + 8s^2)erf[s] + (4)serf[s]}{8s}, \quad (5.42)$$

where  $s = u_p/c_0$ . The error functions are calculated as

$$erf[s] = \left( \frac{2}{\pi^{1/2}} \right) \int_0^s \exp[-t^2] dt, \quad (5.43)$$

and

$$serf[s] = \left( \frac{2}{\pi^{1/2}} \right) \exp[-s^2]s. \quad (5.44)$$

The *rarefiedMultiphaseFoam* results are in excellent agreement with the previous numerical results of Gallis [139] and the analytical results.

### Benchmark Case A-2: Heat flux ratio for a spherical solid particle in a Maxwellian distribution

Similar to the measurement of the force above, heat transfer from gas molecules to a solid particle,  $Q[u_p, 0]$ , is computed in *rarefiedMultiphaseFoam* with the same computational domain -as shown in Figure 5.4- the same initial conditions, and



the same range of particle speed ratio ( $u_p/c_0$ ) as in Section 5.4.1. The heat flux ratio (HFR) is the normalised ratio of the computed heat transfer to the Epstein heat transfer,  $Q_{Epstein}[u_p]$ , which is

$$Q_{Epstein} = (mnc_0^3\pi r_p^2)(1 - \varepsilon_p) \left\{ \left( \frac{2}{\pi^{1/2}} \right) - \left( \frac{T_p}{T_g} \right) \left( \frac{2}{\pi^{1/2}} \right) \right\}. \quad (5.45)$$

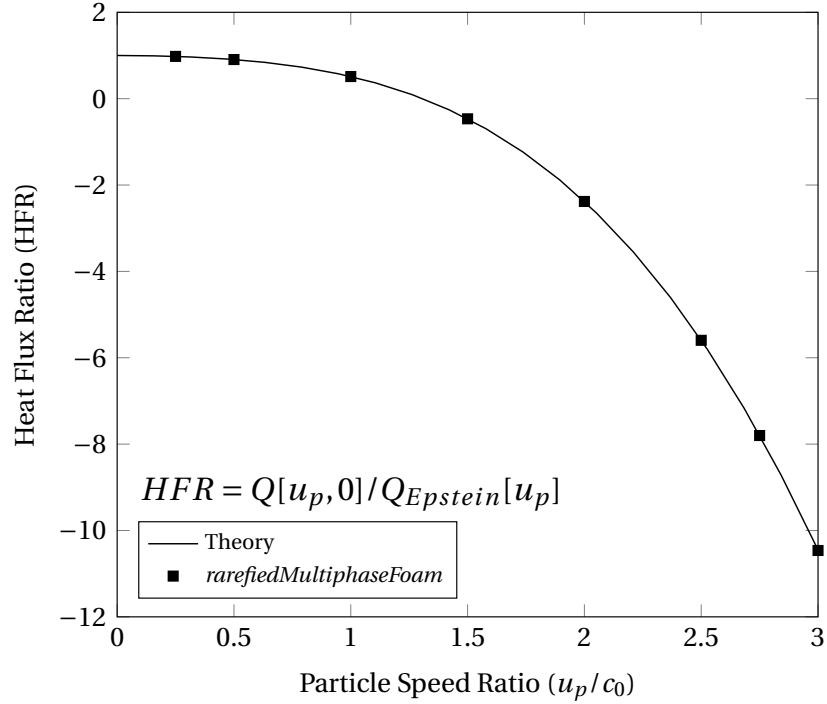


Figure 5.6: Heat flux ratio for a spherical solid particle in a Maxwellian distribution.

Figure 5.6 shows the trend of change in HFR with particle speed ratio. The solid line represents the theoretical calculation, and the squares the *rarefiedMultiphaseFoam* data. The newly developed solver successfully simulates heat transfer physics and provides the same results as those from previous numerical work and the established analytical theory.

### Benchmark Case A-3: A solid particle and surrounding gas molecules between hot and cold parallel plates

This case shows the calculation of thermophoretic forces on a solid particle created by the surrounding gas molecules positioned between two plates at different temperatures, i.e.  $T_{wall1} = 263$  K and  $T_{wall2} = 283$  K, and in a computational domain with a length of  $L = 0.01$  m as shown in Figure 5.4. In [139], eight intermediate cases between continuum [142] and free-molecular [145] limits are

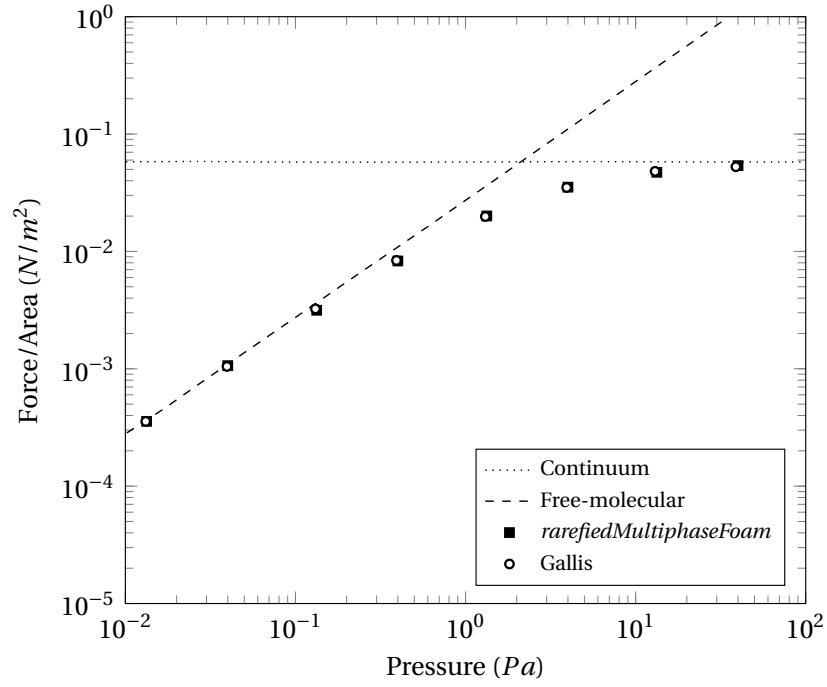


Figure 5.7: Thermophoretic force per unit area on a motionless spherical solid particle. The results of continuum [142] and free-molecular [145], as the two limiting regimes, are included for reference.

simulated by varying the pressure of argon between 0.01333 Pa and 40 Pa. The gas molecules are initialised at a temperature of  $T_g = 273$  K and the solid particle with a diffuse isothermally reflecting surface, i.e.  $\varepsilon_p = 0$  and  $\alpha_p = 1$ , is at the same initial temperature of the gas molecules, i.e.  $T_p = 273$  K. The numerical parameters and properties of the computational cells are summarised in Table 5.1. Similar to the previous two benchmark cases, the solid particle is not allowed to move and its temperature is not updated, as the aim is to measure the averaged thermophoretic force.

Figure 5.7 shows the thermophoretic force per cross-sectional area of a stationary solid particle at different pressures. The dashed and dotted lines present the continuum and free-molecular regime limiting values, respectively, the open dots Gallis *et al.*'s numerical results, and the solid squares the outcomes from *rarefiedMultiphaseFoam*. Even though the gas is stationary, there is a temperature gradient, so there will be a force in the continuum regime too, which is indicated in Figure 5.7. As is evident from the plot, force per unit area is between the limits in the transition regime and the results from *rarefiedMultiphaseFoam* are in excellent agreement with the limiting values and the previous numerical results.

Table 5.1: Parameters for the validation simulations of thermophoretic forces.

Pressure (Pa)	$\lambda$ (m)	N° of cells (x-axis)	N° of DSMC particles/cell	$\Delta x$ (m)	$\Delta t$ (s)
0.01333	$3.77 \times 10^{-1}$	100	100	$1.0 \times 10^{-4}$	$1.0 \times 10^{-7}$
0.04000	$1.26 \times 10^{-1}$	100	100	$1.0 \times 10^{-4}$	$1.0 \times 10^{-7}$
0.1333	$3.77 \times 10^{-2}$	100	100	$1.0 \times 10^{-4}$	$1.0 \times 10^{-7}$
0.4000	$1.26 \times 10^{-2}$	100	100	$1.0 \times 10^{-4}$	$1.0 \times 10^{-7}$
1.333	$3.77 \times 10^{-3}$	100	100	$1.0 \times 10^{-4}$	$1.0 \times 10^{-7}$
4.000	$1.26 \times 10^{-3}$	100	100	$1.0 \times 10^{-4}$	$1.0 \times 10^{-7}$
13.33	$3.77 \times 10^{-4}$	100	100	$1.0 \times 10^{-4}$	$1.0 \times 10^{-7}$
40.00	$1.26 \times 10^{-4}$	350	100	$2.9 \times 10^{-5}$	$3.0 \times 10^{-8}$

### 5.4.2 Benchmark Case B: Free expansion of two-phase jet flow

Two-phase jet flow free expansion simulations were performed in Ref. [147], using the MONACO rarefied gas solver, with the numerical outcomes being compared with the experimental results of Ref. [158]. As described in Refs. [147, 158], a mixture of air and latex particles is discharged into a vacuum environment through a convergent nozzle system. In the vicinity of the nozzle outlet, the particle-laden flow creates a solid particle beam. The formation of the solid particle beam is highly coupled with the stagnation pressure,  $P_0$ , of the carrier gas phase. In order to deduce the expansion angle,  $\Gamma$ , of the solid particle beam as a function of the source pressure, the area of the solid particle deposition downstream of the nozzle exit is measured.

Here, *rarefiedMultiphaseFoam* is applied to the same test case. In order to replicate the experimental setup and reduce the computational expense of the DSMC-solid particle simulations, an axisymmetric mesh configuration is prepared as shown in Figure 5.8. The inlet patch represents the nozzle inlet with a radius of 0.1352 mm, where an inflow boundary is defined. Since the nozzle wall is not parallel to the nozzle axis at the inlet, the velocity components of particles for both phases at the inlet boundary should be treated specially. The angle between the nozzle wall and the nozzle axis is defined as  $\chi$ , which is positive for a convergent nozzle and negative for a divergent nozzle. It is assumed that the inlet velocity angle varies linearly between 0 and  $\chi$  in the radial direction of the nozzle to calculate the velocity components. The converging part of the nozzle, with an angle of 3.25 degrees, is represented by a specularly reflecting wall until the

throat, which has a radius of 0.0785 mm. Afterwards, a square-like deletion patch is imposed to act as a vacuum outlet, representing the gap between the nozzle outlet and the skimmer inlet in the experimental setup. For the representation of the skimmer, an inclined and straight specularly reflecting wall is used. At the outlet patch, a vacuum boundary is assumed, such that both solid and DSMC particles are deleted. The total axial distance of the geometrical setup and the radius of the final outlet become 7 mm and 0.8 mm, respectively. This geometry is similar, but not identical to that used by Burt and Boyd, where the skimmer geometry was assumed unimportant and neglected.

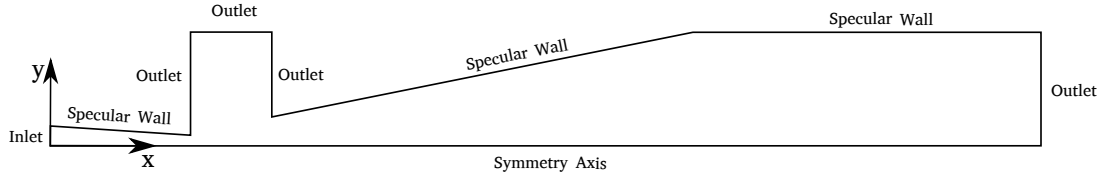


Figure 5.8: Computational domain of two-phase free expansion.

The gas phase is a mixture of 79%  $N_2$  and 21%  $O_2$  and is assumed to be a one-dimensional isentropic flow with a static temperature of 295.63 K and an axial speed of 69.176 m/s at the inlet. The gas number density is then calculated for the cases with various source pressure values,  $P_0$ , from 14 mmHg to 100 mmHg using the inflow pressure and temperature values. In addition to the effect of the source pressure on other flow parameters, the relative weight of the gas molecule,  $W_g$  changes from  $3 \times 10^8$  to  $6 \times 10^8$  as the stagnation pressure increases and the mean free path of the gas phase decreases with the increase in pressure. At the lower source pressures (14-35 mmHg), 50,000 computational cells are utilised, meanwhile for the higher source pressures (50-100 mmHg) 108,750 cells are employed.

In terms of initial conditions for solid particles, they are assigned a temperature of 298 K and it is assumed that their velocity is the same as the velocity of the gas particles, i.e.  $V_g = V_s = 69.176$  m/s. Three sizes of spherical latex with a diameter of  $d = 0.126 \mu\text{m}$ ,  $0.365 \mu\text{m}$ , and  $1.3 \mu\text{m}$  were used in the experiment. Ref. [159] states that the larger solid particles, with a diameter of  $1.3 \mu\text{m}$ , result in too low a Knudsen number. However, a conclusive trend cannot be obtained for the smaller solid particles with a diameter of  $0.126 \mu\text{m}$ . Therefore, the medium-sized solid particles with  $d = 0.365 \mu\text{m}$  were chosen for the simulation of the multiphase flow. It is assumed that these solid particles are heavy enough that Brownian motion can be ignored. The number density, density, specific heat, and thermal accommodation of the solid phase are specified as  $1.386 \times 10^{17} \text{ m}^{-3}$ ,

1,120 kg/m<sup>3</sup>, 2,180 J/kg K, and 0.89, respectively. The variations in gas number density and the number of equivalent gas and solid particles for different pressure values are summarised in Table 5.2, where the number of equivalent particles are the number of gas molecules, or the number of real solid particles, as represented by a single simulator solid particle.

Table 5.2: Simulations parameters of two-phase jet flow free expansion.

Source pressure (mmHg)	Gas phase number Density (m <sup>-3</sup> )		N° of equivalent particles	
	N <sub>2</sub>	O <sub>2</sub>	Gas	Solid
14	$3.8129 \times 10^{23}$	$8.8859 \times 10^{22}$	10,000	1
25	$6.4295 \times 10^{23}$	$1.5082 \times 10^{23}$	4480	1
35	$9.2599 \times 10^{23}$	$2.1721 \times 10^{23}$	6272	1
50	$1.2859 \times 10^{24}$	$3.0163 \times 10^{23}$	4444	1
75	$1.92885 \times 10^{24}$	$4.52445 \times 10^{23}$	6666	1
100	$2.5718 \times 10^{24}$	$6.0325 \times 10^{23}$	8888	1

The particle-laden flow is simulated with the VHS collision model and the LB model for the redistribution of energy between the translational and rotational modes in the gas phase. The number density of the latex particles is not specified in the experimental work and since the one-way coupling model is used in the current work, the actual number density specified will not influence the results and has been chosen simply to have sufficient number of solid particles to reduce the statistical scatter in the macroscopic measurements. Therefore, the multiphase flow properties are sampled for 90,000 time-steps after both the gas and solid phases reach the steady state.

The most important output of the simulations is the solid angle of the solid phase,  $\Gamma$ , which is a function of the source pressure of the gas phase. Axisymmetric simulations from *rarefiedMultiphaseFoam* over a range of source pressures and other initial parameters, given in Table 5.2, are conducted to investigate the change in the solid beam angle by source pressure. Figure 5.9 shows the trend in the number density of the solid phase and the formation of the solid beam trajectory from the nozzle to the outlet of the skimmer. A clear solid particle beam has formed, with a radius beyond which no solid particles escape from the beam. From the centre of the solid beam, a radial distance,  $r_0$ , is measured in the +y-axis direction until it reaches a sharp drop-off to zero, which can be identified as the edge of the beam. In turn, it is then possible to calculate the solid beam expansion angle as  $\Gamma = \pi r_0^2 / L^2$ , where  $L = 6$  mm.

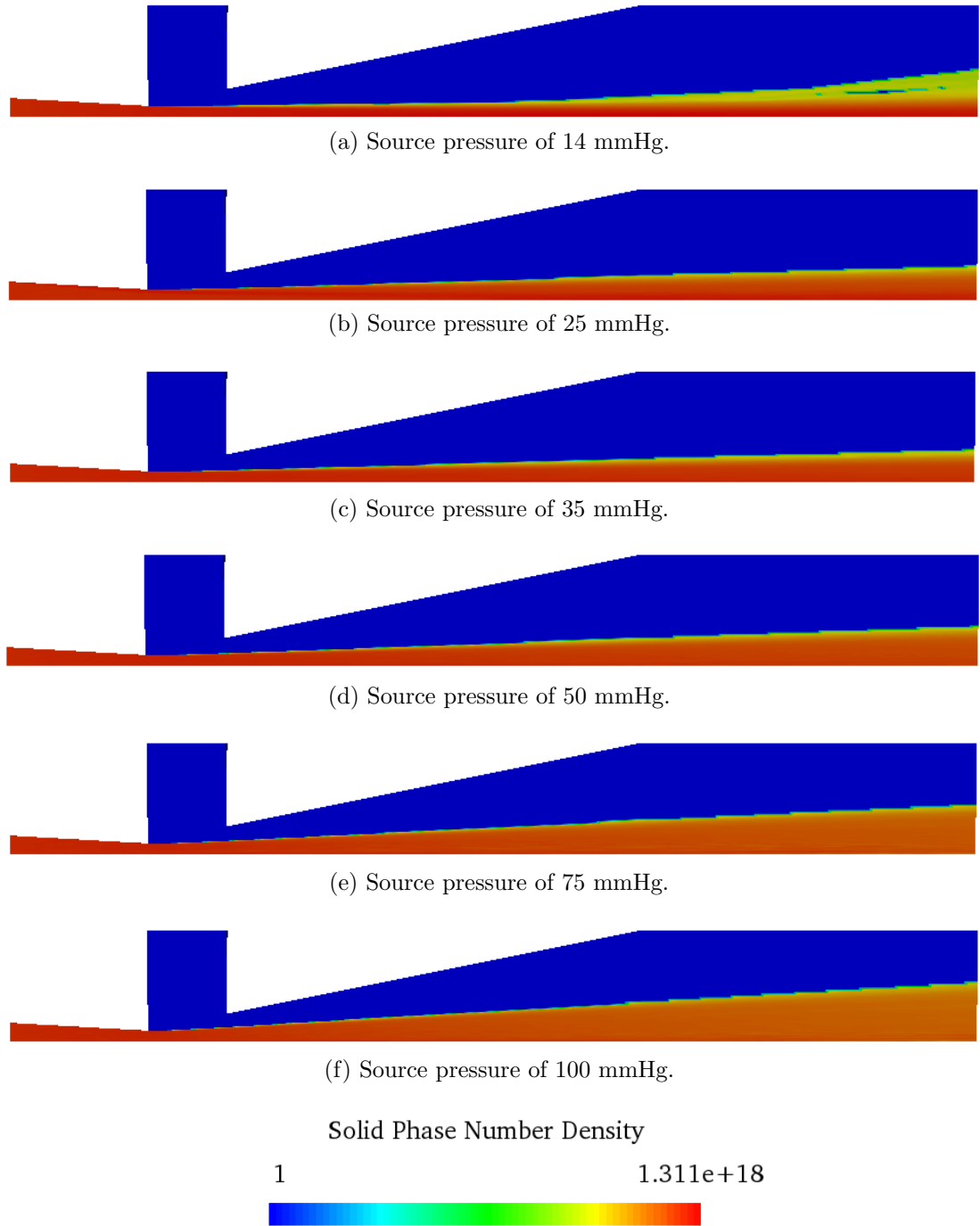


Figure 5.9: Free expansion of two-phase jet flow with varying source pressure, showing the formation of a solid particle beam.

Figure 5.10 shows the trend of the solid angle with source pressure from *rarefiedMultiphaseFoam* and experiment [158]. Although Burt and Boyd [147] have performed the same case, they state that their simulations failed to produce a distinct beam of solid particles, hence, a comparison cannot be made. Both numerical and experimental data show two major trends of  $\Gamma$ .

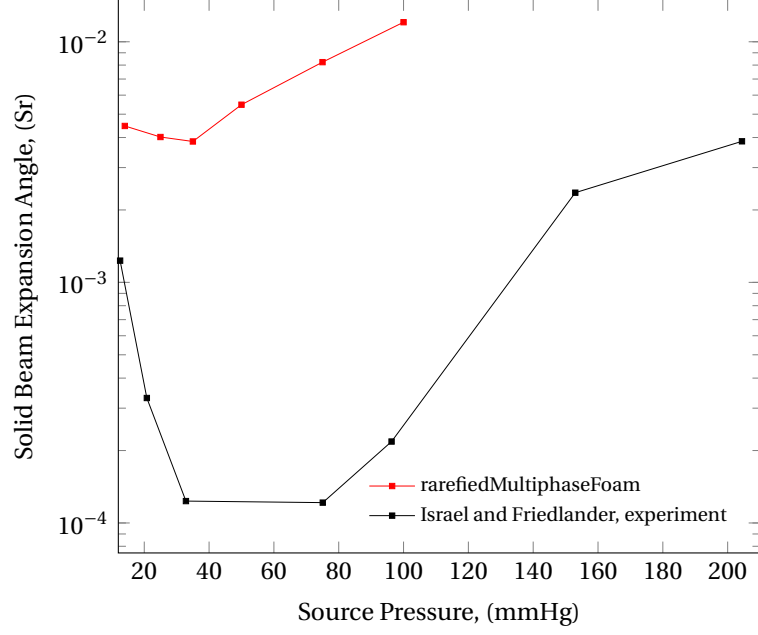


Figure 5.10: Solid angle variation with source pressure. Comparison of results from *rarefiedMultiphaseFoam* and experiment [158].

Firstly, a consistent reduction in beam size with an increasing  $P_0$ , starting from the lowest pressure 14 mmHg and reaching the minimum solid angle at 35 mmHg, is found. If the source pressure is allowed to increase, the beam size begins to expand. This is because when the gas freely expands in the high vacuum environment, the impact of the gas phase on the solid particles at the low source pressure is relatively small. Therefore, the solid particles tend to continue to travel in the same direction that they left the nozzle with. When the source pressure is increased to intermediate values, the particle inertia and drag forces oppose each other. For this reason, the solid particles then follow a trajectory which is parallel to the gas flow axis in the far-field where the beam size reduces. When higher source pressures are applied, the effect of the gas phase preponderates over the inertia of the solid particles. Thus, the gas particles lead the solid phase into an outward radial path in the far-field, where the expansion of the particle-laden flow increases [159]. The *rarefiedMultiphaseFoam* results give consistently higher solid angle values than the experiment, which may be for a variety of reasons, e.g. it is known that the nozzles used by Israel and Friedlander [158] were not perfectly circular in cross-section due to the limitations in manufacturing methods when the experiments were performed. Additionally, the exact distribution of solid particles along the nozzle cross-section is not known in the experiments, but has been assumed even in the numerical work. Considering these significant uncertainties, it is not expected that the numerical results will match the experiments exactly.

## 5.5 A Test Case: Surface Coating by the Aerosol Deposition Method

The Aerosol Deposition Method (ADM) is a widely used technology in coating applications such as MEMS, optical devices, fuel-cells, etc. [160] in order to create thin films on a substrate by the deposition of powder materials. In this technique, solid particles are aerosolised in an aerosol generation unit. Afterwards, the gas-powder mixture is fired towards a substrate by a nozzle. This process is carried out in a vacuum environment, which allows a coating process at room temperature without sintering [161] as the coating takes place by hitting solid particles upon the coating surface [160]. The schematic of the ADM is presented in Figure 5.11.

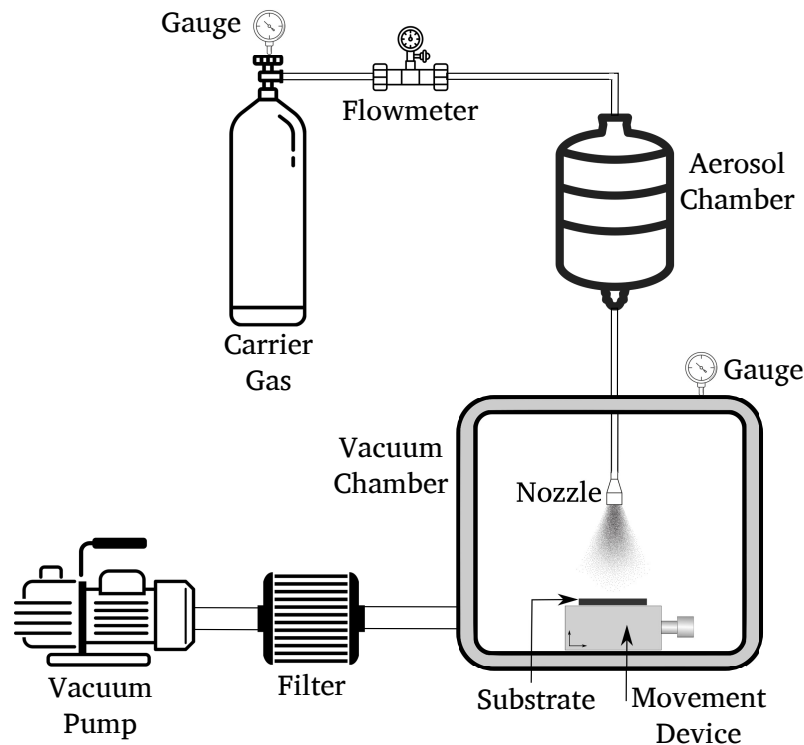


Figure 5.11: Schematic of an ADM application.

Previously, metals and ceramics were sprayed on substrates using evaporation systems and aerosol generators, respectively. This technique was called the Gas Deposition Method (GDM) [162]. Hanft *et al.* [161] states that GDM was evolved into the Jet Molding System (JMS) [163,164], which operates in a vacuum that enables the deposition of different materials. Following this development, ADM was proposed rather than the use of “gas deposition” since vaporisation is generally not used for aerosol generation [165]. Afterwards, this technique has advanced to become quite popular both in industry and academia [161].



The modelling of particle-laden rarefied gas flows has been studied to deduce the interphase interactions, the properties of the solid phase during the transport, the interactions of solid particles with surfaces, etc. Greendyke *et al.* [166] developed a DSMC-MD hybrid code, which is called **Hybrid Direct Simulation (HyDS)**, in order to simulate aerosol kinetics, i.e. (1) gas-gas molecule interactions, (2) interphase collisions, and (3) aerosol-aerosol interactions. In the test simulation, the particle sizes are selected between 30 nm and 260 nm by means of a truncated lognormal distribution. Although HyDS is a promising toolbox for the simulations of fluidised aerosol flows, the authors noted that the code needs improvements for the accuracy of calculations such as

- numerical round-off errors for the interphase collision correction factor,
- physical modelling such as thermal modelling correction for the accumulation of air molecules around the aerosol particles, etc.

Palaniswaamy and Loyalka [167] proposed various collisional sampling algorithms for the DSMC simulations of multi-component aerosol dynamics. Saldivar *et al.* [168] states that DSMC has been used to estimate the aerosol evolution rather than the use of deterministic methods for improving the fidelity of computational models. Therefore, authors develop new integral terms for various benchmarking cases such as coagulation, condensation, deposition, two-component aerosols, etc. Li *et al.* [169] studied the mass, momentum, and energy transfer from the aerosol particles to substrate by combining CFD and the particle trajectory model. Particle drag coefficients are used to simulate trajectories, where the neural network and DSMC data cooperate for the calculation of drag coefficients for various Knudsen numbers in a speed range from 0 to Mach 5. Kim *et al.* [170] proposed another hybrid technique of DSMC and all-atom MD for the simulation of coating of an alumina surface with yttria nanoparticles (YNPs). The method comprehends the correlations between the increment in the coating powder feed rate and the formation of the coating film microstructure by simulating the unsteady plasma spray process.

The various models for gas phase in rarefied regimes have also been applied in the literature to simulate the energy distribution, plasma application, etc. The *dsmcFoam+* code has been developed within the framework of OpenFOAM with powerful toolboxes and constantly updated rarefied gas modelling. Therefore, this subsection aims to build a new approach to develop a numerical solver using *rarefiedMultiphaseFoam*, which is a *dsmcFoam+* based solver, for the application of coating technology. Thus, *rarefiedMultiphaseFoam* is capable of simulating

one-way coupling multiphase flows, such as the transport of ceramic powders, metallic atoms, etc., and the solver is open to further development.

As a test case, aluminium particles are transported as a solid particle beam by the gaseous phase of the mixture of nitrogen and oxygen, which targets a substrate for coating. The computational domain in §5.4.2 is modified to replicate the transport of a solid particle beam by an expanding gas mixture in a vacuum environment. While the dimensional parameters and initial conditions of the benchmarking case in §5.4.2 are maintained, two main changes are carried out in the reference numerical setup. First, aluminium particles are replaced with the latex ones that were used in the previous simulation in §5.4.2. In addition, the changes in the boundary conditions are completed to create a convenient geometry for a coating problem. In the previous geometrical setup, the solid particle beam travels in the skimmer, which is surrounded by specular walls, then going through a deletion patch, i.e. outlet, and vacates the control volume. In this case, the outlet patch is replaced with an adhesive diffuse heat transfer wall patch. In addition, the specular wall adjacent to the outlet patch in the previous setup is altered as the outlet to provide the discharge of the carrier gas phase from the control volume. The adapted axisymmetrical geometrical setup is presented in Figure 5.12.

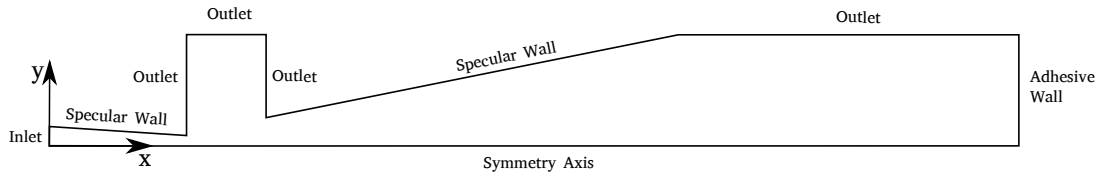


Figure 5.12: Computational domain of two-phase free expansion and sticking solid particle on a surface.

The simulation parameters, which are given in Table 5.2, are also maintained for the gas and solid phases. However, the solid particle is chosen to be aluminium in this case. The properties of aluminium are selected as shown in Table 5.3.

For the sticking solid particle simulation, a thermoplastic is selected as the substrate surface. This material is a good option in terms of being a heat-resistant 3D filament which can resist temperatures up to 100 °C. Thus, the heat transfer model between the sticking solid particles and the surface can be tested by using the temperature differences between the solid particles and substrate. The properties of the substrate are given in Table 5.4.

Table 5.3: Properties of aluminium particles.

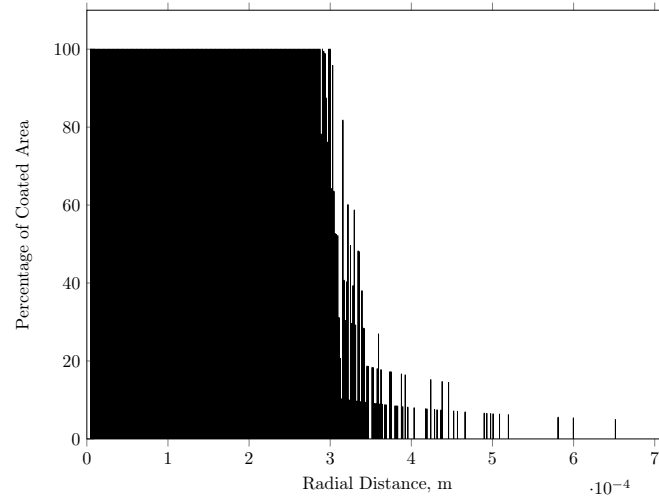
Particle Temperature, $T_{Al}$	300 K
Yield Strength, $S_{y(Al)}$	$1.7 \times 10^8$ Pa
Elastic Modulus, $E_{Al}$	$6.9 \times 10^{10}$ Pa
Poisson's Ratio, $\eta_{Al}$	0.334
Hamaker Constant, $A_H$	$1.5 \times 10^{-19}$
Seperation Distance, $H_0$	$2 \times 10^{-10}$ m
Radius of Hemispherical Asperity, $\mathcal{R}$	0.0025 m
Specific Heat Capacity, $c_{Al}$	$900 \text{ J kg}^{-1} \text{K}^{-1}$
Thermal Conductivity, $k_{Al}$	$88 \text{ W m}^{-1} \text{K}^{-1}$

Table 5.4: Properties of thermoplastic surface.

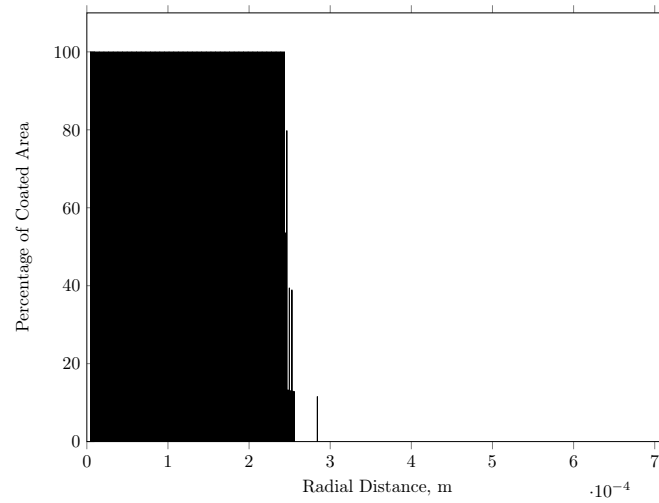
Wall Temperature, $T_{adhWall}$	323.15 K
Root Mean Square, $rms$	$5 \times 10^{-10}$ m
Elastic Modulus, $E_{adhWall}$	$2 \times 10^9$ Pa
Poisson's Ratio, $\eta_{adhWall}$	0.38
Material Density of Wall, $\rho_{adhWall}$	$1000 \text{ kg m}^{-3}$
Specific Heat Capacity, $c_{adhWall}$	$1750 \text{ J kg}^{-1} \text{K}^{-1}$
Thermal Conductivity, $k_{adhWall}$	$0.130 \text{ W m}^{-1} \text{K}^{-1}$

In terms of the initial conditions of the simulation, the gas phase is specified as a mixture of 79%  $\text{N}_2$  and 21%  $\text{O}_2$  with a static temperature of 295.63 K. The gas number density is calculated for the source pressures of 14 mmHg, 25 mmHg, and 35 mmHg. 50,000 computational cells are created for all three different source pressure simulations. It is assumed that the velocities of gas and solid particles are the same, i.e.  $V_g = V_s = 69.176 \text{ ms}^{-1}$ . The solid particles are defined as spherical with a diameter of  $5 \mu\text{m}$  and a number density of  $1.386 \times 10^{17} \text{ m}^{-3}$ .

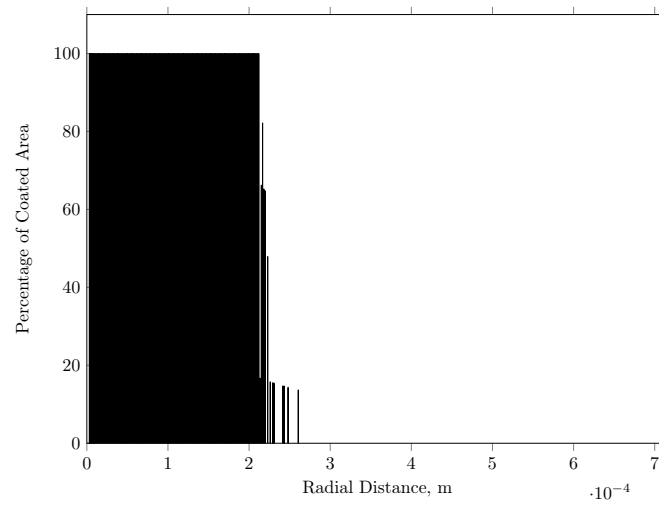
In order to investigate the number of stuck solid particles, the simulations are run until 0.001 s with a time-step of  $2 \times 10^{-9}$  s. Although the gas phase reaches a steady state condition soon after running the simulations, the solid phase shows a transient behaviour as the number of particles in the control volume constantly increases due to the stuck solid particles on the surface. In order to reduce the statistical scatter in the macroscopic properties, the multiphase flow properties are sampled for  $1 \times 10^6$  time-steps.



(a) Source pressure of 14 mmHg.



(b) Source pressure of 25 mmHg.



(c) Source pressure of 35 mmHg.

Figure 5.13: Deposition of aluminium particles on the substrate at  $t = 0.001$  s, showing the distribution percentage of solid particles throughout computational surface cells for the three different source pressures.

Figure 5.13 shows the percentage of solid particle distributions along the surface at the source pressures of 14 mmHg, 25mmHg, and 35 mmHg for the radial distance on the substrate surface from the stagnation point to the far-field vs the percentage of coated area, which is the covered area on each computational cell through the radial axis. The overall cell surface occupation in a radial distance and the source pressure are inversely proportional. In addition, the scattering of solid particles on the surface far-field can be also obtained by decreasing the source pressure. The extracted cell data of stuck solid particles shows two scattered solid particles in the far-field of the surface, which corresponds to the 415<sup>th</sup> surface cell at the source pressure of 14 mmHg. With the increase in the pressure, the scattering area decreases, e.g. two solid particles in the 180<sup>th</sup> surface cell at 25 mmHg, and one solid particle in the 165<sup>th</sup> surface cell at 35 mmHg. The distribution of the bulk number of stuck solid particles is narrowed with an increase in the number of stuck solid particles when the source pressure is increased. In addition to the bulk number of solid particle distribution, a higher number of stuck solid particles can be obtained in the near-field at the pressure of 35 mmHg. The properties of stuck solid particles due to changing pressure is shown in Table 5.5.

Table 5.5: Properties of stuck solid particles at changing source pressures, at  $t = 0.001$  s.

	14 mmHg	25 mmHg	35 mmHg
Number of stuck solid particles	60,115	69,237	74,290
Contact radius of stuck solid particles, m	$1.184 \times 10^{-6}$	$1.193 \times 10^{-6}$	$1.243 \times 10^{-6}$
Calculated coefficient of restitution	0.6611	0.6594	0.6507
Heat transfer rate, J	$3.836 \times 10^{-9}$	$3.828 \times 10^{-9}$	$3.861 \times 10^{-9}$

As seen from Table 5.5, the source pressure and the number density of stuck solid particles are proportional. The coefficient of restitution and contact radius are calculated by Equations 5.13, 5.14, and 5.29 when the solid particles hit the substrate surface. With the increase in contact area at a higher pressure, the heat transfer from the surface to solid particles increases and heat transfer time decreases in inverse proportion. However, there is negligible change in the heat transfer rate from the surface to each solid particle due to the change in the source pressure. As the volume of solid particles is assumed to be constant in the pre- and post-collision stages, the coating thickness also decreases by increasing the source pressure value.

## 5.6 Summary

This chapter presents a study on the one-way coupling interaction of rarefied gas flows and solid particles. In this type of multiphase flow, it is assumed that the rarefied gas regime is assigned as the carrier phase and the solid particle regime is transported. In addition, while the effect of the gas regime on the solid phase is considered, the effect of the solid phase on rarefied gases is not taken into account. Thus, particle-laden rarefied multiphase flows are built on this approach. In order to calculate the force and heat transfer on solid particles, which are spherical and chemically inert with small enough sizes to create a one-way effect, and heavier than gas molecules, the Green's function of force and heat transfer by monatomic and polyatomic rarefied gas regimes is employed. As the rarefied gas-solid particle multiphase flow is not as common as DSMC, the existing DSMC solver, *dsmcFoam+*, is extended to solve these types of two-phase flow problems. The newly developed *dsmcFoam+* based multiphase solver, *rarefied-MultiphaseFoam*, is comprised within the framework of OpenFOAM-2.4.0-MNF version, which provides powerful OpenFOAM toolboxes to users. The new base and derived classes for the multiphase solver provide the capability to track the variables of the gas cloud, predict inter-phase coupling, and particle motion of the solid cloud. For inter-phase collisions, a modified NTC method and a collision pair selection method are developed. Thus, the velocity and temperature of solid particle(s) are updated using the Leapfrog method for the current computational time. In addition to the new solver, new boundary conditions are also developed for the solid phase such as general boundary conditions, which are based on *dsmcFoam+*, and customised boundary conditions for the solid particle-wall interactions. For instance, an adhesive diffuse heat transfer wall patch is one of these customised boundary conditions in order to simulate mechanical and thermal properties of stuck solid particles on a surface during the process. Additional features are also developed for the pre-processing and processing of the one-way coupling solver. The solver is tested by running benchmarking cases such as momentum and energy transfer from gas molecules to a stationary solid particle, and the free expansion of two-phase jet flows. The results of benchmarking simulations provide promising results when compared to theoretical, analytical, and experimental results in the literature. In a test case of the solver, surface coating by ADM is simulated for varying source pressure conditions, wherein the solver provides reasonable results for the process.

# Chapter 6

## Conclusions

### 6.1 Summary

This thesis focuses on the interactions of rarefied gas flows with one another, surfaces, and solid particles at a wide variety of rarefaction levels, and two different collision models, VHS and VSS, in order to simulate a journey from various altitudes of the atmosphere to the space environment. The numerical results in this thesis are compared with other DSMC, theoretical, and experimental results in the literature where available. Before delving deeper into the interactions of rarefied gas flows, and building a new numerical implementation for multiphase problems, the computational code used throughout this thesis, *dsmcFoam+*, is benchmarked with a case in the literature. The capabilities and accuracy of the solver allow for important complex flow physics to be captured.

For the investigation of the interactions of rarefied gas flows at different altitudes, a non-reacting Edney shock-shock interaction problem is simulated. A hypersonic rarefied free-stream flow hits a wedge to generate an oblique shock, which then impinges upon a bow shock from a cylindrical geometry. 11 geometrical setups with three different Knudsen numbers, to examine the formation of Edney shock patterns from I to VI, are simulated. Denser flows create greater surface impacts as they are more focused, however, as the flow becomes more rarefied, the aerodynamic loading expands over a larger proportion of the surface, but has significantly lower peak values. The thickness of the bow shock increases when going through a higher degree of rarefaction; nonetheless, the highest energy of the bow shock is obtained at the lowest Knudsen number. It is also observed that the temporal behaviour of the shock impingement patterns, i.e. steady or unsteady, is a function both of the degree of rarefaction and geometrical parameters. The trend of unsteadiness does not have uniform movements and cyclical periods in either the simulation groups at the same rarefaction level nor in each simulation

individually. Simulations of these unsteady mechanisms are computationally expensive due to the large fluctuations in the number of DSMC simulators.

Another case for the interactions of rarefied gas flow-flow and flow-surface in a high vacuum environment is that of a nozzle exit plume impinging on a surface below the nozzle. The interactions are investigated with a large simulation matrix, which takes into account the effect of the stagnation temperature, the distance between the nozzles, the number of thrusters in multi nozzle configurations, and different impingement heights for a single plume configuration, to investigate the different types of interactions. The impact of the temperature is examined in a single nozzle system by gradually increasing stagnation temperature, where the plume density decreases at the exit of the nozzle in an inverse proportion, while the flow accelerates quickly. It is also obtained that the tighter packed arrays with an increasing number of nozzles create earlier deviations in the axial direction of the plume ejection for the plume-plume impingement compared to the single nozzle system. When comparing the change in the stagnation temperature, the colder resulting plume of a more tightly packed rocket motor disturbs the density trend earlier along the axial data extraction line from the nozzle outlet to the surface. The surface parameters are not affected much by the nozzle-to-nozzle distance in the far-field of the surface. Rather, they are affected by the number of nozzles in the system, which can be demonstrated by the highest surface pressure in the surface stagnation point being induced by the quadruple nozzle configuration. When the nozzle is positioned closer to the impingement surface, its effect on the surface parameters increases. Meanwhile, higher impingement altitudes cause a more distributed impact with lower numerical values.

This thesis provides an insight into the one-way coupling interaction of rarefied gas flows and solid particles, which is another common interaction type in a variety of applications. In a one-way coupling approach, the rarefied gas flow is accepted as the transporter phase, and the solid particles the transported regime. As OpenFOAM does not provide a solver for rarefied multiphase flows, a *dsmcFoam+* based solver, *rarefiedMultiphaseFoam*, is developed. In this two-phase flow, the solver assumes that the gas particles have an influence on the solid particles, which are fully spherical, small enough, and chemically inert in order to create a one-way coupling effect, in terms of force and heat transfer, while the effect of the solid phase on the gas and on itself is neglected. The novel solver not only has the capability to calculate the inter-phase calculations with a modified NTC method but it also provides an ability to track the gas and solid particles with newly developed base and derived classes. In addition, new features, pre-processing, and boundary conditions are also developed in order to present a



more realistic approach to problems and operate the solver more efficiently. The benchmarking of the solver and its extensions are held by running some cases of momentum and energy transfer from gas molecules to a stationary solid particle, and free expansion of two-jet flows, etc. The results of the benchmarking simulations are in a good agreement with the results in the literature where available. A test case is also run to show the capability of the solver for an aerosol coating problem with different source pressures.

## 6.2 Future Work

This thesis provides an opportunity to extend the work carried out as listed in the following:

1. In order to understand the formation of unsteady shock-shock interactions and changes in the value of the surface impingement with an increasing degree of rarefaction, and the location of the bow shock generator in detail, a simulation matrix should be run for longer physical times than the presented results in this thesis. However, the parallel efficiency of the solver should be improved, which will help speed up the simulations. In addition, as the flow at  $Kn = 0.0067$  is in the slip regime, the results of NS and DSMC can be compared for the cases at  $Kn = 0.0067$ .
2. In some cases of plume-plume and plume-surface interaction simulations, only the single nozzle configuration could be applied, such as the effect of the hovering height. In addition, the effect of the background pressure and existence of a supersonic nozzle - as this work has been limited to sonic nozzles - on the presence of/change in the structure of plume-plume and plume-surface interactions can also be investigated. Further simulation runs can be carried out with the changes in the aforementioned parameters. Moreover, the number of nozzles in multi-nozzle configurations should also be increased to obtain results, which provides wide insight for a spacecraft that operates in various conditions.
3. The *rarefiedMultiphaseFoam* solver provides a better understanding for rarefied gas flow and solid particle interactions. However, the solver should be extended to solve various types of interaction problems such as two-way and four-way couplings, the phase change of solid particles such as sublimation during transport, etc. Furthermore, some shortcomings of boundary conditions should be improved, where for instance, more than one particle can

stick at the same point on the surface in the newly developed adhesive wall patch as the solver does not have a solid particle-solid particle interaction model. New boundary conditions should be implemented to enhance the real engineering problem solving capability of the solver.

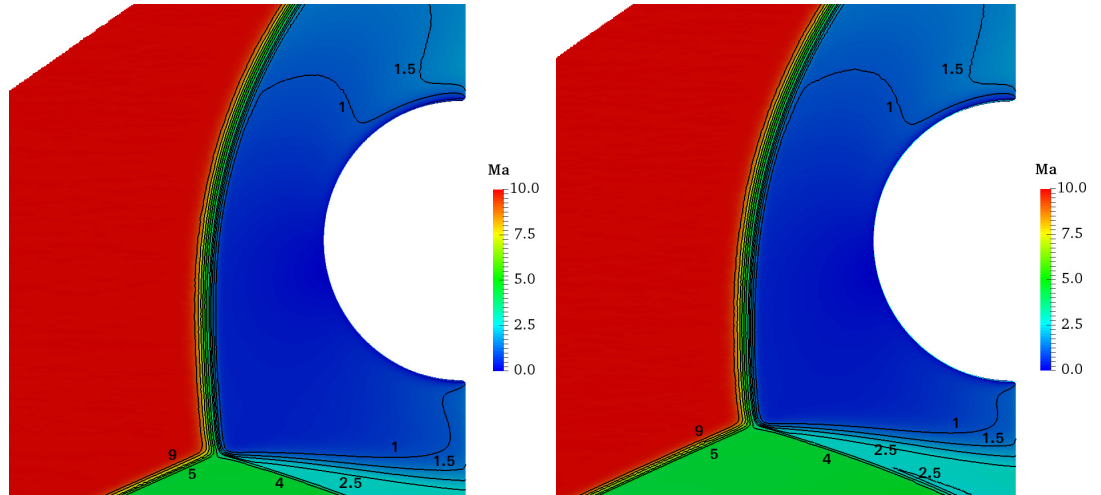
# Chapter 7

## Appendix

### 7.1 The Contours of Mach Number for Altering Knudsen Number and Cylinder Position

The Mach number contours in the steady interaction regions are given for varying rarefaction levels and cylinder positions,  $H$ . The mach contours present the values of the Mach number as 1, 1.5, 2, 2.5, 3, 4, 5, 6, 7, 8, and 9.

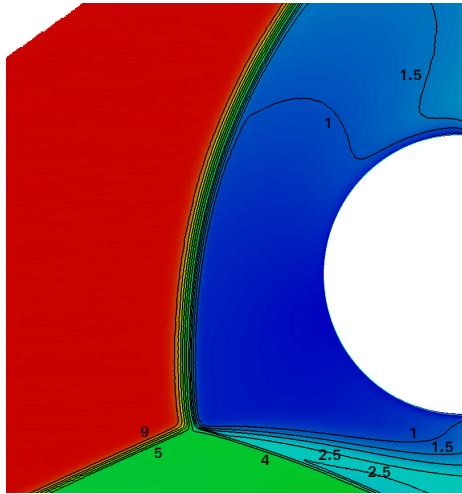
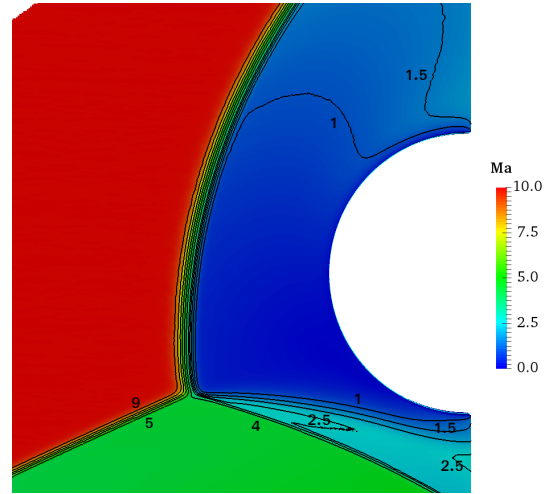
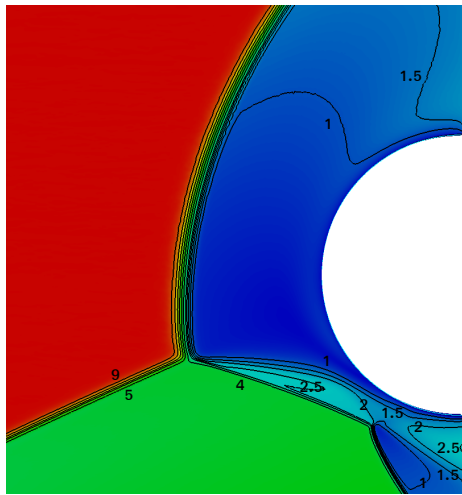
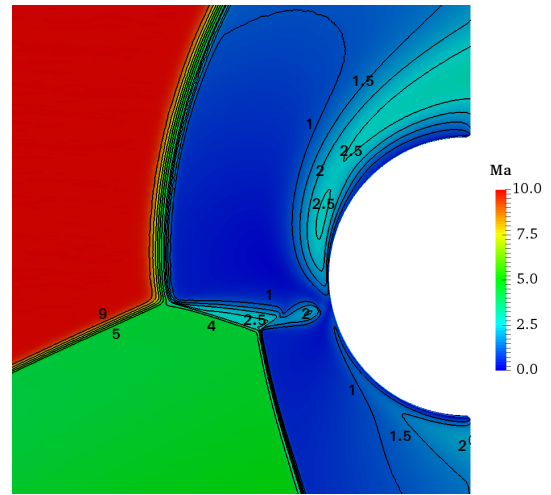
#### 7.1.1 The free-stream flow at $Kn = 0.0067$

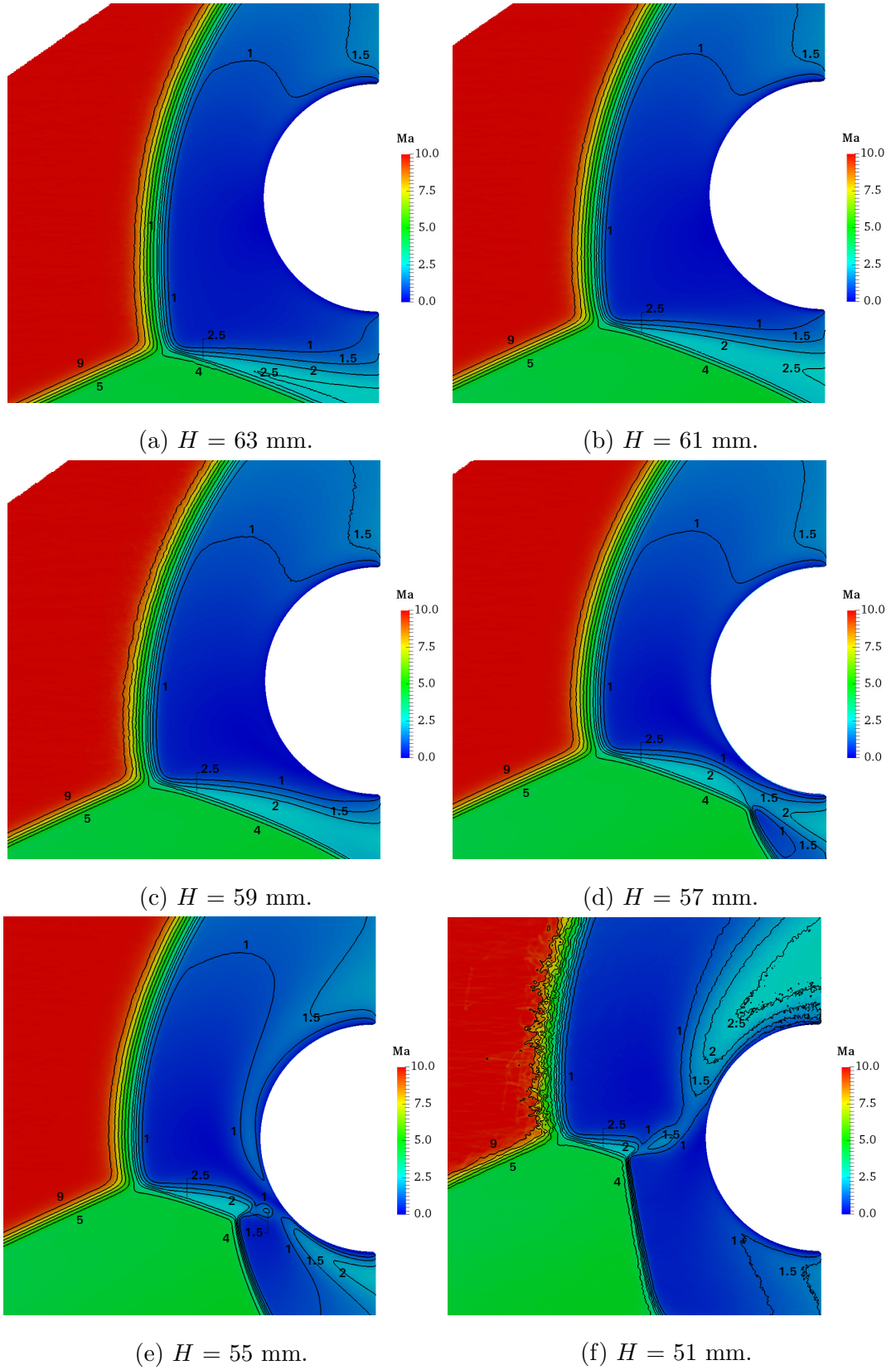


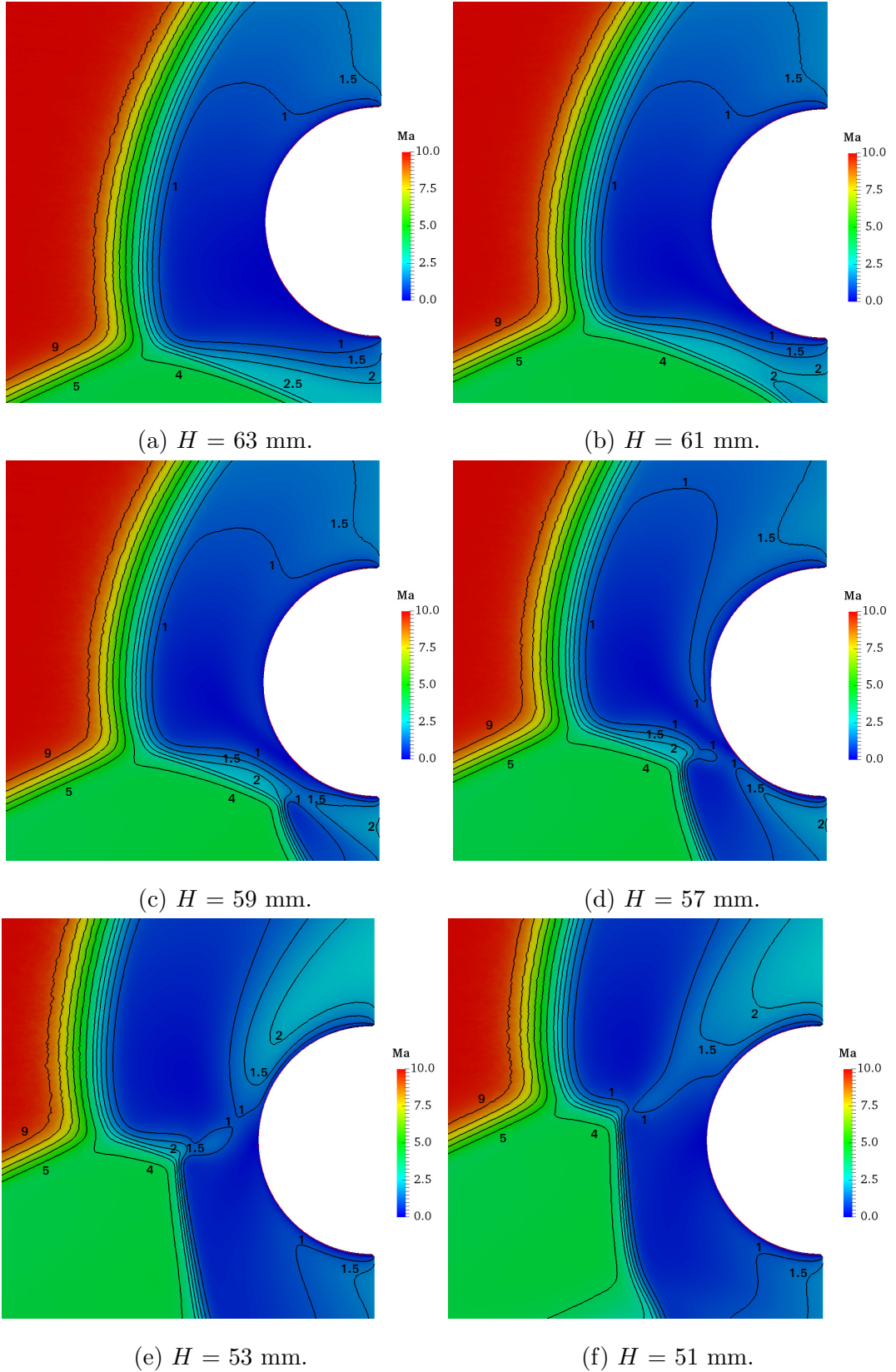
(a)  $H = 63$  mm.

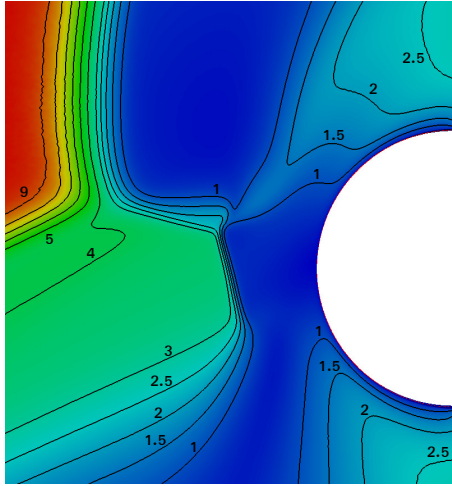
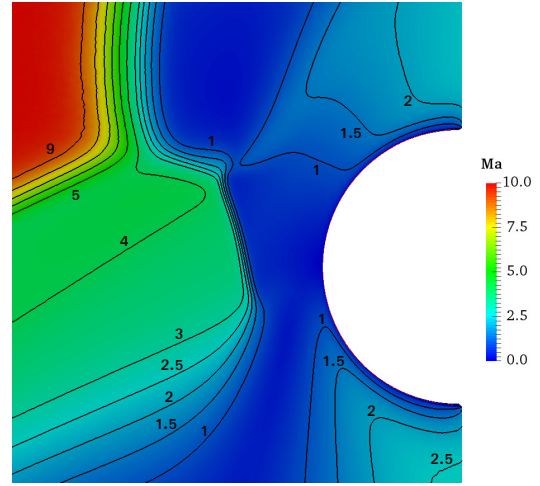
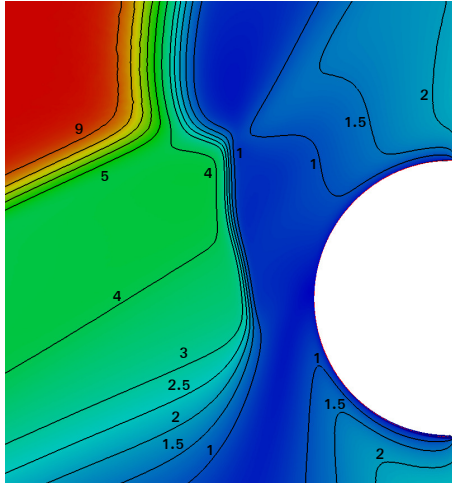
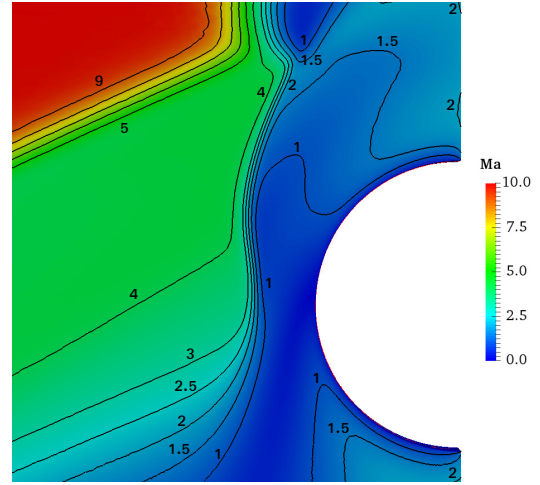
(b)  $H = 61$  mm.

Figure 7.1: The free-stream flow at  $Kn = 0.0067$  - *continued*

(c)  $H = 59$  mm.(d)  $H = 57$  mm.(e)  $H = 55$  mm.(f)  $H = 51$  mm.Figure 7.1: The free-stream flow at  $Kn = 0.0067$

7.1.2 The free-stream flow at  $Kn = 0.0134$ Figure 7.2: The free-stream flow at  $Kn = 0.0134$

7.1.3 The free-stream flow at  $Kn = 0.0268$ Figure 7.3: The free-stream flow at  $Kn = 0.0268$  - *continued*

(g)  $H = 49$  mm.(h)  $H = 47$  mm.(i)  $H = 45$  mm.(j)  $H = 43$  mm.Figure 7.3: The free-stream flow at  $Kn = 0.0268$



## 7.2 Additional Data for Altering Stagnation Temperatures and Orientations of Multi-nozzle Configurations

### 7.2.1 Plume Results for $T_0 = 500$ K

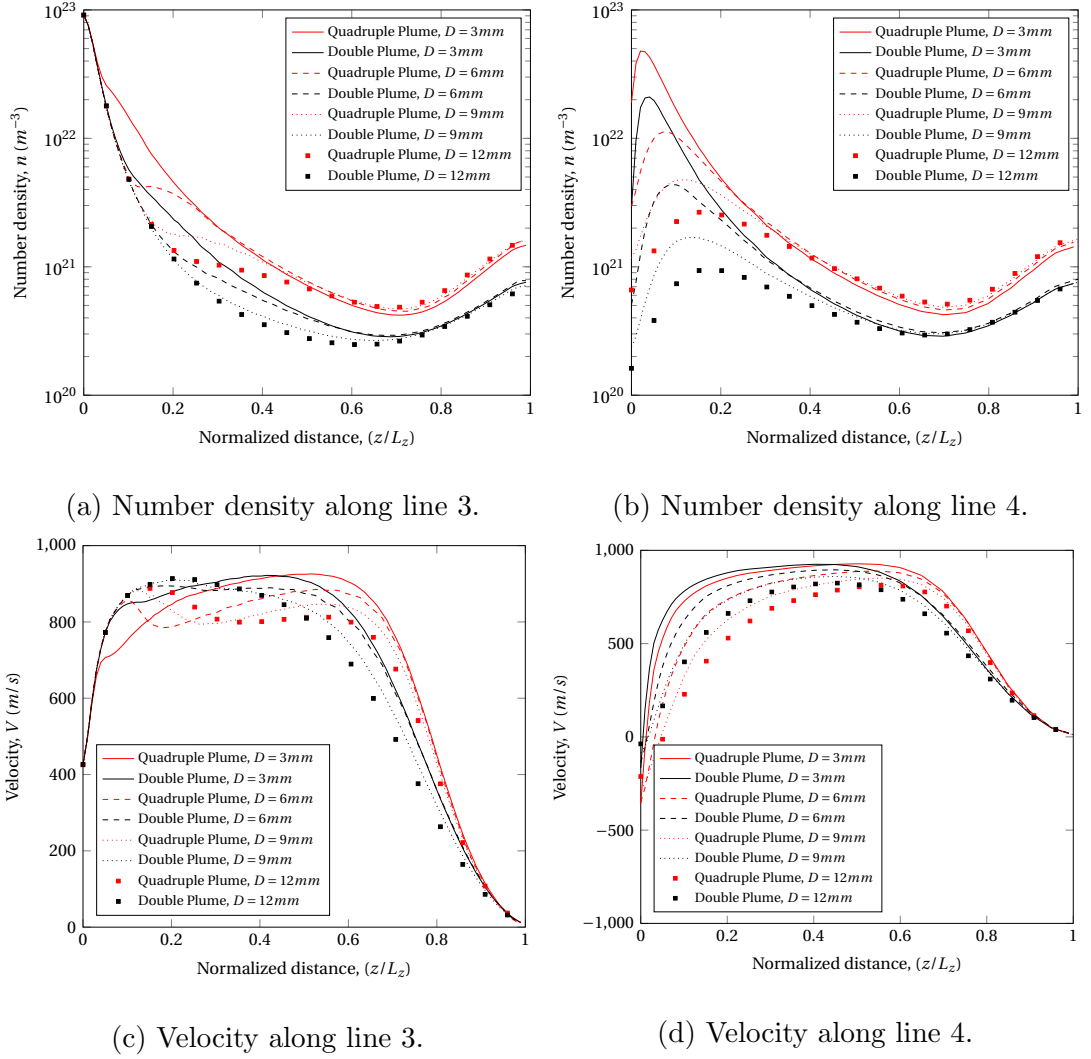
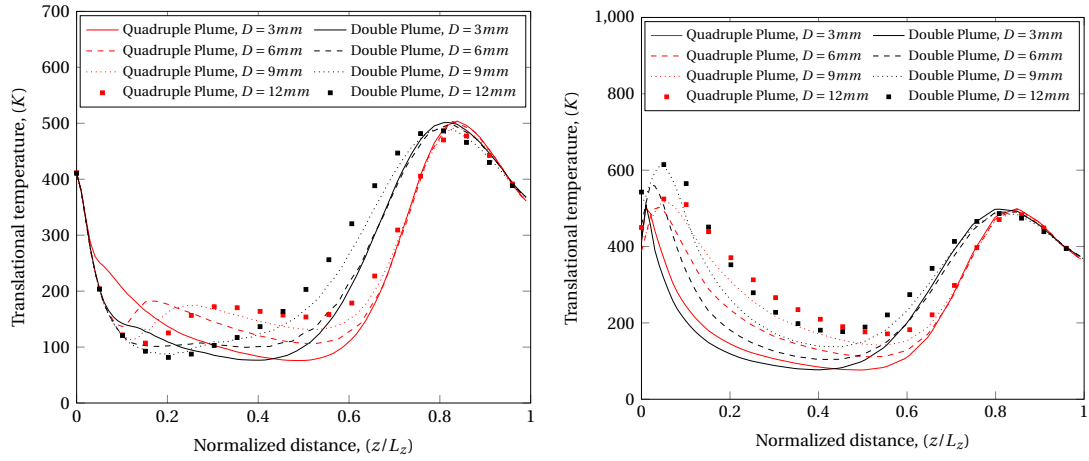


Figure 7.4: *dsMcFoam+* results of multi-nozzle array plume-plume impingement with changing nozzle-to-nozzle distance - *continued*.

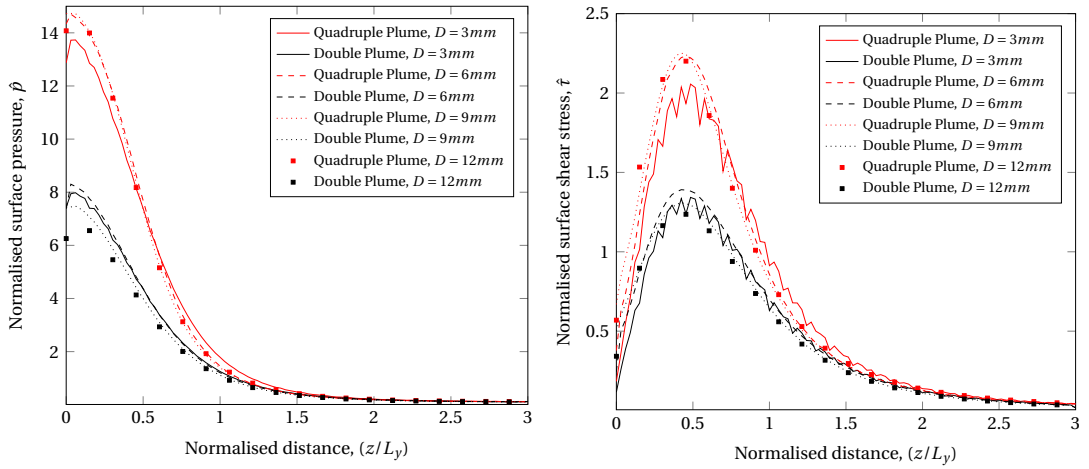




(e) Translational temperature along line 3. (f) Translational temperature along line 4.

Figure 7.4: *dsmcFoam+* results of multi-nozzle array plume-plume impingement with changing nozzle-to-nozzle distance.

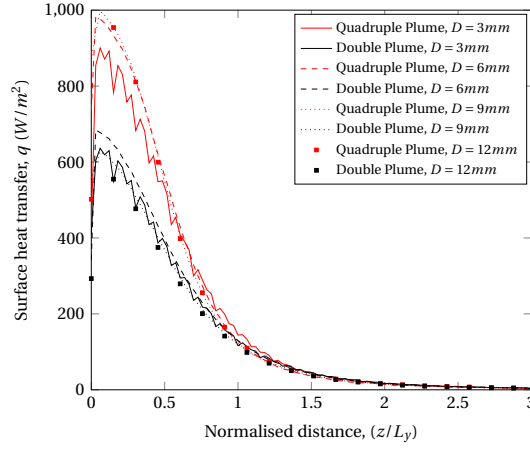
### 7.2.2 Surface Results for $T_0 = 500\text{ K}$



(a) Surface pressure along line 3.

(b) Shear stress along line 3.

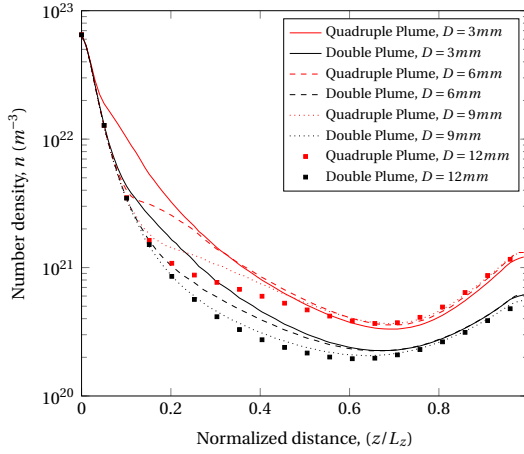
Figure 7.5: *dsmcFoam+* results of multi-nozzle array plume-plume impingement with changing nozzle-to-nozzle distance - *continued*.



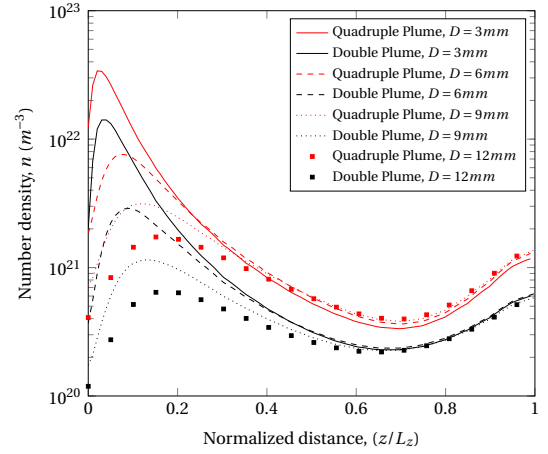
(c) Surface heat transfer along line 3.

Figure 7.5: *dsmcFoam+* results of multi-nozzle array plume-plume impingement with changing nozzle-to-nozzle distance.

### 7.2.3 Plume Results for $T_0 = 700$ K

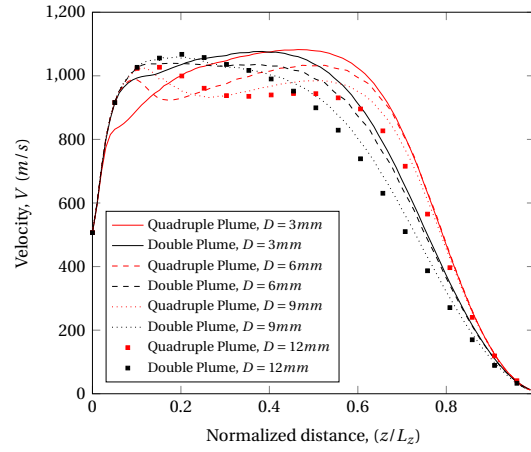


(a) Number density along line 3.

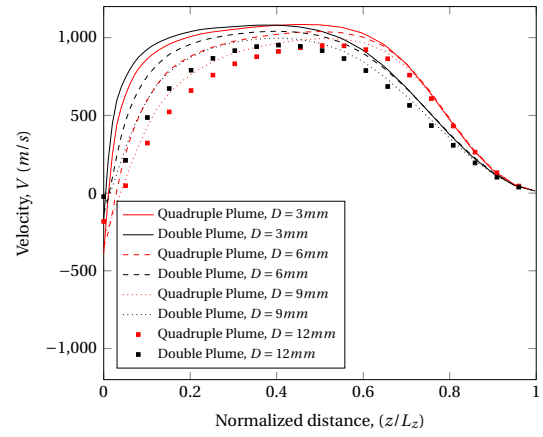


(b) Number density along line 4.

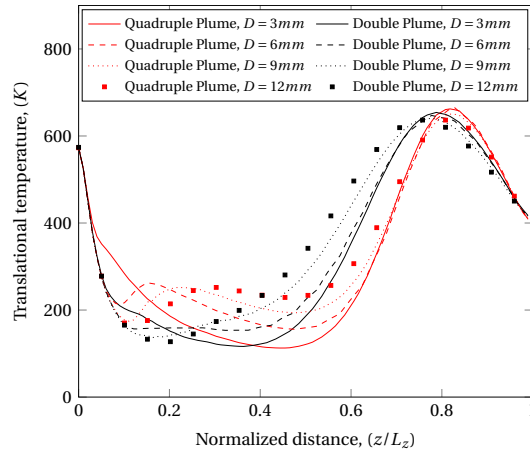
Figure 7.6: *dsmcFoam+* results of multi-nozzle array plume-plume impingement with changing nozzle-to-nozzle distance - *continued*.



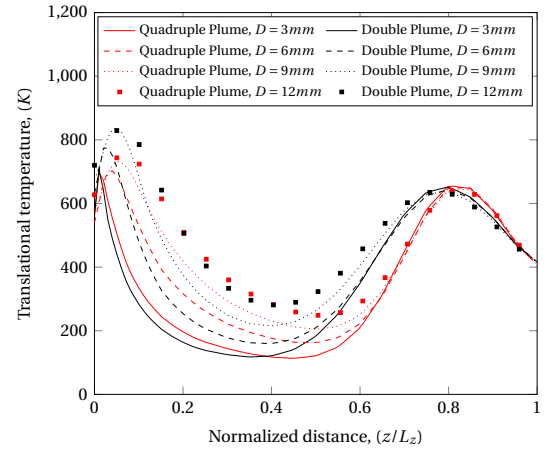
(c) Velocity along line 3.



(d) Velocity along line 4.

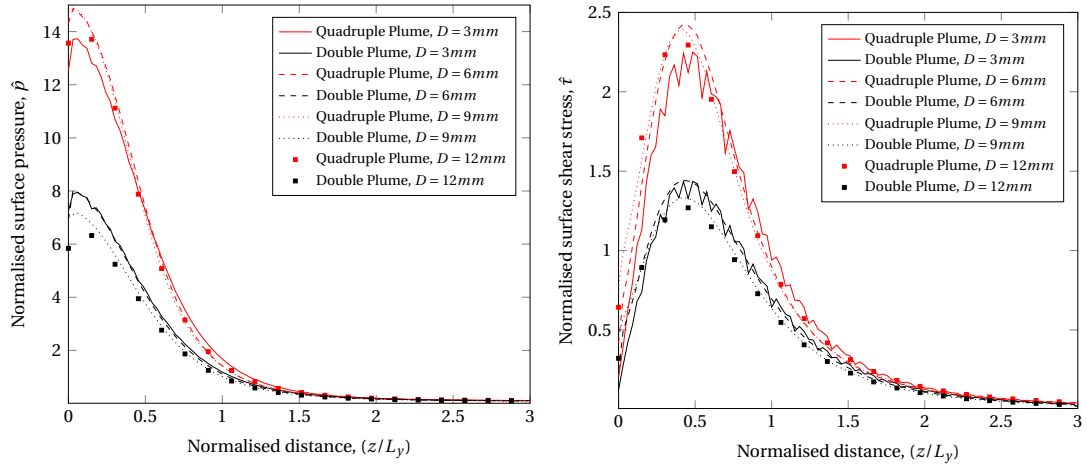


(e) Translational temperature along line 3.



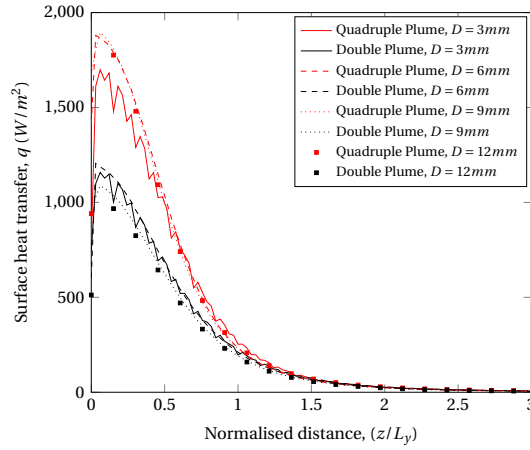
(f) Translational temperature along line 4.

Figure 7.6: *dsmcFoam+* results of multi-nozzle array plume-plume impingement with changing nozzle-to-nozzle distance.

7.2.4 Surface Results for  $T_0 = 700$  K

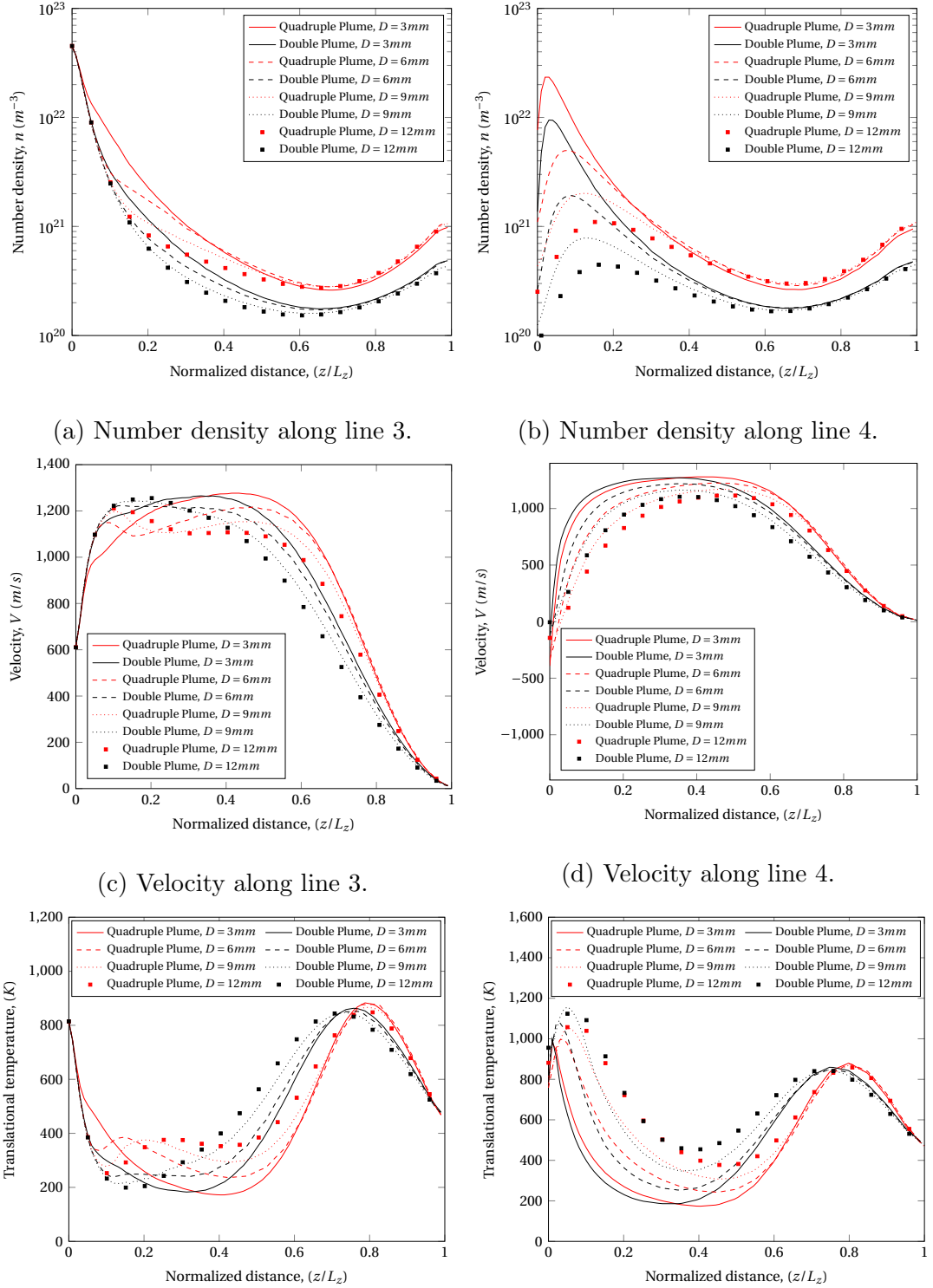
(a) Surface pressure along line 3.

(b) Shear stress along line 3.



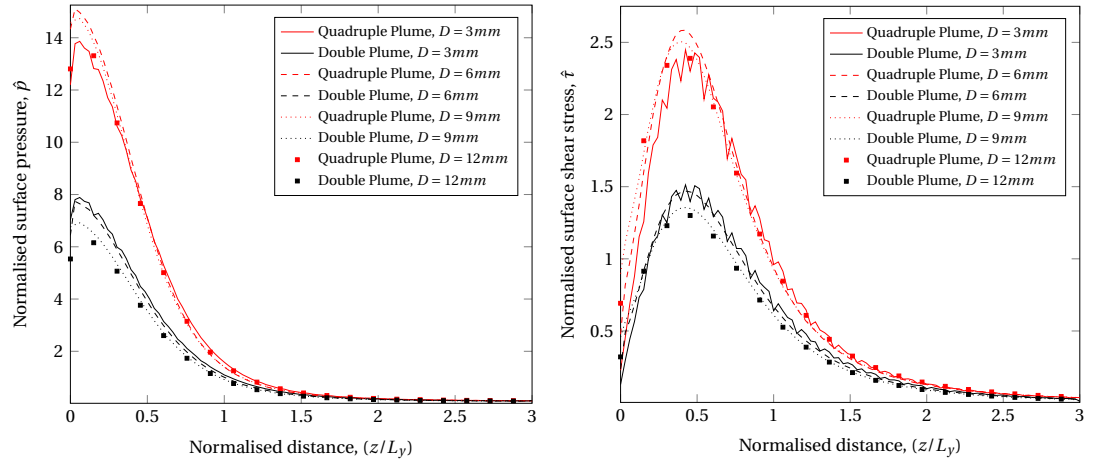
(c) Surface heat transfer along line 3.

Figure 7.7: *dsmcFoam+* results of multi-nozzle array plume-plume impingement with changing nozzle-to-nozzle distance.

7.2.5 Plume Results for  $T_0 = 1000$  K

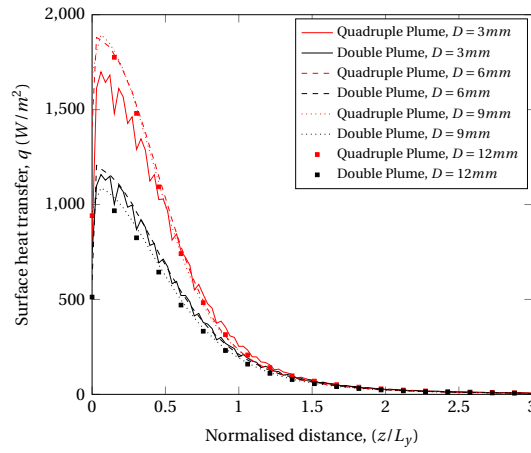
(e) Translational temperature along line 3. (f) Translational temperature along line 4.

Figure 7.8: *dsMcFoam+* results of multi-nozzle array plume-plume impingement with changing nozzle-to-nozzle distance.

7.2.6 Surface Results for  $T_0 = 1000$  K

(a) Surface pressure along line 3.

(b) Shear stress along line 3.



(c) Surface heat transfer along line 3.

Figure 7.9: *dsmcFoam+* results of multi-nozzle array plume-plume impingement with changing nozzle-to-nozzle distance.

### 7.3 Benchmarking of Adhesive Wall Patch

The calculation of restitution is explained in § 5.3. The benchmarking of the implemented model for the calculation of the coefficient of restitution is cited from Ref. [149]. The effect of varying geometry and material properties on the coefficient of restitution is explored while the results of *rarefiedMultiphaseFoam* are compared with the results provided by Eqs. 33 and 35 in [149], and Eqs. 39-41 in Ref. [171]. The material properties and the input parameters for the benchmark case are elastic modulus,  $E$ , yield strength,  $S_y$ , the ratio of yield strength to elastic modulus,  $\varepsilon_y$ , Poisson's ratio,  $\eta$ , radius of solid particle,  $R$ , critical yield stress coefficient,  $c$ , and mass of the solid particle are 200 GPa, 1.12 GPa,  $5.6 \times 10^{-6}$ , 0.33, 0.01 m, 1.651, and 0.0327 kg, respectively.

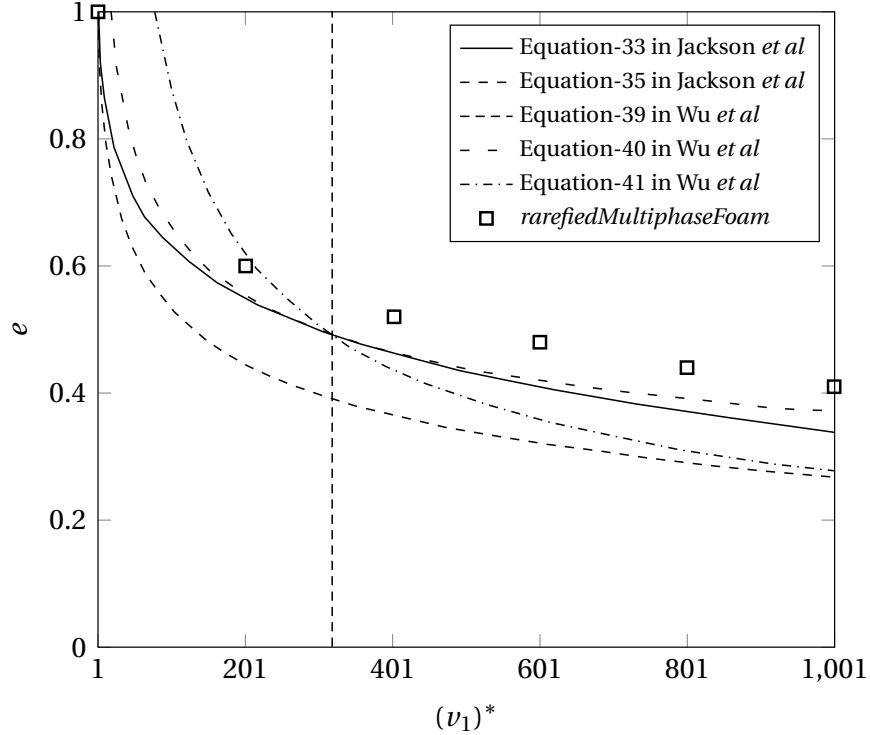


Figure 7.10: The prediction of coefficient of restitution as a function of the residual interference models.

The benchmarking simulations of the *rarefiedMultiphaseFoam* solver provide a reasonable distribution trend as shown in Figure 7.10. The authors of Ref. [149] state that the newly developed numerical model in Ref. [149], which was also implemented in the *rarefiedMultiphaseFoam* solver, has a maximum error range of 8.4% with an average of 5.3% when compared to Eq. 33 in Ref. [149]. Therefore, the application of this new numerical model in Ref. [149] within the newly

developed solver and its prediction performance make the boundary condition capable of solving the coefficient of restitution of the impacting solid particle on a surface. The adhesive wall patch boundary condition comprises of a particle sticking model, which decides whether solid particles are stuck or not once they hit a surface as explained in detail in § 5.3. The adhesion model of the boundary condition is tested by an adhesion force on a rough surface case. In the test case, the diameter of the solid particles, and the Hamaker constant,  $A_H$ , are  $6 \mu\text{m}$ , and  $69.2 \times 10^{-20}$ , respectively. The change in the adhesive force is investigated as a function of changing surface roughness,  $rms$ , and the separation distance. The numerical values of  $rms$  are given in the legend of Figure 7.11.

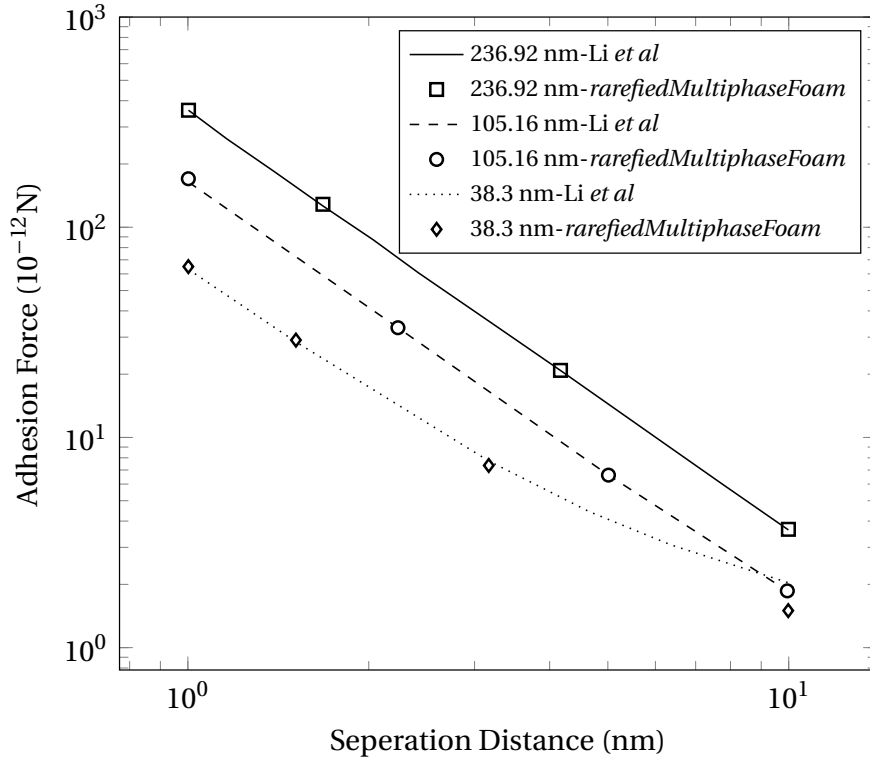


Figure 7.11: Adhesion force versus separation distance with varying surface roughness value of  $rms$ .

As shown in Figure 7.11, the highest adhesion force is obtained at the highest surface roughness and the lowest separation distance, which is explained as *particle-asperity interaction* in Ref. [154]. When the roughness of the surface increases, the non-planarity of the surface increases. Therefore, the separation distance also increases in reality. In this case, the adhesive force decreases. The comparison of the results of Ref. [154] and *rarefiedMultiphaseFoam* shows the calculations of the solver are in a good agreement with the literature, however, a small deviation can be obtained around the value of the highest separation



distance, 10 nm, at the lowest surface roughness, 38.3 nm.

The heat transfer model in the adhesive wall patch is also tested in order to obtain the change in heat transfer with respect to the change in the Fourier number by hitting a solid particle on a surface. Therefore, a test case is run for  $\alpha' = 1$  when thermal conductivity,  $k$ , heat capacity,  $C_p$ , density,  $\rho$ , and the radius of the solid particle,  $R$ , are selected as  $88 \text{ W m}^{-1}\text{K}^{-1}$ ,  $900 \text{ J kg}^{-1}\text{K}^{-1}$ ,  $2700 \text{ kg m}^{-3}$ , and  $1 \times 10^{-3} \text{ m}$ , respectively.

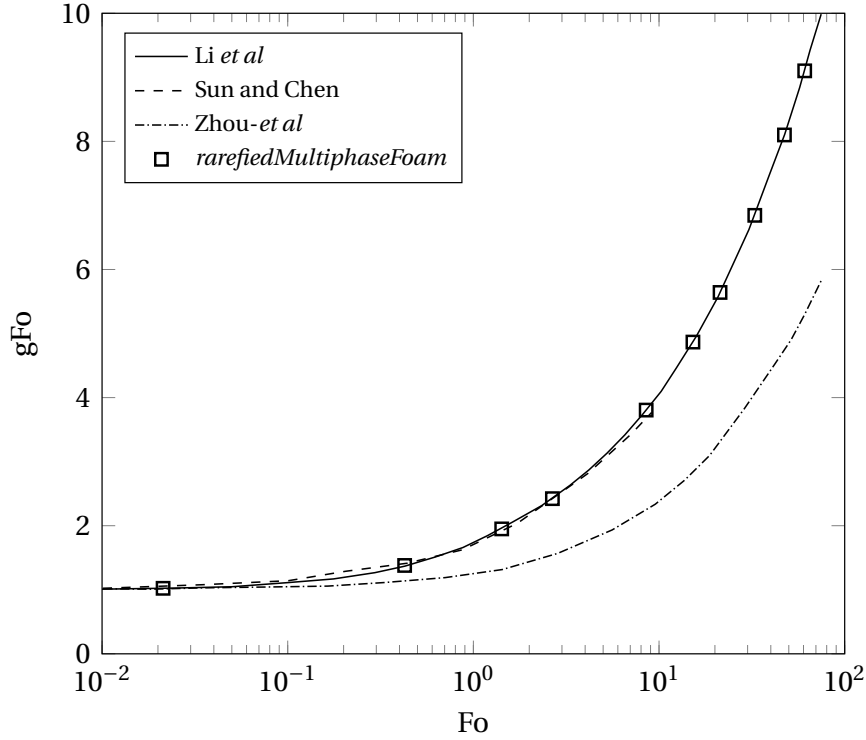


Figure 7.12: Heat transfer between a colliding particle with a wall as a function of the impact  $Fo$ .

Figure 7.12 shows the calculated  $gFo = e/e_0$  versus the Fourier number. The results of *rarefiedMultiphaseFoam* are compared with the data provided by Refs. [150,172,173]. The finite difference solution of Ref. [172] provides an agreement with the reference study [150] for  $Fo < 10$ , however, the Ref. [173] predicts that the heat transfer value is much smaller than the other studies for the larger  $Fo$  values. The results of *rarefiedMultiphaseFoam* provide an excellent agreement with the results of the references that are provided in the literature.

# Bibliography

- [1] G. A. Bird, *Molecular Gas Dynamics and the Direct Simulation Monte Carlo of Gas Flows*. Clarendon, Oxford, 1994.
- [2] M. Gad-el Hak, “The fluid mechanics of microdevices—the Freeman scholar lecture,” *Journal of Fluids Engineering*, vol. 121, no. 1, pp. 5–33, 1999.
- [3] E. H. Kennard, *Kinetic theory of gases: with an introduction to statistical mechanics*. McGraw-Hill Book Company, Inc., 1938.
- [4] G. A. Bird, “Monte Carlo simulation of gas flows,” *Annual Review of Fluid Mechanics*, vol. 10, no. 1, pp. 11–31, 1978.
- [5] E. Oran, C. Oh, and B. Cybyk, “Direct simulation Monte Carlo: recent advances and applications,” *Annual Review of Fluid Mechanics*, vol. 30, no. 1, pp. 403–441, 1998.
- [6] C. White, M. K. Borg, T. J. Scanlon, S. M. Longshaw, B. John, D. Emerson, and J. M. Reese, “dsmcFoam+: An OpenFOAM based direct simulation Monte Carlo solver,” *Computer Physics Communications*, vol. 224, pp. 22–43, 2018.
- [7] R. Cassineli Palharini, *Atmospheric reentry modelling using an open source DSMC code*. PhD thesis, University of Strathclyde, 2014.
- [8] R. K. Zeytounian, *Navier-Stokes-Fourier equations: a rational asymptotic modelling point of view*. Springer Science & Business Media, 2012.
- [9] J. D. Anderson, *Computational Fluid Dynamics: The Basics With Applications*. McGraw-Hill, 1995.
- [10] A. Beskok and G. E. Karniadakis, “Simulation of heat and momentum transfer in complex microgeometries,” *Journal of Thermophysics and Heat Transfer*, vol. 8, no. 4, pp. 647–655, 1994.

- [11] C. White, *Benchmarking, development and applications of an open source DSMC solver*. PhD thesis, University of Strathclyde, 2013.
- [12] J. C. Maxwell, “III. On stresses in rarefied gases arising from inequalities of temperature,” *Proceedings of the Royal Society of London*, vol. 27, no. 185–189, pp. 304–308, 1878.
- [13] M. Smoluchowski von Smolan, “Über wärmeleitung in verdünnten gasen,” *Annalen der Physik*, vol. 300, no. 1, pp. 101–130, 1898.
- [14] P. S. Prasanth and J. K. Kakkassery, “Direct simulation Monte Carlo (DSMC): A numerical method for transition-regime flows – A review,” *Journal of the Indian Institute of Science*, vol. 86, no. 3, p. 169, 2013.
- [15] X.-J. Gu and D. R. Emerson, “A high-order moment approach for capturing non-equilibrium phenomena in the transition regime,” *Journal of Fluid Mechanics*, vol. 636, pp. 177–216, 2009.
- [16] H. Struchtrup and M. Torrilhon, “Regularization of Grad’s 13 moment equations: Derivation and linear analysis,” *Physics of Fluids*, vol. 15, no. 9, pp. 2668–2680, 2003.
- [17] X.-J. Gu, D. R. Emerson, and G.-H. Tang, “Kramers’ problem and the knudsen minimum: a theoretical analysis using a linearized 26-moment approach,” *Continuum Mechanics and Thermodynamics*, vol. 21, no. 5, p. 345, 2009.
- [18] L. Wu, C. White, T. J. Scanlon, J. M. Reese, and Y. Zhang, “Deterministic numerical solutions of the Boltzmann equation using the fast spectral method,” *Journal of Computational Physics*, vol. 250, pp. 27–52, 2013.
- [19] D. Goldstein, B. Sturtevant, and J. Broadwell, “Investigations of the motion of discrete-velocity gases,” *Progress in Astronautics and Aeronautics*, vol. 117, pp. 100–117, 1989.
- [20] A. V. Bobylev, A. Palczewski, and J. Schneider, “On approximation of the Boltzmann equation by discrete velocity models,” *Comptes rendus de l’Académie des sciences. Série I, Mathématique*, vol. 320, no. 5, pp. 639–644, 1995.
- [21] V. Aristov and F. Tcheremissine, “Direct numerical solutions of the kinetic Boltzmann equation, Comp.,” *Center of Russ. Acad. of Sci. Moscow*, 1992.

- [22] W. Wagner, “Approximation of the Boltzmann equation by discrete velocity models,” *Journal of Statistical Physics*, vol. 78, no. 5, pp. 1555–1570, 1995.
- [23] C. Buet, “A discrete-velocity scheme for the Boltzmann operator of rarefied gas dynamics,” *Transport Theory and Statistical Physics*, vol. 25, no. 1, pp. 33–60, 1996.
- [24] F. Tcheremissine, “Solution to the Boltzmann kinetic equation for high-speed flows,” *Computational Mathematics and Mathematical Physics*, vol. 46, no. 2, pp. 315–329, 2006.
- [25] A. Morris, P. Varghese, and D. Goldstein, “Improvement of a Discrete Velocity Boltzmann Equation Solver With Arbitrary Post-Collision Velocities,” in *AIP Conference Proceedings*, vol. 1084, pp. 458–463, American Institute of Physics, 2008.
- [26] A. Morris, P. L. Varghese, and D. B. Goldstein, “Monte carlo solution of the Boltzmann equation via a discrete velocity model,” *Journal of Computational Physics*, vol. 230, no. 4, pp. 1265–1280, 2011.
- [27] C. Mouhot, L. Pareschi, and T. Rey, “Convolutional decomposition and fast summation methods for discrete-velocity approximations of the Boltzmann equation,” *ESAIM: Mathematical Modelling and Numerical Analysis*, vol. 47, no. 5, pp. 1515–1531, 2013.
- [28] Y. Sone, T. Ohwada, and K. Aoki, “Temperature jump and Knudsen layer in a rarefied gas over a plane wall: Numerical analysis of the linearized Boltzmann equation for hard-sphere molecules,” *Physics of Fluids A: Fluid Dynamics*, vol. 1, no. 2, pp. 363–370, 1989.
- [29] T. Ohwada, “Structure of normal shock waves: Direct numerical analysis of the Boltzmann equation for hard-sphere molecules,” *Physics of Fluids A: Fluid Dynamics*, vol. 5, no. 1, pp. 217–234, 1993.
- [30] T. Ohwada, “Heat flow and temperature and density distributions in a rarefied gas between parallel plates with different temperatures. Finite-difference analysis of the nonlinear Boltzmann equation for hard-sphere molecules,” *Physics of Fluids*, vol. 8, no. 8, pp. 2153–2160, 1996.
- [31] L. Pareschi and B. Perthame, “A Fourier spectral method for homogeneous Boltzmann equations,” *Transport Theory and Statistical Physics*, vol. 25, no. 3-5, pp. 369–382, 1996.

- [32] Z. Guo and K. Xu, “Progress of discrete unified gas-kinetic scheme for multiscale flows,” *Advances in Aerodynamics*, vol. 3, no. 1, pp. 1–42, 2021.
- [33] P. L. Bhatnagar, E. P. Gross, and M. Krook, “A Model for Collision Processes in Gases. I. Small Amplitude Processes in Charged and Neutral One-Component Systems,” *Physical Review*, vol. 94, no. 3, p. 511, 1954.
- [34] C. Cercignani, *Mathematical Methods in Kinetic Theory*. Springer, 1969.
- [35] B. J. Alder and T. E. Wainwright, “Studies in Molecular Dynamics. I. General Method,” *The Journal of Chemical Physics*, vol. 31, no. 2, pp. 459–466, 1959.
- [36] A. L. Garcia, *Numerical Methods for Physics*. Prentice Hall Englewood Cliffs, NJ, 2000.
- [37] M. E. Starzak, *Energy and Entropy Equilibrium to Stationary States*. New York: Springer Science & Business Media, 2010.
- [38] G. A. Bird, *The DSMC Method*. CreateSpace Independent Publishing Platform, 2013.
- [39] G. A. Bird, “Approach to Translational Equilibrium in a Rigid Sphere Gas,” *Physics of Fluids*, vol. 6, pp. 1518–1519, 1963.
- [40] B. Alder and T. Wainwright, “Transport Processes in Statistical Mechanics,” in *International Symposium Proceedings* (I. Prigogine, ed.), pp. 97–131, Interscience Publishers, New York, 1958.
- [41] A. L. Garcia, “Direct Simulation Monte Carlo: Theory, Methods, and Open Challenges,” tech. rep., RTO-EN-AVT-194, 2011.
- [42] R. Eckhardt, “STAN ULAM, JOHN VON NEUMANN, and the MONTE CARLO METHOD,” *Los Alamos Science*, vol. 15, no. 131-136, p. 30, 1987.
- [43] C. P. Robert, “Monte Carlo Methods,” *Wiley StatsRef: Statistics Reference Online*, pp. 1–13, 2016.
- [44] G. A. Bird, “Shock-wave structure in a rigid sphere gas,” in *Rarefied Gas Dynamics* (J. H. de Leeuw, ed.), vol. 1, p. 216, Academic, New York, 1965.
- [45] G. A. Bird, “The structure of normal shock waves in a binary gas mixture,” *Journal of Fluid Mechanics*, vol. 31, no. 4, pp. 657–668, 1968.

- [46] F. S. Sherman, "Shock-wave structure in binary mixtures of chemically inert perfect gases," *Journal of Fluid Mechanics*, vol. 8, no. 3, pp. 465–480, 1960.
- [47] G. A. Bird, "The velocity distribution function within a shock wave," *Journal of Fluid Mechanics*, vol. 30, no. 3, pp. 479–487, 1967.
- [48] S. Chapman and T. Cowling, *The Mathematical Theory of Non-uniform Gases*. Cambridge: The University Press, 1940.
- [49] G. A. Bird, "Breakdown of translational and rotational equilibrium in gaseous expansions," *AIAA Journal*, vol. 8, no. 11, pp. 1998–2003, 1970.
- [50] C. Borgnakke and P. S. Larsen, "Statistical collision model for Monte Carlo simulation of polyatomic gas mixture," *Journal of Computational Physics*, vol. 18, no. 4, pp. 405–420, 1975.
- [51] G. A. Bird, "Definition of mean free path for real gases," *The Physics of Fluids*, vol. 26, no. 11, pp. 3222–3223, 1983.
- [52] K. Koura and H. Matsumoto, "Variable soft sphere molecular model for inverse-power-law or Lennard-Jones potential," *Physics of Fluids A: Fluid Dynamics*, vol. 3, no. 10, pp. 2459–2465, 1991.
- [53] M. A. Rieffel, "Concurrent Simulations of Plasma Reactors for VLSI Manufacturing," tech. rep., CaltechCSTR-26885, 1995.
- [54] N. G. Hadjiconstantinou, A. L. Garcia, M. Z. Bazant, and G. He, "Statistical error in particle simulations of hydrodynamic phenomena," *Journal of Computational Physics*, vol. 187, no. 1, pp. 274–297, 2003.
- [55] M. Ivanov and S. Rogasinsky, "Analysis of numerical techniques of the direct simulation Monte Carlo method in the rarefied gas dynamics," *Soviet Journal of Numerical Analysis and Mathematical Modelling*, vol. 3, no. 6, pp. 453–465, 1988.
- [56] S. K. Stefanov, "On DSMC Calculations of Rarefied Gas Flows with Small Number of Particles in Cells," *SIAM Journal on Scientific Computing*, vol. 33, no. 2, pp. 677–702, 2011.
- [57] A. Venkattraman, A. A. Alexeenko, M. Gallis, and M. Ivanov, "A comparative study of no-time-counter and majorant collision frequency numerical schemes in DSMC," in *AIP Conference Proceedings*, vol. 1501, pp. 489–495, American Institute of Physics, 2012.

- [58] B. Goshayeshi, E. Roohi, and S. Stefanov, “Dsmc simulation of hypersonic flows using an improved SBT-TAS technique,” *Journal of Computational Physics*, vol. 303, pp. 28–44, 2015.
- [59] E. Taheri, E. Roohi, and S. Stefanov, “A symmetrized and simplified Bernoulli trial collision scheme in direct simulation Monte Carlo,” *Physics of Fluids*, vol. 34, no. 1, p. 012010, 2022.
- [60] G. A. Bird, “Sophisticated DSMC,” in *Notes prepared for a short course at the DSMC07 meeting, Santa Fe, USA*, 2007.
- [61] T. J. Scanlon, E. Roohi, C. White, M. Darbandi, and J. M. Reese, “An open source, parallel DSMC code for rarefied gas flows in arbitrary geometries,” *Computers & Fluids*, vol. 39, no. 10, pp. 2078–2089, 2010.
- [62] “DSMC resources from Graeme Bird.” <http://gab.com.au>. Accessed: 2021.
- [63] S. Dietrich and I. D. Boyd, “Scalar and Parallel Optimized Implementation of the Direct Simulation Monte Carlo Method,” *Journal of Computational Physics*, vol. 126, no. 2, pp. 328–342, 1996.
- [64] F. Bergemann and I. Boyd, “DSMC Simulation of Inelastic Collisions Using the Borgnakke-Larsen Method Extended to Discrete Distributions of Vibrational Energy,” in *Proceedings of the 18th Symposium on Rarefied Gas Dynamics, Vancouver, Canada*, 1992.
- [65] S. Dietrich, “Improved DSMC-Modeling of Near-Continuum Flows with Chemical Reactions,” in *Proceedings of the 18th Symposium on Rarefied Gas Dynamics, Vancouver, Canada*, pp. 208–217, 1992.
- [66] “SPARTA Direct Simulation Monte Carlo (DSMC) Simulator.” <https://sparta.github.io>. Accessed: 05.05.2022.
- [67] M. A. Gallis, J. R. Torczynski, S. J. Plimpton, D. J. Rader, and T. Koehler, “Direct simulation Monte Carlo: The quest for speed,” *AIP Conference Proceedings*, vol. 1628, no. 1, pp. 27–36, 2014.
- [68] S. J. Plimpton, S. G. Moore, A. Borner, A. K. Stagg, T. P. Koehler, J. R. Torczynski, and M. A. Gallis, “Direct simulation Monte Carlo on petaflop supercomputers and beyond,” *Physics of Fluids*, vol. 31, no. 8, p. 086101, 2019.

- [69] M. Ivanov, A. Kashkovsky, S. Gimelshein, G. Markelov, A. Alexeenko, Y. A. Bondar, G. Zhukova, S. Nikiforov, and P. Vaschenkov, "SMILE System for 2D/3D DSMC Computations," in *Proceedings of 25th International Symposium on Rarefied Gas Dynamics, St. Petersburg, Russia*, pp. 21–28, 2006.
- [70] G. B. Macpherson, *Molecular Dynamics Simulation in Arbitrary Geometries for Nanoscale Fluid Mechanics*. PhD thesis, University Of Strathclyde, 2008.
- [71] M. K. Borg, *Hybrid Molecular-Continuum Modelling of Nano-Scale Flows*. PhD thesis, University of Strathclyde, 2010.
- [72] D. G. Wang and C. S. Campbell, "Reynolds analogy for a shearing granular material," *Journal of Fluid Mechanics*, vol. 244, pp. 527–527, 1992.
- [73] C. E. Glass, "Numerical Simulation of Low-Density Shock-Wave Interactions," tech. rep., NASA/TM-1999-209358, 1999.
- [74] J. D. Watts, "Flight experience with shock impingement and interference heating on the X-15-2 research airplane," tech. rep., NASA/TM-X-1669, 1968.
- [75] B. E. Edney, "ANOMALOUS HEAT TRANSFER AND PRESSURE DISTRIBUTIONS ON BLUNT BODIES AT HYPERSONIC SPEEDS IN THE PRESENCE OF AN IMPINGING SHOCK," tech. rep., Flygtekniska Forsöksanstalten/Report 115, 1968.
- [76] B. E. Edney, "Effects of Shock Impingement on the Heat Transfer around Blunt Bodies," *AIAA Journal*, vol. 6, no. 1, pp. 15–21, 1968.
- [77] D. J. Morris and J. W. Keyes, "COMPUTER PROGRAMS FOR PREDICTING SUPERSONIC AND HYPERSONIC INTERFERENCE FLOW FIELDS AND HEATING," tech. rep., NASA/TM-X-2725, 1973.
- [78] C. E. Glass, "Computer program To Solve Two-Dimensional Shock-Wave Interference Problems With an Equilibrium Chemically Reacting Air Model," tech. rep., NASA/TM-4187, 1990.
- [79] S. R. Sanderson and B. Sturtevant, "Shock wave interactions in hypervelocity flow," in *Shock Waves at Marseille I* (R. Brun and L. Z. Dumitrescu, eds.), pp. 69–74, Springer Berlin Heidelberg, 1995.
- [80] A. Wieting, "Shock Interference Heating in Scramjet Engines," in *2nd International Aerospace Planes Conference*, p. 5238, 1990.



- [81] D. Sobel, "COWL LEADING EDGE HEAT TRANSFER IN THE PRESENCE OF SHOCK IMPINGEMENT," in *2nd International Aerospace Planes Conference*, p. 5256, 1990.
- [82] J. C. Tannehill, T. L. Holst, and J. Rakich, "Numerical Computation of Two-Dimensional Viscous Blunt Body Flows with an Impinging Shock," *AIAA Journal*, vol. 14, no. 2, pp. 204–211, 1976.
- [83] G. R. Vemaganti, "Laminar and Turbulent Flow Computations of Type 4 Shock-Shock Interference Aerothermal Loads Using Unstructured Grids," tech. rep., NASA/CR-195008, 1994.
- [84] T. Prabhu, R. Thareja, and J. Stewart, "Shock interference studies on a circular cylinder at Mach 16," in *28th Aerospace Sciences Meeting*, p. 606, 1990.
- [85] H. Cheng, "Perspectives on Hypersonic Viscous Flow Research," *Annual Review of Fluid Mechanics*, vol. 25, no. 1, pp. 455–484, 1993.
- [86] T. Pot, B. Chanetz, M. Lefebvre, and P. Bouchardy, "Fundamental study of shock/shock interference in low density flow: Flowfield measurements by DLCARS," in *21st Rarefied Gas Dynamics Symposium, Marseille, France*, no. 1998-140, 1999.
- [87] A. B. Carlson and R. G. Wilmoth, "Shock interference prediction using direct simulation Monte Carlo," *Journal of Spacecraft and Rockets*, vol. 29, no. 6, pp. 780–785, 1992.
- [88] J. N. Moss, T. Pot, B. Chanetz, and M. Lefebvre, "DSMC Simulation of Shock/Shock Interactions: Emphasis on Type IV Interactions," tech. rep., NASA/ 20040086965, 1999.
- [89] G. Bird, "The G2/A3 Program System Users Manual," *GAB Consulting Pty Ltd, Killara, NSW, Australia*, 1992.
- [90] H. Xiao, Y. Shang, and D. Wu, "DSMC Simulation and Experimental Validation of Shock Interaction in Hypersonic Low Density Flow," *The Scientific World Journal*, vol. 2014, 2014.
- [91] G. Zuppardi and C. Boffa, "Effects of rarefaction on the shock wave/boundary layer interaction in hypersonic regime," in *AIP Conference Proceedings*, vol. 1501, pp. 673–679, American Institute of Physics, 2012.

- [92] G. Zuppardi, “Effects of Rarefaction on the Shock Wave/Shock Wave Interaction in Hypersonic Regime,” in *Workshop DSMC13, Santa Fe, USA*, 2013.
- [93] C. White and K. Kontis, “The Effect of Increasing Rarefaction on the Edney Type IV Shock Interaction Problem,” in *22nd International Shock Interaction Symposium*, pp. 299–311, Springer, 2016.
- [94] F. Grasso, C. Purpura, B. Chanetz, and J. Détery, “Type III and Type IV shock/shock interferences: theoretical and experimental aspects,” *Aerospace Science and Technology*, vol. 7, no. 2, pp. 93–106, 2003.
- [95] C. A. Lind and M. J. Lewis, “Computational Analysis of the Unsteady Type IV Shock Interaction of Blunt Body Flows,” *Journal of Propulsion and Power*, vol. 12, no. 1, pp. 127–133, 1996.
- [96] S. Yamamoto, N. Takasu, and H. Nagatomo, “Numerical Investigation of Shock/Vortex Interaction in Hypersonic Thermochemical Nonequilibrium Flow,” *Journal of Spacecraft and Rockets*, vol. 36, no. 2, pp. 240–246, 1999.
- [97] C. Windisch, B. U. Reinartz, and S. Müller, “Investigation of Unsteady Edney Type IV and VII Shock–Shock Interactions,” *AIAA Journal*, vol. 54, pp. 1846–1861, 2016.
- [98] M. S. Holden and T. P. Wadhams, “A review of experimental studies for DSMC and Navier–Stokes code validation in laminar regions of shock/shock and shock boundary layer interaction including real gas effects in hypervelocity flows,” in *36th AIAA Thermophysics Conference*, 2003.
- [99] G. Dettleff, “PLUME FLOW AND PLUME IMPINGEMENT IN SPACE TECHNOLOGY,” *Progress in Aerospace Sciences*, vol. 28, no. 1, pp. 1–71, 1991.
- [100] A. R. Vick, J. M. Cubbage, and E. H. Andrews, “Rocket exhaust-plume problems and some recent related research,” *The Fluid Dynamic Aspects of Space Flight, AGARDograph 87*, vol. II, pp. 129–180, 1966.
- [101] R. Boettcher and H. Legge, “A study of rocket exhaust plumes and impingement effects on spacecraft surfaces,” tech. rep., DFVLR/IB 251-80 A 27, 1980.
- [102] J. C. Lengrad, “Plume impingement upon spacecraft surfaces,” in *Proceedings of the 14th International Symposium on Rarefied Gas Dynamics* (H. Oguchi, ed.), pp. 217–228, University of Tokyo Press, Tokyo, 1984.

- [103] I. D. Boyd, Y. Jafry, and J. V. Beukel, “Particle Simulations of Helium Microthruster Flows,” *Journal of Spacecraft and Rockets*, vol. 31, no. 2, pp. 271–277, 1994.
- [104] R. Koppang, E. Piesik, and D. Simkin, “Rocket-Exhaust Impingement on a Flat Plate at High Vacuum,” *Journal of Spacecraft and Rockets*, vol. 3, no. 11, pp. 1650–1657, 1966.
- [105] B. Deependran, R. Sujith, and J. Kurian, “Studies of Low-Density Freejets and Their Impingement Effects,” *AIAA Journal*, vol. 35, no. 9, pp. 1536–1542, 1997.
- [106] K. C. Kannenberg, *COMPUTATIONAL METHODS FOR THE DIRECT SIMULATION MONTE CARLO TECHNIQUE WITH APPLICATION TO PLUME IMPINGEMENT*. PhD thesis, 1998.
- [107] H. Legge, “Plume impingement forces on inclined flat plates,” in *Proceedings of the 17th International Symposium on Rarefied Gas Dynamics*, VCH Verlag, Weinheim, pp. 955–962, 1991.
- [108] S. Döring, “Experimental plume impingement heat transfer on inclined flat plates,” tech. rep., DLR/IB 222-90 A 36, 1990.
- [109] M. Mehta, “Rocket Plume Interactions for NASA Landing Systems.” <https://ntrs.nasa.gov/citations/20200000979>, 2019. Accessed: 21.08.2021.
- [110] M. Ivanov, G. Markelov, Y. I. Gerasimov, A. Krylov, L. Mishina, and E. Sokolov, “Free-Flight Experiment and Numerical Simulation for Cold Thruster Plume,” *Journal of Propulsion and Power*, vol. 15, no. 3, pp. 417–423, 1999.
- [111] S. Ivanov, N. Markelov, V. Kashkovsky, and D. Giordano, “NUMERICAL ANALYSIS OF THRUSTER PLUME INTERACTION PROBLEMS,” in *European Spacecraft Propulsion Conference, Noordwijk, NL*, vol. 398, p. 603, 1997.
- [112] F. E. Lumpkin, III, P. C. Stuart, and G. J. Le Beau, “Enhanced analyses of plume impingement during Shuttle-Mir docking using a combined CFD and DSMC methodology,” in *31st Thermophysics Conference, New Orleans, LA*, p. 1877, 1996.

- [113] K. H. Lee, S. N. Lee, M. J. Yu, S. K. Kim, and S. W. Baek, “Combined Analysis of Thruster Plume Behavior in Rarefied Region by Preconditioned Navier-Stokes and DSMC Methods,” *Transactions of the Japan Society for Aeronautical and Space Sciences*, vol. 52, no. 177, pp. 135–143, 2009.
- [114] J. D. George, *A Combined CFD-DSMC Method for Numerical Simulation of Nozzle Plume Flows*. PhD thesis, Cornell University, 2000.
- [115] I. Boyd and J. Stark, “Modeling of a Small Hydrazine Thruster Plume in the Transition Flow Regime,” *Journal of Propulsion and Power*, vol. 6, no. 2, pp. 121–126, 1990.
- [116] H. Legge and R.-D. Boettcher, “Modelling Control Thruster Plume Flow and Impingement,” in *Rarefied Gas Dynamics* (O. Belotserkovskii, M. Kogan, S. Kutateladze, and A. Rebrov, eds.), pp. 983–992, Springer, Boston, 1985.
- [117] R. Hoffman, A. Kawasaki, H. Trinks, I. Bindemann, and W. Ewering, “The CONTAM 3.2 plume flowfield Analysis and contamination prediction computer program-analysis model and experimental verification,” in *20th Thermophysics Conference*, p. 928, 1985.
- [118] I. Boyd and J. Stark, “Assessment of Impingement Effects in the Isentropic Core of a Small Satellite Control Thruster Plume,” *Proceedings of the Institution of Mechanical Engineers, Part G: Journal of Aerospace Engineering*, vol. 203, no. 2, pp. 97–103, 1989.
- [119] M. Mehta, F. Canabal, S. B. Tashakkor, and S. D. Smith, “Numerical Base Heating Sensitivity Study for a Four-Rocket Engine Core Configuration,” *Journal of Spacecraft and Rockets*, vol. 50, no. 3, pp. 509–526, 2013.
- [120] D. Rault, “Methodology for Thruster Plume Simulation and Impingement Effects Characterization Using DSMC,” in *30th Thermophysics Conference*, p. 2032, 1995.
- [121] I. D. Boyd, P. F. Penko, D. L. Meissner, and K. J. DeWitt, “Experimental and Numerical Investigations of Low-Density Nozzle and Plume Flows of Nitrogen,” *AIAA Journal*, vol. 30, no. 10, pp. 2453–2461, 1992.
- [122] D. S. Liechty, “Modifications to Axially Symmetric Simulations Using New DSMC (2007) Algorithms,” in *AIP Conference Proceedings*, vol. 1084, pp. 251–256, American Institute of Physics, 2008.

- [123] S. A. Schaaf and P. A. Chambre, *Flow of Rarefied Gases*. Princeton, New Jersey, Princeton University Press, 1961.
- [124] G. A. Simons, “Effect of Nozzle Boundary Layers on Rocket Exhaust Plumes,” *AIAA Journal*, vol. 10, no. 11, pp. 1534–1535, 1972.
- [125] L. Roberts, “The Action of a Hypersonic Jet on a Dusty Surface,” *Institute of the Aerospace Sciences*, pp. 63–50, 1963.
- [126] L. Roberts, “The Interaction of a Rocket Exhaust with the Lunar Surface,” *Agard the Fluid Dyn. Aspects of Space Flight*, vol. 2, 1966.
- [127] A. B. Morris, *Simulation of Rocket Plume Impingement and Dust Dispersal on the Lunar Surface*. PhD thesis, University of Texas at Austin, 2012.
- [128] G. Koppenwallner, “Scaling laws for rarefied plume interference with application to satellite thrusters,” in *14th International Symposium on Space Technology and Science, Tokyo, Japan*, pp. 505–512, 1984.
- [129] N. Deen, M. V. S. Annaland, M. A. Van der Hoef, and J. Kuipers, “Review of discrete particle modeling of fluidized beds,” *Chemical Engineering Science*, vol. 62, no. 1-2, pp. 28–44, 2007.
- [130] G. Batchelor, “A new theory of the instability of a uniform fluidized bed,” *Journal of Fluid Mechanics*, vol. 193, pp. 75–110, 1988.
- [131] F. A. Williams, *Combustion Theory*. CRC Press, Taylor & Francis Group, Boca Raton, FL, 2018.
- [132] S. Elghobashi, “Particle-laden turbulent flows: direct simulation and closure models,” in *Computational Fluid Dynamics for the Petrochemical Process Industry* (R. Oliemans, ed.), pp. 91–104, Springer, Dordrecht, 1991.
- [133] M. A. van der Hoef, M. Ye, M. van Sint Annaland, A. Andrews, S. Sundaresan, and J. Kuipers, “Multiscale Modeling of Gas-Fluidized Beds,” *Advances in Chemical Engineering*, vol. 31, pp. 65–149, 2006.
- [134] T. Anderson and R. Jackson, “A FLUID MECHANICAL DESCRIPTION OF FLUIDIZED BEDS. Equations of Motion,” *Industrial & Engineering Chemistry Fundamentals*, vol. 6, no. 4, pp. 527–539, 1967.
- [135] J. M. Burt, *Monte Carlo Simulation of Solid Rocket Exhaust Plumes at High Altitude*. PhD thesis, University of Michigan, 2006.

- [136] B. J. Alder and T. E. Wainwright, "Phase Transition for a Hard Sphere System," *The Journal of Chemical Physics*, vol. 27, no. 5, pp. 1208–1209, 1957.
- [137] P. A. Cundall and O. D. Strack, "A discrete numerical model for granular assemblies," *Géotechnique*, vol. 29, no. 1, pp. 47–65, 1979.
- [138] J. Hueser, F. Brock, L. Melfi, J. R., and G. Bird, "Analysis of large solid propellant rocket engine exhaust plumes using the direct simulation Monte Carlo method," in *22nd Aerospace Sciences Meeting*, p. 496, 1984.
- [139] M. A. Gallis, J. R. Torczynski, and D. J. Rader, "An approach for simulating the transport of spherical particles in a rarefied gas flow via the direct simulation Monte Carlo method," *Physics of Fluids*, vol. 13, no. 11, pp. 3482–3492, 2001.
- [140] P. S. Epstein, "On the Resistance Experienced by Spheres in their Motion through Gases," *Physical Review*, vol. 23, no. 6, p. 710, 1924.
- [141] M. J. Baines, I. P. Williams, A. S. Asebiomo, and R. L. Agacy, "Resistance to the Motion of a Small Sphere Moving Through a Gas," *Monthly Notices of the Royal Astronomical Society*, vol. 130, no. 1, pp. 63–74, 1965.
- [142] L. Waldmann, "Über die Kraft eines inhomogenen Gases auf kleine suspendierte Kugeln," *Zeitschrift für Naturforschung A*, vol. 14, no. 7, pp. 589–599, 1959.
- [143] L. Talbot, R. K. Cheng, R. W. Schefer, and D. R. Willis, "Thermophoresis of particles in a heated boundary layer," *Journal of Fluid Mechanics*, vol. 101, no. 4, pp. 737–758, 1980.
- [144] L. Lees, "A Kinetic Theory Description of Rarefied Gas Flows," tech. rep., Hypersonic Research Project, Memorandum No. 51, Guggenheim Aeronautical Laboratory, California Institute of Technology, 1959.
- [145] W. F. Phillips, "Thermal Force on Spherical Particles in a Rarefied Gas," *The Physics of Fluids*, vol. 15, no. 6, pp. 999–1003, 1972.
- [146] R. G. Lord, "Some extensions to the Cercignani–Lampis gas–surface scattering kernel," *Physics of Fluids A: Fluid Dynamics*, vol. 3, no. 4, pp. 706–710, 1991.

- [147] J. M. Burt and I. D. Boyd, “Evaluation of a Monte Carlo Model for Two Phase Rarefied Flows,” in *36 th AIAA Thermophysics Conference*, no. AIAA 2003-3496, 2003.
- [148] J. Burt and I. Boyd, “Development of a Two-Way Coupled Model for Two Phase Rarefied Flows,” in *42nd AIAA Aerospace Sciences Meeting and Exhibit*, no. AIAA 2004-1351, 2004.
- [149] R. L. Jackson, I. Green, and D. B. Marghitu, “Predicting the coefficient of restitution of impacting elastic-perfectly plastic spheres,” *Nonlinear Dynamics*, vol. 60, no. 3, pp. 217–229, 2010.
- [150] L. Li, R. Mei, J. F. Klausner, and D. W. Hahn, “Heat Transfer Between Colliding Surfaces and Particles,” *Journal of Heat Transfer*, vol. 134, no. 1, 2012.
- [151] J. M. Levins and T. K. Vanderlick, “Impact of Roughness on the Deformation and Adhesion of a Rough Metal and Smooth Mica in Contact,” *The Journal of Physical Chemistry*, vol. 99, no. 14, pp. 5067–5076, 1995.
- [152] K. N. G. Fuller and D. Tabor, “The effect of surface roughness on the adhesion of elastic solids,” *Proceedings of the Royal Society A. Mathematical, Physical, and Engineering Sciences*, vol. 345, no. 1642, pp. 327–342, 1975.
- [153] F. Restagno, J. Crassous, C. Cottin-Bizonne, and E. Charlaix, “Adhesion between weakly rough beads,” *Physical Review E*, vol. 65, no. 4, p. 042301, 2002.
- [154] X. Li, M. Dong, D. Jiang, S. Li, and Y. Shang, “The effect of surface roughness on normal restitution coefficient, adhesion force and friction coefficient of the particle-wall collision,” *Powder Technology*, vol. 362, pp. 17–25, 2020.
- [155] Y. I. Rabinovich, J. J. Adler, A. Ata, R. K. Singh, and B. M. Moudgil, “Adhesion between Nanoscale Rough Surfaces: II. Measurement and Comparison with Theory,” *Journal of Colloid and Interface Science*, vol. 232, no. 1, pp. 17–24, 2000.
- [156] H. Rumpf, *Particle Technology*. Chapman & Hall, London, 1990.
- [157] T. L. Bergman, F. P. Incropera, D. P. DeWitt, and A. S. Lavine, *Fundamentals of Heat and Mass Transfer*. John Wiley & Sons, 2011.
- [158] G. Israel and S. Friedlander, “High-speed beams of small particles,” *Journal of Colloid and Interface Science*, vol. 24, no. 3, pp. 330–337, 1967.

- [159] J. Burt, *Monte Carlo Simulation of Solid Rocket Exhaust Plumes at High Altitude*. PhD thesis, University of Michigan, 2006.
- [160] A. Z. Yeganeh, M. Jadidi, C. Moreau, and A. Dolatabadi, “Numerical modeling of aerosol deposition process,” *Surface and Coatings Technology*, vol. 370, pp. 269–287, 2019.
- [161] D. Hanft, J. Exner, M. Schubert, T. Stöcker, P. Fuierer, and R. Moos, “An Overview of the Aerosol Deposition Method: Process Fundamentals and New Trends in Materials Applications,” *Journal of Ceramic Science Technology*, vol. 6, no. 3, pp. 147–182, 2015.
- [162] S. Kashu, E. Fuchita, T. Manabe, and C. Hayashi, “Deposition of ultra fine particles using a gas jet,” *Japanese journal of applied physics*, vol. 23, no. 12A, p. L910, 1984.
- [163] J. Akedo, M. Ichiki, K. Kikuchi, and R. Maeda, “Jet molding system for realization of three-dimensional micro-structures,” *Sensors and Actuators A: Physical*, vol. 69, no. 1, pp. 106–112, 1998.
- [164] J. Akedo, Masaakiichiki, and R. Maeda, “New functional ceramic deposition method for MEMS,” *Ferroelectrics*, vol. 224, no. 1, pp. 331–337, 1999.
- [165] J. Akedo and M. Lebedev, “Microstructure and Electrical Properties of Lead Zirconate Titanate ( $\text{Pb}(\text{Zr}_{52}/\text{Ti}_{48})\text{O}_3$ ) Thick Films Deposited by Aerosol Deposition Method,” *Japanese Journal of Applied Physics*, vol. 38, no. 9S, p. 5397, 1999.
- [166] R. Greendyke, S. McCaslin, C. Hedge, and C. Hollenshead, “Simulation of Aerosol Deposition by Hybrid DSMC/MD Methods,” in *41st Aerospace Sciences Meeting and Exhibit*, no. AIAA 2013-1029, 2003.
- [167] G. Palaniswaamy and S. K. Loyalka, “Direct simulation Monte Carlo aerosol dynamics: Collisional sampling algorithms,” *Annals of Nuclear Energy*, vol. 34, no. 1, pp. 13–21, 2007.
- [168] I. Saldivar, F. De La Torre Aguilar, M. Boraas, and S. K. Loyalka, “Benchmark problems in aerosol evolution: Comparison of some exact and DSMC results,” *Annals of Nuclear Energy*, vol. 117, pp. 213–222, 2018.
- [169] C. Li, N. Singh, A. Andrews, B. A. Olson, T. E. Schwartzentruber, and C. J. Hogan-Jr., “Mass, momentum, and energy transfer in supersonic aerosol



- deposition processes,” *International Journal of Heat and Mass Transfer*, vol. 129, pp. 1161–1171, 2019.
- [170] Y. Kim, J. Kim, J.-W. Han, and J. Choi, “Multiscale mechanics of yttria film formation during plasma spray coating,” *Applied Surface Science*, vol. 572, p. 151416, 2022.
- [171] C.-y. Wu, L.-y. Li, and C. Thornton, “Rebound behaviour of spheres for plastic impacts,” *International Journal of Impact Engineering*, vol. 28, no. 9, pp. 929–946, 2003.
- [172] J. Sun and M. M. Chen, “A theoretical analysis of heat transfer due to particle impact,” *International Journal of Heat and Mass Transfer*, vol. 31, no. 5, pp. 969–975, 1988.
- [173] J. H. Zhou, A. B. Yu, and M. Horio, “Finite element modeling of the transient heat conduction between colliding particles,” *Chemical Engineering Journal*, vol. 139, no. 3, pp. 510–516, 2008.